Form Approved
OMB No 0704-0188

1. AG

29 MARCH 1994

3. REPORT TYPE AND DATES COVERED
FINAL 30 Sep 91 - 1 Jan 94

4. TITLE AND SUBTITLE
(U) NONLINEAR ACOUSTIC PROCESSES IN A SOLID ROCKET ENGINE

5. FUNDING NUMBERS
PE-61102F
PR-2308
SA-A1
G-AFOSR-89-0023

6. AUTHOR(S)
DAVID R. KASSOY
KADIR KIRKKOPN, QING ZHAO

7. PERFORMING ORGANIZATION NAME(S) AND ADDRESS(ES)
CENTER FOR COMBUSTION RESEARCH
DEPT OF MECHANICAL ENGINEERING
UNIVERSITY OF COLORADO AT BOULDER
BOULDER, CO 80309-0427

8. PERFORMING ORGANIZATION REPORT NUMBER

AFOSR-TR- 94 0653

9. SPONSORING / MONITORING AGENCY NAME(S) AND ADDRESS(ES)
AFOSR/NA
110 DUNCAN AVENUE, SUITE B115
BOLLING AFB DC 20332-0001

10. SPONSORING / MONITORING AGENCY REPORT NUMBER

11. SUPPLEMENTARY NOTES
APPROVED FOR PUBLIC RELEASE;
DISTRIBUTION IS UNLIMITED

12a. DISTRIBUTION / AVAILABILITY STATEMENT

A

12b. DISTRIBUTION CODE

13. ABSTRACT (Maximum 200 words)

A new formulation for chamber flow dynamics in a model of solid rocket engine shows that vorticity generation and convection are prominent physical features of the flow field. Analytical and fully computational methods are employed to describe a basically inviscid interaction between acoustic disturbances arising from specified boundary disturbances and a sidewall injected flow field which simulates propellant burning. The mathematical model, based on the Navier-Stokes equations, is developed in terms of an initial value problem in order to describe the complete, natural chamber flow evolution arising from boundary driven disturbances. The approach is analogous to a direct numerical simulation, although contemporary perturbation methods are employed to extract specific spatial and temporal scales from the equations and boundary conditions. The results show that large unsteady vorticity is created at the injected surface (sidewall) and convects into the cylinder with the radial component of the injection flow velocity.

14. SUBJECT TERMS
ACOUSTIC INSTABILITY, ROCKETS, NONLINEAR

15. NUMBER OF PAGES
52

16. PRICE CODE

17. SECURITY CLASSIFICATION OF REPORT	18. SECURITY CLASSIFICATION OF THIS PAGE	19. SECURITY CLASSIFICATION OF ABSTRACT	20. LIMITATION OF ABSTRACT
UNCLASSIFIED	UNCLASSIFIED	UNCLASSIFIED	UNCLASSIFIED

Center for Combustion Research

NONLINEAR ACOUSTIC PROCESSES IN A SOLID ROCKET ENGINE

Grant No. AFOSR-89-0023

Final Technical Report

prepared for

Dr. Mitat Birkan

Air Force Office of Scientific Research

David R. Kassoy, Kadir Kirkkopru, and Qing Zhao

March 29, 1994

Center for Combustion Research
Department of Mechanical Engineering
University of Colorado at Boulder
Boulder, CO 80309-0427

University of Colorado at Boulder

NONLINEAR ACOUSTIC PROCESSES IN A SOLID ROCKET ENGINE

Grant No. AFOSR-89-0023

Final Technical Report

prepared for

Dr. Mitat Birkan

Air Force Office of Scientific Research

David R. Kassoy, Kadir Kirkkopru, and Qing Zhao

March 29, 1994

Center for Combustion Research
Department of Mechanical Engineering
University of Colorado at Boulder
Boulder, CO 80309-0427

Contents

1. Abstract

A new formulation for chamber flow dynamics in a model of solid rocket engine shows that vorticity generation and convection are prominent physical features of the flow field. Analytical and fully computational methods are employed to describe a basically inviscid interaction between acoustic disturbances arising from specified boundary disturbances and a sidewall injected flow field which simulates propellant burning. The mathematical model, based on the Navier-Stokes equations, is developed in terms of an initial value problem in order to describe the complete, natural chamber flow evolution arising from boundary driven disturbances. The approach is analogous to a direct numerical simulation, although con porary perturbation methods are employed to extract specific spatial and temporal scales from the equations and boundary conditions. The results show that large unsteady vorticity is created at the injected surface (sidewall) and convects into the cylinder with the radial component of the injection flow velocity. Eventually, the entire chamber is filled with an intense, rotational flow field containing relatively large velocity gradients. The presence of significant distributed vorticity calls into question the predictions of traditional acoustic stability theory, based on a fundamentally irrotational concept. The flow field predicted by the present theory includes an essentially acoustic pressure distribution, and a velocity distribution composed of a weakly rotational steady component, an irrotational acoustic component and a strongly rotational, weakly nonlinear and viscous component. The high Reynolds number, low Mach number flow field has many similarities to a conventionally defined internal turbulent flow.

2. Project Objectives, Status and Accomplishments

Our research program is concerned with modelling transient flow dynamics in a solid rocket engine chamber. Gaseous mass addition from propellant burning is simulated by fluid injection through the internal wall of a cylinder with one closed end. The impact of spatially distributed burning rate transients and/or igniter processes on the evolving chamber flow is assessed from the perspective of an initial value problem. In particular, chamber flow disturbances are created by specifically defined, spatially distributed, time dependent variations of injection velocity or pressure on boundary surfaces. Solution development is based on analytical and computational methods, using a route analogous to direct numerical simulation (DNS), where the entire natural evolution of the chamber dynamics is described. This paradigm shift from more familiar acoustic stability theory has enabled us to recognize the presence of new and pertinent physical phenomena in the chamber flow. In particular, we demonstrate that vorticity is generated near the injection (burning propellant) surface and transported into the entire chamber by the injected flow field. The presence of significant levels of time-dependent vorticity in the chamber has three important consequences. First, traditional acoustic stability theory, involving a primarily irrotational disturbance flow field, cannot describe the rotational fields found in our analysis. Secondly, the shear stress near the propellant surface is relatively large (compared with that for a time averaged mean flow) and may be an important source of scouring of the exposed, degraded propellant surface. Finally, the time-dependent rotational flow field in our high Reynolds number, low Mach number chamber has similarities to turbulent flow as traditionally conceived.

During the project period, our own research progress enabled us to create very specific programmatic objectives:

1. Employ the complete equations of motion in an initial value analysis to study the evolution of chamber flow transients initiated by specified boundary driven disturbances.

2. Use perturbation methods, based on viable parameter extremes (large Reynolds number, small Mach number), to prove that; (1) unsteady vorticity is created

on the injection surface by an inviscid interaction between acoustic waves and the injected velocity field, and (2) the vorticity is convected into the chamber by the radial component of the injected velocity.

3. Demonstrate the impact of relatively weak nonlinearity and viscous effects on the spatial distribution of the transient vorticity.

4. Relate the present modelling approach for solid rocket engine chamber dynamics to the traditional acoustic stability theory.

The present modelling effort is used to demonstrate how and where unsteady vorticity is created by an interaction between axially propagating acoustic waves and a flow field caused by steady sidewall mass injection in a finite length cylinder. Additionally, the formulation and analysis describes the transport and time-history of the spatial distribution of vorticity within the cylinder. Finally, the results show that transient rotational flow effects are crucial to the evolution and stability of internal fluid dynamics when the characteristic cylinder Reynolds number (Re) and Mach number (M) are very large and small, respectively.

The mathematical model first describes a steady flow field in a cylinder with one closed end, induced by strong normal, steady sidewall injection. In particular, the injected flow is characterized by a radial speed much larger than the ratio of the characteristic axial speed to $Re^{1/2}$. Following Taylor (1956), Culick (1966) shows that the steady flow is described in a first approximation by an inviscid, rotational equation system. Axial acoustic disturbances of $O(M)$ are created by either a prescribed time-dependent axial velocity variation at the closed end of the cylinder or a similar pressure variation on an exit boundary upstream of the chamber nozzle. They propagate through the basic inviscid shear flow field, and perhaps unexpectedly, create significant unsteady vorticity at the surface of the porous cylinder. The radial component of the steady injected flow field carries the vorticity into the entire cylinder. Earlier related work (Wang and Kassoy, 1992 a,b) demonstrates that refraction of the primary axial waves can generate oblique and even transverse wave disturbances that propagate through the shear flow.

Predictions of flow dynamics in closely related systems have been obtained in the past from traditional acoustic stability theory as formulated and described by Grad (1949). Culick and co-workers, (See Culick (1990) for a comprehensive review) in particular, have developed since the mid-1970's an increasingly sophisticated linear and weakly nonlinear stability theory to describe disturbance behavior observed in laboratory experiments and practical systems like solid rocket engine chambers. Comparisons with experiments appear to be reasonably good, although the theory as formulated cannot describe the generation and evolution of vorticity.

Recent experimental (Brown et al. 1986a,b, Brown and Shaeffer, 1992) and computational (Vuillot and Avalon,1991; Vuillot,1991) studies include definitive evidence of significant transient rotational flow structures distributed throughout the injected cylinder flow. In addition, Price and Flandro (1993) and Flandro and Roach (1992) have formulated approximate mathematical models for describing the generation and evolution of vorticity in an injected cylinder flow field. These contributions provide the motivation for developing a comprehensive flow dynamics model which includes both the irrotational acoustical phenomena of traditional stability theory and important rotational flow effects.

Stability predictions for these flow systems are usually obtained from mathematical models that reflect linear and weakly nonlinear, inviscid, irrotational acoustic concepts (see Culick, 1990, Williams,1985, Price and Flandro, 1993, Jahnke and Culick, 1993). The basic acoustic waves propagate through a fluid at rest, in the first approximation, and are described in terms of Fourier series of eigenfunctions that satisfy ' tally impermeable boundary conditions. Strictly speaking , these solutions do not accomodate sidewall injection nor exit plane flow at the downstream end of the cylinder. As a result the model cannot account for an interaction between the acoustic signals and a sidewall injected cylinder flow, now known to be a source of vorticity generation (Flandro and Roach,1992).

Flandro (1974) recognized that rotational flow effects play a role in relatively thin acoustic boundary layers where viscosity is of significance. Related studies for inert flows have been carried out by Tien (1972), Flandro (1986), Hegde et al.(1986) and Price and Flandro (1993). Chemically and thermally active acoustic boundary layer flows are described by Hegde and Zinn (1986), Sankar et al.(1988a,b), Chen et al. (1990) and Matta and Zinn (1993). In these studies the boundary layer responds passively to externally imposed disturbances. The investigations are motivated by a need to understand how energy is exchanged between the acoustic disturbances and mean flow as fluid injected normally from the wall is turned towards the axial direction. Until recently, conceptual understanding of this flow turning process has been based largely on the viscous properties of the thin acoustic boundary layer.

Significant efforts have been made to develop computational models for acoustic boundary layer processes. Baum and Levine(1987), Baum (1990), Vuillot and Avalon (1991) and Vuillot (1991) have employed complete Navier-Stokes solvers to evaluate the general cylinder flow response to imposed disturbances. The last two cited works in particular demonstrate that rotational disturbances can exist in a substantial portion of the cylinder for appropriate values of Re and M. In other words, the vorticity distribution is not always confined to the traditional, viscous acoustic boundary layer adjacent to the cylinder wall. Rather, for appropriate parameter ranges it appears to

be convected from the wall, out into the main portion of the basically inviscid cylinder flow by the mean injected flow field. Clearly, the pervasive presence of vortical structures in the internal flow field has significant consequences for the conceptual validity of traditional irrotational acoustic stability models.

The presence of rotational inviscid "acoustic" disturbances in a laboratory flow field was first implied by the experiments of Brown et al. (1986a,b) and Brown and Shaeffer (1992). The book manuscript of Price and Flandro (1993) contains an important discussion of these issues, and several idealized mathematical models are used to predict the structure of basically inviscid , but weakly viscous, vortical flow structures. More recently, Flandro and Roach (1992) have extended the theoretical effort to generate a purely inviscid model for boundary generated rotational disturbances that arise from an inviscid interaction between an injected flow field and axial, planar pressure waves propagating in the cylinder. Here again the vortical structures are convected out into the cylinder by the radial component of the injected velocity field. The length scale of the local vorticity variation is O(M) smaller than the cylinder radius, implying that viscous shear stress may be important on the local level. This work suggests that the interaction of "acoustic disturbances" with a strongly injected flow field leads to the presence of important vortical structure in the entire flow field.

Zhao and Kassoy (1994) and Zhao et al. (1994) (see Appendices (a) and (b)) provide an initial step in formulating a rational mathematical model for internal flow dynamics which incorporates both acoustic phenomena and vorticity distributions. Perturbation methods are used to derive systematic approximations to the complete compressible Navier-Stokes equations. An initial-boundary value approach is used to formulate a generalized unsteady mathematical model capable of describing both non-resonant and resonant time history of solutions. The boundary disturbance is an $O(M)$ axial, harmonic velocity variation on the closed end wall. The complete axial velocity is found from a superposition of three components of equal magnituide. First, the steady component arises from a solution to inviscid, rotational Euler equations known by Culick (1966). Secondly, there is a planar irrotational acoustic field, derived from a traditional linear wave equation which satisfies boundary conditions at the closed and open ends of the cylinder. Finally, the rotational, weakly nonlinear viscous component varies on two disparate length scales. The global spatial distribution occurs on the radial length scale, while locally there are velocity gradients on a scale O(M) smaller. As a result the vorticity of the transient field is $O(M^{-1})$ larger than that in the steady field. The convection of the vorticity is found to be described by a linear equation. Most significantly, the diffusion of vorticity on the shorter length scale is described by a nonlinear diffusion equation. Solutions are found numerically by using a finite difference method, as well as semi-analytically with a Galerkin-like

method developed by Wang and Kassoy (1990a,b,c, 1992a,b, 1993).

Evaluation and interpretation of the full results show that rather complex vorticity distributions are present throughout the cylinder. Initially, the vorticity is confined to a growing region between the sidewall and a well defined front propagating toward the cylinder axis with the local radial steady speed. The region between the front and the axis contains the weakly vortical steady flow along with the irrotational acoustic solution. Eventually, the entire chamber flow is filled with vorticity which vanishes only on the axis.

Fully computational methods are used by Kirkkopru et al.(1994) (see Appendix c) to provide qualitative supporting evidence for the solutions described in Appendices a and b. In this case the driving disturbance is a harmonic pressure transient applied on the downstream exit plane of the cylinder. Grid size and spatial distribution are chosen to accomodate the multiple lengthscale structure known from the formulation exercise. The unsteady rotational component of the axial velocity is extracted from the total value found from a MacCormack scheme. Solution properties and characteristics are identical to those found previously and support the basic concepts of vorticity generation and transport.

Results obtained to date are associated with single frequency harmonic boundary forcing. Even then the time response curves for the total axial velocity are surprisingly complex, resulting from a combination of the expected acoustic response and the newly described rotational component. One may speculate that multiple frequency drivers, and/or those with greater complexity of spatial distribution will generate pointwise time response curves with considerable irregularity, perhaps reminiscent of a turbulent flow. In fact, it should be recognized that the calculated or computed rotational velocity field has certain characteristics and properties that are similar to those of a turbulent flow.

One is observing the evolution of a primarily inviscid, rotational, unsteady flow associated with a large Reynolds number. The weakly viscous effect has an impact on the shorter length scale, and the rotational flow distribution is weakly nonlinear. Given that the results are obtained from a quasi-analytical initial value analysis, the evolving flow field is described much like that in a direct numerical simulation. The front separates a strongly rotational flow from one that is characterized by an irrotational acoustic field. Although not shown in the present work, we now know that if disturbances are generated directly by sidewall injection transients of sufficient spatial complexity, the front morphology can be quite corrugated. As a result, one can find intermittent regions of strongly rotational unsteady flow on an axial traverse at a fixed radial distance from the wall. In the present theoretical framework the front configuration can actually be described analytically !

3. Bibliography

Baum,J.D.(1990), (personal communication), "Energy Exchange Mechanisms Between the Mean and Acoustic Fields in a Simulated Rocket Combustor," AFOSR Contractors Meeting, Atlanta, GA, June.

Brown, R. S., Blackner, A. M., Willoughby, P. G., and Dunlap, R.(1986a) " Coupling Between Acoustic Velocity oscillations and Solid Propellant Combustion", *J. Propulsion and Power*, **2**,428-437.

Brown,R.S., Blackner,A.M., Willoughby,P.G., and Dunlap,R.(1986b) "Coupling Between Velocity Oscillations and Solid Propellant Combustion," AIAA Paper 86-0531, AIAA Aerospace Sciences Meeting, January 1986.

Brown,R.S.and Shaeffer,C.W. (1992) (personal communication) " Oscillatory Internal Flow Field Studies," AFOSR Contractors Meeting in Propulsion, LaJolla, California, June 1992.

Chen, T., Hegde, U., and Zinn, B. (1990) "Driving of axial acoustic fields by side wall stabilized diffusion flames," AIAA 90-0037, AIAA Aerospace Sciences Meeting, January.

Culick, F.E.C. (1966),"Rotational Axisymmetric Mean Flow and Damping of Acoustic Waves in Solid Propellant Rocket", *AIAA J.* **4**,1462-1463.

Culick, F.E.C. (1990)" Some Recent Results for Nonlinear Acoustics in Combustion Chambers," AIAA 90-3927, Aeroacoustics Conference, October.

Flandro, G.A. (1974)"Solid Propellant Admittance Correction," *J. Sound and Vibration*, **36**, No.22 97-312.

Flandro, G.A., (1986) "Vortex Driving Mechanism in Oscillatory Rocket Flows,"*J. Prop. Pow*, **2**, 2,206-214.

Flandro, G.A. and Roach, R.L. (1992) (personal communication) *Effects of Vorticity Production on Acoustic Waves in a Combustion Chamber.* Final Technical Report AFOSR-90-0159

Grad, H.(1949) " Resonance Burning in Rocket Motors, " *Comm. Pure Appl. Math.*, **2**, 79-102.

Hegde, U. G., Chen, F., and Zinn, B. T. (1986) " Investigation of the Acoustic Boundary Layer in Porous-Walled Ducts with flow," *AIAA J.* **24**, 1474-1482.

Hegde, U.G. and Zinn,B.T. (1986), "The Acoustic Boundary Layer in Porous-Walled Ducts with a reacting flow," 21st Symp. (Int'l.) Combust. 1993-2000

Jahnke, C.C. and Culick, F.E.C.(1993) " An Application of Dynamical Systems Theroy to Nonlinear Combustion Instabilities, "AIAA-93-0114, 31st Aerospace Sciences Meeting, Reno NV.,January.

Kirkkopru, K., Kassoy, D. R. and Zhao, Q. (1994) "Unsteady Vorticity Generation and Evolution in a Model of a Solid Rocket Engine Chamber". *submitted to the AIAA J.*

Matta, L.M. and Zinn, B.T. (1993) " Investigation of Flow Turning Loss in a Simulated Unstable Solid Propellant Rocket Motor," AIAA 93-0115,31st Aerospace Sciences Meeting, Reno, NV, January.

Price, E.W. and Flandro, G.A. (1993) *Combustion Instability in Solid Propellant Rockets.* Book manuscript in preparation.

Sankar, S.V., Hegde, U.G., Jagoda, J.I., and Zinn, B.T.(1988a) "Driving of Axial Acoustic Waves by side wall Stabilized Premixed Flames", 22nd Symp. (Int'l) on Combustion, 1865-1873

Sankar, S.V., Jagoda, J.I., Daniel, B.R., and Zinn, B.T.(1988b) "Measured and Predicted Characteristics of Premixed Flames Stabilized in Axial Acoustic Field," AIAA 88-0541, AIAA Aerospace Sciences Meeting, January.

Taylor,G.I. (1956) "Fluid Flow in Regions Bounded by Porous Surfaces," *Proc. Roy. Soc.* London **A 234**,456-475

Tien, J.S. (1972) "Oscillatory Burning of Solid Propellant; including Gas Phase Time Lag", *Comb. Science and Tech.***5**, 47-54.

Vuillot,F. and Avalon,G. (1991) "Acoustic Boundary Layers in Solid Propellant Rocket Motors Using Navier-Stokes Equations", *J.Propulsion* **7**,#2 231-239.

Vuillot,F.(1991) " Numerical Computation of Acoustic Boundary Layers in Large Solid Propellant Space Booster," AIAA-91-0206, 29th Aerospace Sciences Meeting, Reno, NV, January.

Wang, M. and Kassoy, D. R. (1990a) "Dynamic response of an inert gas to slow piston acceleration," *J. Acoust. Soc. Am rica* **87**,1466-1472

Wang, M. and Kassoy, D. R. (1990b) "Dynamic compression and weak shock formation in an inert gas due to fast piston acceleration," *J. Fluid Mech.***220**, 267-292.

Wang, M. and Kassoy, D. R. (1990c) "Evolution of weakly nonlinear waves in a cylinder with a movable piston," *J. Fluid Mech.* **221**, 23-52.

Wang, M. and Kassoy, D. R. (1992a) "Transient acoustic processes in a low Mach number shear flow," *J. Fluid Mech.* **238**, 509-536.

Wang, M. and Kassoy, D. R.(1992b) " Standing Acoustic Waves in a Low Mach Number Shear Flow," *AIAA J.* **30**, 1708-1715.

Wang, M. and Kassoy, D. R. (1993) " Nonlinear Acoustic Oscillation in Resonant System: An Initial-Boundary Value Study", *submitted to SIAM J. Appl. Math.*

Williams, F.A.(1985) *Combustion Theory*, Benjamin/Cummings, Menlo Park.

Zhao, Q. and Kassoy, D.R.(1994), " The Generation and Evolution of Unsteady Vorticity in a Model of a Solid Rocket Engine Chamber ", *AIAA 94-0779*, 32nd Aerospace Sciences Meeting, Reno NV, January 1994.

Zhao, Q., Kassoy, D.R. and Kirkkopru, K.(1994)," Nonlinear Vorticity Generation by Acoustic Wave Interaction with an Injected Gas Velocity Field in a Cylinder ", *submitted to the J. Fluid Mech.*

4. Project Personnel

1. **David R. Kassoy**, Principal Investigator, Associate Vice Chancellor for Academic Affairs, Professor of Mechanical Engineering, University of Colorado at Boulder.

2. **Kadir Kirkkopru**, Research Associate, Assoc. Professor of Mechanical Engineering, Istanbul Technical University (permanent position).

3. **Qing Zhao** , Research Assistant, Graduate Student, Department of Mechanical Engineering, University of Colorado at Boulder, PhD degree expected in August 1994.

5. Publications

The following technical documents have been completed with support from AFOSR for the study of flow dynamics in solid rocket engine chambers:

1. Wang, M. and Kassoy, D. R. (1992), Transient acoustic processes in a low Mach number shear flow, *J. Fluid Mech.* **238**, 509-536.

2. Wang, M. and Kassoy, D. R.(1992), Standing Acoustic Waves in a Low Mach Number Shear Flow, *AIAA J.* **30**, 1708-1715.

3. Wang, M. and Kassoy, D. R. (1993), Nonlinear Acoustic Oscillation in a Resonant System: An Initial-Boundary Value Study, *submitted to SIAM J. Appl. Math.*

4. Zhao, Q. and Kassoy, D.R.(1994), The Generation and Evolution of Unsteady Vorticity in a Model of a Solid Rocket Engine Chamber, *AIAA 94-0779*, 32nd Aerospace Sciences Meeting, Reno NV, January 1994.

5. Zhao, Q., Kassoy, D.R. and Kirkkopru, K.(1994), Nonlinear Vorticity Generation by Acoustic Wave Interaction with an Injected Gas Velocity Field in a Cylinder, *submitted to the J. Fluid Mech.*

6. Kirkkopru, K., Kassoy, D.R. and Zhao, Q. (1994), Unsteady Vorticity Generation and Evolution in a Model of a Solid Rocket Engine Chamber, *submitted to the AIAA J.*

6. Papers Presented

1. 1991

   (a) Division of Fluid Dynamics Meeting, American Physical Society, Nov. 25 1991, Scottsdale, AZ; " Resonant Acoustic Oscillations in Shear Flows".

2. 1992

   (a) AFOSR Contractors Meeting, June 10, 1992, La Jolla, CA; " Vorticity Generation in Solid Rocket Engines".

   (b) Division of Fluid Dynamics Meeting, American Physical Society, Nov. 22 1992, Tallahassee, Fl; " Nonlinear Evolution of Acoustic Resonances in Open and Closed Tubes".

3. 1993

   (a) AFOSR Contractors Meeting, June 14-18, 1993, Atlantic City, N.J.; " Nonlinear Acoustic Processes in Solid Rocket Engines".

   (b) Program in Applied Mathematics, University of Colorado, August 17-19, 1993; " Vorticity Generation in Models of Solid Rocket Engines".

   (c) Division of Fluid Dynamics Meeting, American Physical Society, Nov. 21 1993, Albuquerque, N.M.; " Nonlinear Vorticity Generation by Acoustic Wave Interaction with an Injected Gas in a Tube: Formulation and Analysis", " Nonlinear Vorticity Generation by Acoustic Wave Interaction with an Injected Gas in a Tube: Computational Results".

   (d) Center for Combustion Research, Mechanical Engineering Department, University of Colorado, November 30, 1993; " Nonlinear Unsteady Vorticity Generation in a Model of a Solid Rocket Engine Chamber".

4. 1994

   (a) AIAA Aerospace Sciences Meeting, January 10-13, 1994, Reno, NV.;" The Generation and Evolution of Unsteady Vorticity in a Model of a Solid Rocket Engine Chamber".

7. Appendices: Technical Manuscripts

Appendix a

The Generation and Evolution of Unsteady Vorticity in a Model of a Solid Rocket Engine Chamber

AIAA 94-0779

The Generation and Evolution of Unsteady Vorticity in a Model of a Solid Rocket Engine Chamber

Q. Zhao and D. R. Kassoy
University of Colorado at Boulder
Boulder, CO

32nd Aerospace Sciences Meeting & Exhibit
January 10-13, 1994 / Reno, NV

The Generation and Evolution of Unsteady Vorticity in a Model of a Solid Rocket Engine Chamber *

Q. Zhao and D. R. Kassoy†
Mechanical Engineering Department; Center for Combustion Research
University of Colorado at Boulder; Boulder,CO 80309-0427‡

Abstract

A mathematical model is formulated to describe the initiation and evolution of vorticity in a low Mach number (M), weakly viscous internal flow sustained by mass addition through the side wall of a long, narrow cylinder. An O(M) acoustical disturbance, generated by a prescribed harmonic transient endwall velocity, interacts with the basically inviscid rotational steady injected flow to generate time dependent vorticity at the wall. The steady radial velocity component convects the vorticity into the chamber. The axial velocity associated with the vorticity field varies across the cylinder radius and in particular has an instantaneous oscillatory spatial distribution with a characteristic wave length $\overline{O(M)}$ smaller than the radius. As the spatial structures are convected from the wall toward the axis, weak viscous effects cause the vorticity to diffuse. The magnitude of the vorticity distribution in the transient field is much larger than that in the steady flow because the velocity gradients associated with the former occur on the smaller length scale.

An initial-boundary value formulation is employed and a finite difference scheme is used to find the nonlinear unsteady solutions when a pressure node exists at the downstream exit of the cylinder. The complete velocity consists of a superposition of the steady flow, an acoustic (irrotational) field and the vortical component, all of the same magnitude. Results for the velocity solutions are given when the endwall driving frequency is nonresonant. Time response output at a given location shows that the complete axial velocity field can be quite irregular, particularly if the end wall driving frequency is high. The formulation and results provide a conceptual framwork for the study of solid rocket engine chamber flow dynamics which supplements traditional acoustic stability theory by providing information about the generation and evolution of vortical structures.

1 Introduction

Predictions of flow dynamics in solid rocket engine chambers have been obtained in the past from acoustic stability theory, first formulated and described by Grad[1]. Culick and co-workers, (See Culick[2] for a comprehensive review) in particular, have developed since mid-1970's an increasingly sophisticated linear and weakly nonlinear stability theory to describe disturbance behavior observed in laboratory and full-scale engines. Comparisons of predicted pressure transients with those in experiments appear to be reasonably good.

Recent experimental measurements (Brown et al[3-4]., Brown and Shaeffer[5],) and computational predictions (Vuillot and Avalon[6]; Vuillot[7]) of velocity profiles show definitive evidence of significant rotational flow structures distributed throughout the engine chamber. In addition, Price and Flandro[8] and Flandro and Roach[9] have formulated approximate mathematical models for describing the generation and evolution of vorticity in analogies of solid rocket engine chamber. These contributions provide the motivation for developing a comprehensive chamber flow dynamics model which includes both the irrotational acoustical phenomena of traditional stability theory and important rotational flow structure.

Solid rocket engine stability predictions are usually

*Research is supported by the Air Force Office of Scientific Research through AFOSR 89-0023

†mailing address: Graduate School B-26; University of Colorado at Boulder; Boulder, CO 80309

obtained from mathematical models that reflect linear and weakly nonlinear, inviscid, irrotational acoustic concepts (Culick[10-19]; William[20]; Price and Flandro [8]). The basic acoustic waves propagate through a fluid at rest, in the first approximation, and are described in terms of Fourier series of eigenfunctions that satisfy totally impermeable boundary conditions. Strictly speaking, these eigenfunctions do not accomodate side wall injection (propellant gasification) nor chamber exit plane flow (upstream of the nozzle). As a result the model cannot account for an interaction between the acoustic signals and a sidewall injected chamber flow, now known to be a source of vorticity generation (Flandro and Roach[9]).

Flandro[21] recognised that rotational flow effects play a role in acoustic boundary layers where viscosity is of some significance. Related studies for inert flows have been carried out by Tien[22], Flandro[23], Hegde et al[24]. and Price and Flandro[8]. Chemically and thermally active acoustic boundary layer flows are described by Hegde and Zinn[25], Sankar et al[26-27]., Chen et al.[28] and Matta and Zinn[29]. In these studies the boundary layer responds passively to externally imposed disturbances. The investigation are motivated by a need to understand the energy exchange between acoustic disturbances and the mean flow as the normally injected fluid is turned towards the axial direction. Until recently, conceptual understanding of flow turning has been based largely on the viscous properties of the thin acoustic boundary layer.

Significant efforts have been made to develop computational models for acoustic boundary processes. Baum and Levine[30], Baum[31], Vuillot and Avalon[6] and Vuillot[7] have employed complete Navier-Stokes solvers to evaluate the general chamber flow response to imposed disturbances. The last two cited works in particular demonstrate that rotational disturbances exist in a substantial portion of the chamber flow. In other words, vorticity distributions are not confined to traditional, viscous acoustic boundary layers adjacent to the chamber wall. Rather, they appear to be convected by the mean injected flow field from the wall out into the main portion of the basically inviscid chamber flow. Clearly, the pervasive presence of vortical structures in the chamber flow field has significant consequences for the conceptual validity of traditional irrotational acoustic stability models.

The presence of rotational inviscid "acoustic" disturbances in a model (cold flow) chamber flow was first inferred from the experiments of Brown et al.[3-4] and Shaeffer and Brown[5]. The book manuscript of Price and Flandro[8] contains an important discussion of these issues, and several mathematical models are used to predict the structure of basically inviscid , but weakly viscous, vortical flow structures. More recently, Flandro and Roach[9] have extended the theoretical effort to generate a purely inviscid model for boundary generated rotational disturbances that arise from an inviscid interaction between an injected flow field and axial, planar pressure waves propagating in the chamber. Here again the vortical structures are convected out into the chamber by the radial component of the injected velocity field. The length scale of the local vorticity variation is O(M) smaller than the chamber radius. This work suggests that the interaction of "acoustic disturbances" with a strongly injected flow field leads to the presence of important vortical structure in the entire flow field of a model solid rocket engine.

These rotational flow models also demonstrate unequivocally that the velocity field near the wall is a composite of an axial planar, irrotational acoustic flow and a rotational flow. The short wave length transverse spatial oscillations of the axial disturbance velocity, seen in the numerical results of Vuillot and Avalon[6] as well as more clearly in the theory of Flandro and Roach [9] provide a transition between the wall and a traditional planar, axial acoustic driving disturbance present near the axis. This suggests that the concept of velocity coupling should be reconsidered, or perhaps replaced by an improved understanding of rotational, basically inviscid disturbance processes adjacent to a burning propellant surface.

The present study is an initial step in formulating a mathematical model for solid rocket engine chamber flow dynamics which incorporates both acoustic phenomena and vortical flow structures. A low Mach number (M), large Reynolds number (Re) internal flow, sustained by constant steady mass addition through the wall of a long narrow cylinder, is disturbed by an O(M) harmonic, transient endwall velocity. Acoustic waves created by the boundary disturbance interact with the basically inviscid rotational injected flow field to create vorticity on the wall. The vorticity is convected into the cylinder by the radial component of the steady injected flow field although the flow structure is altered locally by nonlinear and viscous effects.

Perturbation methods are used to derive systematic approximations to the complete compressible Navier-Stokes equations. An initial-boundary value approach is used to formulate a generalised unsteady

mathematical model capable of describing the complete time history of solutions. Fourier series representations of the velocity and pressure are obtained in terms of eigenfunctions that satisfy all the prescribed boundary conditions. The complete axial velocity is found from a superposition of three components of comparable magnituide. First, the steady component arises from a solution to inviscid, rotational Euler equations known by Culick[10]. Secondly, there is a planar irrotational acoustic field, derived from a traditional linear wave equation. Finally, there is a rotational, weakly viscous component which varies on two distinctly different length scales. The global spatial distribution occurs on the radial length scale, while locally there are velocity gradients on a scale O(M) smaller. As a result the vorticity of the transient field is $O(M^{-1})$ larger than that in the steady field. The convection of the vorticity is found to be described by a linear equation. Most significantly, the diffusion of vorticity on the shorter length scale is described by a nonlinear equation. It is demonstrated that the global spatial distribution on the radial length scale arises from the interaction between the "acoustic disturbance" and the strongly injected flow field present in the solid rocket chamber. The nonlinear and viscous effects are of quantitative importance,but do not have much impact on the overall flow structure.

Solutions are found by invoking a direct finite difference scheme and a Galerkin-like method used by Wang and Kassoy [33–38]. In the latter case, a coupled, infinite system of ordinary differential equations for Fourier coefficients is truncated systematically to find solutions in terms of a finite mode representation. The two different approaches enable us to compare results for the same cases, providing a means by which one can verify the results.

Evaluation and interpretation of the full results show that rather complex vortical structures are present throughtout the cylinder sufficiently long after the disturbance is initiated at the end wall. When the input from several different Fourier modes is important, the time response curves are quite irregular and could be mistaken for "turbulent" response.

2 Mathematical Formulation

The geometrical configuration for a cylindrical chamber with side wall injection is shown schematically in Figure 1. in which L' is the axial length and D' is the diameter. The radius R' is related to D' by $D' = 2R'$. The complete non-dimensional equations describing the fluid dynamics and acoustics for an axisymmetric system can be written in the form

$$\frac{\partial \rho}{\partial t} + M\left[\frac{1}{r}\frac{\partial(\rho r V_r)}{\partial r} + \frac{\partial(\rho V_z)}{\partial z}\right] = 0, \tag{1}$$

$$\begin{aligned}\rho\frac{DV_r}{Dt} &= -\delta^2\frac{1}{\gamma M}\frac{\partial P}{\partial r} \\ &+\delta^2\frac{M}{Re}\left\{\frac{\partial}{\partial z}\mu\left[\frac{1}{\delta^2}\frac{\partial V_r}{\partial z} + \frac{\partial V_z}{\partial r}\right]\right. \\ &+2\frac{\partial}{\partial r}\mu\left[\frac{\partial V_r}{\partial r} - \frac{1}{3}\left(\frac{1}{r}\frac{(rV_r)}{\partial r} + \frac{\partial V_z}{\partial z}\right)\right] \\ &\left.+\frac{2\mu}{r}\left[\frac{\partial V_r}{\partial r} - \frac{V_r}{r}\right]\right\},\end{aligned} \tag{2}$$

$$\begin{aligned}\rho\frac{DV_z}{Dt} &= -\frac{1}{\gamma M}\frac{\partial P}{\partial z} \\ &+\delta^2\frac{M}{Re}\left\{\frac{\mu}{r}\left[\frac{1}{\delta^2}\frac{\partial V_r}{\partial z} + \frac{\partial V_z}{\partial r}\right]\right. \\ &\left.+\frac{\partial}{\partial r}\mu\left[\frac{1}{\delta^2}\frac{\partial V_r}{\partial z} + \frac{\partial V_z}{\partial r}\right]\right\} + 2\frac{M}{Re}\frac{\partial}{\partial z}\mu \\ &\left[\frac{\partial V_z}{\partial z} - \frac{1}{3}\left(\frac{1}{r}\frac{(rV_r)}{\partial r} + \frac{\partial V_z}{\partial z}\right)\right],\end{aligned} \tag{3}$$

$$\begin{aligned}\rho C_v\frac{DT}{Dt} &= -(\gamma-1)MP\left[\frac{1}{r}\frac{\partial(rV_r)}{\partial r} + \frac{\partial V_z}{\partial z}\right] \\ &+\frac{M}{Re}\frac{\gamma}{Pr}\left[\frac{1}{r}\frac{\partial}{\partial z}\left(kr\frac{\partial T}{\partial z}\right)\right. \\ &\left.+\delta^2\frac{1}{r}\frac{\partial}{\partial r}\left(kr\frac{\partial T}{\partial r}\right)\right] + \Phi,\end{aligned} \tag{4}$$

$$P = \rho T \tag{5}$$

where

$$\frac{D}{Dt} = \frac{\partial}{\partial t} + M\left(V_r\frac{\partial}{\partial r} + V_z\frac{\partial}{\partial z}\right),$$

and Φ is the viscous dissipation function. The non-dimensional variables are defined in terms of dimensional quantities (with a prime) by

$$\rho = \frac{\rho'}{\rho_0'}, P = \frac{p'}{p_0'}, T = \frac{T'}{T_0'}, V_r = \frac{V_r'}{V_{r0}'},$$

$$V_z = \frac{V_z'}{V_{z0}'}, z = \frac{z'}{L'}, r = \frac{r'}{R'}, t = \frac{t'}{t_c'},$$

$$k = \frac{k'}{k_0'}, \mu = \frac{\mu'}{\mu_0'}, C_v = \frac{C_v'}{C_{v0}'}. \quad (6)$$

The reference value p_0' measures the basic static pressure in the chamber, while the analogous density and temperature values ρ_0', T_0', respectively, represent properties of the fluid injected from the walls. The characteristic injection speed V_{r0}' is related to the characteristic axial speed V_{z0}' by the approximate mass conservation relationship $V_{z0}' = \delta V_{r0}'$ where the aspect ratio $\delta = \frac{L'}{R'}$. Characteristic length scales for the axial and radial dimensions are defined by L' and R' respectively. Time is nondimensionalized with respect to the axial acoustic time $t_a' = \frac{L'}{C_0'}$, where $C_0' = (\gamma R' T_0')^{\frac{1}{2}}$ is the characteristic sound speed. The reference material properties k_0', μ_0' and C_{v0}' are defined at temperature T_0'. The parameter γ is the ratio of specific heats and

$$Re = \frac{\rho_0' V_{z0}' L'}{\mu_0'}, Pr = \frac{\mu_0' C_{p0}'}{k_0'}, M = \frac{V_{z0}'}{C_0'}, \quad (7)$$

where typically the Prandtl number Pr= O(1), the axial Mach number $M \ll 1$ and axial Reynolds number $Re \gg 1$ in the chamber.

Initially, the steady flow in the system is driven by a spatially distributed normal injection from the wall where the no-slip condition is satisfied. Symmetry prevails along the axis at the cylinder. The closed end of the cylinder is impermeable, and the exit is assumed to be a pressure node. The latter assumption is a mathematical modelling convenience. The boundary conditions may be written as

$$r = 0; \quad V_r = \frac{\partial V_z}{\partial r} = 0,$$

$$r = 1; \; V_r = -V_{rw}(z), \; V_z = 0, \; T = 1 \quad (8)$$

$$z = 0; \; V_z = 0, \; z = 1; \; P = 1. \quad (9)$$

Flow disturbances are created at $z = 0$ by imposing a harmonic end wall disturbance in the axial velocity which is independent of the radial coordinate;

$$z = 0; \; V_z = A \sin \omega t, t \geq 0; \; 0 \leq r \leq 1, \quad (10)$$

where the amplitude A=O(1).

It should be noted that the imposed disturbance on the left end wall is comparable in magnitude to that of the steady axial speed. As a result this fluid system will be weakly nonlinear, and the theory developed here differs from traditional linear small disturbance theory.

The injection rate is characteristic of the gasification velocity created by solid propellant burning. Large injection prevails, in the sense that $V_{r0}' \gg \frac{V_{z0}'}{Re^{\frac{1}{2}}}$ (Cole and Aroesty[39]), which implies that $Re \gg \delta^2$, where $\delta \gg 1$ is used to describe a long, narrow chamber.

3 Steady State Flow

The steady state flow generated by time independent mass addition on the side wall can be described in terms of the variables:

$$(P, \rho, T) \sim 1 + M^2(P_{0s}, \rho_{0s}, T_{0s}) + \cdots,$$

$$(V_z, V_r) \sim (V_{z0s}, V_{r0s}) + \cdots \quad (11)$$

Equation (11) can be used in (1)—(6) to find the leading order equations valid for the limit M→0, describing an inviscid rotational flow that satisfies

$$\frac{1}{r}\frac{\partial (r V_{r0s})}{\partial r} + \frac{\partial V_{z0s}}{\partial z} = 0 \quad (12)$$

$$P_{0s} = P_{0s}(z) \quad (13)$$

$$V_{r0s}\frac{\partial V_{z0s}}{\partial r} + V_{z0s}\frac{\partial V_{z0s}}{\partial z} = -\frac{1}{\gamma}\frac{\partial P_{0s}}{\partial z}, \quad (14)$$

and boundary conditions in (8)-(9). The transport terms are excluded from the leading order equations because $\frac{Re}{\delta^2} \gg 1$. Equation (13) arises because the aspect ratio $\delta \gg 1$. The solutions for the radial and axial velocity, as well as the pressure distribution can be written in the form

$$V_{r0s} = -\frac{V_{rw}(z)}{r}\sin(\tfrac{\pi}{2}r^2),$$

$$V_{z0s} = \left(\pi \int_0^z V_{rw}(\tau)d\tau\right)\cos(\tfrac{\pi}{2}r^2), \quad (15)$$

$$P_{0s} = \gamma\pi^2 \int_z^1 \left[V_{rw}(\hat{z}) \int_0^{\hat{z}} V_{rw}(\tau)d\tau\right] d\hat{z}, \quad (16)$$

where $-V_{rw}(z)$ is an arbitary time-independent side wall injection distribution. Related solutions can be found in Culick[10], Price and Flandro[8] and Flandro and Roach[9].

4 Rotational Flow Across the Cylinder

4.1 Problem statement

The objective now is to develop a mathematical model for the disturbance evolution when weak rotational effects are significant across the entire cylinder. The asymptotic expansions for the velocity components and thermodynamic variables are

$$V_z \sim V_{z0_s}(z,r) + \sum_{n=0} M^n V_{zn}(z,r,t) \qquad (17)$$

$$V_r \sim V_{r0_s}(z,r) + \sum_{n=0} M^n V_{rn}(z,r,t) \qquad (18)$$

$$(P,\rho,T) \sim 1 + M \sum_{n=0} M^n (P_n,\rho_n,\theta_n) \qquad (19)$$

It is recognised that two disparate length scales are important; the tube radius and a much shorter length associated with the radial distance traveled by a fluid particle on the acoustic timescale. A multiple scale analysis will be carried out in terms of the variables r_1 and r_2 defined by

$$r_1 = 1 - r; \qquad r_2 = \int_0^{r_1} \frac{1}{-MV_{r0_s}(\sigma)} d\sigma. \qquad (20)$$

The second transformation includes an integral of the steady radial velocity field for the case of constant steady wall injection $V_{r_w} = 1$. The integral transformation simplifies the describing equations considerably. It is noted that when the center line is approached, $r_1 \to 1$, the integral diverges and $r_2 \to \infty$.

The partial derivatives with respect to r in equations (1)-(5) must be replaced by

$$\left(\frac{\partial}{\partial r}\right) = -\left(\frac{\partial}{\partial r_1}\right) + \frac{1}{MV_{r0_s}}\left(\frac{\partial}{\partial r_2}\right), \qquad (21)$$

$$\left(\frac{\partial^2}{\partial r^2}\right) = \left(\frac{\partial^2}{\partial r_1^2}\right) - \left(\frac{2}{MV_{r0_s}}\frac{\partial^2}{\partial r_1 \partial r_2}\right) + \left(\frac{1}{MV_{r0_s}}\right)^2 \left(\frac{\partial^2}{\partial r_2^2}\right) + \frac{1}{MV_{r0_s}^2}\frac{\partial V_{r0_s}}{\partial r_1}\left(\frac{\partial}{\partial r_2}\right). \qquad (22)$$

4.2 Lowest order mathematical model

The relations (7)—(19) can be substituted into (1)—(5) to find the leading order equations in the limit $M \to 0$. First, the spatially homogeneous boundary forcing in (10) and the condition $\delta \gg 1$ imply that $V_{r0} = 0$. Then,

$$\frac{\partial R_0}{\partial t} + \frac{\partial R_0}{\partial r_2} = -\frac{\partial V_{z0}}{\partial z} - \left(\frac{1}{V_{r0_s}}\right)\frac{\partial V_{r1}}{\partial r_2}, \qquad (23)$$

$$\frac{\partial V_{z0}}{\partial t} + \frac{\partial V_{z0}}{\partial r_2} = -\frac{1}{\gamma}\frac{\partial P_0}{\partial z}, \qquad (24)$$

$$\frac{\partial P_0}{\partial r_1} = \frac{\partial P_0}{\partial r_2} = 0, \qquad (25)$$

$$\frac{\partial \theta_0}{\partial t} + \frac{\partial \theta_0}{\partial r_2} = \frac{(\gamma-1)}{\gamma}\frac{\partial P_0}{\partial t}, \qquad (26)$$

$$P_0 = R_0 + \theta_0. \qquad (27)$$

Following a procedure related to that described by Lagerstrom[40], and similar to that employed by Price and Flandro[8] and Flandro and Roach[9], the variables, except for P_0, are divided into irrotational planar and rotational nonplanar parts,

$$V_{z0} = W_{0p}(z,t) + \hat{W}_0(z,t,r_1,r_2), \qquad (28)$$

$$R_0 = R_{0p}(z,t) + \hat{R}_0(z,t,r_1,r_2), \qquad (29)$$

$$\theta_0 = \theta_{0p}(z,t) + \hat{\theta}_0(z,t,r_1,r_2). \qquad (30)$$

When (28)—(30) are used in (23)—(27), the planar equations are found to be in the form

$$\frac{\partial R_{0p}}{\partial t} = -\frac{\partial W_{0p}}{\partial z}, \qquad (31)$$

$$\frac{\partial W_{0p}}{\partial t} = -\frac{1}{\gamma}\frac{\partial P_0}{\partial z}, \qquad (32)$$

$$\frac{\partial \theta_{0p}}{\partial t} = \frac{\gamma-1}{\gamma}\frac{\partial P_0}{\partial t}, \qquad (33)$$

$$P_0 = R_{0p} + \theta_{0p} \qquad (34)$$

The initial/boundary conditions are given by:

$$t = 0, \quad W_{0p} = 0, \quad \frac{\partial W_{0p}}{\partial t} = 0, \qquad (35)$$

$$z = 0, \quad W_{0p} = \sin\omega t; \qquad (36)$$

$$z = 1, \quad \frac{\partial W_{0p}}{\partial z} = 0. \qquad (37)$$

The nonresonant acoustic solution for the planar contribution is

$$W_{0p}(t,z) = -\frac{1}{\gamma}\sum_{n=1}^{\infty} a_n \left(\frac{\lambda_n}{\omega}\sin(\omega t)\right.$$

$$- \sin(\lambda_n t)) \sin(\lambda_n z), \lambda_n \neq \omega, \quad (38)$$

$$P_0(t,z) = \sum_{n=1}^{\infty} a_n \left(-\cos(\omega t) + \cos(\lambda_n t)\right) \cos(\lambda_n z), \lambda_n \neq \omega, \quad (39)$$

$$P_0 = \gamma R_{0p} \quad (40)$$

where $a_n = -\frac{2\gamma\omega}{\lambda_n^2 - \omega^2}$ and $\lambda_n = (n - \frac{1}{2})\pi$. The first terms in the sums of (38) and (39) arise from the forcing at frequency ω, and the second terms describes the eigenfunction response. Only the nonresonant case will be considered in the present work.

The equations for the rotational components are

$$\frac{\partial \hat{R}_0}{\partial t} + \frac{\partial \hat{R}_0}{\partial r_2} = -\frac{\partial \hat{W}_0}{\partial z} - \left(\frac{1}{V_{r0_s}}\right) \frac{\partial V_{r1}}{\partial r_2}, \quad (41)$$

$$\frac{\partial \hat{W}_0}{\partial t} + \frac{\partial \hat{W}_0}{\partial r_2} = 0, \quad (42)$$

$$\frac{\partial \hat{\theta}_0}{\partial t} + \frac{\partial \hat{\theta}_0}{\partial r_2} = 0, \quad (43)$$

$$\hat{R}_0 + \hat{\theta}_0 = 0. \quad (44)$$

Equations (43) and (44) can be combined to show that the leading order vortical flow is incompressible:

$$\frac{\partial \hat{R}_0}{\partial t} + \frac{\partial \hat{R}_0}{\partial r_2} = 0 \quad (45)$$

Therefore, equation (41)—(44) can be rewritten in simpler forms

$$\frac{\partial \hat{W}_0}{\partial z} + \left(\frac{1}{V_{r0_s}}\right) \frac{\partial V_{r1}}{\partial r_2} = 0, \quad (46)$$

$$\frac{\partial \hat{W}_0}{\partial t} + \frac{\partial \hat{W}_0}{\partial r_2} = 0, \quad (47)$$

$$\frac{\partial \hat{\theta}_0}{\partial t} + \frac{\partial \hat{\theta}_0}{\partial r_2} = 0, \quad (48)$$

$$\hat{R}_0 + \hat{\theta}_0 = 0. \quad (49)$$

and must be solved with respect to the initial and boundary conditions:

$$t = 0; \quad \hat{W}_0 = 0, \quad \frac{\partial \hat{W}_0}{\partial t} = 0, \quad (50)$$

$$z = 0; \quad \hat{W}_0 = 0, \quad (51)$$

$$z = 1; \quad \frac{\partial \hat{W}_0}{\partial z} = 0, \quad (52)$$

$$r_1 = 1, \ r_2 \to \infty; \frac{\partial \hat{W}_0}{\partial r_2} = 0, \quad \frac{\partial \hat{\theta}_0}{\partial r_2} = 0, \quad (53)$$

$$r_1 = r_2 = 0; \hat{W}_0 = -W_{0p}(t,z), \hat{\theta}_0 = -\theta_{0p}(t,z) \quad (54)$$

Equation (54) corresponds to the no-slip condition and isothermal flow injection. Equations (42), (43) and (45) show that $\hat{W}_0$, $\hat{\theta}_0$ and $\hat{R}_0$ are invariant on a characteristic line defined by

$$\eta = t - r_2, \quad (55)$$

but vary across the η lines. The $r_1 = 0$ line enters the chamber at $t = 0$ through side wall ($r_2 = 0$) and subsequently, at $t = c$, $\eta = c$ appears at $r_2 = 0$. At a particular time T, constant η lines, which range from 0 to T, are transported toward the axis by convection at the local radial steady velocity.

The inviscid equation in (42) can be combined with the first of (54) to show that the wall is a source of vorticity because

$$\frac{\partial \hat{W}_0(t,z,0,0)}{\partial r_2} = -\frac{\partial \hat{W}_0}{\partial t} = \frac{\partial W_{0p}(t,z)}{\partial t} \quad (56)$$

where W_{0p} is known from (38). It is noted that the largest unsteady nondimensional vorticity term is given by $\Omega_\theta = (\frac{1}{M V_{r0_s}}) \frac{\partial \hat{W}_0}{\partial r_2}$. The parameter, $\frac{1}{M}$, arises from large gradients occuring in the spatially oscillatory velocity profile on the short length scale r_2. Equation (47) also shows that the vorticity generated at the wall is convected into the cylinder by the steady radial velocity field $V_{r0_s}(r)$.

In general solutions to the inviscid first order hyperbolic equations in (47)–(49) can be written symbolically as,

$$\hat{W}_0 = \hat{W}_0(\eta, r_1, z), \qquad \eta = t - r_2 \quad (57)$$

$$\hat{\theta}_0 = \hat{\theta}_0(\eta, r_1, z) = -\hat{R}_0, \quad (58)$$

In order to derive the explicit functional dependence of the variables, higher order equations need to be investigated. Once $\hat{W}_0$ is found, then the mass conservation equation (46) can be integrated with respect to r_2 to find the radial velocity V_{r1}. The vortical temperature and density fields can be found using related methods.

4.3 Higher order consideration

Equations (17)—(19) can be combined with (1)—(5) to find the O(M) equation set. The same procedure used to find the leading order solution is employed so that the variables, except for P_1, are divided into irrotational planar and rotational nonplanar parts,

$$V_{z1} = W_{1p}(z,t) + \hat{W}_1(z,t,r_1,r_2), \quad (59)$$

$$R_1 = R_{1p}(z,t) + \hat{R}_1(z,t,r_1,r_2), \quad (60)$$

$$\theta_1 = \theta_{1p}(z,t) + \hat{\theta}_1(z,t,r_1,r_2). \quad (61)$$

The planar, acoustic equations,

$$\frac{\partial R_{1p}}{\partial t} + \frac{\partial (R_{0p} W_{0P})}{\partial z} = -\frac{\partial W_{1p}}{\partial z}, \quad (62)$$

$$\frac{\partial W_{1p}}{\partial t} = -W_{0p}\frac{\partial W_{0p}}{\partial z} - \frac{1}{\gamma}\frac{\partial (P_1 - P_{0s})}{\partial z} + \frac{1}{\gamma} R_{0p}\frac{\partial P_0}{\partial z}, \quad (63)$$

$$\frac{\partial \theta_{1p}}{\partial t} = -R_{0p}\frac{\gamma-1}{\gamma}\frac{\partial P_0}{\partial t} - (\gamma-1)\frac{\partial W_{1p}}{\partial z} - P_0(\gamma-1)\frac{\partial R_{0p}}{\partial t}, \quad (64)$$

$$P_1 = R_{1p} + \theta_{1p} + R_{0p}\theta_{0p} \quad (65)$$

are not considered further here.

The largest possible viscous effect occurs when $\delta^2/\mathrm{Re}{=}M^2$ and leads to the higher order rotational equation for axial momentum

$$\frac{\partial \hat{W}_1}{\partial t} + \frac{\partial \hat{W}_1}{\partial r_2} = \frac{1}{V_{r0s}^2}\frac{\partial^2 \hat{W}_0}{\partial r_2^2} + \frac{1}{\gamma}\hat{R}_0\frac{\partial P_0}{\partial z} - (V_{z0s} + V_{z0})\frac{\partial (V_{z0s} + V_{z0})}{\partial z} + V_{z0s}\frac{\partial V_{z0s}}{\partial z} + W_{0p}\frac{\partial W_{0p}}{\partial z} + V_{r0s}\frac{\partial (V_{z0s} + V_{z0})}{\partial r_1} - \left(\frac{V_{r1}}{V_{r0s}}\right)\frac{\partial V_{z0}}{\partial r_2} - V_{r0s}\frac{\partial V_{z0s}}{\partial r_1}. \quad (66)$$

It is (66) that will give us information about the behaviour of the leading order axial speed solution.

If the transformation of the coordinate system from (t, r_1, r_2, z) to (η, r_1, r_2, z) is made, then the derivatives with respect to t and r_2 must be replaced by

$$\left(\frac{\partial}{\partial t}\right) = \left(\frac{\partial}{\partial \eta}\right)_{r_2}, \quad (67)$$

$$\left(\frac{\partial}{\partial r_2}\right) = \left(\frac{\partial}{\partial r_2}\right)_{\eta} - \left(\frac{\partial}{\partial \eta}\right)_{r_2}, \quad (68)$$

It follows that (66) can be written as

$$\left.\frac{\partial \hat{W}_1}{\partial r_2}\right|_{\eta} = \frac{1}{V_{r0s}^2}\frac{\partial^2 \hat{W}_0}{\partial \eta^2} - V_{z0}\frac{\partial (V_{z0s} + \hat{W}_0)}{\partial z} - \hat{W}_0\frac{\partial \hat{W}_0}{\partial z} - \frac{1}{V_{r0s}}\left[\frac{\partial (V_{r1}\hat{W}_0)}{\partial r_2} - \frac{\partial (V_{r1}\hat{W}_0)}{\partial \eta}\right] - V_{z0s}\frac{\partial V_{z0}}{\partial z} - \hat{W}_0\frac{\partial W_{0p}}{\partial z} + V_{r0s}\frac{\partial \hat{W}_0}{\partial r_1} + \frac{1}{\gamma}\hat{R}_0\frac{\partial P_0}{\partial z}, \quad (69)$$

An integration of (69) with respect to r_2, holding η, r_1 and z fixed will generate secular growth in r_2 unless certain terms are suppressed. In considering the impact of each term, it is important to remember that the harmonic t-dependence of the planar acoustic solutions in (38)-(40) must be rewritten in terms of η and r_2 by using the transformation $\eta = t - r_2$ in (55). When written in the coordinate system (z, t, r_1, r_2) the suppressed terms take the form;

$$\frac{1}{V_{r0s}^2}\frac{\partial^2 \hat{W}_0}{\partial r_2^2} + V_{r0s}\frac{\partial \hat{W}_0}{\partial r_1} - 2\hat{W}_0\frac{\partial \hat{W}_0}{\partial z} - \hat{W}_0\frac{\partial V_{z0s}}{\partial z} - V_{z0s}\frac{\partial W_0}{\partial z} = 0, \quad (70)$$

which is a nonlinear diffusion equation for the rotational axial velocity $\hat{W}_0$ with a time-like variable r_1. The solution for $\hat{W}_0$ must satisfy an "initial" condition:

$$\hat{W}_0(t, z, r_1 = 0, r_2) = -W_{0p}(\eta, z) \qquad \eta > 0$$
$$= \tfrac{1}{\gamma}\textstyle\sum_{n=1}^{\infty} a_n \left(\frac{\lambda_n}{\omega}\sin(\omega\eta) - \sin(\lambda_n\eta)\right)\sin(\lambda_n z), \lambda_n \neq \omega,$$
$$\hat{W}_0(t, z, r_1 = 0, r_2) = 0 \qquad \eta < 0 \quad (71)$$

and a boundary condition at the center line:

$$r_2 \longrightarrow \infty, \qquad \frac{\partial \hat{W}_0}{\partial r_2} = 0. \quad (72)$$

In addition a condition must be specified on $r_1 > 0, r_2 = 0$ which is compatable with (71) at the point $r_1 = r_2 = 0$. This is necessary because r_1 and r_2 are treated as independent variables in (70). The reasonable choice is given by

$$\hat{W}_0(t, z, r_1, r_2 = 0) = -W_{0p}(t, z). \quad (73)$$

The nonlinear term in (70), $\hat{W}_0 \hat{W}_{0z}$ is present in our problem because the $O(M)$ boundary disturbance is larger than that used in earlier, basically linear studies (Flandro and Roach[9]). Its presence suggests that wave steepening, acoustic streaming and other forms of instability may occur in the evolving flow field. If the imposed piston driven disturbance is smaller,and/or axial variations are ignored, then a linear, viscous diffusion equation is derived, which is related to that used by Price and Flandro[8].

Given the forcing condition in (71), one approach to finding the solution to (70) is based on using the eigenfunction set $\{\sin(\lambda_n z)\}, n = 1, 2, \cdots;$

$$\hat{W}_0(t, z, r_1, r_2) = \sum_{n=1}^{\infty} A_n(t, r_1, r_2) \sin(\lambda_n z) \quad (74)$$

Coupled partial differential equations for the Fourier coefficients A_n, are found by using (74) in (70) and invoking orthogonality conditions for the eigenfunction set on the interval [0,1]. The results are;

$$\frac{1}{V_{r0_s}^3} \frac{\partial^2 A_n}{\partial r_2^2} + \frac{\partial A_n}{\partial r_1} - \frac{1}{V_{r0_s}} \frac{\partial V_{z0_s}}{\partial z} A_n - \frac{2}{V_{r0_s}} \left(\sum_{n_1=1}^{\infty} \left[\sum_{n_2=1}^{\infty} a_{nn_1n_2} A_{n_1} A_{n_2} + \left(\frac{V_{z0_s}}{z} \right) b_{nn_1} A_{n_1} \right] \right) = 0 \quad (75)$$

and are subject to;

(a) Initial Condition:

$$A_n(t, r_1 = 0, r_2) = \frac{1}{\gamma} a_n \left(\frac{\lambda_n}{\omega} \sin \omega(t - r_2) - \sin \lambda_n (t - r_2) \right) \quad 0 < r_2 \leq t$$

$$= 0 \quad r_2 > t \quad (76)$$

(b) Boundary Conditions:

$$r_2 \longrightarrow \infty, \quad \frac{\partial A_n}{\partial r_2} = 0 \quad (77)$$

$$A_n(t, r_1, r_2 = 0) = \frac{1}{\gamma} a_n \left(\frac{\lambda_n}{\omega} \sin(\omega t) - \sin(\lambda_n t) \right) \quad (78)$$

where

$$a_{nn_1n_2} = 2\lambda_{n_2} \int_0^1 \sin(\lambda_{n_1} z) \cos(\lambda_{n_2} z) \sin(\lambda_n z) dz \quad (79)$$

$$b_{nn_1} = \lambda_{n_1} \int_0^1 z \cos(\lambda_{n_1} z) \sin(\lambda_n z) dz \quad (80)$$

Equation (75) is a coupled system of quasi-linear diffusion equations with a time like variable r_1, and nonlinear source terms. The physical time t is a parameter of the differential equations, appearing explicitly only in the boundary conditions. Solutions to (75)-(80) are described in Section 6, based on a system truncation approach to find a finite number of A_n's.

A second solution approach is based on a finite difference approximation to (70)-(73). Solutions for $\hat{W}_0(z, t, r_1, r_2)$ are found by employing a second order accurate Adam-Bashforth/Crank-Nicolson scheme. It is relatively easy to implement and can be used to test the accuracy of the truncated mode solution. Most of the results presented here have been found in this way.

5 Finite Difference Solutions for the Nonlinear System

Solutions to (70)-(73) for $\hat{W}_0(z, t, r_1, r_2)$ have been found by using a finite difference method based on the second order accurate $O(\delta r_1^2, \delta r_2^2)$ Adam-Bashforth/Crank-Nicolson scheme. The real solution lies on the locus defined by (20) relating r_1 and r_2. In general this curve does not coincide with the computational grid points. Hence cubic spline interpolations in r_2 are employed at every chosen r_1 value to obtain the desired real solution. The far end boundary condition for $r_2 \rightarrow \infty$ is implemented by providing a sufficiently large number of grid points between the convected outer edge of the rotational layer and the finite location of the computational boundary with respect to r_2. A total of 1000 grid points in the r_2 direction with δr_2=0.1 is chosen. The function and derivatives must remain zero at a significant number of nodes in order to ensure that conditions at the computational boundary do not constrain the solution.

At each value of the "parameter" t, the integration is initiated with the initial conditions in (71), subject to the boundary conditions in (72) and (73) . The spatial distribution of the solution with respect to r_2

evolves as the "time-like" variable r_1 increases. Integration is carried out to a sufficiently large value of r_1 to ensure that adequate data fields $\hat{W}_0(z,t,r_1,r_2)$ are available on the locus curve relating r_1 and r_2 defined by (20). Then the actual solution is found from the intersection of the surface defined by $\hat{W}_0(z,t,r_1,r_2)$ and the vertical plane from the locus curve relating r_1 and r_2.

The first test case studied is for $\omega = 1.0$, which is a nonresonant frequency smaller than the first natural frequency $\lambda_1 = \frac{\pi}{2}$. This particular case allows us to develop a relatively simple solution with minimal computational time.

It is important to resolve the solution in the axial direction by choosing a sufficiently large number of grid points in the z-direction, K_{max}. Solution comparisons for $K_{max} = 9, 21$ and 37 at $t = 40$, M=0.01 and Z=0.25, 0.5 and 0.75 show considerable difference for the smallest number. Excellent comparisons for $K_{max} = 21$ and 37 suggest that the former is adequate for $\omega = 1.0$.

Figures 2,3 and 4b give results for the rotational axial velocity $\hat{W}_0$ as a function of r_1 at s=0.5 when t= 20,30 and 40. At each time, the solution consists of several spatial oscillations and a thin region of exponential damping near a specific radial location $r_{1e}(t)$ beyond which vorticity is exponentially small. For a given value of t, one first finds r_{2e} from $\eta = 0 = t - r_{2e}$ and then uses the inverse of (20) to determine r_{1e}. It should also be noted from the definition of η in (55) and the second of (20) that the front moves at the nondimensional speed $\frac{\partial r}{\partial t}|_{\eta=0} = -MV_{ros}(r)$ which corresponds to the steady radial speed in dimensional terms. The front speed vanishes as the cylinder axis is approached. At $t = 40$ the rotational flow distribution in Figure 4b extends out about 44% of the cylinder radius.

The corresponding scaled vorticity distribution, calculated from $\frac{1}{V_{ros}(r)}\frac{\partial \hat{W}_0}{\partial r_2}$ is given in Figure 5. The dimensionless vorticity Ω_θ, defined below (56) is $O(M^{-1})$. One should note the significant magnitude of the spatial variations in vorticity given the scaling factor $\frac{1}{M}$. The large amplitude is associated with the O(M) length scale of the axial speed gradient and the factor M^{-1}.

The spatial distribution of the axial rotational velocity at each time can be explained in physical terms by considering the interaction between the propagating planar acoustic wave solution, described by (38) and (39), and the steady injected flow field in (15). Fluid particles injected normally from the wall with $V_{rw} = 1$ at a specified z-location experience an approximately harmonic variation in the local pressure gradient given by (39). During periods of negative (positive)gradients the particles are accelerated downstream (upstream). As a result, near the wall one will observe alternating periods of positive and negative axial velocity. The steady radial velocity field carries these alternating regions of forward and reverse flow away from the wall toward the axis. Part of the fluid particle response is purely acoustic. The remainder is given by $\hat{W}_0$. In this sense the spatial pattern of the rotational axial velocity at fixed z as shown in Figures 2,3 and 4b reflects the historical behaviour of the local pressure gradient at the axial location. The O(M) length scale of the transverse spatial oscillations can now be explained easily since the approximately harmonic pressure gradient variation occurs on the acoustic time scale t'_A (for ω=O(1)) during which only limited radial motion is possible.

Two additional results should be noted. The wave length of the spatial oscillations decrease as r_1 increases toward the axis. This occurs because the vorticity front speed (the steady radial velocity) declines as r_1 increases. Finally, a comparison of Figures 4a,b,c demonstrates that the rotaional axial velocity dependes on the axial location as well as the radial location.

Figures 6 shows a "linear" solution for the rotational axial velocity $\hat{W}_0$ as a function of r_1 at t=40, M=0.01 and s=0.5 obtained by solving (70) with nonlinear term $\hat{W}_0\frac{\partial \hat{W}_0}{\partial z}$ reduced by a factor of 10^{-5}. $K_{max} = 21$ is used in the calculation. This calculation is done to assess the impact of the nonlinear convection term on the spatial structure of the solution in Figure 4b. A comparison shows that the nonlinear term has a quantitative effect on the spatial distribution of $\hat{W}_0$, but does not fundamentally control the qualitative spatial oscillations.

Figure 7 is the counterpart to Figure 4b with a reduced viscous effect. In this case (70) is solved with the viscous term, $\frac{1}{V_{ros}^2}\frac{\partial^2 \hat{W}_0}{\partial r_2^2}$, multiplied by a factor of 0.5. The basic patterns of the complete solution in Figure 4 persist. There exist some differences in the amplitudes of the curves in these figures that can be attributed to the viscosity reduction.

Figure 8 and Figure 9 are the counterparts of the nonlinear result in Figure 4b with M=0.05 and 0.1 respectively, and t=40. These Mach numbers are more reflective of the flow conditions in a rocket engine.

One can see that the larger Mach number (stronger blowing) is associated with a thicker unsteady vortical region. The vorticity has filled the entire chamber for M=0.05 and for M=0.1 at t=40 while only 44% of the chamber is filled in Figure 4 with M=0.01. This is expected because of faster radial convection of vorticity by the steady radial velocity. It should be noted that the local velocity gradients are smaller in Figures 8 and 9 so that the magnitude of the unsteady vorticity is similarly reduced for higher Mach number systems. Larger velocity gradients can be obtained at a given Mach number for larger forcing frequency ω.

Figure 10 provides results at $r_1 = 0.2$ for the time-variation of the planar acoustic axial speed W_{0p}, the rotational axial speed $\hat{W}_0$ and their sum V_{z0}, defined in (28), at z=0.5 with $K_{max} = 31$ and M=0.01. It can be seen from Figure 10b that the curve for the rotational solution resembles the planar acoustic response in Figure 10a but differs in amplitude and phase. At $r_1 = 0.2$ the rotational response appears after a delay of almost 18 axial acoustic time units, the time needed for the vorticity wave front initiated at the wall to travel out to the specified radial location. It is noted that the amplitude of the rotational response is a little smaller than that of the acoustic solution. At the location $r_1 = 0.2$, phase differences are relatively small and the sum in Figure 10c shows a total response of significant amplitude. This amplitude will actually increase as r_1 decreases until locations very close to the wall are reached, then the no-slip conditions prevails as $r_1 \rightarrow 0$.

The smaller amplitude vortical radial velocity can be calculated by integrating equation (46). Figure 11 describes the rotational radial velocity V_{r1} as a function of r_1 at t=40, M=0.01 and z= 0.5 . Beyond the vorticity front the transient radial velocity distribution is a known constant multiplying the steady radial velocity.

The second case studied is for a driving frequency $\omega = 2.5$. The solution for $\hat{W}_0$ at t=40, M=0.01 and z=0.5 is given in Figure 12 for $K_{max} = 21$. The absolute maximum amplitude of the $\omega = 1$ solution at z=0.25 is about 4. In comparison, the analogous quantity is a quarter as large for the case $\omega = 2.5$.

The graphs show that the spatial distribution and the time-response curves for $\omega = 1.0$ and 2.5 have similar characteristics. The curves for $\omega = 2.5$ are more irregular than their $\omega = 1.0$ counterparts because the driving frequency is higher. The relative complexity for $\omega = 2.5$ suggests that if a multidimensional irrotational acoustic field were present, involving many Fourier modes, the vortical time-response might be quite irregular. In this sense, one could ask whether "turbulent" responses observed in solid rocket chamber models are caused by wall generated vorticity that is convected into the chamber by the injected field.

6 Modal Solutions to the Nonlinear System

Solutions found from (74)-(80) enable one to demonstrate how the energy is distributed among different Fourier modes. The coefficients $A_n(r_1, r_2)$, n=1-N for specified N, have been found by using a finite difference method based on the same second order accurate $O(\delta r_1^2, \delta r_2^2)$ Adam-Bashforth/Crank-Nicolson scheme. The same procedure applied in finding the solution of $\hat{W}_0$ on the real locus is applied to each one of the $A_n(r_1, r_2)$ to find the solution of $A_n's$ on the real locus. Once the $A_n's$ are known, the solution for $\hat{W}_0$ is found by summing up N modal contributions according to (74). Careful attention must be given to the value of N in order to assure that the solutions are sufficiently accurate. In particular, solutions for $\hat{W}_0$ based on N and $N + L$ modes, $L > 0$, are compared until the results exhibit no appreciable change for an incremental L value. In Figures 13 and 14, 6 and 10 mode solutions for $\hat{W}_0$ vs r_1 at M=0.01,z=0.5 and t=40 for $\omega = 1.0$ have been compared with each other to ascertain that the former are sufficiently resolved, implying that energy are concentrated in the first 6 modes. The comparison of Figures 13 and 14 with Figure 9b reveals that there is little difference between the spatial distribution curve from the 6 mode solution and that from the direct finite difference solution of nonlinear equation with $K_{max} = 21$. This is no coincidence because the grid size in the axial direction for K_{max}=21 is 0.05 which is just small enough to resolve the first six Fourier modes in axial direction according to $(\Delta z)_{max} = \frac{2\pi}{\lambda_n}\frac{1}{10}$, where $\lambda_n = (n - \frac{1}{2})\pi$.

The satisfying comparison between the finite difference and modal solutions provide strong confidence in the characteristic solution properties. Solutions to the former system are less expensive in terms of CPU time and more complete if a sufficient number of grid points are provided in z direction . Solutions to the latter system are able to demonstrate the energy distribution among different modes.

7 Conclusions

Systematic mathematical methods have been employed to formulate a mathematical model for the creation and evolution of rotational flow in an idealised solid rocket engine chamber. Boundary driven axial, planar acoustic waves interact with an inviscid, rotational , injection induced steady flow to produce time dependent vorticity at the sidewall of the cylinder. The vorticity is convected into the entire chamber by the steady radial velocity field.

In contrast to traditional acoustic stability theory, solutions are developed in the context of an initial-boundary value problem, in order to study the natural evolution of the flow disturbances arising from specified boundary forcing. This study parallels typical computational studies of similar problems (Baum and Levine[29]; Vuillot and Avalon[6]; Vuillot[7]). The solutions found in this work describe nonresonant boundary driven disturbances on the axial acoustic time scale of the chamber.

The analysis demonstrates that the chamber flow is basically inviscid and rotational. The axial velocity gradients associated with radial spatial oscillations occur on a short length scale, O(M) less than the radius. Hence the unsteady vorticity distribution in the chamber is the dominant rotational flow effect in comparison to the steady inviscid rotational flow caused by steady side wall injection. The basic unsteady vorticity structure arises from an interaction between the "acoustic disturbance" and the strongly injected flow field. The nonlinear and viscous effects on the O(M) length scale, affect the specific velocity distribution, but have little impact on the overall structure.

Solutions are sought from the direct finite difference calculation of equation (70) and of the Fourier mode presentation (75) compatible with a downstream pressure node boundary condition. The former calculation requires sufficient number of grid points in the axial direction in order to resolve sufficient number of spatial mode in the axial direction. The second system is truncated to find a limited number of Fourier modal amplitudes. As long as the transient flow system is nonresonant (the forcing frequency of the boundary disturbance is not equal to some Fourier mode frequency), one can expect a smooth flow, describable with a relatively small number of grid points in the axial direction or Fourier modes if ω=O(1).

The results in the present work are for nonresonant frequencies $\omega = 1.0$ and $\omega = 2.5$. These cases are chosen because the first several modes dominate the solution and only the first six modes are needed to resolve the flow field in the former case. At $\omega = 2.5$, the energy is more equally distributed among several modes, so that the time response curves (not shown here) are more irregular. This suggests that quite complex time response curves are likely to be found in systems containing complex acoustic wave fields.

The conceptual approach used here can be extended to disturbances driven by sidewall injection transients, reminiscent of burning rate variation in real systems. Further, it is likely that the formulation will be useful for a reconsideration of flow turning and velocity coupling concepts. Finally, the variable scaling reported here will enable the development of more accurate numerical methods.

8 Acknowledgement

The authors would like to thank the Air Force Office of Scientific Research for continuing support through AFROSR 89-0023. A substantial discussion with Professor N. Riley of the University of East Anglia is much appreciated. Professor Gary Flandro was kind enough to provide a copy of his Final Report (Flandro and Roach, 1992). We acknowledge his inspirational contributions to the study of chamber flow dynamics.

REFERENCES

1. Grad,H.(1949) *Comm. Pure Appl. Math.*,2,79-102.

2. Culick, F.E.C. (1990)" Some Recent Results for Nonlinear Acoustics in Combustion Chambers," AIAA 90-3927, Aeroacoustics Conference, October, 1990.

3. Brown,R.S., Blackner,A.M., Willoughby,P.G., and Dunlap,R.(1986a) ,*J. Propulsion and Power*, 2,428-437.

4. Brown,R.S., Blackner,A.M., Willoughby,P.G., and Dunlap,R.(1986b) "Coupling Between Velocity Oscillations and Solid Propellant Combustion," AIAA Paper 86-0531, AIAA Aerospace Sciences Meeting, January 1986.

5. Brown,R.S.and Shaeffer,C.W. (1992)" Oscillatory Internal Flow Field Studies," AFOSR Contractors Meeting in Propulsion, LaJolla, California, June 1992.

6. Vuillot,F. and Avalon,G. (1991) *J.Propulsion* 7,#2 231-239.

7. Vuillot,F.(1991) " Numerical Computation of Acoustic Boundary Layers in Large Solid Propellant Space Booster," AIAA 29th Aerospace Sciences Meeting, Reno, NV, January,1991.

8. Price, E.W. & Flandro, G.A. (1993) *Combustion Instability in Solid Propellant Rockets*. Book manuscript in preparation.

9. Flandro, G.A. & Roach, R.L. (1992) *Effects of Vorticity Production on Acoustic Waves in a Combustion Chamber*. Final Technical Report AFOSR-90-0159

10. Culick, F.E.C. (1966a)*AIAA J.* 4,1462-1463.

11. Culick, F.E.C. (1966b) *Astron. Acta* 12,113-126.

12. Culick, F.E.C. (1967) *Astron. Acta* 13,221-238.

13. Culick, F.E.C. (1968) *AIAA J.* 6,2241-2255.

14. Culick, F.E.C. (1970) *Comb. Sci. Tech.* 2,179-201.

15. Culick, F.E.C. (1971) *Comb. Sci. Tech.* 3,1-16.

16. Culick, F.E.C. (1973) *Comb. Sci. Tech.* 7,165-175.

17. Culick, F.E.C. (1975) *Comb. Sci. Tech.* 10,109-124.

18. Culick, F.E.C. (1976) *Comb. Sci. Tech.* 3,715-756.

19. Culick, F.E.C. (1988)," Combustion Instability in Liquid-fueled propulsion System–An Overview," AGARD 72B PEP Meeting, October

20. Williams, F.A.(1985) *Combustion Theory*, Benjamin/Cummings, Menlo Park.

21. Flandro, G.A. (1974) *J. Sound and Vibration*, 36, 297-312.

22. Tien, J.S. (1972) *Comb. Science and Tech.*5, 47-54.

23. Hegde, U.G., Chen ,F., and Zinn,B.T. (1986), *AIAA J.* 24, 1474-1482.

24. Hegde, U.G. and Zinn,B.T. (1986),21st Symp. (Int'l.) Combust. 1993-2000

25. Sankar, S.V., Hegde, U.G., Jagoda, J.I., and Zinn, B.T.(1988a) , 22nd Symp. (Int'l) on Combustion, 1865-1873

26. Sankar, S.V., Jagoda, J.I., Daniel, B.R., and Zinn, B.T.(1988b) AIAA 88-0541, AIAA Aerospace Sciences Meeting, January,1988.

27. Chen, T., Hegde, U., and Zinn, B. (1990) AIAA 90-0037, AIAA Aerospace Sciences Meeting, January,1990.

28. Matta, L.M. and Zinn, B.T. (1993)"Investigation of Flow Turning Loss in a Simulated Unstable Solid Propellant Rocket Motor," AIAA 93-0115,31st Aerospace Sciences Meeting, Reno, NV, January,1993.

29. Baum,J.D. and Levine, J.N.(1987) *AIAA J.*25,1577-1586

30. Baum,J.D.(1990),"Energy Exchange Mechanisms Between the Mean and Acoustic Fields in a Simulated Rocket Combustor," AFOSR Contractors Meeting, Atlanta, GA, June.

31. Wang, M. and Kassoy, D. R. (1990a) *J. Acoust. Soc. America* 87,1466-1472

32. Wang, M. and Kassoy, D. R. (1990b) *J. Fluid Mech.*220, 267-292.

33. Wang, M. and Kassoy, D. R. (1990c) *J. Fluid Mech.*221, 23-52.

34. Wang, M. and Kassoy, D. R. (1992a) *J. Fluid Mech.*238, 509-536.

35. Wang, M. and Kassoy, D. R.(1992b) *AIAA J.*30, 1708-1715.

36. Wang, M. and Kassoy, D. R. (1992c) Nonlinear Acoustic Oscillation in Resonant System: An Initial-Boundary Value Study, *submitted to SIAM J. Appl. Math.*

37. Cole, J.D. and Aroesty, J. (1967) " The Blowhard Problem— Inviscid Flows with Surface Injection,"RM-5194-ARPA, The RAND Corp.

38. Lagerstrom, P.A. (1964) in *Theory of Laminar Flows*, Section B. Moore,F.K.,ed., Princeton University Press.

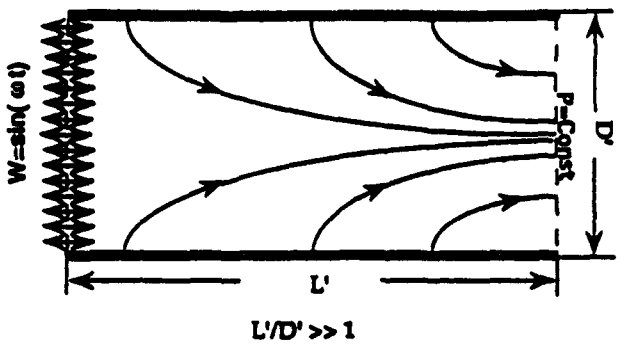

Figure 1: The cylindrical rocket engine chamber model of length L', diameter D', with endwall oscillations of frequency ω

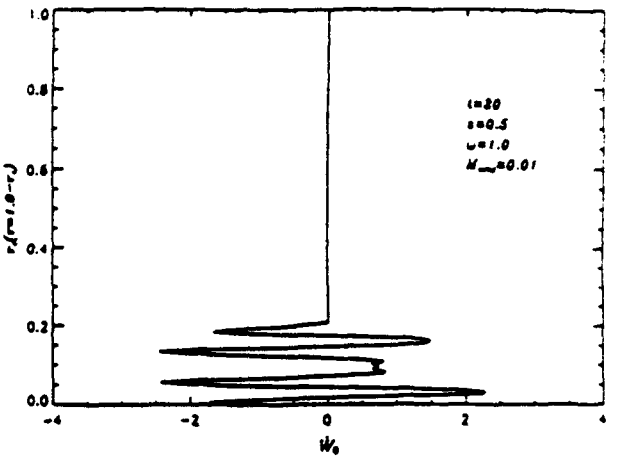

Figure 2: The spatial variation of the rotational axial velocity component $\hat{W}_\theta$ with the radial variable r_i at t=20.

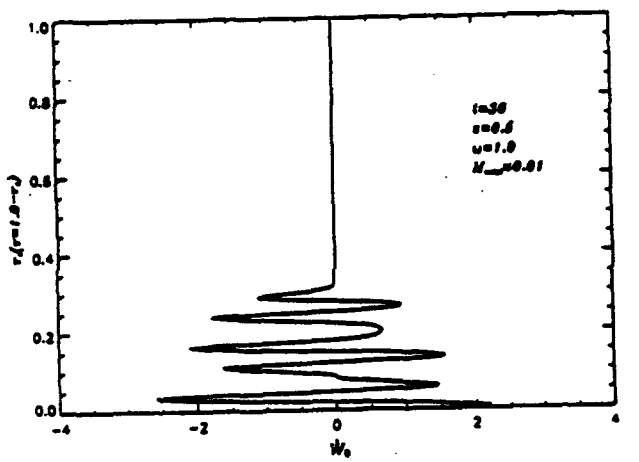

Figure 3: The spatial variation of the rotational axial velocity component $\hat{W}_\theta$ with the radial variable r_i at t=30.

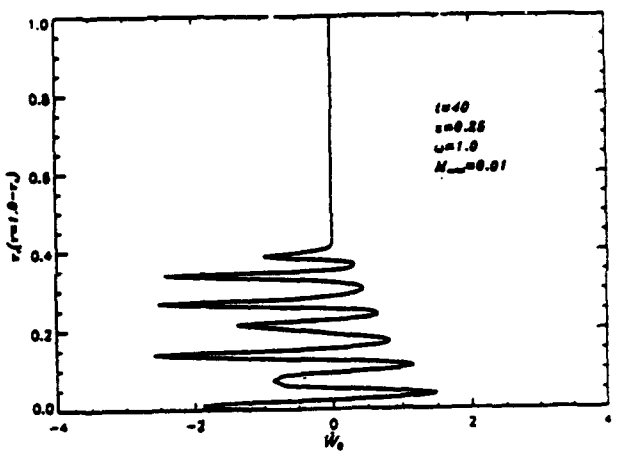

Figure 4a: The spatial variation of the rotational axial velocity component $\hat{W}_\theta$ with the radial variable r_i at t=40, s=0.25.

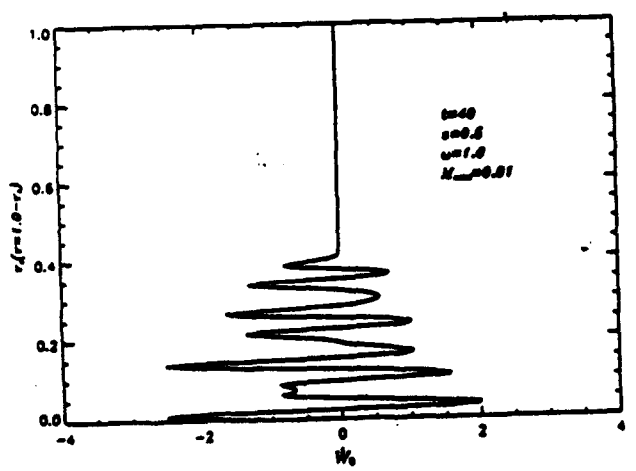

Figure 4b: The spatial variation of the rotational axial velocity component $\hat{W}_\theta$ with the radial variable r_i at t=40, s=0.5.

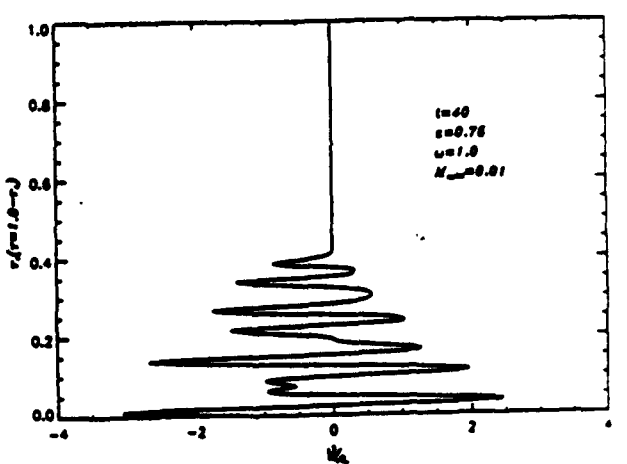

Figure 4c: The spatial variation of the rotational axial velocity component $\hat{W}_\theta$ with the radial variable r_i at t=40, s=0.75 .

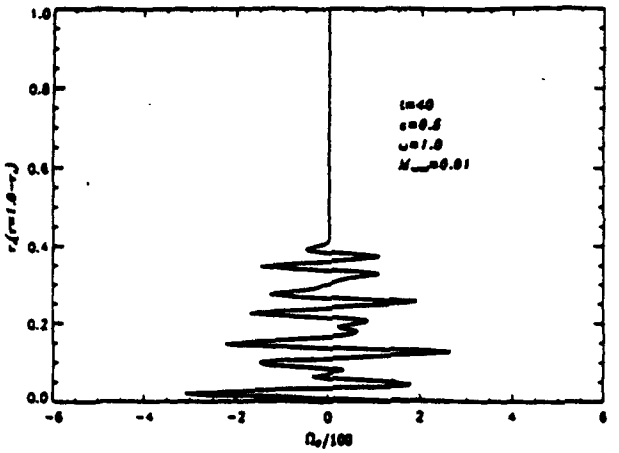

Figure 5: The spatial variation of unsteady vorticity $\Omega_0/100$, with the radial variable r_1.

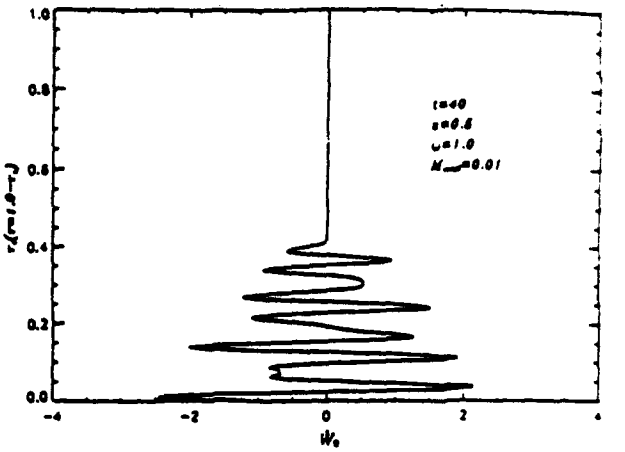

Figure 6: The spatial variation of the rotational axial velocity component $\dot{W}_0$ with the radial variable r_1 with nonlinear term suppressed.

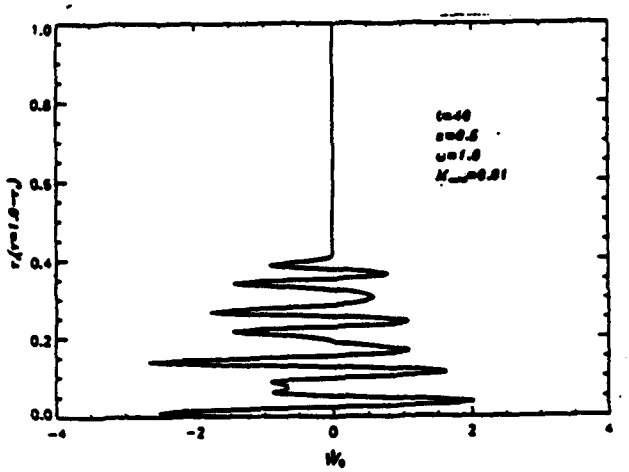

Figure 7: The spatial variation of the rotational axial velocity component $\dot{W}_0$ with the radial variable r_1 with viscous term reduced by 50%.

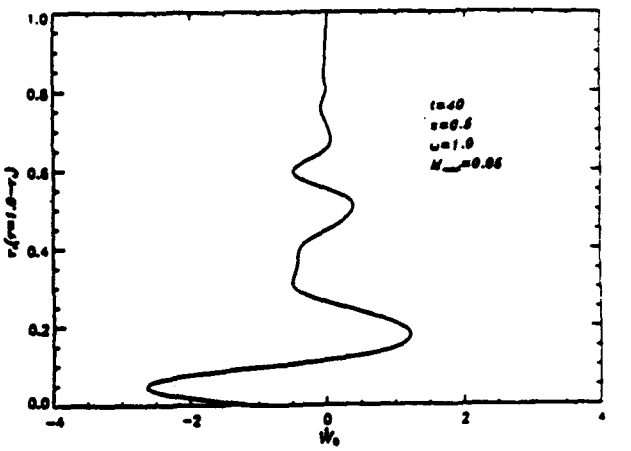

Figure 8: The spatial variation of the rotational axial velocity component $\dot{W}_0$ with the radial variable r_1 at M=0.05

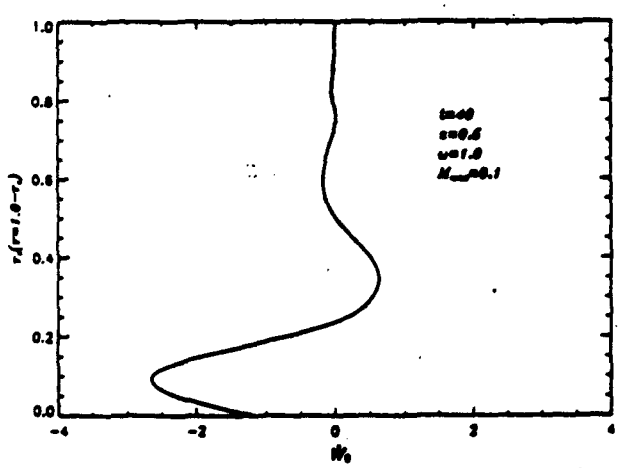

Figure 9: The spatial variation of the rotational axial velocity component $\dot{W}_0$ with the radial variable r_1 at M=0.1

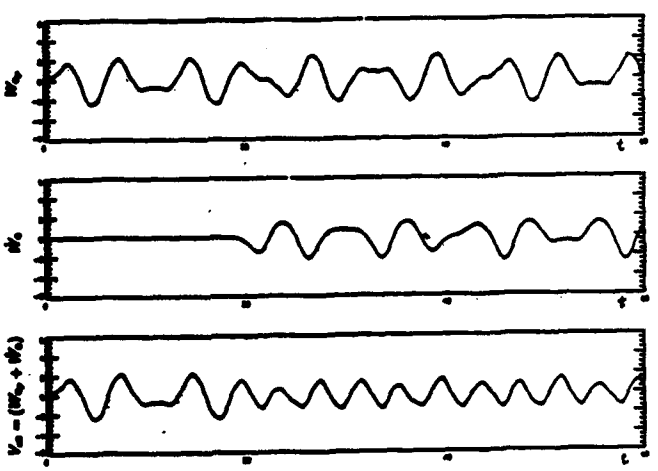

Figure 10 a,b,c (from top to bottom): The time response of the axial acoustic speed W_∞, the rotational axial speed $\dot{W}_0$ and the complete axial speed $V_{ax} = (W_\infty + \dot{W}_0)$ for r_1=0.2,s=0.5, M=0.01 and ω = 1.0

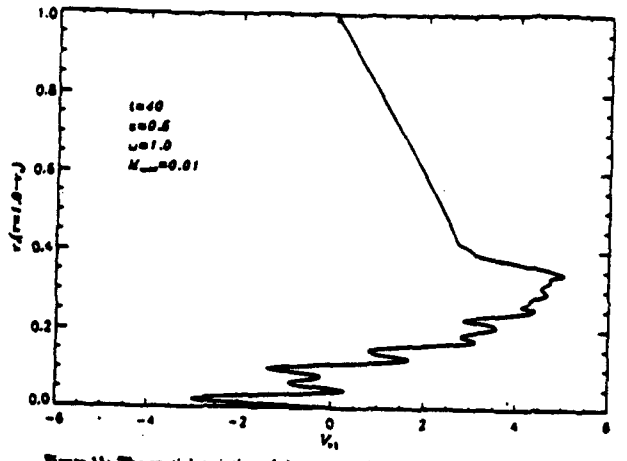

Figure 11: The spatial variation of the rotational radial velocity component V_{r_1} with the radial variable r_1

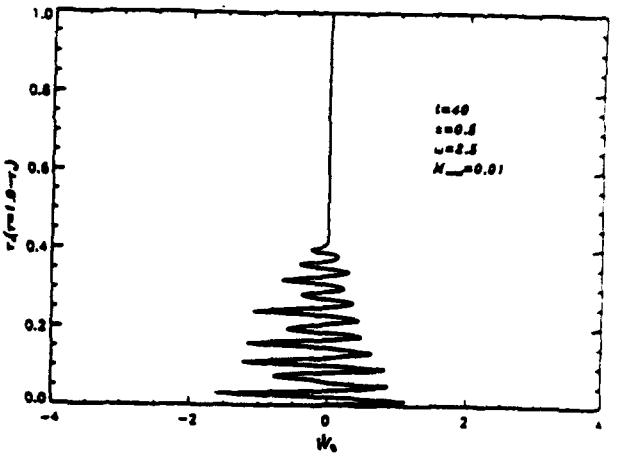

Figure 12: The spatial variation of the rotational axial velocity component W_θ with the radial variable r_1 at $\omega = 2.5$

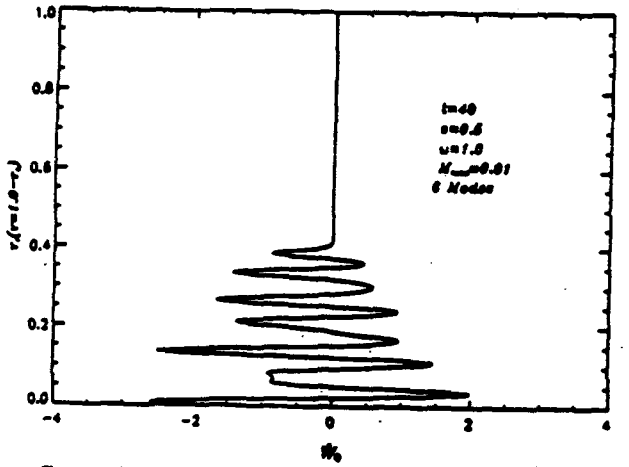

Figure 13: The spatial variation of the rotational axial velocity component W_θ with the radial variable r_1 based on a six mode, nonlinear solution (N=6).

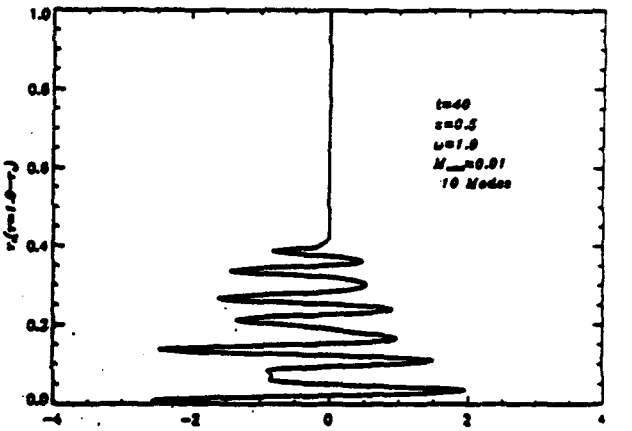

Figure 14: The spatial variation of the rotational axial velocity component W_θ with the radial variable r_1 based on a ten mode, nonlinear solution (N=10).

Appendix b

Nonlinear Vorticity Generation by Acoustic Wave Interaction with an Injected Gas Velocity Field in a Cylinder

Nonlinear Vorticity Generation by Acoustic Wave Interaction with an Injected Gas Velocity Field in a Cylinder*

Q. Zhao, D. R. Kassoy† and K. Kirkkopru
Mechanical Engineering Department;
Center for Combustion Research
University of Colorado at Boulder; Boulder,CO 80309-0427

Abstract

A mathematical model is formulated to describe the initiation and evolution of unsteady vorticity in a low Mach number (M), weakly viscous internal flow sustained by mass addition through the side wall of a long, narrow cylinder. An O(M) acoustical disturbance, generated by a prescribed harmonic transient endwall velocity, interacts with the basically inviscid rotational steady injected flow to generate time dependent vorticity at the side wall. The steady radial velocity component convects the vorticity into the flow. The axial velocity associated with the vorticity field varies across the cylinder radius and in particular has an instantaneous oscillatory spatial distribution with a characteristic wave length O(M) smaller than the radius. Weak viscous effects cause the vorticity to diffuse, as the spatial structures are convected from the wall toward the axis. The magnitude of the transient vorticity field is larger by $O(M^{-1})$ than that in the steady flow.

An initial-boundary value formulation is employed to find nonlinear unsteady solutions when a pressure node exists at the downstream exit of the cylinder. The complete velocity consists of a superposition of the steady flow, an acoustic (irrotational) field and the vortical component, all of the same magnitude. The formulation and results provide a conceptual framwork for the study of injected cylinder flow dynamics which supplements traditional acoustic stability theory by providing information about the generation and evolution of vortical structures.

*Research is supported by the Air Force Office of Scientific Research through AFOSR 89-0023
†Mailing address: Graduate School B-26; University of Colorado at Boulder; Boulder, CO 80309

1 Introduction

The objective of this study is to demonstrate how and where unsteady vorticity is created by an interaction between axially propagating acoustic waves and a flow field caused by steady sidewall mass injection in a finite length cylinder. Additionally, the formulation and analysis describes the transport and time-history of the spatial distribution of vorticity within the cylinder. Finally, the results show that transient rotational flow effects are crucial to the evolution and stability of internal fluid dynamics when the characteristic cylinder Reynolds number (Re) and Mach number (M) are very large and small, respectively.

The mathematical model describes the transient response of a flow field in a cylinder with one closed end, induced by strong normal, steady sidewall injection. In particular the injected flow is characterized by a radial speed much larger than the ratio of the characteristic axial speed to $Re^{1/2}$. Following Taylor (1956), Culick (1966a) shows that the steady flow is described in a first approximation by an inviscid, rotational equation system. Acoustic disturbances of $O(M)$ are created by a prescribed time-dependent axial velocity variation at the closed end of the cylinder. They propagate through the basic inviscid shear flow field, and perhaps unexpectedly, create significant vorticity at the surface of the porous cylinder. The radial component of the steady injected flow field carries the vorticity into the entire cylinder.

Predictions of flow dynamics in closely related systems have been obtained in the past from traditional acoustic stability theory as formulated and described by Grad (1949). Culick and co-workers, (See Culick (1990) for a comprehensive review) in particular, have developed since the mid-1970's an increasingly sophisticated linear and weakly nonlinear stability theory to describe disturbance behavior observed in laboratory experiments and practical systems like solid rocket engine chambers. Comparisons with experiments appear to be reasonably good, although the theory as formulated cannot describe the generation and evolution of vorticity.

Recent experimental (Brown et al. 1986a,b, Brown and Shaeffer, 1992) and computational (Vuillot and Avalon,1991; Vuillot,1991) studies include definitive evidence of significant transient rotational flow structures distributed throughout the injected cylinder flow. In addition, Price and Flandro (1993) and Flandro and Roach (1992) have formulated approximate mathematical models for describing the generation and evolution of vorticity in an injected cylinder flow field. These contributions provide the motivation for developing a comprehensive flow dynamics model which includes both the irrotational acoustical phenomena of traditional stability theory and important rotational flow effects.

Stability predictions for these flow systems are usually obtained from mathematical models that reflect linear and weakly nonlinear , inviscid , irrotational acoustic concepts (Culick, 1966a,1966b, 1967,1968,1970,1971,1973,1975,1976,1988,1990; Williams, 1985; Price and Flandro, 1993; Jahnke and Culick, 1993). The basic acoustic waves propagate through a fluid at rest, in the first approximation, and are described in terms of Fourier series of eigenfunctions that satisfy totally impermeable boundary conditions. Strictly speaking , these solutions do not accomodate sidewall injection nor exit plane flow at the downstream end of the cylinder. As a result the model cannot account for an interaction between the acoustic signals and a sidewall injected cylinder flow, now known to be a source of vorticity generation (Flandro and Roach,1992).

Flandro (1974) recognized that rotational flow effects play a role in relatively thin acoustic boundary layers where viscosity is of significance. Related studies for inert

flows have been carried out by Tien (1972), Flandro (1986), Hegde et al.(1986) and Price and Flandro (1993). Chemically and thermally active acoustic boundary layer flows are described by Hegde and Zinn (1986), Sankar et al.(1988a,b), Chen et al. (1990) and Matta and Zinn (1993). In these studies the boundary layer responds passively to externally imposed disturbances. The investigations are motivated by a need to understand how energy is exchanged between the acoustic disturbances and mean flow as fluid injected normally from the wall is turned towards the axial direction. Until recently, conceptual understanding of this flow turning process has been based largely on the viscous properties of the thin acoustic boundary layer.

Significant efforts have been made to develop computational models for acoustic boundary layer processes. Baum and Levine(1987), Baum (1990), Vuillot and Avalon (1991) and Vuillot (1991) have employed complete Navier-Stokes solvers to evaluate the general cylinder flow response to imposed disturbances. The last two cited works in particular demonstrate that rotational disturbances can exist in a substantial portion of the cylinder for appropriate values of Re and M. In other words, the vorticity distribution is not always confined to the traditional, viscous acoustic boundary layer adjacent to the cylinder wall. Rather, for appropriate parameter ranges it appears to be convected from the wall, out into the main portion of the basically inviscid cylinder flow by the mean injected flow field. Clearly, the pervasive presence of vortical structures in the internal flow field has significant consequences for the conceptual validity of traditional irrotational acoustic stability models.

The presence of rotational inviscid "acoustic" disturbances in a laboratory flow field was first implied by the experiments of Brown et al. (1986a,b) and Brown and Shaeffer (1992). The book manuscript of Price and Flandro (1993) contains an important discussion of these issues, and several idealized mathematical models are used to predict the structure of basically inviscid , but weakly viscous, vortical flow structures. More recently, Flandro and Roach (1992) have extended the theoretical effort to generate a purely inviscid model for boundary generated rotational disturbances that arise from an inviscid interaction between an injected flow field and axial, planar pressure waves propagating in the cylinder. Here again the vortical structures are convected out into the cylinder by the radial component of the injected velocity field. The length scale of the local vorticity variation is O(M) smaller than the cylinder radius, implying that viscous shear stress may be important on the local level. This work suggests that the interaction of "acoustic disturbances" with a strongly injected flow field leads to the presence of important vortical structure in the entire flow field.

The present study is an initial step in formulating a rational mathematical model for internal flow dynamics which incorporates both acoustic phenomena and vortical flow structures. Perturbation methods are used to derive systematic approximations to the complete compressible Navier-Stokes equations. An initial-boundary value approach is used to formulate a generalized unsteady mathematical model capable of describing both non-resonant and resonant time history of solutions. Fourier series representations of the velocity and pressure are obtained in terms of eigenfunctions that satisfy all the prescribed boundary conditions. The complete axial velocity is found from a superposition of three components of equal magnituide. First, the steady component arises from a solution to inviscid, rotational Euler equations known by Culick (1966a). Secondly, there is a planar irrotational acoustic field, derived from a traditional linear wave equation which satisfies boundary conditions at the closed and open ends of the cylinder. Finally, there is a rotational, weakly viscous component which varies on two distinctly different length scales. The global spatial distribution occurs on the radial length scale, while locally there are velocity gradients on a scale O(M) smaller. As a result the vorticity of the transient field is $O(M^{-1})$ larger than

that in the steady field. The convection of the vorticity is found to be described by a linear equation. Most significantly, the diffusion of vorticity on the shorter length scale is described by a nonlinear diffusion equation. Solutions are found numerically by using a finite difference method, as well as semi-analytically with a Galerkin-like method developed by Wang and Kassoy (1990a,b,c, 1992a,b, 1993).

Evaluation and interpretation of the full results show that rather complex vortical structures are present throughtout the cylinder sufficiently long after the disturbance is initiated at the end wall. When the input from several different Fourier modes is important, the time response curves are quite irregular and may be mistaken for a "turbulent" response.

Fully computational methods are used by Kirkkopru et al.(1994) to provide supporting evidence for the solutions found here by quasianalytical means.

2 Mathematical Formulation

A cylindrical tube with side wall injection is shown schematically in Figure 1. in which L' is the axial length and D' is the diameter. The radius is $R' = D'/2$. The complete non-dimensional equations describing the fluid dynamics and acoustics for an axisymmetric system can be written in the form

$$\frac{\partial \rho}{\partial t} + M\left[\frac{1}{r}\frac{\partial(\rho r V_r)}{\partial r} + \frac{\partial(\rho V_z)}{\partial z}\right] = 0, \tag{1}$$

$$\rho\frac{DV_r}{Dt} = -\delta^2\frac{1}{\gamma M}\frac{\partial P}{\partial r} + \delta^2\frac{M}{Re}\left\{\frac{\partial}{\partial z}\mu\left[\frac{1}{\delta^2}\frac{\partial V_r}{\partial z} + \frac{\partial V_z}{\partial r}\right] + 2\frac{\partial}{\partial r}\mu\left[\frac{\partial V_r}{\partial r} - \frac{1}{3}\left(\frac{1}{r}\frac{\partial(rV_r)}{\partial r} + \frac{\partial V_z}{\partial z}\right)\right] + \frac{2\mu}{r}\left[\frac{\partial V_r}{\partial r} - \frac{V_r}{r}\right]\right\}, \tag{2}$$

$$\rho\frac{DV_z}{Dt} = -\frac{1}{\gamma M}\frac{\partial P}{\partial z} + \delta^2\frac{M}{Re}\left\{\frac{\mu}{r}\left[\frac{1}{\delta^2}\frac{\partial V_r}{\partial z} + \frac{\partial V_z}{\partial r}\right] + \frac{\partial}{\partial r}\mu\left[\frac{1}{\delta^2}\frac{\partial V_r}{\partial z} + \frac{\partial V_z}{\partial r}\right]\right\} + 2\frac{M}{Re}\frac{\partial}{\partial z}\mu\left[\frac{\partial V_z}{\partial z} - \frac{1}{3}\left(\frac{1}{r}\frac{\partial(rV_r)}{\partial r} + \frac{\partial V_z}{\partial z}\right)\right], \tag{3}$$

$$\rho C_v\frac{DT}{Dt} = -(\gamma-1)MP\left[\frac{1}{r}\frac{\partial(rV_r)}{\partial r} + \frac{\partial V_z}{\partial z}\right] + \frac{M}{Re}\frac{\gamma}{Pr}\left[\frac{1}{r}\frac{\partial}{\partial z}\left(kr\frac{\partial T}{\partial z}\right) + \delta^2\frac{1}{r}\frac{\partial}{\partial r}\left(kr\frac{\partial T}{\partial r}\right)\right] + \frac{M^3\delta^2}{Re}\Phi, \tag{4}$$

$$P = \rho T \tag{5}$$

where

$$\frac{D}{Dt} = \frac{\partial}{\partial t} + M\left(V_r\frac{\partial}{\partial r} + V_z\frac{\partial}{\partial z}\right),$$

and Φ is the viscous dissipation function. The non-dimensional variables are defined in terms of dimensional quantities (with a prime) by

$$\rho = \frac{\rho'}{\rho_0'}, P = \frac{p'}{p_0'}, T = \frac{T'}{T_0'}, V_r = \frac{V_r'}{V_{r0}'}, V_z = \frac{V_z'}{V_{z0}'},$$

$$z = \frac{z'}{L'}, r = \frac{r'}{R'}, t = \frac{t'}{t'_a}, k = \frac{k'}{k'_0}, \mu = \frac{\mu'}{\mu'_0}, C_v = \frac{C'_v}{C'_{v0}}. \quad (6)$$

The reference value p'_0 measures the basic static pressure in the cylinder, while the analogous density and temperature values ρ'_0, T'_0 respectively represent properties of the injected fluid. The known characteristic injection speed V'_{r0} is related to the derived characteristic axial speed V'_{z0} by the approximate mass conservation relationship $V'_{z0} = \delta V'_{r0}$ where the aspect ratio $\delta = \frac{L'}{R'}$. Characteristic length scales for the axial and radial dimensions are defined by L' and R' respectively. Time is nondimensionalized with respect to the axial acoustic time $t'_a = \frac{L'}{C'_0}$, where $C'_0 = (\gamma R' T'_0)^{\frac{1}{2}}$ is the characteristic sound speed. The reference material properties k'_0, μ'_0 and C'_{v0} are defined at temperature T'_0. The parameter γ is the ratio of specific heat and

$$Re = \frac{\rho'_0 V'_{z0} L'}{\mu'_0}, Pr = \frac{\mu'_0 C'_{p0}}{k'_0}, M = \frac{V'_{z0}}{C'_0}, \quad (7)$$

where typically the Prandtl number Pr= O(1), the axial Mach number $M \ll 1$ and axial Reynolds number $Re \gg 1$.

Initially, a steady flow exists in the system, driven by spatially distributed normal injection from the wall where the no-slip condition is satisfied. Symmetry prevails along the axis at the cylinder. The closed end of the cylinder is impermeable and for simplicity the exit is assumed to be a pressure node. The mathematical form of the boundary conditions may be written as

$$r = 0; \quad V_r = \frac{\partial V_z}{\partial r} = 0, \quad r = 1; \quad V_r = -V_{rw}(z), \; V_z = 0, \; T = 1 \quad (8)$$

$$z = 0; \quad V_z = 0, \qquad z = 1; \quad P = 1. \quad (9)$$

The steady flow is disturbed at $z = 0$ by imposing a harmonic end wall axial velocity variation that is independent of the radial coordinate;

$$z = 0; \quad V_z = A \sin \omega t, \quad t \geq 0; \quad 0 \leq r \leq 1, \quad (10)$$

where the amplitude A=O(1).

It should be noted that the imposed end wall disturbance, of the same order of magnitude as that of the steady axial speed, induces both mechanical and thermodynamical disturbances of similar magnitude into the gas. These relatively large variations cannot be described by linear theory alone. Therefore, the weakly nonlinear theory developed here differs from traditional small disturbance theory.

Strong injection prevails, in the sense that $V'_{r0} \gg \frac{V'_{z0}}{Re^{\frac{1}{2}}}$ (Cole and Aroesty 1967), which implies that $Re \gg \delta^2$. Also note that in this modelling effort it is assumed that $\delta \gg 1$, to describe a long, narrow cylinder.

3 Steady State Flow

The steady state flow generated by time independent mass addition on the side wall can be described in terms of the variables:

$$(P, \rho, T) \sim 1 + M^2 (P_{0s}, \rho_{0s}, T_{0s}) + \cdots, \qquad (V_z, V_r) \sim (V_{z0s}, V_{r0s}) + \cdots; \quad (11)$$

valid for the asymptotic limit $M \to 0$. Equation (11) can be used in (1)—(5) to find the leading order equations describing an incompressible, inviscid, rotational flow that satisfies the no-slip and injection boundary conditions on the side wall and symmetry conditions on the axis, given in (8) and (9)

$$\frac{1}{r}\frac{\partial(rV_{r0_s})}{\partial r} + \frac{\partial V_{z0_s}}{\partial z} = 0 \tag{12}$$

$$P_{0_s} = P_{0_s}(z) \tag{13}$$

$$V_{r0_s}\frac{\partial V_{z0_s}}{\partial r} + V_{z0_s}\frac{\partial V_{z0_s}}{\partial z} = -\frac{1}{\gamma}\frac{\partial P_{0_s}}{\partial z}, \tag{14}$$

The transport terms are excluded from the leading order equations because $\frac{Re}{\delta^2} \gg 1$. Equation (13) arises because the aspect ratio $\delta \gg 1$. The solutions for the radial and axial velocity, as well as the pressure distribution can be written in the form

$$V_{r0_s} = -\frac{V_{rw}(z)}{r}\sin(\frac{\pi}{2}r^2), \quad V_{z0_s} = \left(\pi\int_0^z V_{rw}(\tau)d\tau\right)\cos(\frac{\pi}{2}r^2), \tag{15}$$

$$P_{0_s} = \gamma\pi^2\int_z^1\left[V_{rw}(\hat{z})\int_0^{\hat{z}} V_{rw}(\tau)d\tau\right]d\hat{z}, \tag{16}$$

where $-V_{rw}(z)$ is an arbitary time-independent side wall injection distribution. Related solutions can be found in Culick (1966a), Price and Flandro (1993) and Flandro and Roach(1992). It should be noted that recently Balakrishnan et al.(1991) derived a related solution valid for $M = O(1) < 1$.

4 Core/Boundary Layer Solutions

For certain parameter values the flow response to the endwall driven disturbance in (10) can be described in terms of an irrotational acoustical core and a relative thinner weakly viscous, rotational boundary layer adjacent to the cylinder wall. Aspects of this traditional model have been described by Wang and Kassoy(1992a). Here, the objective is to use the solutions themselves to determine the conditions for which the core-boundary layer structure is valid.

The asymptotic expansions for the unsteady core flow can be written as

$$(P,\rho,T) \sim 1 + M\sum_{n=0} M^n(P_n,\rho_n,T_n), \qquad (V_z,V_r) \sim \sum_{n=0} M^n(V_{zn},V_{rn}); \tag{17}$$

in the limit $M \to 0$. Equation (17) can be used in (1)—(5) to derive the lowest order acoustic system valid in the limit $M \to 0$, $Re \to \infty$, $\delta M = O(1)$;

$$\frac{\partial\rho_0}{\partial t} + \frac{1}{r}\frac{\partial(rV_{r0})}{\partial r} + \frac{\partial(V_{z0})}{\partial z} = 0; \tag{18}$$

$$\frac{\partial V_{z0}}{\partial t} = -\frac{1}{\gamma}\frac{\partial P_0}{\partial z}, \qquad P_0 = P_0(z,t); \tag{19}$$

$$\frac{\partial T_0}{\partial t} = (\gamma-1)\frac{\partial\rho_0}{\partial t}; \tag{20}$$

$$\rho_0 = P_0 - T_0. \tag{21}$$

The velocity components consist in general of both a steady state part and an unsteady part respectively; $(V_{z0}, V_{r0}) = (V_{z0s}, V_{r0s}) + (\tilde{V}_{z0}, \tilde{V}_{r0})$. It follows that the unsteady flow equations can be derived by substracting the steady state equations (12)-(14) from (18)—(21). Given the boundary condition in (10) the lowest order radial speed $\tilde{V}_{r0} = 0$.

4.1 Linear Planar Solution

The unsteady part of the leading order equations can be combined into a planar wave equation in terms of the axial velocity component:

$$\frac{\partial^2 \tilde{V}_{z0}}{\partial t^2} = \frac{\partial^2 \tilde{V}_{z0}}{\partial z^2} \tag{22}$$

The corresponding initial and boundary conditions are given by

$$t = 0, \quad \tilde{V}_{z0} = 0, \quad \frac{\partial \tilde{V}_{z0}}{\partial t} = 0, \tag{23}$$

$$z = 0, \quad \tilde{V}_{z0} = \sin \omega t; \tag{24}$$

$$z = 1, \quad \frac{\partial \tilde{V}_{z0}}{\partial z} = 0. \tag{25}$$

The simplicity of the equation can be attributed to the large aspect ratio condition $\delta \gg 1$. The boundary condition at the exit is derived from the pressure node condition in (9).

The general solution for $\tilde{V}_{z0}$ is :

$$\begin{aligned} \tilde{V}_{z0}(z,t) \;=\; & \sin \omega t \\ & + \sum_{n=0, n \neq n^*}^{\infty} \left\{ -\frac{2\omega}{b_n^2} \left[\left(\frac{b_n^2}{b_n^2 - \omega^2} \right) \sin(b_n t) - \frac{b_n \omega}{b_n^2 - \omega^2} \sin(\omega t) \right] \right\} \sin(b_n z) \\ & - \left\{ \left(\frac{1}{b_{n^*}} \right) \sin(b_{n^*} t) + t \cos(b_{n^*} t) \right\} \sin(b_{n^*} z), \end{aligned} \tag{26}$$

where $b_n = (n + \frac{1}{2})\pi$, and the last set of terms represents a resonant effect present only when $\omega = b_{n^*}$. A careful look into the solution provides us with some insight into the properties of the acoustical flow.

- The first term itself and the second part of the nonresonant Fourier series represent quasi-steady motion oscillating at the driving frequency. The other Fourier series terms can be decomposed into two counter-propagating planar travelling waves.
- If the driving frequency ω is not equal to one of the natural frequencies b_n, the solution is bounded. If ω is very close to one of these natural frequencies, then beats will appear due to the interaction between the quasi-steady motion and one pair of travelling waves.

- Resonance occurs when $\omega = b_n$, and the amplitude of one mode grows linearly with time.

Table 1 contains results for a system where $t'_A = 10^{-3}$ s so that dimensional frequencies can be considered. When $\omega' \approx 159$ Hz, the response shown in Figure 2 for $\bar{V}_{z0}$ at $z = 0.5$ is bounded and the contributions are mainly from the first harmonic oscillation term, the first few axial modes and quasi-steady modes in (26). Beats are observed in Figure 3 when $\omega' \approx 238$ Hz. The period of the beat is about 90s. due to the interaction between the quasi-steady modes and the first axial mode. Linear monotonic amplitude growth seen in Figure 4 is primarily from the resonant axial mode in (26) when $\omega' = 250$ Hz.

The pressure solution $P_0(z,t)$ can be obtained from a first integral of the unsteady part of (18) and the isentropic relationship $P_0 = \gamma\rho_0$.

4.2 Boundary Layer Correction

The leading order core acoustic solution does not satisfy the no-slip boundary condition. Under certain conditions to be defined quantitatively, the transition to zero axial velocity at the wall occurs in a relatively thin boundary layer which has a multiple scale structure. In particular the overall radial thickness of the layer is defined by viscous considerations. But within it there is a smaller length scale associated with the distance traveled by an injected fluid particle on the time scale $t'_A = \frac{L'}{C'_0}$. Due to the relatively large injection condition $V'_{r0} \gg V'_{z0}/Re^{\frac{1}{2}}$ the boundary layer flow is inviscid and rotational in the first approximation. Viscous stresses appear in the second order description, but are essential to finding the complete solution, as might be expected in a multiple scale analysis.

The multiple scale structure is defined in terms of the variables;

$$\xi = \frac{1-r}{M}, \qquad \eta = \frac{1-r}{\beta}, \tag{27}$$

where $\beta = ReM^2/\delta^2$ and $M \ll \beta \ll 1$ when the core/boundary layer concept is valid. The partial derivatives with respect to r must be replaced by

$$\left(\frac{\partial}{\partial r}\right) = -\frac{1}{M}\left(\frac{\partial}{\partial \xi}\right) - \frac{1}{\beta}\left(\frac{\partial}{\partial \eta}\right), \tag{28}$$

$$\left(\frac{\partial^2}{\partial r^2}\right) = \frac{1}{M^2}\left(\frac{\partial^2}{\partial \xi^2}\right) + \frac{2}{M\beta}\left(\frac{\partial^2}{\partial \eta \partial \xi}\right) + \frac{1}{\beta^2}\left(\frac{\partial^2}{\partial \eta^2}\right). \tag{29}$$

The variables are expanded as

$$(P, \rho, T) \sim 1 + \sum_{n=0} M^{n+1}(P_n, \rho_n, T_n), \tag{30}$$

$$V_z \sim V_{z0} + \frac{M}{\beta}V_{z1} + \cdots, \quad V_r \sim -V_{rw}(z) + \cdots, \tag{31}$$

The lowest order boundary layer equations are;

$$\frac{\partial V_{z0}}{\partial t} + V_{rw}\frac{\partial V_{z0}}{\partial \xi} = -\frac{1}{\gamma}\frac{\partial P_0}{\partial z}; \tag{32}$$

$$P_0 = P_0(z,t). \tag{33}$$

Equation (32) is an inviscid rotational equation which can satisfy the no-slip boundary conditions on $\xi = \eta = 0$. Vorticity transport can be described by the first derivative of (33) with respect to ξ, keeping in mind that V_{rw} and $\frac{\partial P_0}{\partial z}$ are independent of the short length scale variable. The resulting equation shows that vorticity is convected invariantly by the radial wall injection velocity into the boundary layer along well defined characteristic lines, $\varphi = t - (\frac{\xi}{V_{rw}})$.

The second order momentum equation is obtained from terms of $O(\frac{M}{\beta})$;

$$\frac{\partial V_{z1}}{\partial t} + V_{rw}\frac{\partial V_{z1}}{\partial \xi} = V_{rw}\frac{\partial V_{z0}}{\partial \eta} + \frac{\partial^2 V_{z0}}{\partial \xi^2}, \tag{34}$$

where a viscous stress term is present and the pressure gradient term is absent since $\frac{M}{\beta} \gg M$.

The acoustic solution in the core provides an outer boundary condition and the no-slip condition on the side wall provides an inner boundary condition for (32) and (34). The leading order acoustic core solution shows that all the terms can be classified into the following two forms: $\bar{V}_{z0}(z)e^{i\Omega t}$ with $\Omega = \omega$ or b_n, and $-t\cos(b_n \cdot t)\sin(b_n \cdot z)$. Thus the boundary conditions are

$$\xi = \eta = 0, \quad V_{z0} = 0; \tag{35}$$

$$\xi, \eta \to \infty; \quad V_{z0} \sim \bar{V}_{z0}(z,t). \tag{36}$$

Equations (32)—(34) and (35)—(36) are used to find quasi-steady solutions to every driving frequency in the core solution. For any of the nonresonant modes $\Omega = \omega$ or b_n but $\omega \neq b_n$ for any integer n, the boundary layer solutions can be written as

$$V_{z0} = F(\xi,\eta,z)e^{i\Omega t}; \quad V_{z1} = G(\xi,\eta,z)e^{i\Omega t}. \tag{37}$$

These solution forms can be substituted into (32) and (34) to determine F and G. The former found from (32) , (35) and (36), is

$$F(\xi,\eta,z) = C(\eta,z)\exp(-\frac{i\Omega}{V_{rw}}\xi) + \bar{V}_{z0} \tag{38}$$

where the undetermined coefficient function $C(\eta,z)$ must satisfy the conditions

$$\eta = 0; \quad C = -\bar{V}_{z0}(z), \tag{39}$$

$$\eta \longrightarrow \infty; \quad C = 0. \tag{40}$$

Equation (34) can then be rewritten in terms of G and C as

$$\frac{\partial G}{\partial \xi} + \frac{i\Omega}{V_{rw}}G = -\exp(-\frac{i\Omega}{V_{rw}})\left[\frac{\partial C}{\partial \eta} + \frac{\Omega^2}{V_{rw}^3}C\right] \tag{41}$$

In order to avoid secular growth of G with respect to the variable ξ, the quantities in the square bracket must be set to zero. Therefore,

$$\frac{\partial C}{\partial \eta} + \frac{\Omega^2}{V_{rw}^3} C = 0 \tag{42}$$

together with boundary conditions (39)-(40) are solved to find

$$C(\eta, z) = -\bar{V}_{z0} \exp(-\frac{\Omega^2}{V_{rw}^3}\eta). \tag{43}$$

The multiple scale solution for a given single frequency Ω has the form:

$$V_{z0}(\xi, \eta, z, t) = -\bar{V}_{z0}(z) \left\{ \exp\left[-\frac{\Omega^2}{V_{rw}^3(z)}\eta - \frac{i\Omega}{V_{rw}(z)}\xi \right] - 1 \right\} e^{i\Omega t} \tag{44}$$

where $-V_{rw}(z)$ is the steady side wall injection velocity. The exponential term represents the vortical part of the axial unsteady flow in the boundary layer. The combination of this vortical component and $e^{i\Omega t}$ term can be written as:

$$\exp\left[-\frac{\Omega^2}{V_{rw}^3(z)}\eta - \frac{i\Omega}{V_{rw}(z)}\xi + i\Omega t \right] = \exp\left(-\frac{\Omega^2}{V_{rw}^3(z)}\eta \right) e^{i\Omega\varphi} \tag{45}$$

where $\varphi = t - \frac{\xi}{V_{rw}}$ is the constant phase line or characteristic line for the unsteady axial vortical velocity. The radial traveling speed for constant φ line can be therefore described by:

$$\left.\frac{\partial r}{\partial t}\right|_{\varphi} = -M \left.\frac{\partial \xi}{\partial t}\right|_{\varphi} = -M V_{rw}(z) \tag{46}$$

This shows explicitly that the vorticity is convected by the steady injected fluid velocity in the boundary layer.

The first part of the exponential term in (45) describes amplitude damping arising from viscous effects because the η-variable defined in (27) is scaled with respect to Re, in part. The second part describes harmonic spatial oscillations.

When resonant driving is present $\Omega = \omega = b_{n^*}$, and V_{z0} has the form

$$\begin{aligned} V_{z0}(\xi, \eta, z, t) \;=\; & -t \sin(b_{n^*} z) \sin(b_{n^*} t) \\ & + \{ t \sin(k\xi) \sin(b_{n^*} t) + b_{n^*} t \cos(k\xi) \cos(b_n t) \\ & - \left[\frac{\eta}{(1 + b_{n^*})} \cos(k\xi) + \frac{b_{n^*}\xi}{2k^2(1 + b_{n^*})} \sin(k\xi) \right] \sin(b_{n^*} t) \cdot \\ & - \frac{1}{\omega} \left[\frac{V_{rw}^2(z)}{2(1 + b_{n^*})} \xi \cos(k\xi) - \left(1 - \frac{b_{n^*}^2}{1 + b_{n^*}} \right) \sin(k\xi) \right] \\ & \cos(b_{n^*} t) \} \frac{1}{b_{n^*}} \sin(b_{n^*} z) \exp(-\frac{b_{n^*}^2}{V_{rw}^3(z)}\eta) \end{aligned} \tag{47}$$

where $k = \frac{b_n}{V_{rw}(z)}$.

When $\xi = \eta = 0$, the solutions satisfy the no-slip boundary condition on the wall. On the other hand, when ξ and $\eta \to \infty$, the core solution is recovered in an oscillatory manner since the amplitude of the exponential term goes to zero harmonically. The effective thickness of the boundary layer depends strongly on Ω and V_w. A large value of Ω promotes relatively rapid exponential decay, implying that a high frequency disturbance is associated with a thinner transition boundary layer. Alternatively, low frequency forcing fosters thick boundary layers. Thus, higher order modes tend to be associated with effectively thinner boundary layers. The same type of argument demonstrates that increasing the value of $V_w(z)$ enhances the overall boundary layer thickness.

A complete solution for the axial velocity in the boundary layer consists of an infinite sum of terms obtained from (44) and (47) ; one for each frequency ω and b_n in (26). The spatial structure of such a solution will be quite complex, given the oscillatory dependence on the value of Ω. It is perhaps more illustrative to look at the results for a single frequency.

The reduced axial velocity inside the vortical layer, $\frac{V_{z0}}{[-V_{z0}e^{i\Omega t}]}$ is plotted against ξ in Figure 5 with $M = 0.01, \beta = 0.1$ and $V_{rw} = 1$ for $\Omega = 2.5$ and $\Omega = 3.0$. The core solution is recovered at about $\xi = 10$ for $\Omega = 2.5$ which correspondes to $r = 0.9$. In contrast, the boundary layer thickness is a little smaller for the higher frequency $\Omega = 3.0$. Of course the overall boundary thickness is determined by the lowest mode in the system. The core/boundary layer structure is valid only when $V_{rw}^3\beta/\Omega^2$ is sufficiently small, where $\beta \ll 1$, to permit exponential decay in (45) to occur close to the cylinder wall (say $r \geq 0.9$). If $\beta = O(1)$, and V_{rw} is sufficiently large and/or Ω is sufficiently small, then a new multiple scale perturbation technique is needed to find solutions where rotational effects fill the entire chamber.

5 Rotational Flow Across the Cylinder

5.1 Problem statement

The objective now is to develop a mathematical model for the disturbance evolution when rotational effects are significant across the entire cylinder. The asymptotic expansions for the velocity components and thermodynamic variables in the limit $M \to 0$ are

$$V_z \sim V_{z0s}(z,r) + \sum_{n=0} M^n V_{zn}(z,r,t) \tag{48}$$

$$V_r \sim V_{r0s}(z,r) + \sum_{n=0} M^n V_{rn}(z,r,t) \tag{49}$$

$$(P,\rho,T) \sim 1 + M \sum_{n=0} M^n (P_n, \rho_n, \theta_n) \tag{50}$$

It is recognized that two disparate length scales are important; the tube radius and a much shorter length associated with the radial distance traveled by a fluid particle on the acoustic timescale. A multiple scale analysis will be carried out in

terms of the variables r_1 and r_2 defined by

$$r_1 = 1 - r; \qquad r_2 = \int_0^{r_1} \frac{1}{-MV_{r0_s}(\sigma)} d\sigma. \tag{51}$$

The second transformation includes an integral of the steady radial velocity field for the case of **constant steady wall injection** $V_{rw} = 1$ which simplifies the describing equations considerably. It is noted that when the center line is approached $r_1 \to 1$ the integral diverges and $r_2 \to \infty$.

Each of the dependent variables is written in terms of r_1 and r_2 instead of r alone. The partial derivatives with respect to r in equations (1)–(5) must be replaced by

$$\left(\frac{\partial}{\partial r}\right) = -\left(\frac{\partial}{\partial r_1}\right) + \frac{1}{MV_{r0_s}}\left(\frac{\partial}{\partial r_2}\right), \tag{52}$$

$$\left(\frac{\partial^2}{\partial r^2}\right) = \left(\frac{\partial^2}{\partial r_1^2}\right) - \left(\frac{2}{MV_{r0_s}}\frac{\partial^2}{\partial r_1 \partial r_2}\right) + \left(\frac{1}{MV_{r0_s}}\right)^2 \left(\frac{\partial^2}{\partial r_2^2}\right) + \frac{1}{MV_{r0_s}^2}\frac{\partial V_{r0_s}}{\partial r_1}\left(\frac{\partial}{\partial r_2}\right). \tag{53}$$

5.2 Lowest order mathematical model

The relations (48)—(50) can be substituted into (1)—(5) to find the leading order equations in the limit $M \to 0$. First, the spatially homogeneous boundary forcing in (10) and the condition $\delta \gg 1$ imply that $V_{r0} = 0$. Then,

$$\frac{\partial R_0}{\partial t} + \frac{\partial R_0}{\partial r_2} = -\frac{\partial V_{z0}}{\partial z} - \left(\frac{1}{V_{r0_s}}\right)\frac{\partial V_{r1}}{\partial r_2}, \tag{54}$$

$$\frac{\partial V_{z0}}{\partial t} + \frac{\partial V_{z0}}{\partial r_2} = -\frac{1}{\gamma}\frac{\partial P_0}{\partial z}, \tag{55}$$

$$\frac{\partial P_0}{\partial r_1} = \frac{\partial P_0}{\partial r_2} = 0, \tag{56}$$

$$\frac{\partial \theta_0}{\partial t} + \frac{\partial \theta_0}{\partial r_2} = \frac{(\gamma - 1)}{\gamma}\frac{\partial P_0}{\partial t}, \tag{57}$$

$$P_0 = R_0 + \theta_0. \tag{58}$$

Following a procedure related to that described by Lagerstrom(1964), and similar to that employed by Price and Flandro (1993) and Flandro and Roach (1992), the variables, except for P_0, are divided into irrotational planar and rotational nonplanar parts,

$$V_{z0} = W_{0_p}(z,t) + \hat{W}_0(z,t,r_1,r_2), \tag{59}$$

$$R_0 = R_{0_p}(z,t) + \hat{R}_0(z,t,r_1,r_2), \tag{60}$$

$$\theta_0 = \theta_{0_p}(z,t) + \hat{\theta}_0(z,t,r_1,r_2). \tag{61}$$

Equations (59)—(61) can be used in (54)—(58) to show that the planar functions are described by

$$\frac{\partial R_{0p}}{\partial t} = -\frac{\partial W_{0p}}{\partial z}, \tag{62}$$

$$\frac{\partial W_{0p}}{\partial t} = -\frac{1}{\gamma}\frac{\partial P_0}{\partial z}, \qquad P_0 = P_0(z,t), \tag{63}$$

$$\frac{\partial \theta_{0p}}{\partial t} = \frac{\gamma - 1}{\gamma}\frac{\partial P_0}{\partial t}, \tag{64}$$

$$P_0 = R_{0p} + \theta_{0p}, \tag{65}$$

a system nearly identical to (18)—(21). The initial/boundary conditions are:

$$t = 0, \quad W_{0p} = 0, \quad \frac{\partial W_{0p}}{\partial t} = 0, \tag{66}$$

$$z = 0, \quad W_{0p} = \sin \omega t; \tag{67}$$

$$z = 1, \quad \frac{\partial W_{0p}}{\partial z} = 0. \tag{68}$$

in analogy to (23)—(25).

The nonresonant acoustic solution for the planar contribution is

$$W_{0p}(t,z) = -\frac{1}{\gamma}\sum_{n=1}^{\infty} a_n \left(\frac{\lambda_n}{\omega}\sin(\omega t) - \sin(\lambda_n t)\right)\sin(\lambda_n z), \lambda_n \neq \omega, \tag{69}$$

$$P_0(t,z) = \sum_{n=1}^{\infty} a_n \left(-\cos(\omega t) + \cos(\lambda_n t)\right)\cos(\lambda_n z), \lambda_n \neq \omega, \tag{70}$$

$$P_0 = \gamma R_{0p} \tag{71}$$

where $a_n = -\frac{2\gamma\omega}{\lambda_n^2 - \omega^2}$ and $\lambda_n = (n - \frac{1}{2})\pi$. Equation (69) is equivalent to (26) for the nonresonant case. The first term in the sums of (69) and (70) arises from forcing at frequency ω, and the second term describes the eigenfunction response. Only the nonresonant case will be considered in the present work.

The equations for the rotational components are

$$\frac{\partial \hat{R}_0}{\partial t} + \frac{\partial \hat{R}_0}{\partial r_2} = -\frac{\partial \hat{W}_0}{\partial z} - \left(\frac{1}{V_{r0_e}}\right)\frac{\partial V_{r1}}{\partial r_2}, \tag{72}$$

$$\frac{\partial \hat{W}_0}{\partial t} + \frac{\partial \hat{W}_0}{\partial r_2} = 0, \tag{73}$$

$$\frac{\partial \hat{\theta}_0}{\partial t} + \frac{\partial \hat{\theta}_0}{\partial r_2} = 0, \tag{74}$$

$$\hat{R}_0 + \hat{\theta}_0 = 0. \tag{75}$$

Equations (74) and (75) can be combined to show that the leading order vortical flow is incompressible:

$$\frac{\partial \hat{R}_0}{\partial t} + \frac{\partial \hat{R}_0}{\partial r_2} = 0 \tag{76}$$

Therefore, (72) can be rewritten as

$$\frac{\partial \hat{W}_0}{\partial z} + \left(\frac{1}{V_{r0_s}}\right)\frac{\partial V_{r1}}{\partial r_2} = 0, \tag{77}$$

which can be used to find V_{r1} once $\hat{W}_0$ is known.

The relevant initial and boundary conditions are

$$t = 0; \quad \hat{W}_0 = 0, \quad \frac{\partial \hat{W}_0}{\partial t} = 0, \tag{78}$$

$$z = 0; \quad \hat{W}_0 = 0, \tag{79}$$

$$z = 1; \quad \frac{\partial \hat{W}_0}{\partial z} = 0, \tag{80}$$

$$r_1 = 1, \ r_2 \to \infty; \frac{\partial \hat{W}_0}{\partial r_2} = 0, \quad \frac{\partial \hat{\theta}_0}{\partial r_2} = 0, \tag{81}$$

$$r_1 = r_2 = 0; \hat{W}_0 = -W_{0p}(t,z), \hat{\theta}_0 = -\theta_{0p}(t,z) \tag{82}$$

The first of (81) can be combined with (73) and the initial condition (78) to prove that $\hat{W}_0 = 0$ on the axis $r_1 = 0$ for all t. Equation (82) corresponds to the no-slip condition and isothermal flow injection. Equations (73), (74) and (76) show that $\hat{W}_0$, $\hat{\theta}_0$ and $\hat{R}_0$ are invariant on a characteristic line defined by

$$\eta = t - r_2, \tag{83}$$

but vary across the η lines. The $\eta = 0$ line enters the cylinder at $t = 0$ through side wall ($r_2 = 0$) and subsequently, at $t = c$, $\eta = c$ appears at $r_2 = 0$. At a particular time T, constant η lines, which range from 0 to T, are transported toward the axis by convection at the local radial steady velocity, as found from a time derivative of (83) after using (51).

The inviscid equation in (73) can be combined with the first of (82) to show that the wall is a source of vorticity because

$$\frac{\partial \hat{W}_0(t,z,0,0)}{\partial r_2} = -\frac{\partial \hat{W}_0}{\partial t} = \frac{\partial W_{0p}(t,z)}{\partial t} \tag{84}$$

where W_{0p} is known from (69). It is noted that the largest unsteady nondimensional vorticity term is given by $\Omega_\theta = (\frac{1}{MV_{r0_s}})\frac{\partial \hat{W}_0}{\partial r_2}$. The parameter, $\frac{1}{M}$, arises from large gradients occuring in the spatially oscillatory velocity profile on the short length scale r_2. Equation (73) also shows that the vorticity generated at the wall is convected into the cylinder by the steady radial velocity field $V_{r0_s}(r)$.

In general, solutions to the inviscid first order hyperbolic equations in (73)-(75) can be written symbolically as,

$$\hat{W}_0 = \hat{W}_0(\eta, r_1, z), \qquad \eta = t - r_2 \tag{85}$$

$$\hat{\theta}_0 = \hat{\theta}_0(\eta, r_1, z) = -\hat{R}_0, \tag{86}$$

Explicit functional dependence of the variables can be found from consideration of the higher order equations, as is typical in a multivariable study. Once $\hat{W}_0$ is found, then the mass conservation equation (77) can be integrated with respect to r_2 to find the radial velocity V_{r1}. The vortical temperature and density fields can be found using related methods.

5.3 Higher order consideration

Equations (48)—(50) can be combined with (1)—(5) to find the O(M) equation set in the limit $M \to 0$. The same procedure used to find the leading order solution is employed so that the variables, except for P_1, are divided into irrotational planar and rotational nonplanar parts,

$$V_{z1} = W_{1p}(z,t) + \hat{W}_1(z,t,r_1,r_2), \tag{87}$$

$$R_1 = R_{1p}(z,t) + \hat{R}_1(z,t,r_1,r_2), \tag{88}$$

$$\theta_1 = \theta_{1p}(z,t) + \hat{\theta}_1(z,t,r_1,r_2). \tag{89}$$

The planar, acoustic equations,

$$\frac{\partial R_{1p}}{\partial t} = -\frac{\partial}{\partial z}\left[W_{1p} + R_{0p}W_{0p}\right], \tag{90}$$

$$\frac{\partial W_{1p}}{\partial t} = \frac{\partial}{\partial z}\left[-\frac{1}{\gamma}(P_1 - P_{0s}) + \frac{R_{0p}^2}{2} - \frac{W_{0p}^2}{2}\right], \tag{91}$$

$$\frac{\partial \theta_{1p}}{\partial t} = \frac{\partial}{\partial t}\left[(\gamma-1)R_{1p} + \frac{(\gamma-2)(\gamma-1)}{2}R_{0p}^2\right] \tag{92}$$

$$P_1 = R_{1p} + \theta_{1p} + R_{0p}\theta_{0p} \tag{93}$$

containing quadratic driving terms associated with lower order acoustics are not considered further here, although they may be important for studying acoustic streaming effects.

The largest possible viscous effect occurs when $\delta^2/\mathrm{Re}=M^2$, in which case the higher order axial momentum equation for $\hat{W}_1$ has the form

$$\begin{aligned}\frac{\partial \hat{W}_1}{\partial t} + \frac{\partial \hat{W}_1}{\partial r_2} = {} & \frac{1}{V_{r0s}^2}\frac{\partial^2 \hat{W}_0}{\partial r_2^2} + \frac{1}{\gamma}\hat{R}_0\frac{\partial P_0}{\partial z} - (V_{z0s} + V_{z0})\frac{\partial (V_{z0s} + V_{z0})}{\partial z} \\ & + V_{z0s}\frac{\partial V_{z0s}}{\partial z} + W_{0p}\frac{\partial W_{0p}}{\partial z} + V_{r0s}\frac{\partial (V_{z0s} + V_{z0})}{\partial r_1} \\ & - \left(\frac{V_{r1}}{V_{r0s}}\right)\frac{\partial V_{z0}}{\partial r_2} - V_{r0s}\frac{\partial V_{z0s}}{\partial r_1}.\end{aligned} \tag{94}$$

the analogue to (73). It is (94) that will give us information about the behaviour of the leading order axial speed solution.

The corresponding energy equation for $\hat{\theta}_1$ analogous to (74) contains a conduction term. Thus, transport effects are important conceptually in the distribution and evolution of the rotational variables.

If the transformation of the coordinate system from (t,r_1,r_2,z) to (η, r_1, r_2, z) is made, then the derivatives with respect to t and r_2 must be replaced by

$$\left(\frac{\partial}{\partial t}\right) = \left(\frac{\partial}{\partial \eta}\right)_{r_2}, \quad \left(\frac{\partial}{\partial r_2}\right) = \left(\frac{\partial}{\partial r_2}\right)_{\eta} - \left(\frac{\partial}{\partial \eta}\right)_{r_2}, \tag{95}$$

It follows that (94) can be written as

$$\begin{aligned}\left.\frac{\partial \hat{W}_1}{\partial r_2}\right|_{\eta} &= \frac{1}{V_{r0_s}^2}\frac{\partial^2 \hat{W}_0}{\partial \eta^2} - V_{z0}\frac{\partial (V_{z0_s} + \hat{W}_0)}{\partial z} \\ &\quad - \hat{W}_0\frac{\partial \hat{W}_0}{\partial z} - \frac{1}{V_{r0_s}}\left[\frac{\partial (V_{r1}\hat{W}_0)}{\partial r_2} - \frac{\partial (V_{r1}\hat{W}_0)}{\partial \eta}\right] \\ &\quad - V_{z0_s}\frac{\partial V_{z0}}{\partial z} - \hat{W}_0\frac{\partial W_{0p}}{\partial z} + V_{r0_s}\frac{\partial \hat{W}_0}{\partial r_1} + \frac{1}{\gamma}\hat{R}_0\frac{\partial P_0}{\partial z},\end{aligned} \tag{96}$$

An integration of (96) with respect to r_2, holding η, r_1 and z fixed will generate secular growth in r_2 unless certain terms are suppressed. In considering the impact of each term, it is important to remember that the harmonic t-dependence of the planar acoustic solutions in (69)-(71) must be rewritten in terms of η and r_2 by using the transformation $\eta = t - r_2$ in (83). When written in the coordinate system (z, t, r_1, r_2) the suppressed terms take the form;

$$\frac{1}{V_{r0_s}^2}\frac{\partial^2 \hat{W}_0}{\partial r_2^2} + V_{r0_s}\frac{\partial \hat{W}_0}{\partial r_1} - 2\hat{W}_0\frac{\partial \hat{W}_0}{\partial z} - \hat{W}_0\frac{\partial V_{z0_s}}{\partial z} - V_{z0_s}\frac{\partial \hat{W}_0}{\partial z} = 0, \tag{97}$$

which is a nonlinear diffusion equation for the rotational axial velocity $\hat{W}_0$ with a time-like variable r_1. The solution for $\hat{W}_0$ must satisfy an"initial" condition from (82)

$$\begin{aligned}\hat{W}_0(t, z, r_1 = 0, r_2) &= -W_{0p}(\eta, z) \qquad \eta > 0 \\ &= \frac{1}{\gamma}\sum_{n=1}^{\infty} a_n \left(\frac{\lambda_n}{\omega}\sin(\omega\eta) - \sin(\lambda_n\eta)\right)\sin(\lambda_n z), \lambda_n \neq \omega, \\ \hat{W}_0(t, z, r_1 = 0, r_2) &= 0 \qquad \eta < 0\end{aligned} \tag{98}$$

and a boundary condition at the center line from (81)

$$r_2 \longrightarrow \infty, \qquad \frac{\partial \hat{W}_0}{\partial r_2} = 0. \tag{99}$$

In addition a condition must be specified on $r_1 > 0, r_2 = 0$ which is compatable with (98) at the point $r_1 = r_2 = 0$. This is necessary because r_1 and r_2 are treated as independent variables in (102). The reasonable choice is given by

$$\hat{W}_0(t, z, r_1, r_2 = 0) = -W_{0p}(t, z). \tag{100}$$

The nonlinear term in (97), $2\dot{W}_0\dot{W}_{0z}$ is present in our problem because the $O(M)$ boundary disturbance is larger than that used in earlier, basically linear studies (Flandro and Roach,1993). Its presence suggests that wave steepening and other forms of instability may occur in the evolving flow field. If the imposed endwall disturbance is smaller,and/or axial variations are ignored, then a linear, viscous diffusion equation is derived, which is related to that used by Price and Flandro (1992).

One solution approach is based on a finite difference approximation to (97)-(100). Solutions for $\dot{W}_0(z,t,r_1,r_2)$ can be found by employing a second order accurate Adam-Bashforth/Crank-Nicolson scheme. Most of the results presented here (see section 6) have been found in this way.

Given the forcing condition in (98), it is also possible to find solutions in terms of the eigenfunction set $\{\sin(\lambda_n z)\}, n = 1, 2, \cdots$;

$$\dot{W}_0(t,z,r_1,r_2) = \sum_{n=1}^{\infty} A_n(t,r_1,r_2)\sin(\lambda_n z) \tag{101}$$

Coupled partial differential equations for the Fourier coefficients A_n, are found by using (101) in (97) and invoking orthogonality conditions for the eigenfunction set on the interval [0,1]. The results are;

$$\frac{1}{V_{r0_s}^3}\frac{\partial^2 A_n}{\partial r_2^2} + \frac{\partial A_n}{\partial r_1} - \frac{1}{V_{r0_s}}\frac{\partial V_{z0_s}}{\partial z}A_n - \frac{2}{V_{r0_s}}\left(\sum_{n_1=1}^{\infty}\left[\sum_{n_2=1}^{\infty} a_{nn_1n_2}A_{n_1}A_{n_2} + \left(\frac{V_{z0_s}}{z}\right)b_{nn_1}A_{n_1}\right]\right) = 0 \tag{102}$$

and are subject to conditions obtained from (98) and (99).

(a) Initial Condition:

$$\begin{aligned} A_n(t,r_1=0,r_2) &= \frac{1}{\gamma}a_n\left(\frac{\lambda_n}{\omega}\sin\omega(t-r_2) - \sin\lambda_n(t-r_2)\right) \quad 0 < r_2 \le t \\ &= 0 \quad r_2 > t \end{aligned} \tag{103}$$

(b) Boundary Conditions:

$$r_2 \longrightarrow \infty, \quad \frac{\partial A_n}{\partial r_2} = 0 \tag{104}$$

$$A_n(t,r_1,r_2=0) = \frac{1}{\gamma}a_n\left(\frac{\lambda_n}{\omega}\sin(\omega t) - \sin(\lambda_n t)\right) \tag{105}$$

where

$$a_{nn_1n_2} = 2\lambda_{n_2}\int_0^1 \sin(\lambda_{n_1}z)\cos(\lambda_{n_2}z)\sin(\lambda_n z)dz \tag{106}$$

$$b_{nn_1} = \lambda_{n_1}\int_0^1 z\cos(\lambda_{n_1}z)\sin(\lambda_n z)dz \tag{107}$$

Equation (102) is a coupled system of quasi-linear diffusion equations with a time like variable r_1, and nonlinear source terms. The physical time t is a parameter of the differential equations, appearing explicitly only in the boundary conditions. Solutions to (102)-(107) are described in Section 7. A system truncation approach is used to find a finite number of A_n's.

6 Finite Difference Solutions for the Nonlinear System

Solutions to (97)-(100) for $\hat{W}_0(z,t,r_1,r_2)$ have been found by using a finite difference method based on the second order accurate $O(\delta r_1^2, \delta r_2^2)$ Adam-Bashforth/Crank-Nicolson scheme. This scheme is a semi-implicit and neutrally unstable in the sense that it works well if the nonlinear effect is moderate in comparison with the viscous effect. For example, instability results if the amplitude of the initial condition for a given ω is larger than a threshold value. The real solution lies on the locus defined by (51) relating r_1 and r_2. In general this curve does not coincide with the computational grid points. Hence cubic spline interpolations in r_2 are employed at every chosen r_1 value to obtain the desired real solution. The far end boundary condition for $r_2 \rightarrow \infty$ is implemented by providing a sufficiently large number of grid points between the convected outer edge of the rotational layer and the finite location of the computational boundary with respect to r_2. A total of 1000 grid points in the r_2 direction with δr_2=0.1 is chosen. The function and derivatives must remain zero at a significant number of nodes in order to ensure that conditions at the computational boundary do not constrain the solution.

At each value of the "parameter" t, the integration is initiated with the initial conditions in (98), subject to the boundary conditions in (99) . The spatial distribution of the solution with respect to r_2 evolves as the "time-like" variable r_1 increases. Integration is carried out to a sufficiently large value of r_1 to ensure that adequate data fields $\hat{W}_0(z,t,r_1,r_2)$ are available on the locus curve relating r_1 and r_2 defined by (51). Then the actual solution is found from the intersection of the surface defined by $\hat{W}_0(z,t,r_1,r_2)$ and the vertical plane from the locus curve relating r_1 and r_2.

The first test case studied is for $\omega = 1.0$, which is a nonresonant frequency smaller than the first natural frequency $\lambda_1 = \frac{\pi}{2}$. This particular case allows us to develop a relatively simple solution with minimal computational time. The initial condition was obtained from (98) by using the first 20 Fourier modes.

It is important to resolve the solution in the axial direction by choosing a sufficiently large number of grid points in the z-direction, K_{max}. Solution comparisons for $K_{max} = 9, 21$ and 28 at $t = 40$, M=0.01 and Z=0.25, 0.5 and 0.75 show considerable difference for the smallest number. Excellent comparisons for $K_{max} = 21$ and 28 suggest that the former is adequate for $\omega = 1.0$.

Figures 6,7 and 8b give results for the rotational axial velocity $\hat{W}_0$ as a function of r_1 at z=0.5 when t= 20,30 and 40. At each time, the solution consists of several spatial oscillations and a thin region of exponential damping near a specific radial location $r_{1e}(t)$ beyond which vorticity is exponentially small. For a given value of t, one first finds r_{2e} from $\eta = 0 = t - r_{2e}$ and then uses the inverse of (51) to determine r_{1e}. It should also be noted from the definition of η in (86) and the second of (51) that the front moves at the nondimensional speed $\left.\frac{\partial r}{\partial t}\right|_{\eta=0} = -MV_{r0s}(r)$ which corresponds to the steady radial speed in dimensional terms. The front speed vanishes as the cylinder axis is approached. At $t = 40$ the rotational flow distribution in Figure 4b extends out about 44% of the cylinder radius.

The corresponding scaled vorticity distribution, calculated from $\frac{1}{V_{r0s}(r)} \frac{\partial \hat{W}_0}{\partial r_2}$ is given in Figure 9. The dimensionless vorticity Ω_θ, defined below (84) is $O(M^{-1})$. One should note the significant magnitude of the spatial variations in vorticity given the

scaling factor $\frac{1}{M}$. The large amplitude is associated with the O(M) length scale of the axial speed gradient and the factor M^{-1}.

The spatial distribution of the axial rotational velocity at each time can be explained in physical terms by considering the interaction between the propagating planar acoustic wave solution, described by (69) and (70), and the steady injected flow field in (15). Fluid particles injected normally from the wall with $V_{r_w} = 1$ at a specified z-location experience an approximately harmonic variation in the local pressure gradient given by (70). During periods of negative (positive)gradients the particles are accelerated downstream (upstream). As a result, near the wall one will observe alternating periods of positive and negative axial velocity. The steady radial velocity field carries these alternating regions of forward and reverse flow away from the wall toward the axis. Part of the fluid particle response is purely acoustic. The remainder is given by $\hat{W}_0$. In this sense the spatial pattern of the rotational axial velocity at fixed z as shown in Figures 6,7 and 8b reflects the historical behaviour of the local pressure gradient at the axial location. The O(M) length scale of the transverse spatial oscillations can now be explained easily since the approximately harmonic pressure gradient variation occurs on the acoustic time scale t'_A (for ω=O(1)) during which only limited radial motion is possible.

Three additional results should be noted. First, the amplitude of a given oscillation in the vortical velocity component becomes smaller as is convected deeper into the cylinder. Local viscous and nonlinear effects have some influence on the amplitude reduction which must occur because the vorticity vanishes near the front and certainly at the axis $r_1 = 1$. Second, the wave length of the spatial oscillations decrease as r_1 increases toward the axis. This occurs because the vorticity front speed (the steady radial velocity) declines as r_1 increases. Finally, a comparison of Figures 8a,b,c demonstrates that the rotaional axial velocity varies with the axial as well as the radial variables.

Figures 10a-c show a "linear" solution for the rotational axial velocity $\hat{W}_0$ as a function of r_1 at t=40, M=0.01 and z=0.25, 0.5 and 0.75 obtained by solving (97) with nonlinear term $\hat{W}_0 \frac{\partial \hat{W}_0}{\partial z}$ reduced by a factor of 10^{-5}. $K_{max} = 21$ is used in the calculation. This calculation is done to assess the impact of the nonlinear convection term on the spatial structure of the solution in Figures 8a-c. A comparison shows that the nonlinear term has a quantitative effect on the spatial distribution of $\hat{W}_0$, but does not fundamentally control the qualitative spatial oscillations. The nonlinear effect is more important in the fore end at $z = 0.25$ than in the rear end at $z = 0.75$ near the the exit where nonlinear effect disappears due to the pressure node.

Figures 11a, c are the counterparts to Figures 8a, c with a reduced viscous effect. In this case (97) is solved with the viscous term, $\frac{1}{V_{r0_s}^2} \frac{\partial^2 \hat{W}_0}{\partial r_1^2}$, multiplied by a factor of 0.25. The basic patterns of the complete solution in Figure 8 persist. One notes that oscillation peak amplitude in Figure 7a,c are considerably larger than their analogues in Figure 8a, c, particularly away from the wall. Smaller differences are seen in Figure 7b. In general, the impact of viscosity is greater at an axial location where the maximum oscillation amplitudes are relatively large.

Figure 12 and Figure 13 are the counterparts of the nonlinear result in Figure 8b with larger axial Mach numbers M=0.05 and 0.1 respectively, and t=40. One can see that the larger Mach numbers (stronger wall injection) are associated with a thicker unsteady vortical region. The vorticity has filled the entire cylinder for M=0.05 and for M=0.1 at t=40 while only 44% of the chamber is filled in Figure 8 with M=0.01. This is expected because radial convection of vorticity occurs more

quickly for a relatively larger steady radial velocity. Although vorticity is present everywhere in the cylinder, the value at the axis is zero, as explained below (82). It should be noted that the local velocity gradients are smaller in Figures 12 and 13 so that the magnitude of the unsteady vorticity is similarly reduced for higher Mach number systems. Larger velocity gradients can be obtained at a given Mach number for larger forcing frequency ω.

Figure 14 provides results at $r_1 = 0.2$ for the time-variation of the planar acoustic axial speed W_{0p}, the rotational axial speed $\hat{W}_0$ and their sum V_{z0}, defined in (59), at z=0.5 with $K_{max} = 21$ and M=0.01. It can be seen from Figure 14b that the curve for the rotational solution resembles the planar acoustic response in Figure 14a but differs in amplitude and phase. At $r_1 = 0.2$ the rotational response appears after a delay of almost 18 axial acoustic time units, the time needed for the vorticity wave front initiated at the wall to travel out to the specified radial location. At the location $r_1 = 0.2$, phase differences are relatively small and the sum in Figure 14c shows a total response of significant amplitude. This amplitude actually increases as r_1 decreases until locations very close to the wall are reached, where the impact of the no-slip condition at $r_1 = r_2 = 0$ forces $V_{z0} \to 0$.

The second case studied is for a driving frequency $\omega = 2.5$ with the initial condition for $\hat{W}_0$ in (98) half the magnitude of the previous calculation. The solution for $\hat{W}_0$ at t=40, M=0.01 is given in Figures 15a-c for $K_{max} = 21$. The results show that the spatial distribution curves for $\omega = 1.0$ and 2.5 have similar characteristics. However, the latter have more oscillation cycles because the driving frequency is higher. One should note that the axial variation of $\hat{W}_0$ is quite different from the lower frequency analogue in Figure 8a-c.

The relative solution complexity for $\omega = 2.5$ suggests that a less restricted acoustic field, arising from multiple driving frequencies or perhaps sidewall injection oscillations, may initiate a relatively irregular vortical time-response. In this sense, one could ask whether "turbulent" responses observed in similar situations such as solid rocket chamber models are caused in part by wall generated vorticity that is convected into the chamber by the injected field.

7 Modal Solutions to the Nonlinear System

Solutions found from (101)-(107) enable one to demonstrate how the energy is distributed among the spectrum of Fourier modes. The coefficients $A_n(r_1, r_2)$, n=1-N for specified N, have been found by using a finite difference method based on the Adam-Bashforth/Crank-Nicolson scheme described in Section 6. The procedure used previously to find $\hat{W}_0$ on the real locus is applied to each $A_n(r_1, r_2)$. Once the $A_n's$ are known, the solution for $\hat{W}_0$ is found by summing up N modal contributions according to (101). Careful attention must be given to the value of N in order to assure that the solutions are sufficiently accurate. In particular, solutions for $\hat{W}_0$ based on N and $N + L$ modes, $L > 0$, are compared until the results exhibit little appreciable change for an incremental L value. Valuable insights into the solution development for this problem have been found from the transient solution to a Fisher equation (Fisher, 1936) in terms of a Galerkin expansion. Details are given in Appendix A.

Figures 16-18 show $\hat{W}_0$ results at t=40 for $N = 6, 8, 10$ respectively for the case M=0.01,z=0.5 and $\omega = 1.0$. Each figure includes partial sums of even numbers of modes up to the complete finite summation. A comparison of partial sum results

implies that the energy is concentrated primarily in the first two modes for $\omega = 1$. A comparison of results in Figures 16-18 with those in Figure 8b reveals that there is little difference between the modal solutions and that from a direct finite difference solution with $K_{max} = 21$. It is noted that the grid size in the axial direction for K_{max}=21 is 0.05, just small enough to resolve the first six axial Fourier modes according to $(\Delta z)_{max} = \frac{2\pi}{\lambda_6}\frac{1}{10}$, where $\lambda_6 = \frac{11}{2}\pi$. Hence the most meaningful comparisons should be carried out with $N = 6$.

It has been found that the 6 mode partial sum from the 10 mode computation is closer to the finite difference result than the 6 mode summation from the 6 mode computation. A reasonable explanation of this observation may be based on the restricted energy transfer for modes near the truncation limit. Adding a few more modes permits realistic exchange between the lower modes. Hence a 6 mode partial sum from an $N = 10$ calculation provides better results than the $N = 6$ calculation alone. This effect occurs in a related work by Wang and Kassoy (1993).

Similar modal computations done for $\omega = 2.5$ with the initial mode amplitude reduced by 50% are shown in Figure 18 for $N = 6$. Reasonably good comparisons are found from a six mode summation. Partial sum comparisons suggest that the energy is again concentrated in the first few modes.

The smaller amplitude vortical radial velocity can be calculated by integrating equation (77). Figure 19 describes the rotational radial velocity V_{r1} as a function of r_1 at t=40, M=0.01 and z= 0.5 with a 6 mode partial sum from a 8 mode computation. Beyond the vorticity front the transient radial velocity distribution is a known constant multiplying the steady radial velocity.

The satisfying comparison between finite difference and modal solutions provides strong confidence in the characteristic solution properties. It is noted that CPU time requirement for direct finite diffence computations is considerably less than that for modal solutions, given equivalent resolution requirements. However, the modal solutions can be used to obtain insights to the energy distribution at various length scales, not easy to find from finite difference calculations.

8 Conclusions

Systematic methods have been employed to formulate a mathematical model to describe the creation and evolution of unsteady rotational flow in a long, narrow cylinder. Boundary driven axial, planar acoustic waves interact with an inviscid, weakly rotational, injection induced steady flow to produce time dependent vorticity at the sidewall of the cylinder. The relatively intense vorticity is convected into the entire chamber by the steady radial velocity field for appropriate ranges of Reynolds and Mach number and frequency. The amplitude and distribution of the vorticity is impacted by viscous and nonlinear effects.

It is also demonstrated that there are parameter ranges of Mach number (injection rate), driving frequency and Reynolds number for which vorticity is really confined to thin, classical, but injected acoustic boundary layers like those discussed by Flandro (1974), Baum and Levine (1987) . These structures can appear for relatively small injection rates, relatively high driving frequency and low Reynolds numbers, so that viscous damping of the vorticity amplitude is profound. Then, the cylinder core will contain the relatively weak vorticity of the steady Culick (1966a) solution and irrotational acoustic waves driven by the boundary forcing.

There is now a considerable body of evidence in support of the presence of an

unsteady vorticity distribution within an appropriately high Reynolds number wall injected flow in a cylinder. The experiments of Brown et al.(1986a,1986b), the quasi-analytical modeling of Flandro and Roach (1993) and the computational solutions of Vuillot and Avalon (1991),Flandro and Roach (1993), and that of Kirkkopru et al. (1994) as well as the current work show unequivocally that unsteady vorticity is generated at the cylindrical surface and is convected away by the injected fluid. The core of the cylinder is free of vorticity only during the very early phases of the transient process, prior to the arrival of a well defined unsteady vorticity front.

The amplitude of the transient vorticity distributions described by Kirkkopru et al.(1994), and in the present work are $O(M^{-1})$ larger than that of the Culick(1966a) steady solution. It follows that there will be a relatively large axial shear stress on the cylinder surface,which can be calculated from equation (84), particularly for smaller M values. This result is important for applications of the theory to solid rocket engines.

One can speculate that the large transient shear stresses will impact the burning rate of a propellant which is the source of the "injected" fluid used in the present model. Perhaps there is a direct relationship between the effect of surface shear stress transients, predicted in the present work, and erosive burning concepts used in the solid rocket engineering literature (Williams,1985).

One may reasonably conclude from the results of the aforementioned studies that the classical acoustic stability predictions used for scientific and engineering purposes(e.g. Culick,1990) should be reassessed to determine the prediction reliability. It is conceivable that the acoustic pressure predictions are reasonable because the presence of vorticity does not impact the primary acoustic pressure transient found in the current theory. However, it is unlikely that velocity and shear stress predictions are accurate, given the irrotational basis of the acoustic stability analysis.

The conceptual approach used here can be extended to disturbances driven by sidewall injection transients, rather than those applied at the closed endwall. The former type of disturbance emulates the effects of propellant burning rate variations in solid rocket engines. Additionally it is noted that the variable scaling reported here will enable the development of more accurate numerical methods like those described in Kirkkopru et al.(1994).

Acknowledgement

The authors would like to thank the Air Force Office of Scientific Research for continuing support through AFROSR 89-0023. A substantial discussion with Professor N. Riley of the University of East Anglia is much appreciated. Professor Gary Flandro was kind enough to provide a copy of his Final Report (Flandro and Roach, 1992). We acknowledge his inspirational contributions to the study of vorticity generation in wall injected flow systems.

REFERENCES

Balakrishnan,G., Liñán,A. and Williams,F.A.(1991), "Compressibility effects in thin channels with injection ", *AIAA J.* **29** No.12, 2149-2154

Baum,J.D.(1990), (personal communication), "Energy Exchange Mechanisms Between the Mean and Acoustic Fields in a Simulated Rocket Combustor," AFOSR Contractors Meeting, Atlanta, GA, June.

Baum,J.D. and Levine, J.N.(1982)" Numerical Techniques for Solving Nonlinear Instability Problems in Solid Rocket Motors", *AIAA J.***20**,955-961

Baum, J. D. and Levine, J. N.(1987)" Numerical Investigation of Acoustic Refraction ", *AIAA J.* **25**, 1577-1586

Baum, J. D.(1989) " Investigation of Flow Turning Phenomenon; Effects of Frequency and Blowing Rate," AIAA-89-0293, AIAA 27th Aerospace Sciences Meeting, Reno, NV, January.

Baum,J.D.(1988) " Investigation of Flow Turning Phenomenon; Effects of Upstream and Downstream Propagation," AIAA-88-0544,AIAA 26th Aerospace Sciences Meeting,Reno,NV, January.

Baum,J.D.(1987) " Acoustic Energy Exchange Through Flow Turning,"AIAA-87-0217, AIAA 25th Aerospace Sciences Meeting,Reno,NV, January.

Brown, R. S., Blackner, A. M., Willoughby, P. G., and Dunlap, R.(1986a) " Coupling Between Acoustic Velocity oscillations and Solid Propellant Combustion", *J. Propulsion and Power*, **2**,428-437.

Brown,R.S., Blackner,A.M., Willoughby,P.G., and Dunlap,R.(1986b) "Coupling Between Velocity Oscillations and Solid Propellant Combustion," AIAA Paper 86-0531, AIAA Aerospace Sciences Meeting, January 1986.

Brown,R.S.and Shaeffer,C.W. (1992) (personal communication) " Oscillatory Internal Flow Field Studies," AFOSR Contractors Meeting in Propulsion, LaJolla, California, June 1992.

Chen, T., Hegde, U., and Zinn, B. (1990) "Driving of axial acoustic fields by side wall stabilized diffusion flames," AIAA 90-0037, AIAA Aerospace Sciences Meeting, January.

Cole, J.D. and Aroesty, J. (1968) " The Blowhard Problem— Inviscid Flows with Surface Injection," *Int. J. HEAT Mass Transfer*, **11** No.7, 1167-1183

Culick, F.E.C. (1966a),"Rotational Axisymmetric Mean Flow and Damping of Acoustic Waves in Solid Propellant Rocket", *AIAA J.* **4**,1462-1463.

Culick, F.E.C. (1966b) "Acoustic Oscillations in Solid Propellant Rocket Chambers," *Astron. Acta* **12**,113-126.

Culick, F.E.C. (1967) "Calculation of the Admittance Function for a Burning Surface," *Astron. Acta* **13**,221-238.

Culick, F.E.C. (1968) "A Review of Calculations for unsteady burning of a Solid Propellant," *AIAA J.* **6**,2241-2255.

Culick, F.E.C. (1970)"Stability of Longitudinal Oscillations with Pressure and Velocity coupling in a Solid Propellant Rocket," *Comb. Sci. Tech.* **2**,179-201.

Culick, F.E.C. (1971)"Nonlinear Growth and Limiting Amplitude of Acoustic Oscillations in Combustion Chambers," *Comb. Sci. Tech.* **3**,1-16.

Culick, F.E.C. (1973)"The stability of One-dimensional motion in Rocket Motor," *Comb. Sci. Tech.* **7**,165-175.

Culick, F.E.C. (1975) "Stability of Three Dimensional Motions in a Combustion Chamber," *Comb. Sci. Tech.* **10**,109-124.

Culick, F.E.C. (1976)"Nonlinear behavior of Acoustic Waves in Combustion Chambers," *Comb. Sci. Tech.* **15**,95-97.

Culick, F.E.C. (1988)," Combustion Instability in Liquid-fueled propulsion System–An Overview," AGARD 72B PEP Meeting, October.

Culick, F.E.C. (1990)" Some Recent Results for Nonlinear Acoustics in Combustion Chambers," AIAA 90-3927, Aeroacoustics Conference, October.

Flandro, G.A. (1974)"Solid Propellant Admittance Correction," *J. Sound and Vibration*, **36**, No.22 97-312.

Flandro, G.A., (1986) "Vortex Driving Mechanism in Oscillatory Rocket Flows," *J. Prop. Pow*, **2**, 2,206-214.

Flandro, G.A. and Roach, R.L. (1992) (personal communication) *Effects of Vorticity Production on Acoustic Waves in a Combustion Chamber*. Final Technical Report AFOSR-90-0159

Fisher, R.A. (1936) The Wave of Advance of an Advantageous Gene. *Ann. Eugen.* **7**,355-369.

Grad, H.(1949) " Resonance Burning in Rocket Motors, " *Comm. Pure Appl. Math.*, **2**, 79-102.

Hegde, U. G., Chen, F., and Zinn, B. T. (1986) " Investigation of the Acoustic Boundary Layer in Porous-Walled Ducts with flow," *AIAA J.* **24**, 1474-1482.

Hegde, U.G. and Zinn,B.T. (1986), "The Acoustic Boundary Layer in Porous-Walled Ducts with a reacting flow," 21st Symp. (Int'l.) Combust. 1993-2000

Jahnke,C.C. and Culick, F.E.C.(1993) " An Application of Dynamical Systems Theroy to Nonlinear Combustion Instabilities, "AIAA-93-0114, 31st Aerospace Sciences Meeting, Reno NV.,January.

Kirkkopru, K., Kassoy, D. R. and Zhao, Q. (1994) "Unsteady Vorticity Generation and Evolution in a Model of a Solid Rocket Engine Chamber". *submitted to AIAA J.*

Matta, L.M. and Zinn, B.T. (1993) " Investigation of Flow Turning Loss in a Simulated Unstable Solid Propellant Rocket Motor," AIAA 93-0115,31st Aerospace Sciences Meeting, Reno, NV, January.

Lagerstrom, P.A. (1964) *Theory of Laminar Flows.* Section **B**, 90-92, Moore, F.K. ed., Princeton University Press.

Price, E.W. and Flandro, G.A. (1993) *Combustion Instability in Solid Propellant Rockets.* Book manuscript in preparation.

Sankar, S.V., Hegde, U.G., Jagoda, J.I., and Zinn, B.T.(1988a) "Driving of Axial Acoustic Waves by side wall Stabilized Premixed Flames", 22nd Symp. (Int'l) on Combustion, 1865-1873

Sankar, S.V., Jagoda, J.I., Daniel, B.R., and Zinn, B.T.(1988b) "Measured and Predicted Characteristics of Premixed Flames Stabilized in Axial Acoustic Field," AIAA 88-0541, AIAA Aerospace Sciences Meeting, January.

Taylor,G.I. (1956) "Fluid Flow in Regions Bounded by Porous Surfaces," *Proc. Roy. Soc.* London **A 234**,456-475

Tien, J.S. (1972) "Oscillatory Burning of Solid Propellant; including Gas Phase Time Lag", *Comb. Science and Tech.***5**, 47-54.

Vuillot,F. and Avalon,G. (1991) "Acoustic Boundary Layers in Solid Propellant Rocket Motors Using Navier-Stokes Equations", *J.Propulsion* **7**,#2 231-239.

Vuillot,F.(1991) " Numerical Computation of Acoustic Boundary Layers in Large Solid Propellant Space Booster," AIAA-91-0206, 29th Aerospace Sciences Meeting, Reno, NV, January.

Wang, M. and Kassoy, D. R. (1990a) "Dynamic response of an inert gas to slow piston acceleration," *J. Acoust. Soc. America* **87**,1466-1472

Wang, M. and Kassoy, D. R. (1990b) "Dynamic compression and weak shock formation in an inert gas due to fast piston acceleration," *J. Fluid Mech.***220**, 267-292.

Wang, M. and Kassoy, D. R. (1990c) "Evolution of weakly nonlinear waves in a cylinder with a movable piston," *J. Fluid Mech.* **221**, 23-52.

Wang, M. and Kassoy, D. R. (1992a) "Transient acoustic processes in a low Mach number shear flow," *J. Fluid Mech.* **238**, 509-536.

Wang, M. and Kassoy, D. R.(1992b) " Standing Acoustic Waves in a Low Mach Number Shear Flow," *AIAA J.* **30**, 1708-1715.

Wang, M. and Kassoy, D. R. (1993) Nonlinear Acoustic Oscillation in Resonant System: An Initial-Boundary Value Study, ***submitted to SIAM J. Appl. Math.***

Williams, F.A.(1985) *Combustion Theory*, Benjamin/Cummings, Menlo Park.

Appendix A: Solution to a Related Model Problem

The nonlinear coupled system in (102) is sufficiently complex to require a computational solution. In order to develop an effective numerical approach, it is desirable to consider the solution to an elementary model problem with related properties. A

simple Fisher equation (Fisher,1936) with appropriate periodic initial and boundary conditions can be used:

$$\frac{\partial U}{\partial s} = \frac{\partial^2 U}{\partial y^2} + \nu U^2, \qquad y > 0, t > 0 \qquad (A-1)$$

Initial Condition:

$$U(0,y) = -\sin(t-y) \quad for\ 0 \le y \le t; \qquad (A-2)$$
$$U(0,y) = 0 \quad for\ y > t \qquad (A-3)$$

Boundary Condition:

$$U(y=0) = -\sin(t) \qquad (A-4)$$

When the parameter t is increased, the nonzero portion of the initial condition is spread farther into the y-domain. In the spirit of (102), the multiple scale independent variables are related by $y = \Omega^2 s$ and $\Omega \gg 1$.

An analytical solution for linear diffusion ($\nu = 0$) is constructed for the odd extension of (A-2) and (A-3) for the domain $0 < y < \infty$:

$$U(s,y) = -\frac{1}{2\sqrt{\pi s}} \int_0^t \sin(t-y') \left[e^{-\frac{(y-y')^2}{4s}} - e^{-\frac{(y+y')^2}{4s}} \right] dy'$$
$$-\frac{y \sin(t)}{2\sqrt{\pi}} \int_0^s \frac{e^{-\frac{y^2}{4(s-s')}}}{(s-s')^{\frac{3}{2}}} ds', \quad y > 0 \qquad (A-5)$$

A quasi-steady solution form $U(s,y) = -\sin(t-y)e^{-s}$, $y > 0$ can be recovered by taking the limits $(\frac{y \pm t}{2\sqrt{s}}) \to \pm\infty$ and $s \to 0^+$ simultanously. Physically, this means that the solution has a quasi-steady form at a specific value of t if y lies between y=0 and the inner edge of a diffusive boundary layer centered at $y = t$ which is needed to smooth the discontinuous slope of the initial condition (A-2) and (A-3) at that location. Inside the diffusive layer, the solution is given by the full form of (A-5). The diffusive layer thickness is $\delta \sim O(\frac{\sqrt{s}}{\Omega^2})$.

The solution to (A-1)-(A-4) along the locus $y = \Omega^2 s$, for $\nu = 1$ and $\Omega^2 \approx 66$,has been found from a computational analysis based on an elementary explicit finite different method. The boundary condition (A-4) is enforced at $y = 0$ for each integration step in s direction. The integration of U with respect to s is carried out for $0 \le s \le 2.25$ with step size $\delta s = 0.0015$. The far end boundary condition is implemented in such a way that there are a sufficient number of grid points with zero value lying between the furthest grid point with nonzero value and the finite location of the computational boundary with respect to y after each integration in s direction. The dashed line in Figure 20 describes the linear solution when $t = 100$ obtained from (A-5). An analogous numerical result ($\nu = 0$) is indistinguishable from the analytical solution on the scale of the graph, thus verifying the numerical code. The linear solution shows regular, nearly harmonic spatial oscillations that decay until the diffusive layer is reached near $s \approx 1.5$. There the solution makes a rapid transition to a vanishingly small value for $s > 1.5$. In comparison the solid line represents the nonlinear numerical solution for $\nu = 1$. The frequency is nearly identical to the linear solution.

However, the drift of the solution toward positive values of U is due to the positive definite source effect, νU^2. Again the deviation from the pattern of oscillations near $s \approx 1.5$ is associated with the diffusive layer behavior. Given the parameters used in the calculation, the diffusive layer thickness with respect to the s coordinate is about 0.1. The analogous results for $\nu = -1$, corresponding to a nonlinear sink, are given in Figure 21. There is no expectation of symmetry.

The basic properties of the model problem solution can be used to develop an effective numerical method for (102).

Table 1: Acoustic Response Properties for Several Driving Frequencies

ω	ω'(Hz)	Properties	Primary Response
1	159	stable	axial + quasi-steady modes
1.5	238	beats	quasi-steady modes with axial wave modulation
$\pi/2$	250	axial amplification	linear growth

9 CAPTIONS

Figure 1: The cylindrical rocket engime chamber model of length L', diameter D', with endwall oscillations of frequency ω.

Figure 2: The time response of the axial acoustic velocity $\tilde{V}_{z0}$ at z=0.5 and $\omega = 1.0$.

Figure 3: The time response (beats) of the axial acoustic velocity $\tilde{V}_{z0}/30$ at z=0.5 and $\omega = 1.5$.

Figure 4: The time response of the axial acoustic velocity $\tilde{V}_{z0}$ at z=0.5 and $\omega = \pi/2$,linear growth.

Figure 5: The axial velocity in the boundary layer as a function of the variable of ξ fo M=0.01,$\beta = 0.1$ when $\Omega = 2.5$ and 3.0 . The boundary layer is thicker for the smaller frequency value.

Figure 6: The spatial variation of the rotational axial velocity component $\hat{W}_0$ with the radial variable r_1 at t=20. It can be seen that the front is about 23% of the way to the centerline and nearly 4 spatial oscillations have entered the cylinder.

Figure 7a,b,c: The spatial variation of the rotational axial velocity component $\hat{W}_0$ at t=30 for (a)z=0.25,(b)z=0.5 (c)z=0.75 with the radial variabler_1. The front is about 35% of the way to the centerline and nearly 5.5 spatial oscillations have entered the cylinder. The amplitude of the oscillations near the front at this moment is noticably smaller those at t=20, an accumulative effect of viscosity on M scale.

Figure 8a: The spatial variation of the rotational axial velocity component $\hat{W}_0$ with the radial variable r_1 at t=40, z=0.25. The front is about 45% of the way to the centerline and nearly 7.5 spatial oscillations have entered the cylinder. Strong nonlinear effects alter the overall pattern.

Figure 8b: The spatial variation of the rotational axial velocity component $\hat{W}_0$ with the radial variable r_1 at t=40, z=0.5. The front is about 45% of the way to the centerline and nearly 7.5 spatial oscillations have entered the cylinder. The amplitude of the oscillations near the front at this moment is substantially smaller those at t=20, an accumulative effect of viscosity on M scale.

Figure 8c: The spatial variation of the rotational axial velocity component $\hat{W}_0$ with the radial variable r_1 at t=40, z=0.75 . It has the generic features as in Figure 8b.

Figure 9: The spatial variation of unsteady vorticity $\Omega_\theta/100$, with the radial variable r_1 . The magnitude of Ω_θ is O(1/M) bigger than the steady vorticity and therefore dominant in the cylinder. The shear stress on the wall imposed by the unsteady vorticity is significant.

Figure 10a,b,c: The spatial variation of the rotational axial velocity component $\hat{W}_0$ at t=40 for (a)z=0.25,(b)z=0.5,(c)z=0.75, with the radial variable r_1 when the nonlinear term is suppressed. A comparison of these with Figures 8a,b,c demonstrates nonlinear effects are strong near the fore end, moderate at the middle, small at the rear end.

Figure 11a,b,c: The spatial variation of the rotational axial velocity component $\hat{W}_0$ at t=40 for (a)z=0.25,(b)z=0.5,(c)z=0.75, with the radial variable r_1 with the viscous term reduced by 50%. A comparison with Figures 8a,b,c demonstrates that local structure is altered by the reduction of viscosity.

Figure 12: The spatial variation of the rotational axial velocity component $\hat{W}_0$ with the radial variable r_1 at M=0.05, z=0.5, ω=1.0 and t=40. The larger M corresponds to stronger injection rate on the cylinder wall. As a result, almost all the cylinder has been filled with the rotational flow compared to only 45% in the case of M=0.01 in Figure 8c.

Figure 13: The spatial variation of the rotational axial velocity component $\hat{W}_0$ with the radial variable r_1 at M=0.1, z=0.5, ω=1.0 and t=40. The larger M corresponds to a stronger injection rate on the cylinder wall.

Figure 14 a,b,c (from top to buttom): The time response of; (a) the axial acoustic

speed W_{0_p},(b) the rotational axial speed $\hat{W}_0$ and (c) the complete axial speed $V_{z0} = (W_{0_p} + \hat{W}_0)$ for r_1=0.2,z=0.5, M=0.01 and $\omega = 1.0$.

Figure 15a,b,c: The spatial variation of the rotational axial velocity component $\hat{W}_0$ with the radial variable r_1 at $\omega = 2.5$,t=40 for (a)z=0.25,(b)z=0.5, (c)z=0.75 with the amplitude of the disturbance reduced by a half. More spatial oscillations are present in the structure due to the higher driving frequency, in comparison Figures 8a,b,c.

Figure 16: The spatial variation of the rotational axial velocity component $\hat{W}_0$ with the radial variable r_1 based on a 6 mode summation from a 6 mode, nonlinear computation (N=6).

Figure 17: The spatial variation of the rotational axial velocity component $\hat{W}_0$ with the radial variable r_1 based on a 6 mode partial summation from an 8 mode, nonlinear computation (N=8).

Figure 18: The spatial variation of the rotational axial velocity component $\hat{W}_0$ with the radial variable r_1 based on a 6 mode partial summation from a 10 mode, nonlinear computation (N=10).

Figure 19: The spatial variation of the rotational radial velocity component $\hat{V}_{r1}$ with the radial variable r_1 based on the 6 mode partial summation from an 8 mode computation.

Figure 20: Solution U vs z for the nonlinear model problem on the locus curve $y = \Omega^2 z$ with $\Omega^2 \approx 66$ and $\nu = 1$ The dashed line is the plot of U vs z from (A-5) on the same locus curve.

Figure 21: Solution U vs z for the nonlinear model problem on the locus curve $y = \Omega^2 z$ with $\Omega^2 \approx 66$ and $\nu = -1$ The dashed line is the plot of U vs z from (A-5) on the same locus curve.

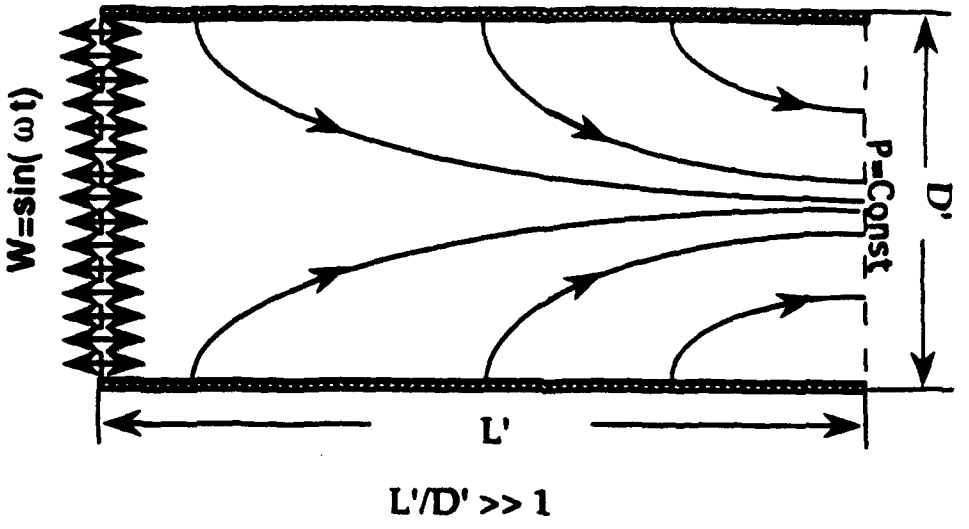

Figure 1 : The cylindrical rocket engine chamber model of length L' , diameter D' , with endwall oscillations of frequency ω

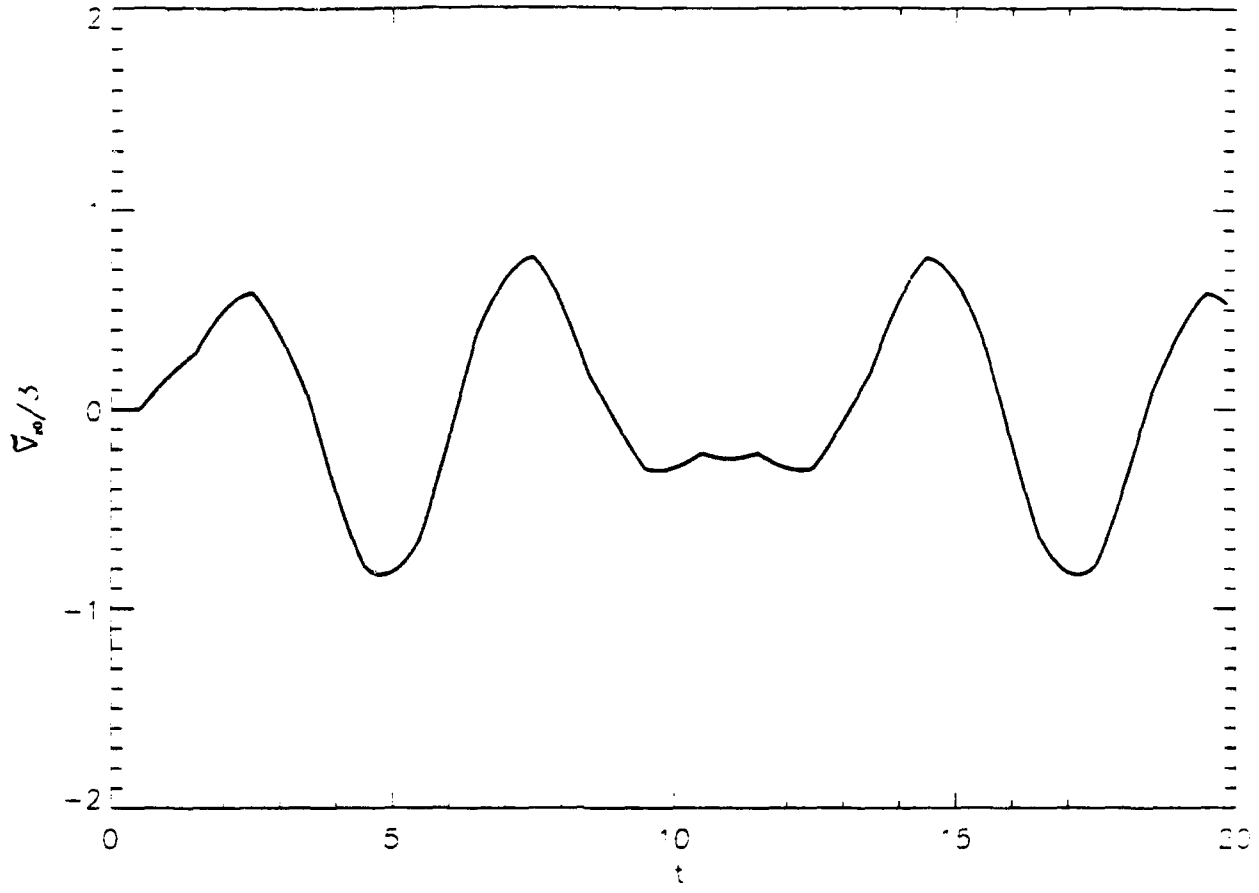

ZKK

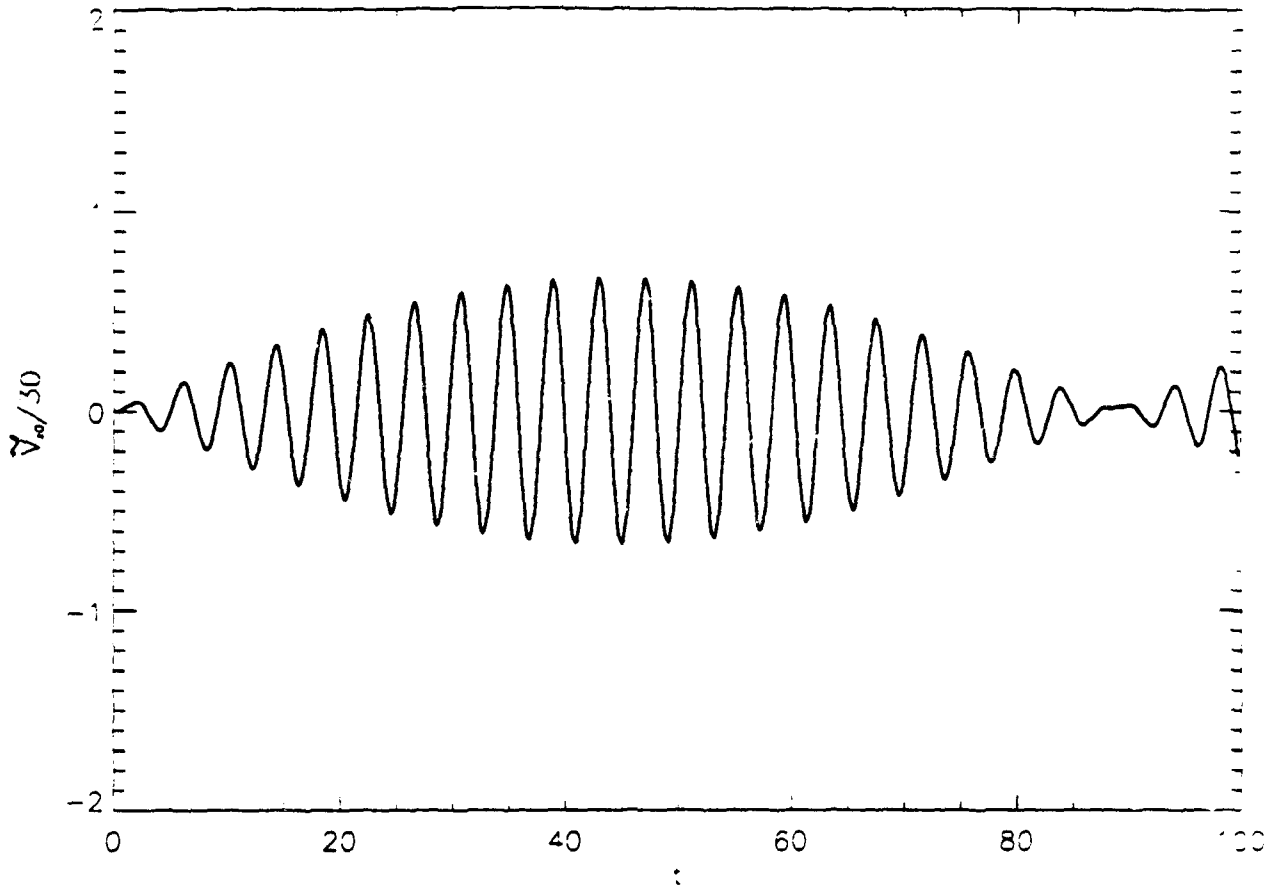

2KK

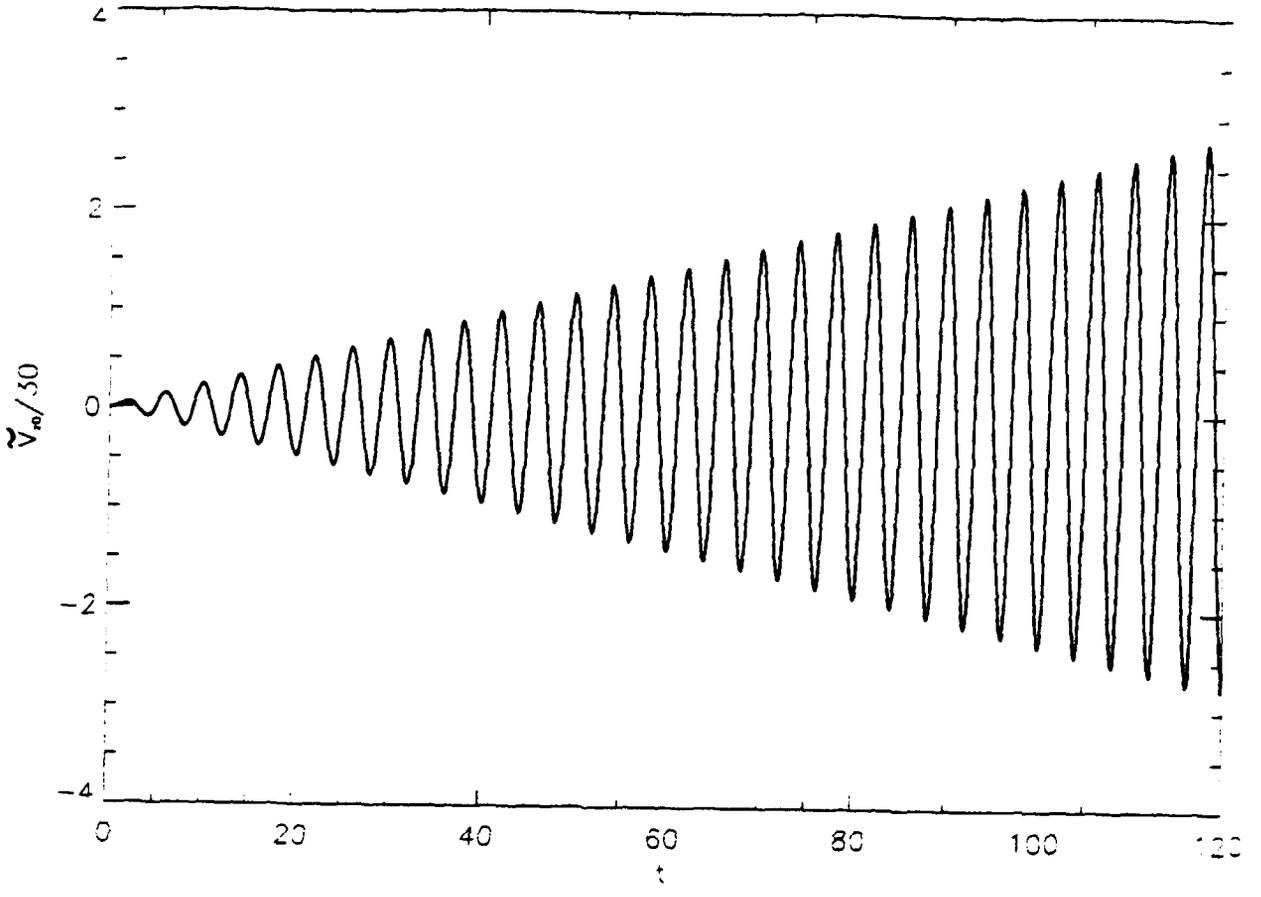

ZKK

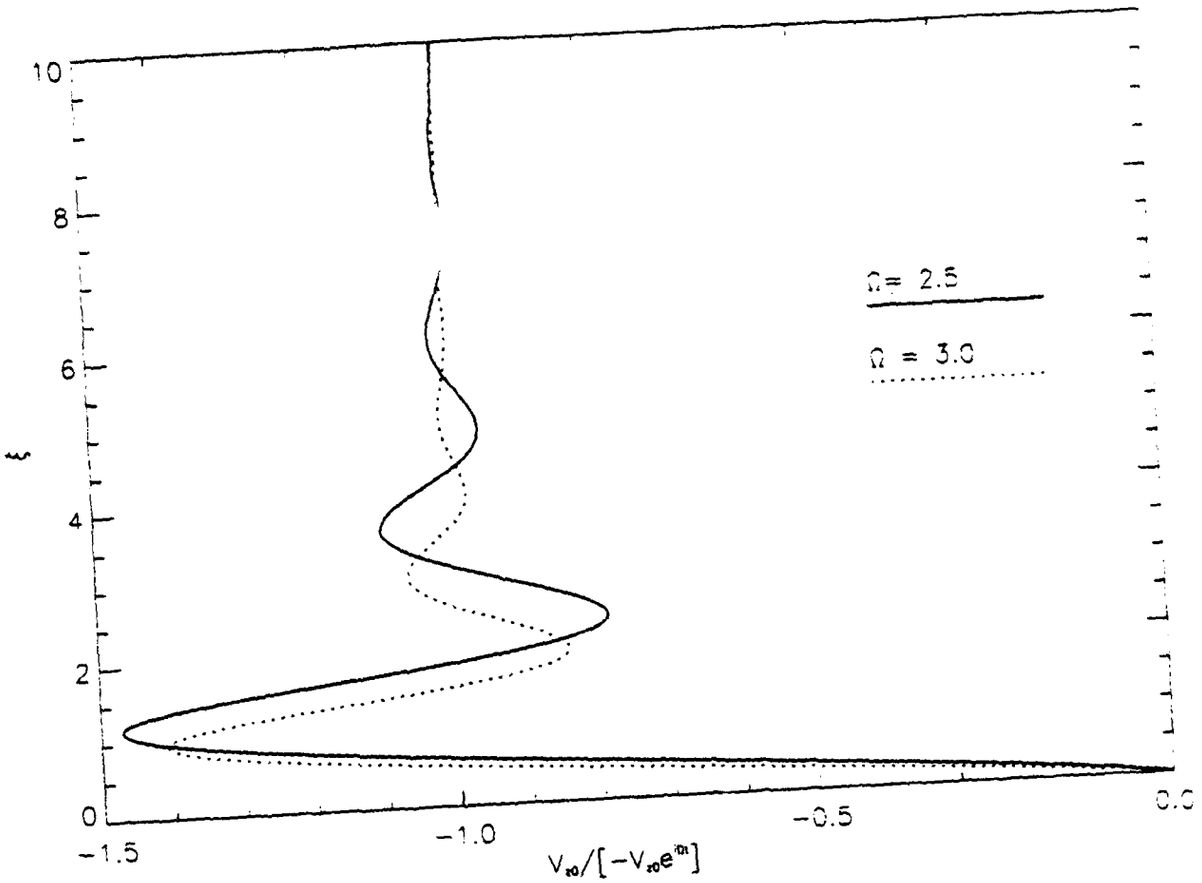

EKK

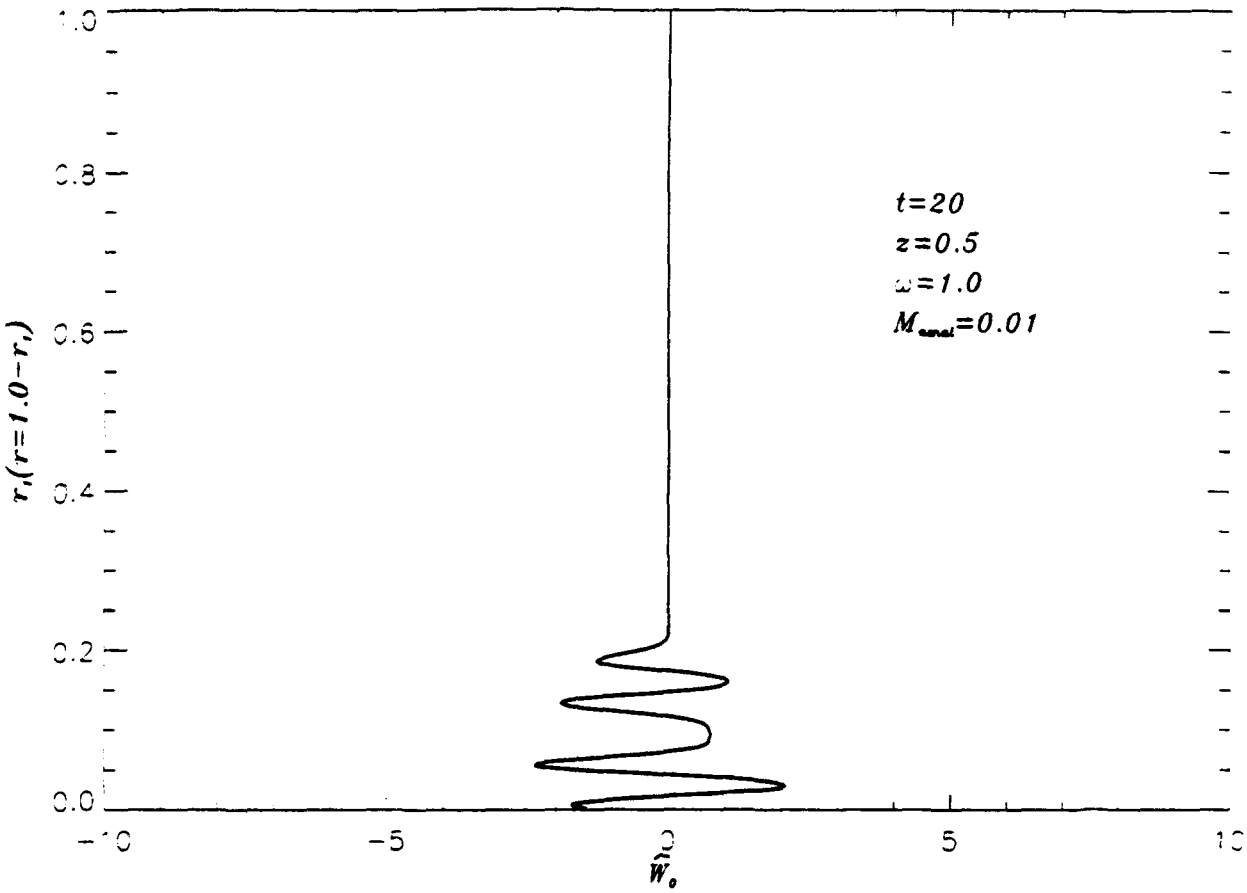
1.0
0.8
0.6
0.4
0.2
0.0
−10
−5
0
5
10
$r_i(r=1.0-r_i)$
$\tilde{w}_o$
$t=20$
$z=0.5$
$\omega=1.0$
$M_{axial}=0.01$

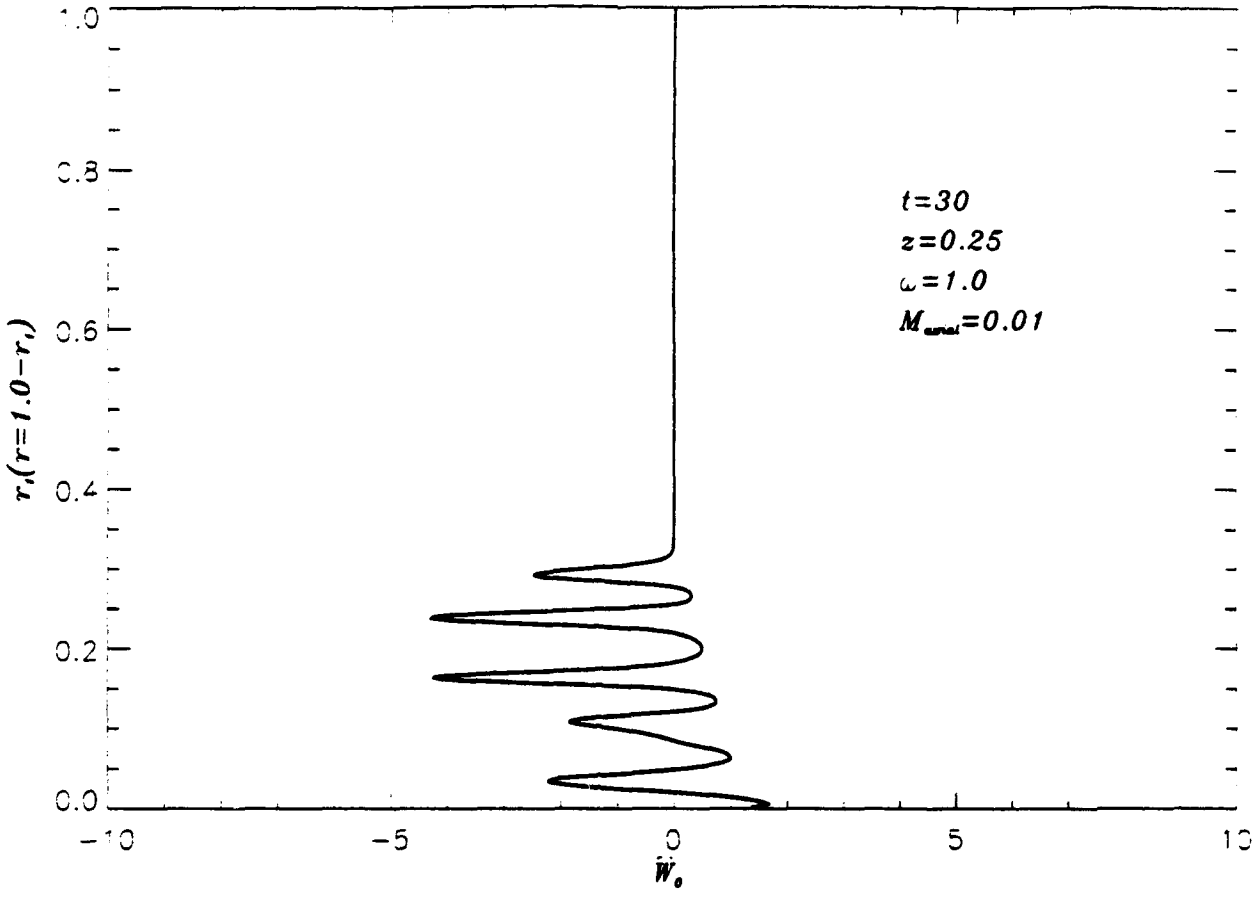
1.0
0.8
0.6
0.4
0.2
0.0
$r_i(r=1.0-r_i)$
t=30
z=0.25
ω=1.0
M_{wind}=0.01
−10
−5
0
5
10
$\tilde{W}_o$

7a

3K

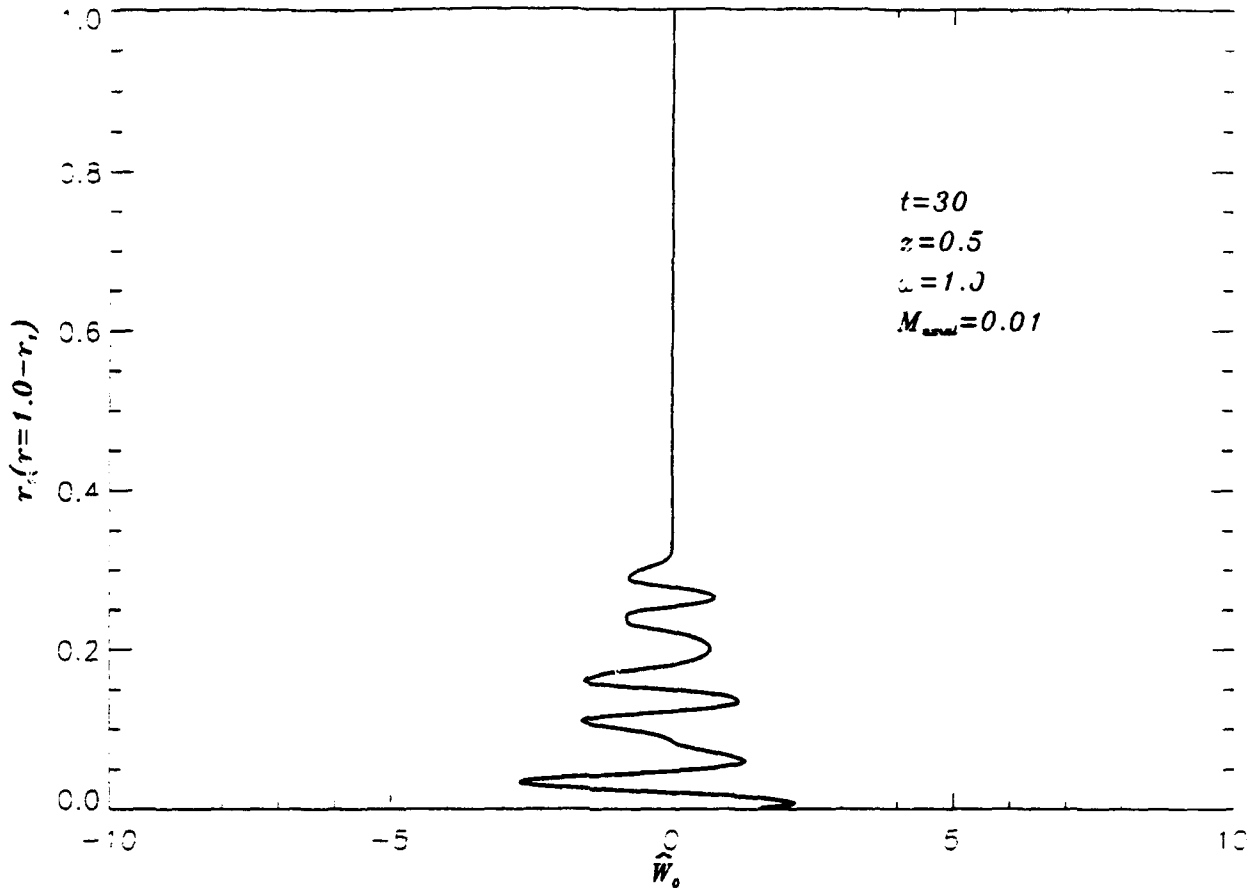
1.0
0.8
0.6
0.4
0.2
0.0
−10
−5
0
5
10
$r_s(r=1.0-r_s)$
$\widetilde{W}_0$
t=30
z=0.5
a=1.0
M_{wind}=0.01

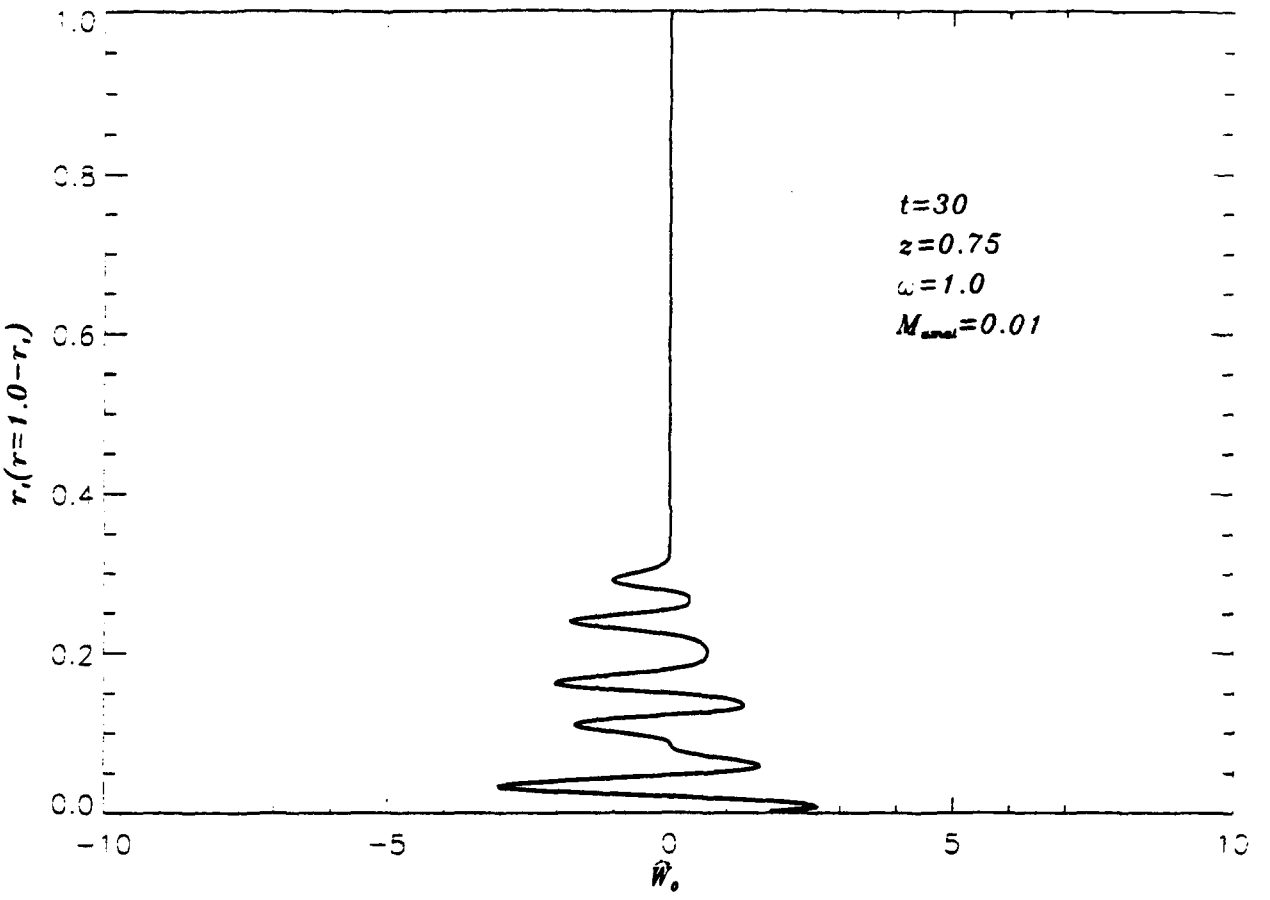
1.0
0.8
0.6
0.4
0.2
0.0
$r_i(r=1.0-r_i)$
t=30
z=0.75
ω=1.0
M_{axial}=0.01
−10
−5
0
5
10
$\hat{W}_o$

7C

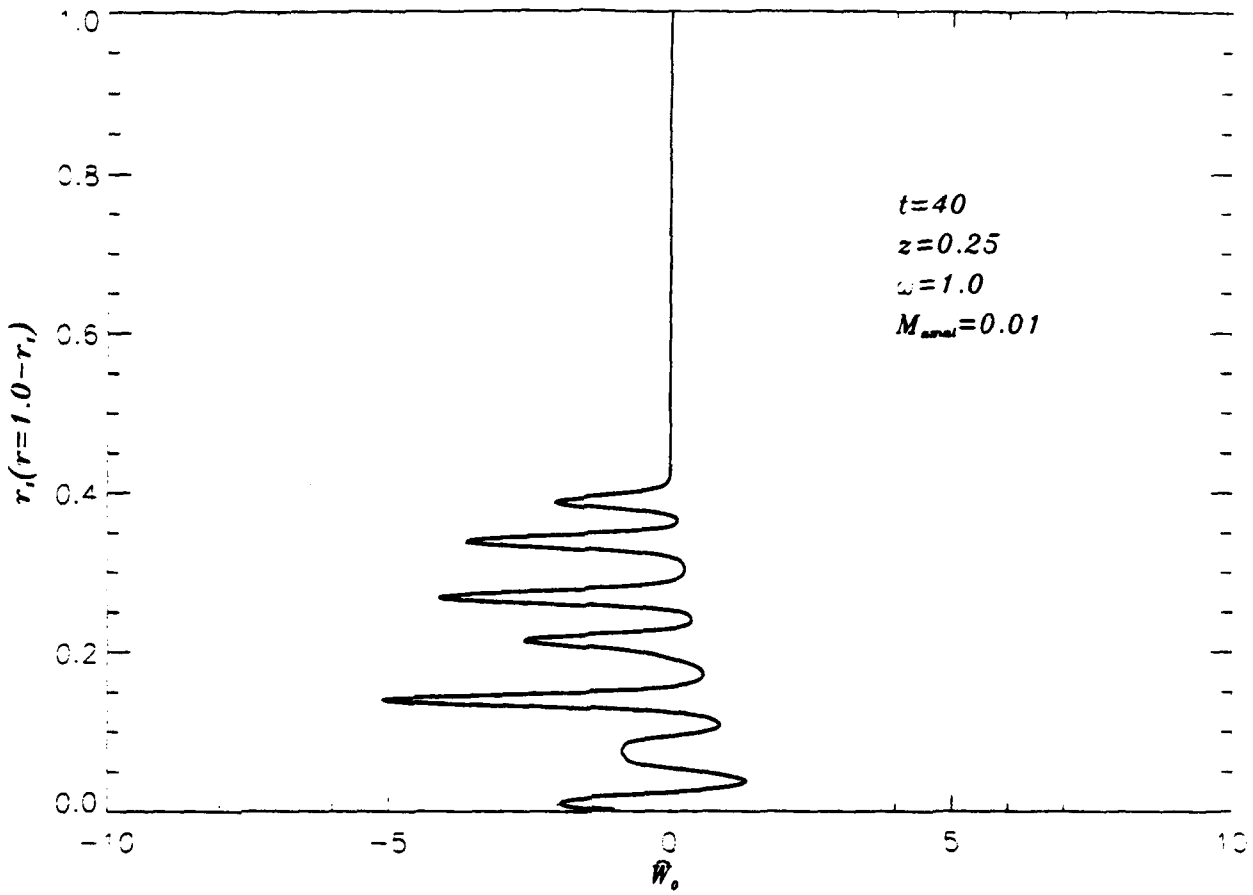
1.0
0.8
0.6
0.4
0.2
0.0
−10
−5
0
5
10
$r_t(r=1.0-r_t)$
$\tilde{w}_o$
t=40
z=0.25
ω=1.0
M_{axial}=0.01

8a

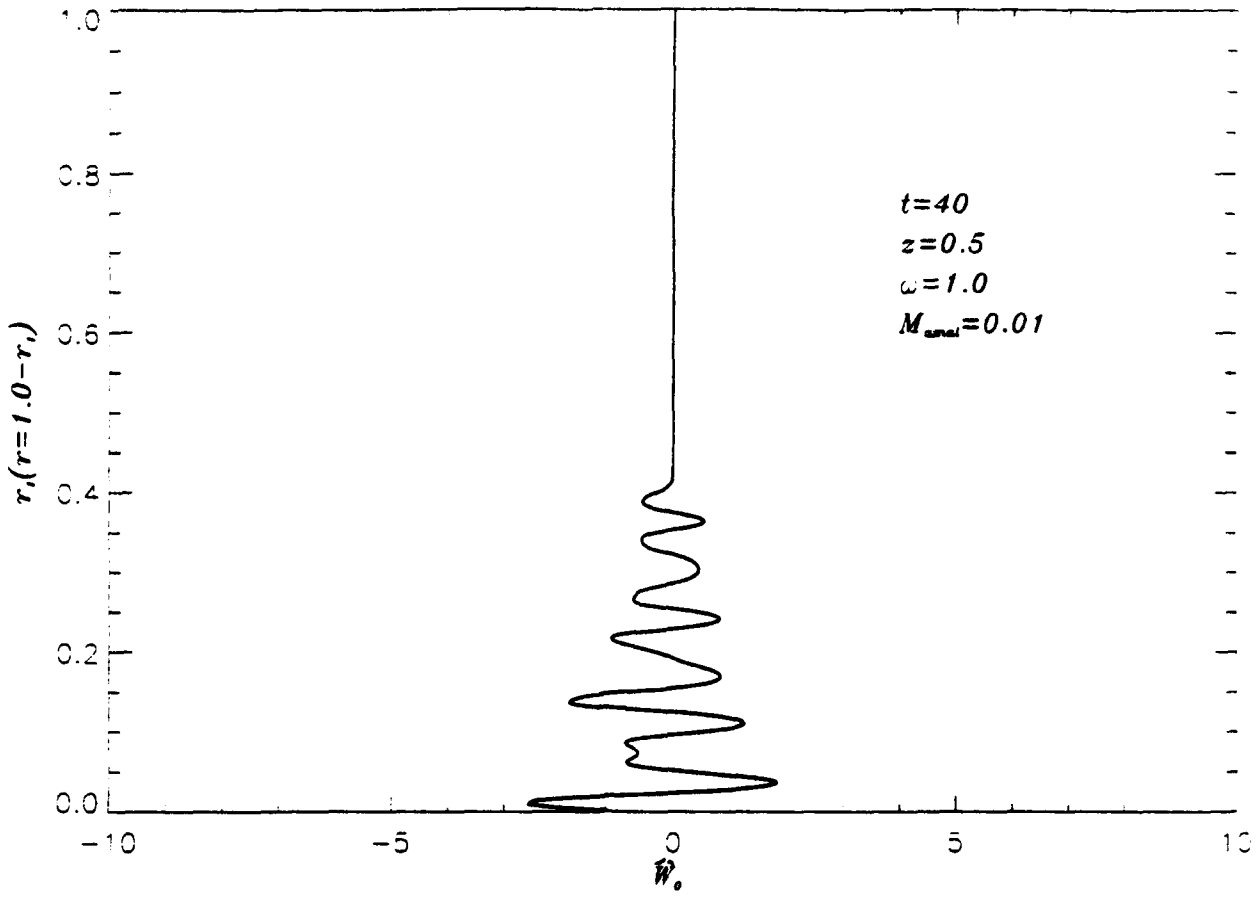
1.0
0.8
0.6
0.4
0.2
0.0
−10
−5
0
5
10
$r_i(r=1.0-r_i)$
W_o
t=40
z=0.5
ω=1.0
M_{small}=0.01

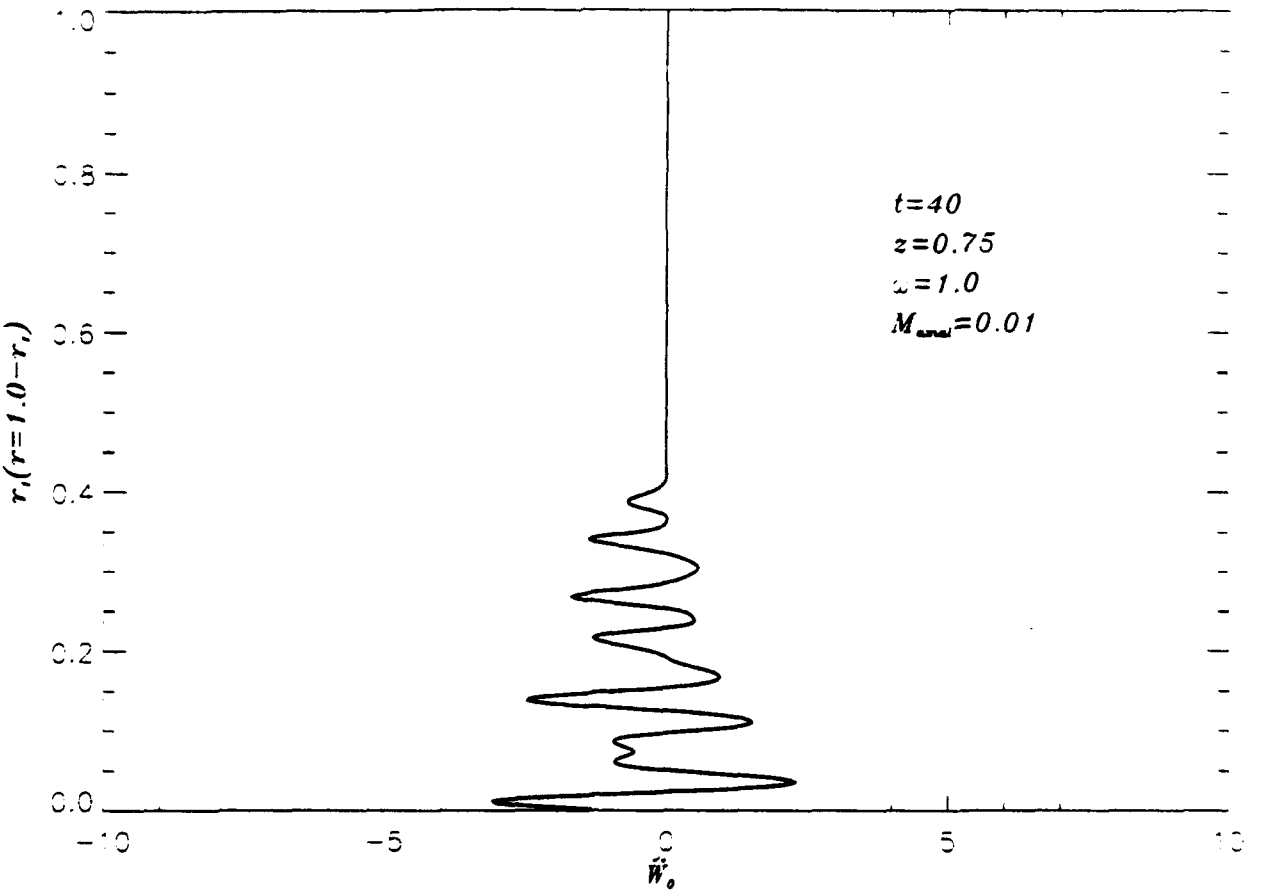
1.0
0.8
0.6
0.4
0.2
0.0
$r_t(r=1.0-r_t)$
t=40
z=0.75
ω=1.0
M_{wind}=0.01
−10
−5
0
5
10
$\tilde{W}_o$

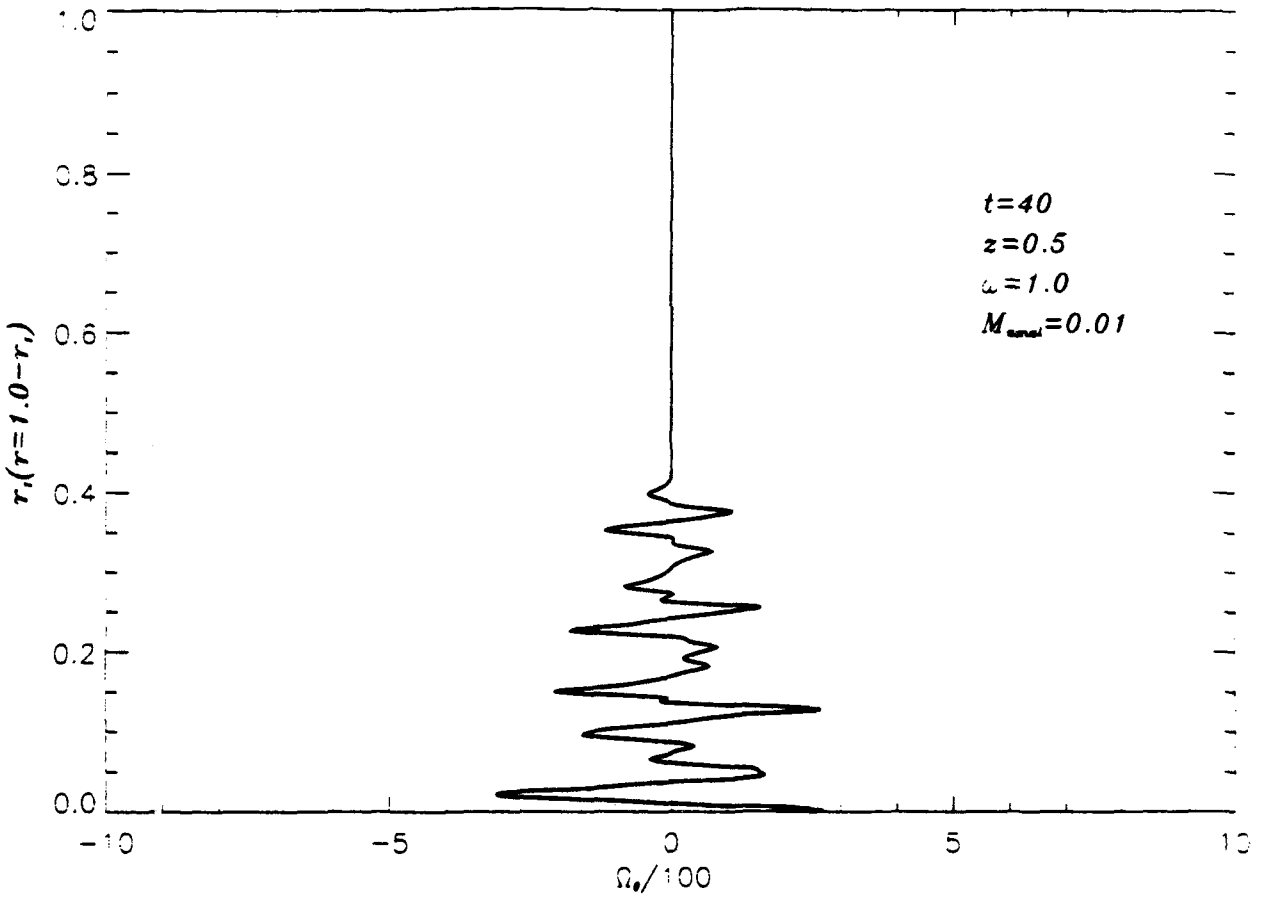
1.0
0.8
0.6
0.4
0.2
0.0
$r_i(r=1.0-r_i)$
t=40
z=0.5
ω=1.0
M_{wind}=0.01
−10
−5
0
5
10
$\Omega_\theta/100$

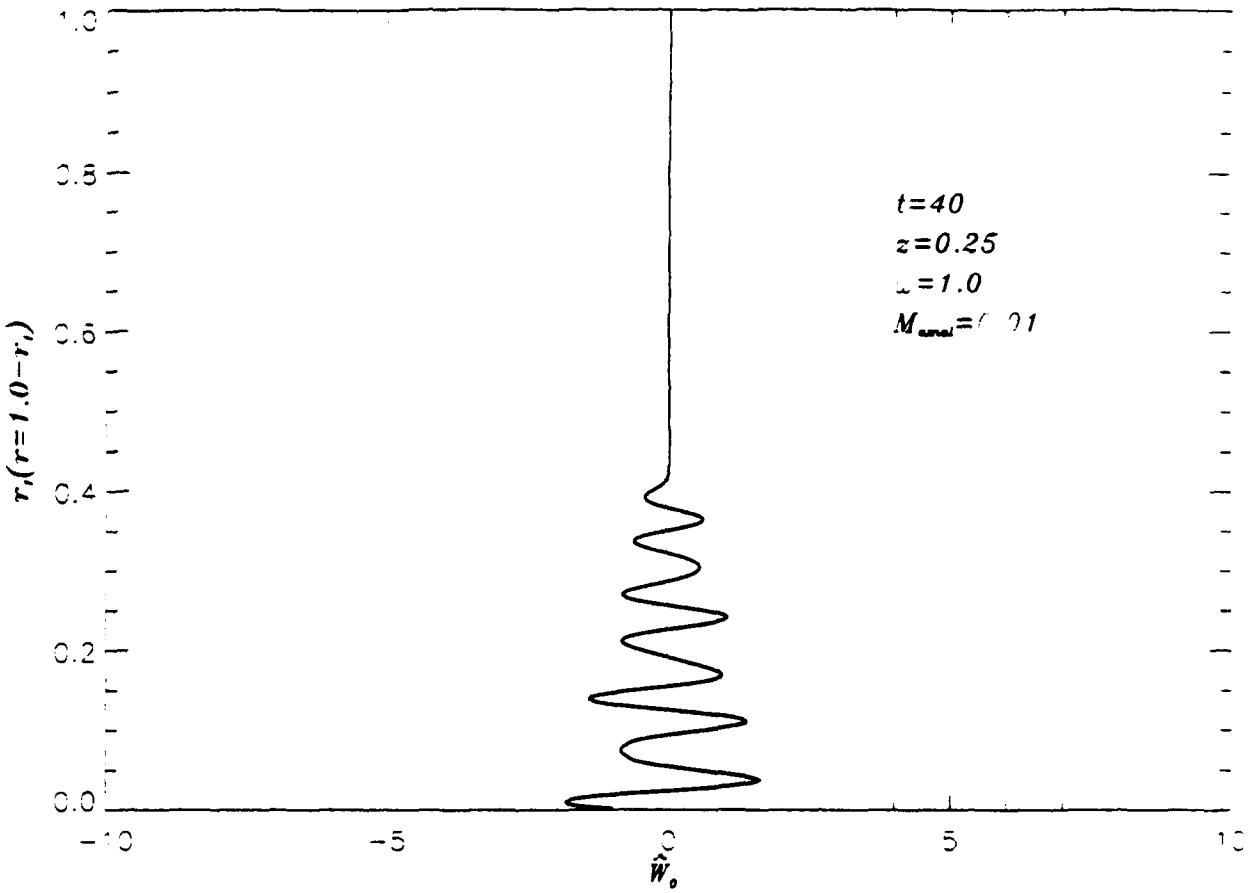

10a

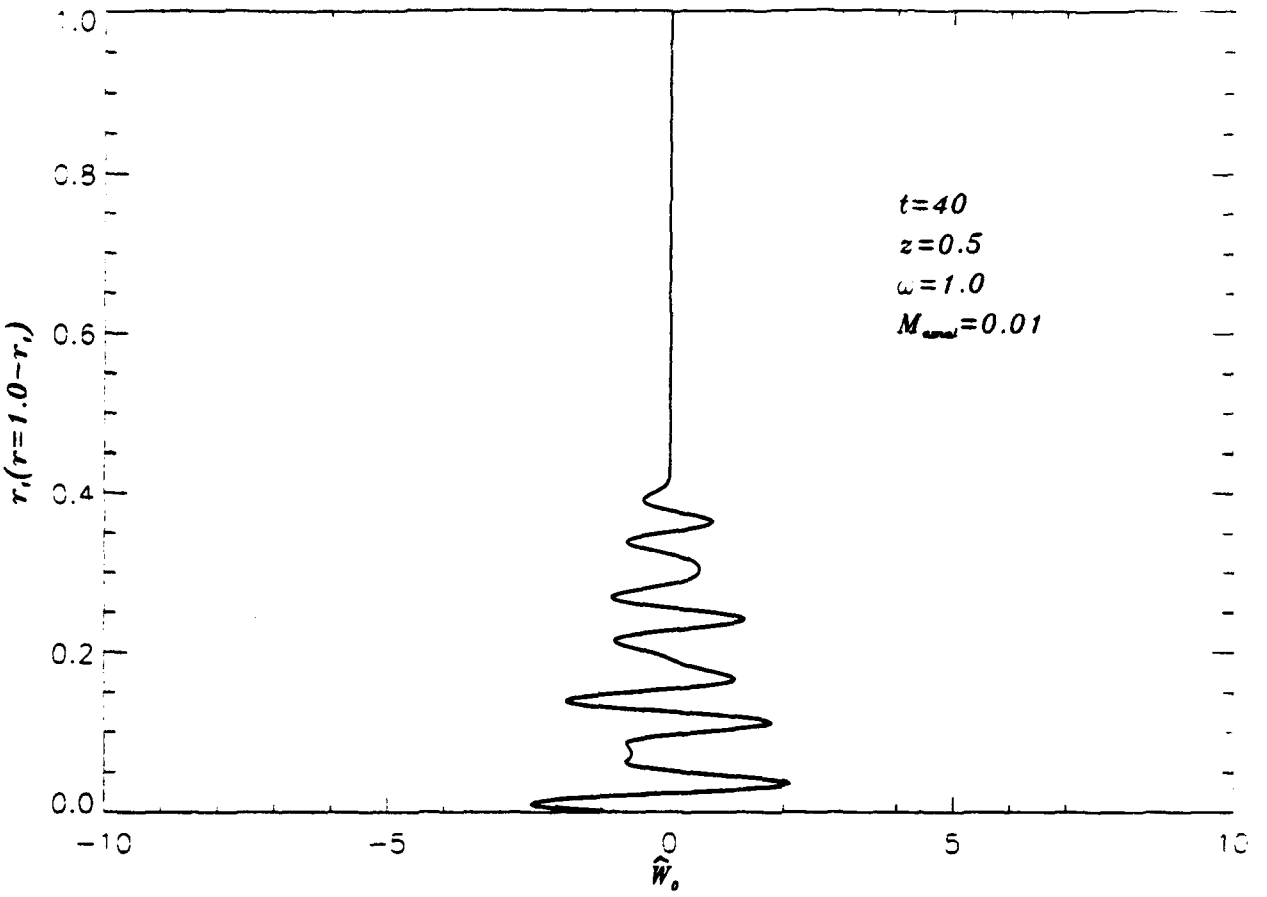
1.0
0.8
0.6
0.4
0.2
0.0
$r_i(r=1.0-r_i)$
t=40
z=0.5
ω=1.0
M_{cent}=0.01
−10
−5
0
5
10
$\hat{W}_0$

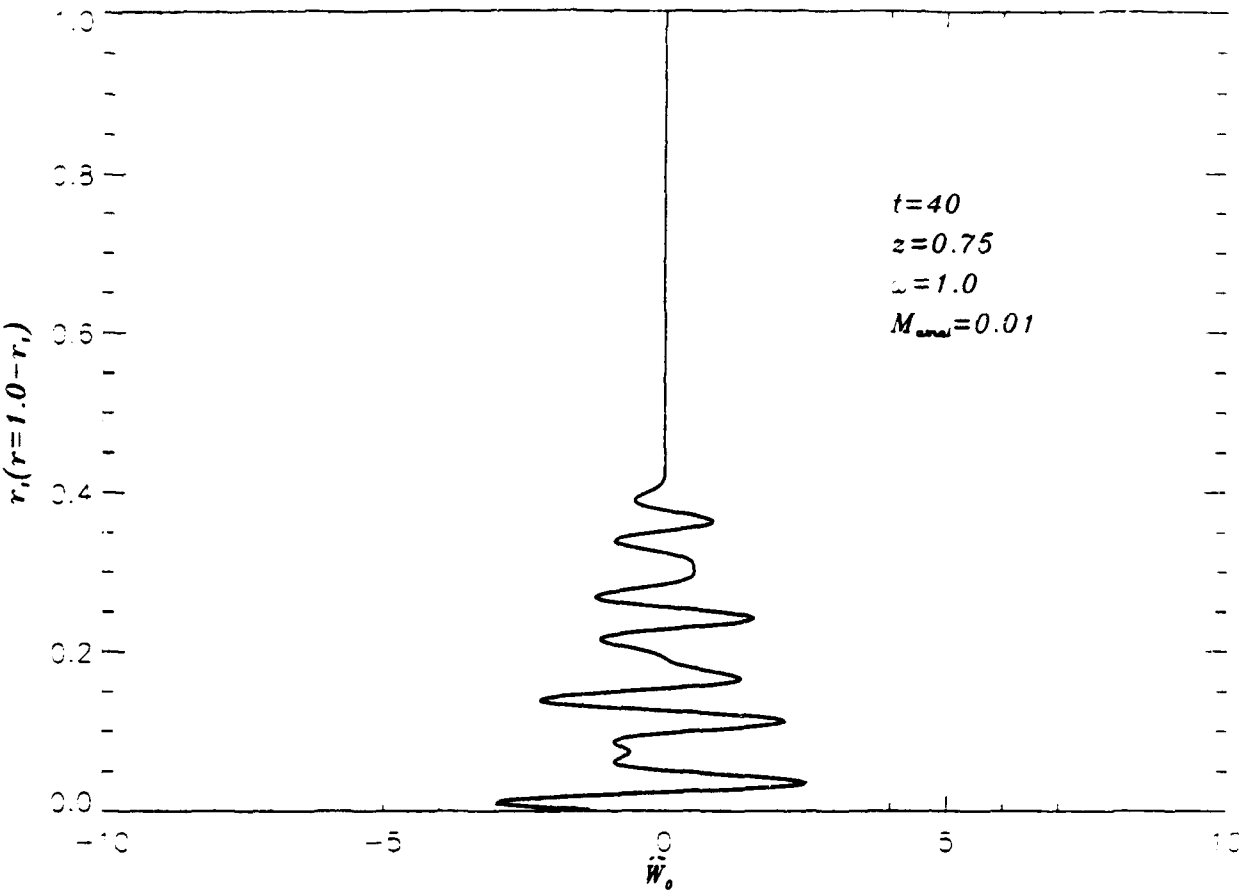
1.0
0.8
0.6
0.4
0.2
0.0
$r_1(r=1.0-r_1)$
t=40
z=0.75
ω=1.0
M_{wall}=0.01
−10
−5
0
5
10
$\ddot{W}_0$

10 C

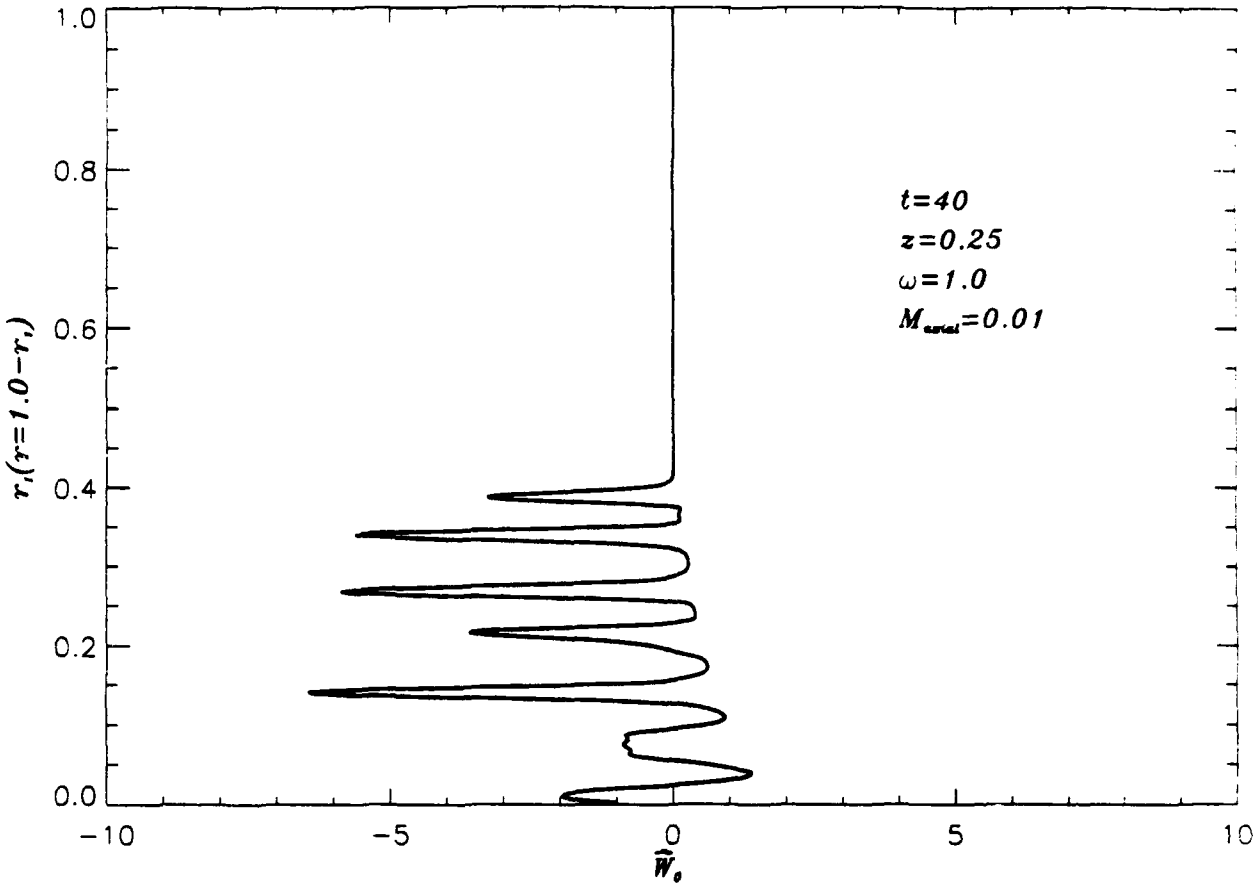
1.0
0.8
0.6
0.4
0.2
0.0
−10
−5
0
5
10
$r_i(r=1.0-r_i)$
$\widetilde{W}_0$
$t=40$
$z=0.25$
$\omega=1.0$
$M_{axial}=0.01$

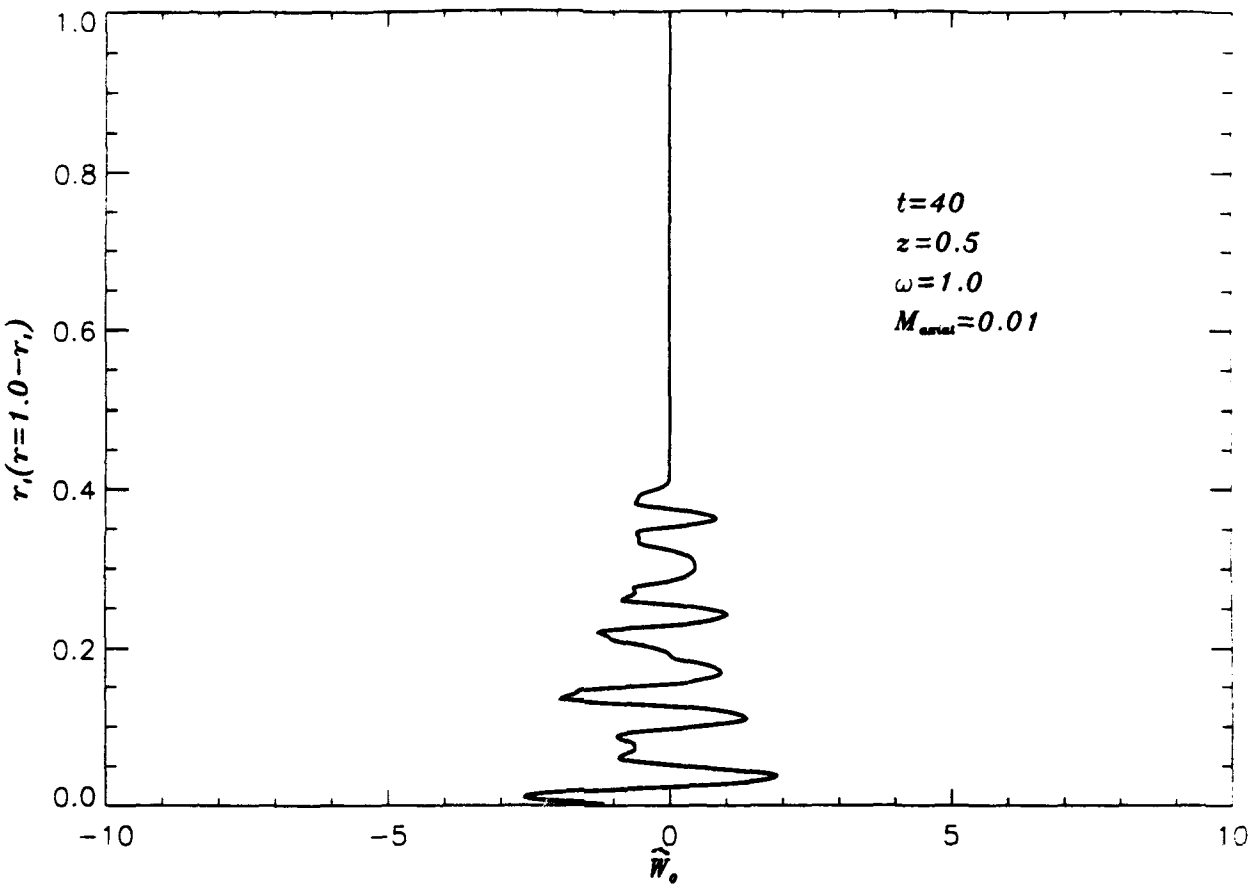
1.0
0.8
0.6
0.4
0.2
0.0
$r_i(r=1.0-r_i)$
−10
−5
0
5
10
$\hat{W}_\theta$
$t=40$
$z=0.5$
$\omega=1.0$
$M_{axial}=0.01$

2kk

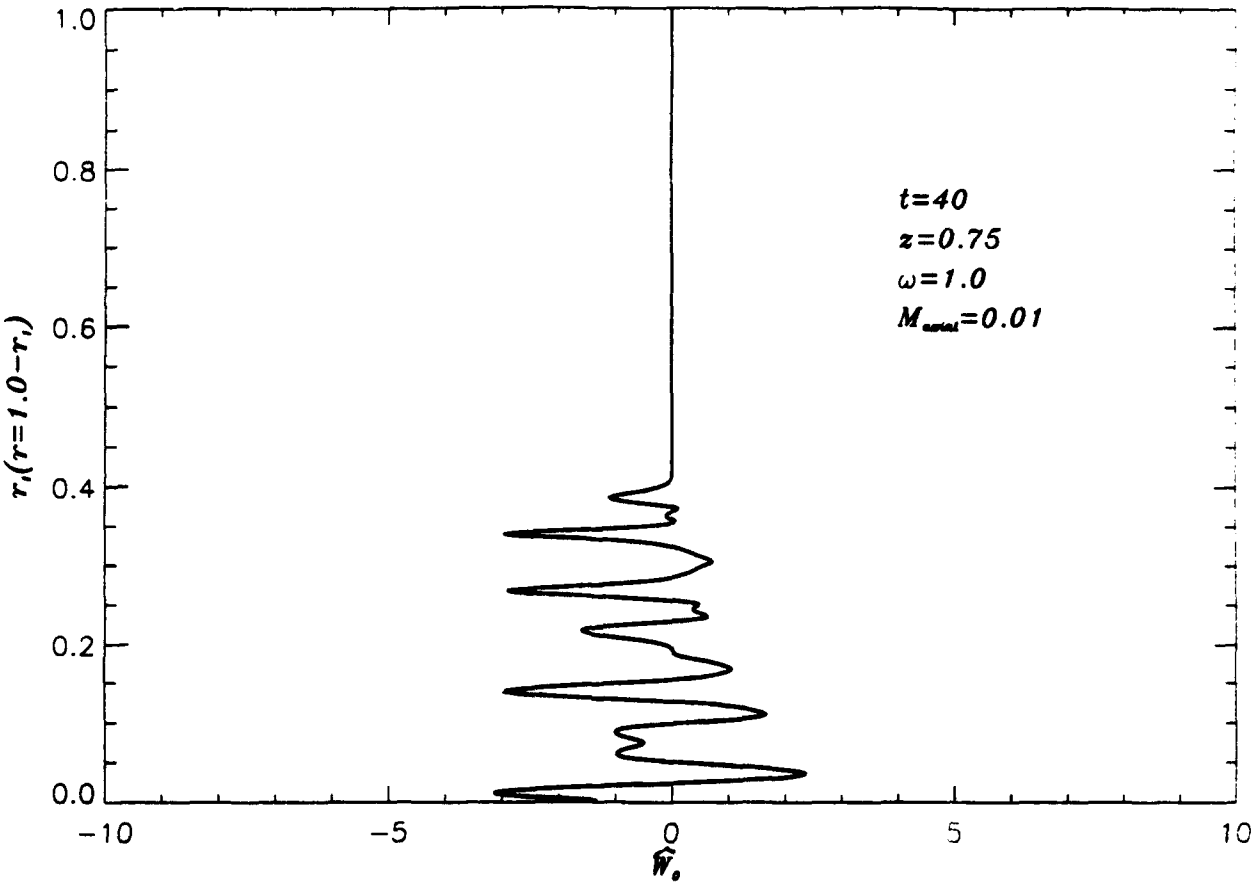
1.0
0.8
0.6
0.4
0.2
0.0
$r_i(r=1.0-r_i)$
−10
−5
0
5
10
$\hat{W}_0$
t=40
z=0.75
ω=1.0
M_{axial}=0.01

11C

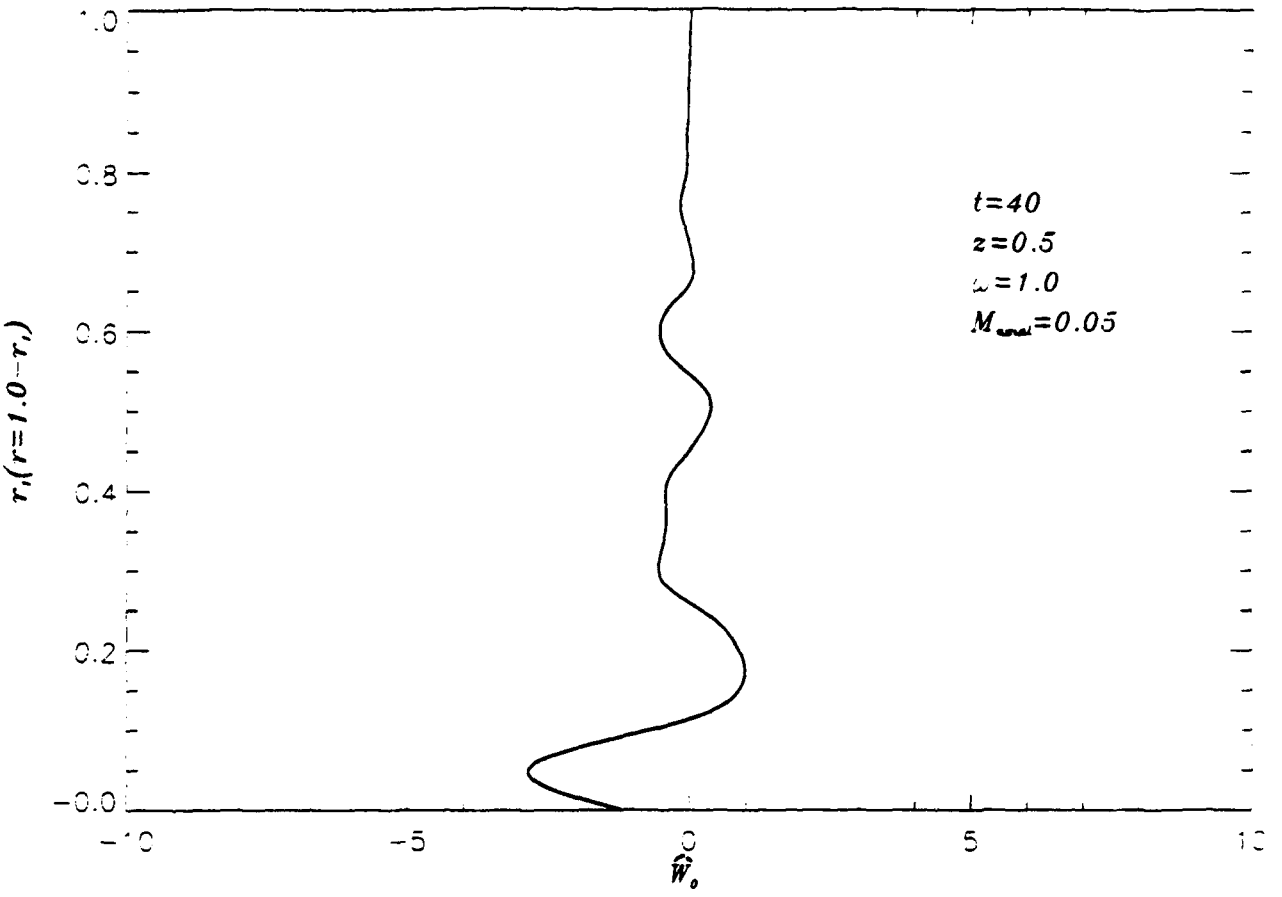
1.0
0.8
0.6
0.4
0.2
−0.0
−10
−5
0
5
10
$r_i(r=1.0-r_i)$
$\hat{W}_0$
t=40
z=0.5
ω=1.0
M_{wall}=0.05

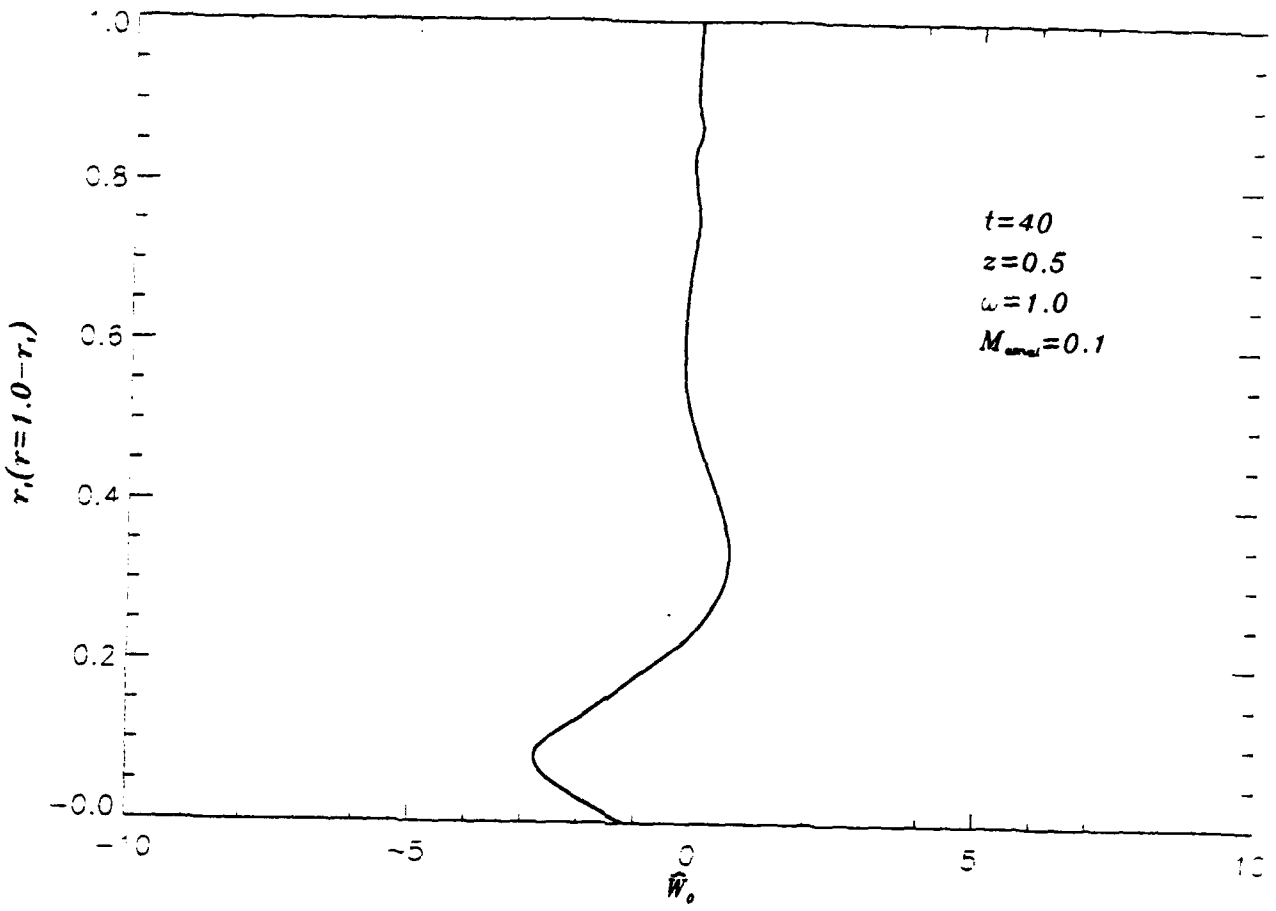
1.0
0.8
0.6
0.4
0.2
−0.0
−10
−5
0
5
10
$r_i(r=1.0-r_i)$
$\hat{W}_0$
t=40
z=0.5
ω=1.0
M_{cond}=0.1

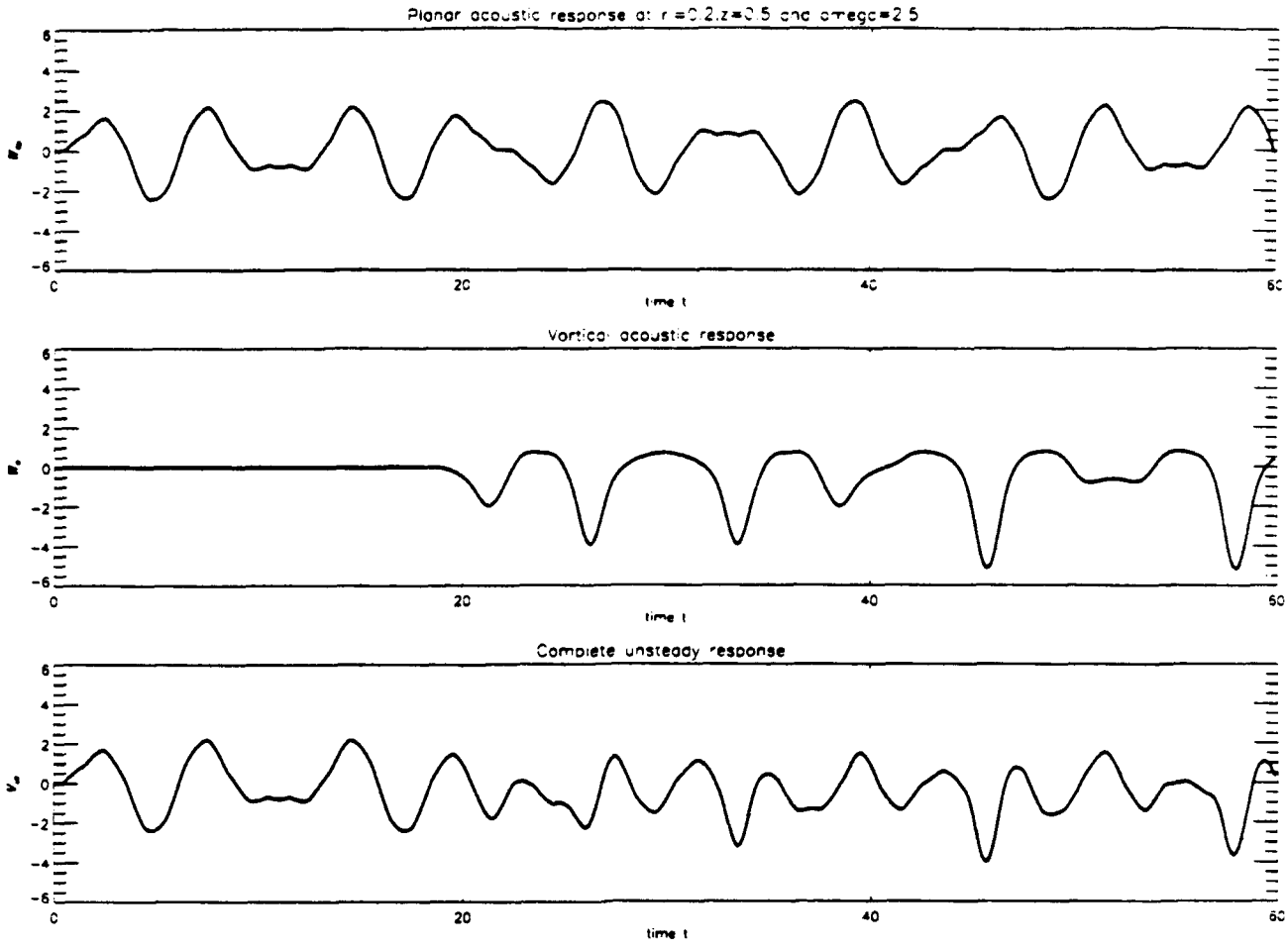
Planar acoustic response at r=0.2,z=0.5 and omega=2.5
Vortical acoustic response
Complete unsteady response
time t
time t
time t

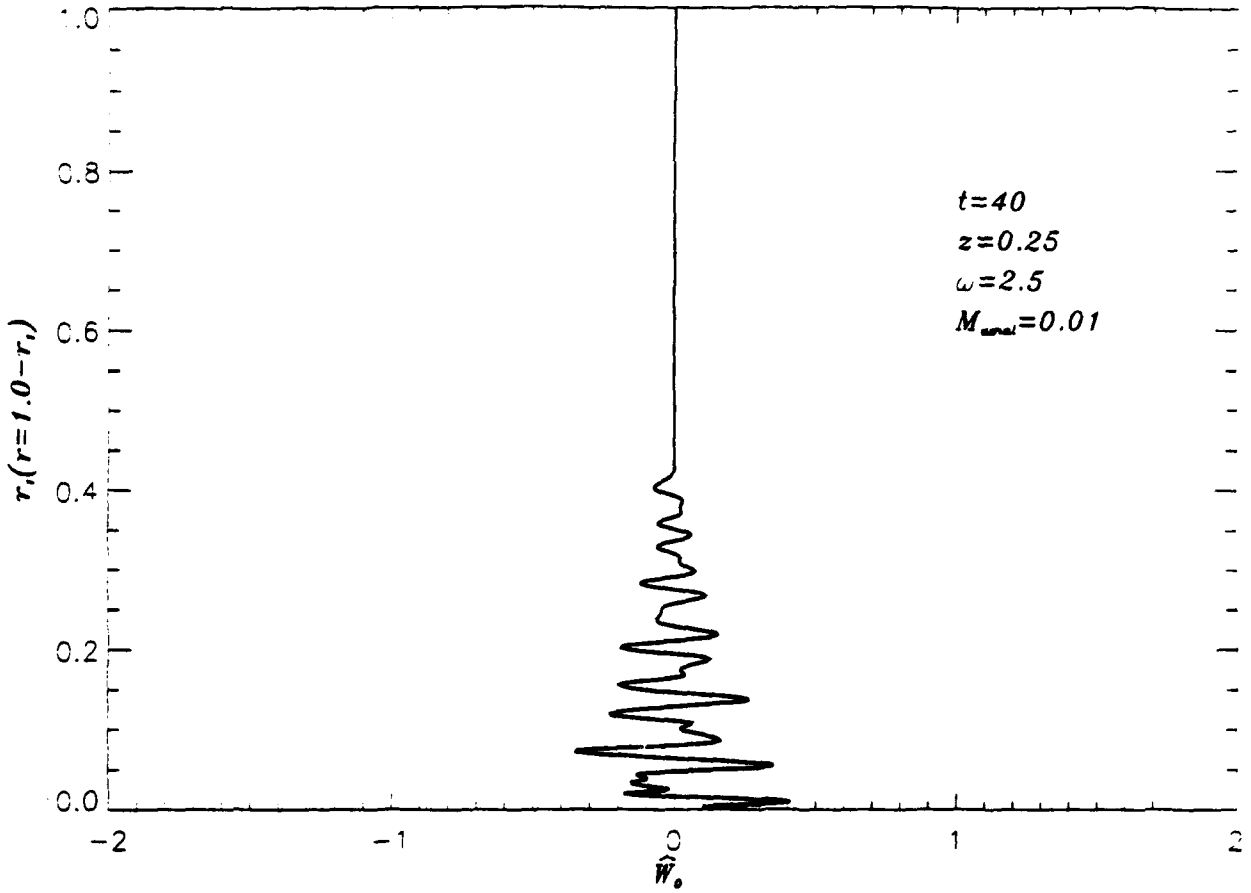
1.0
0.8
0.6
0.4
0.2
0.0
−2
−1
0
1
2
$r_i(r=1.0-r_i)$
$\hat{W}_\theta$
t=40
z=0.25
ω=2.5
M_{wall}=0.01

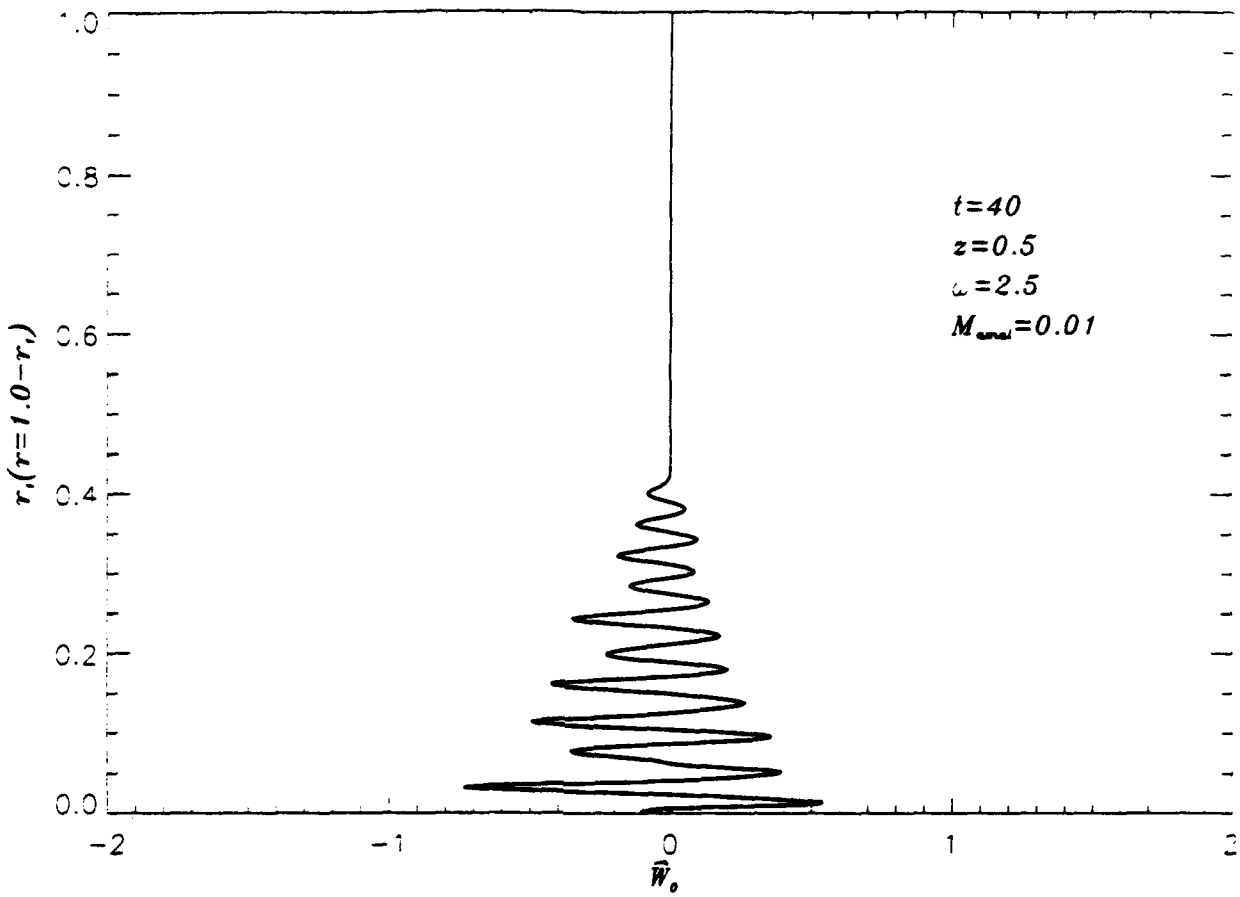

15b

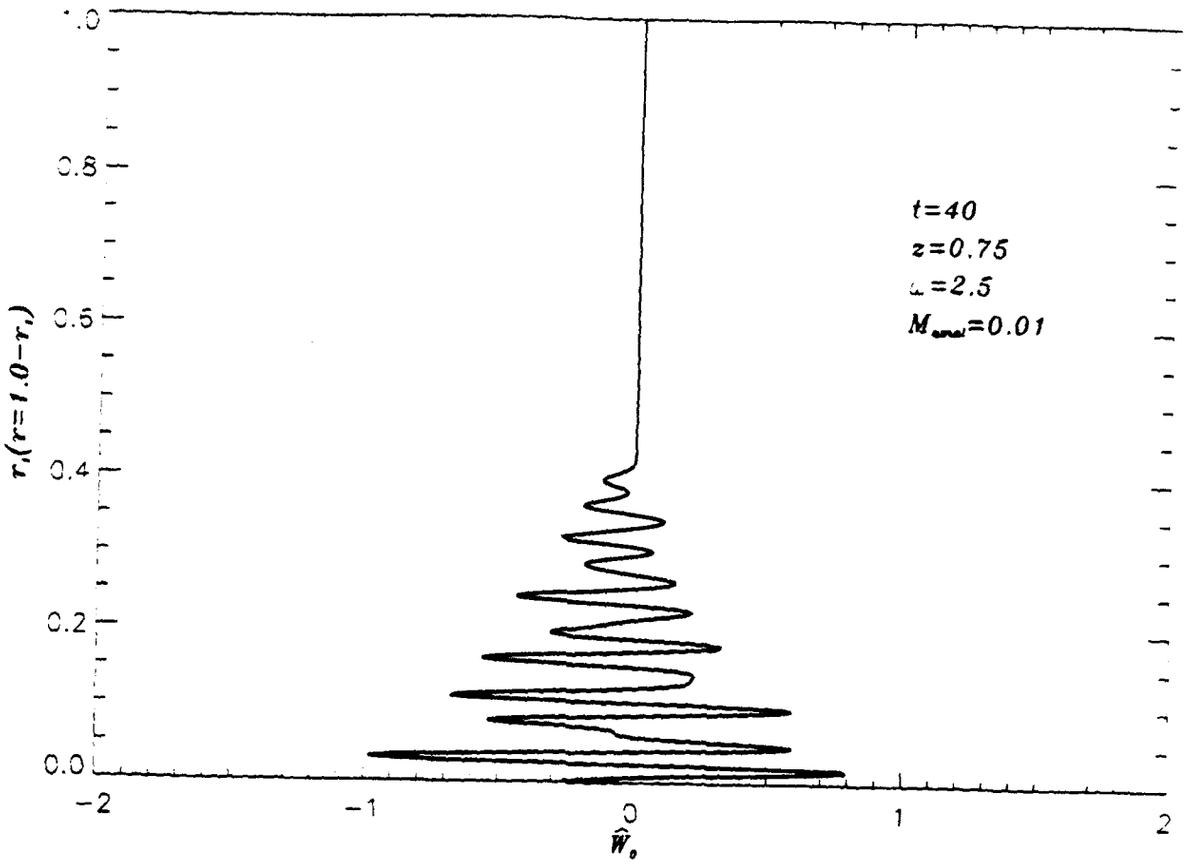
1.0
0.8
0.6
0.4
0.2
0.0
$r_c(r=1.0-r_c)$
−2
−1
0
1
2
$\hat{W}_0$
$t=40$
$z=0.75$
$\omega=2.5$
$M_{\infty\infty}=0.01$

15C

2kk

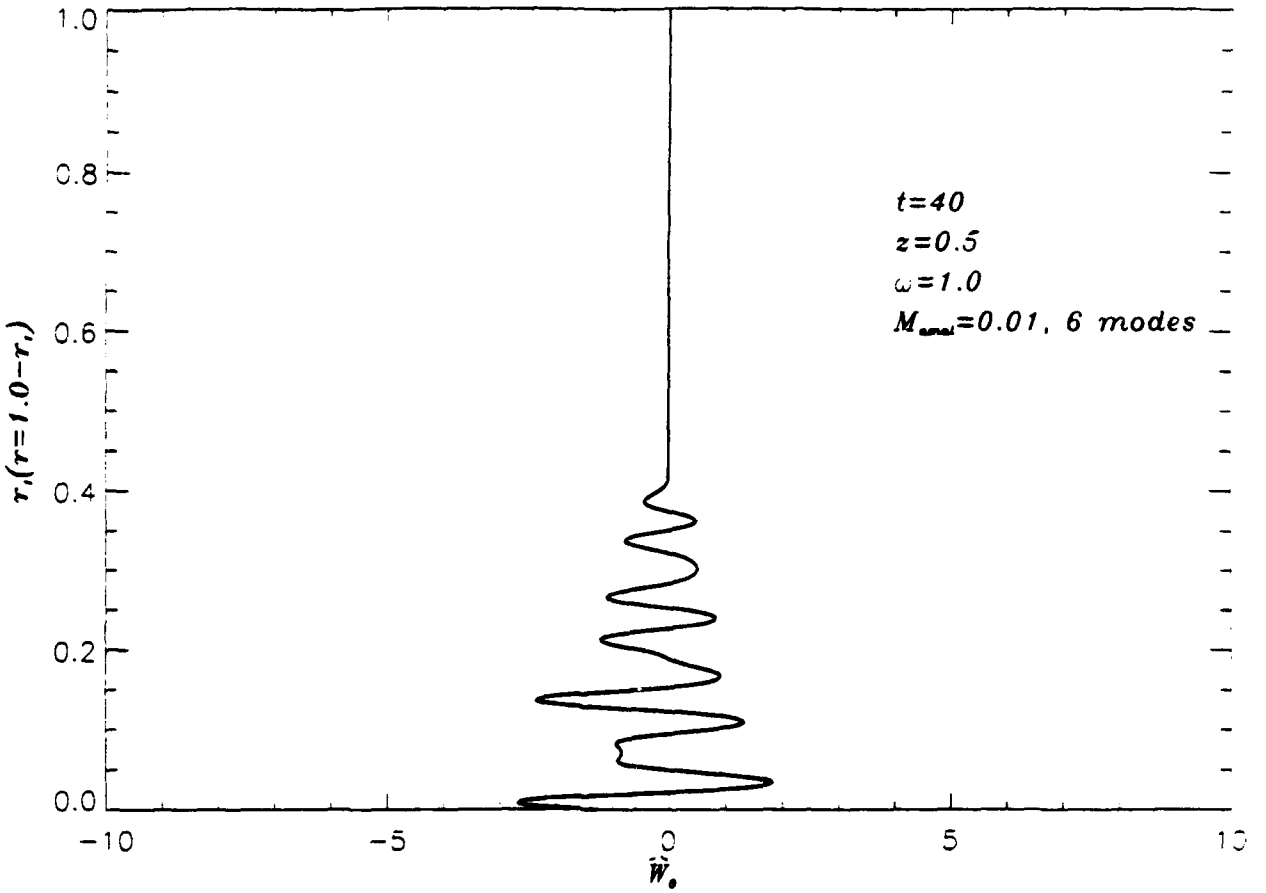
1.0
0.8
0.6
0.4
0.2
0.0
−10
−5
0
5
10
$r_i(r=1.0-r_i)$
$\tilde{w}_o$
t=40
z=0.5
ω=1.0
M_{max}=0.01, 6 modes

ZKK

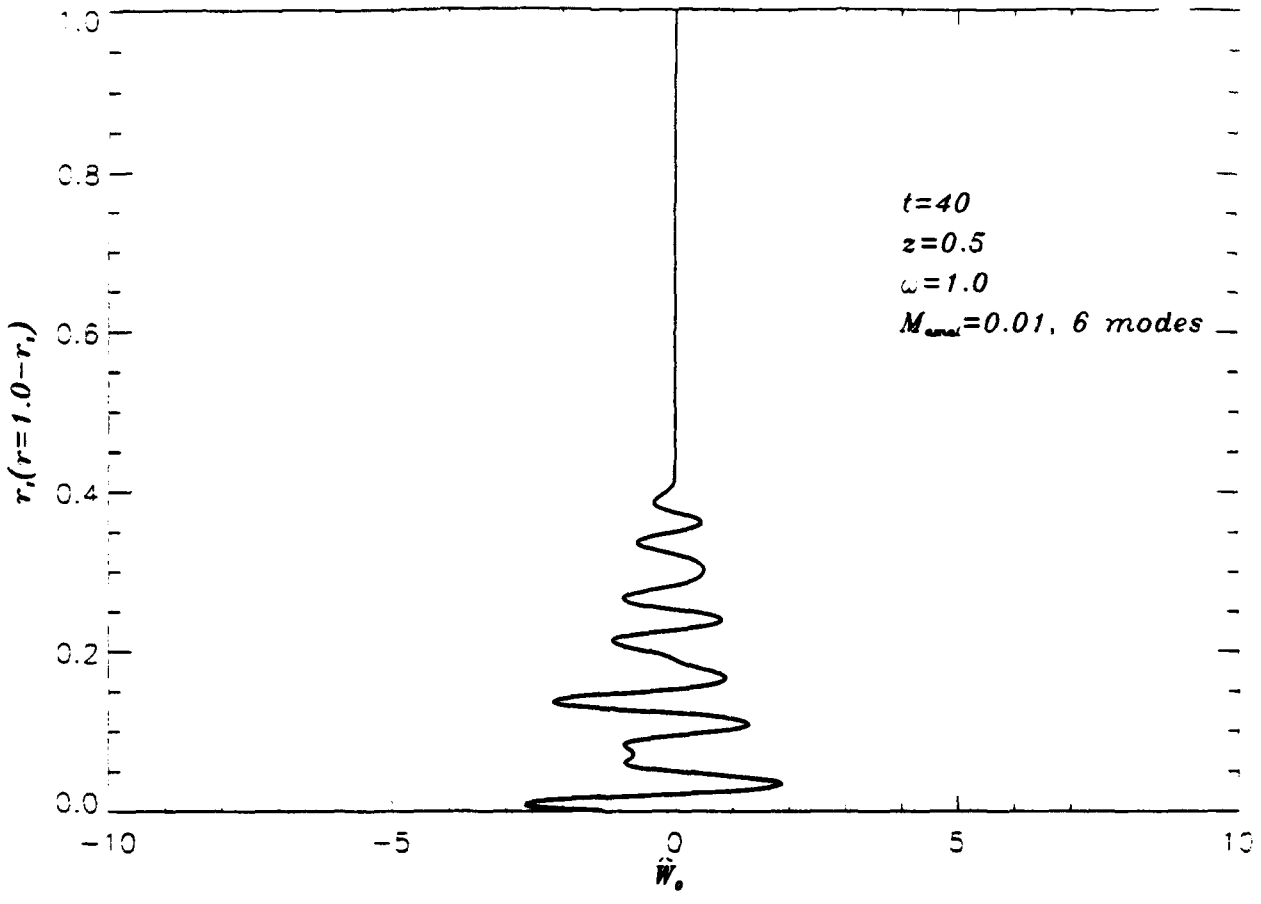
1.0
0.8
0.6
0.4
0.2
0.0
$r_s(r=1.0-r_s)$
−10
−5
0
5
10
$\tilde{W}_\theta$
t=40
z=0.5
ω=1.0
M_{max}=0.01, 6 modes

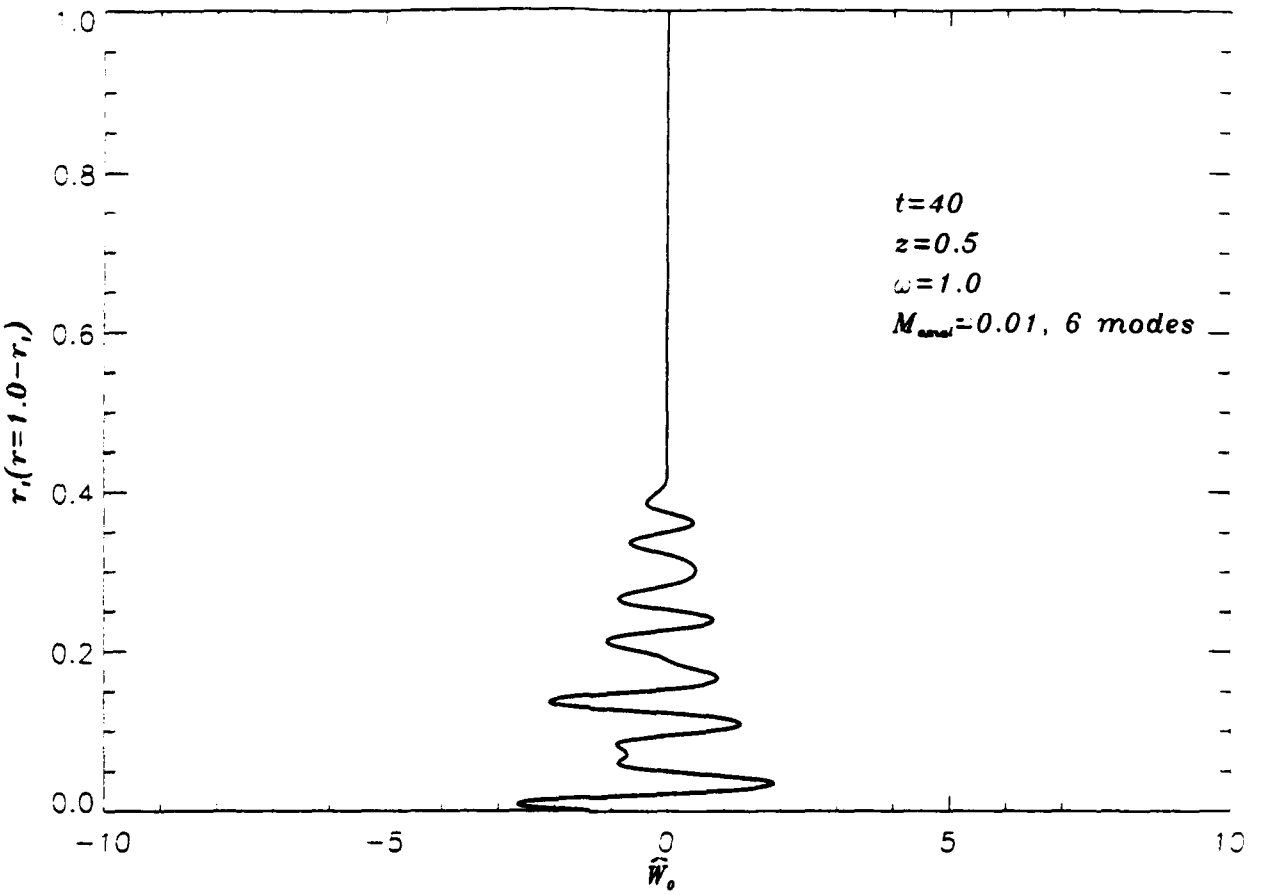
1.0
0.8
0.6
0.4
0.2
0.0
$r_i(r=1.0-r_i)$
−10
−5
0
5
10
$\hat{W}_o$
t=40
z=0.5
ω=1.0
M_{max}=0.01, 6 modes

ZKK

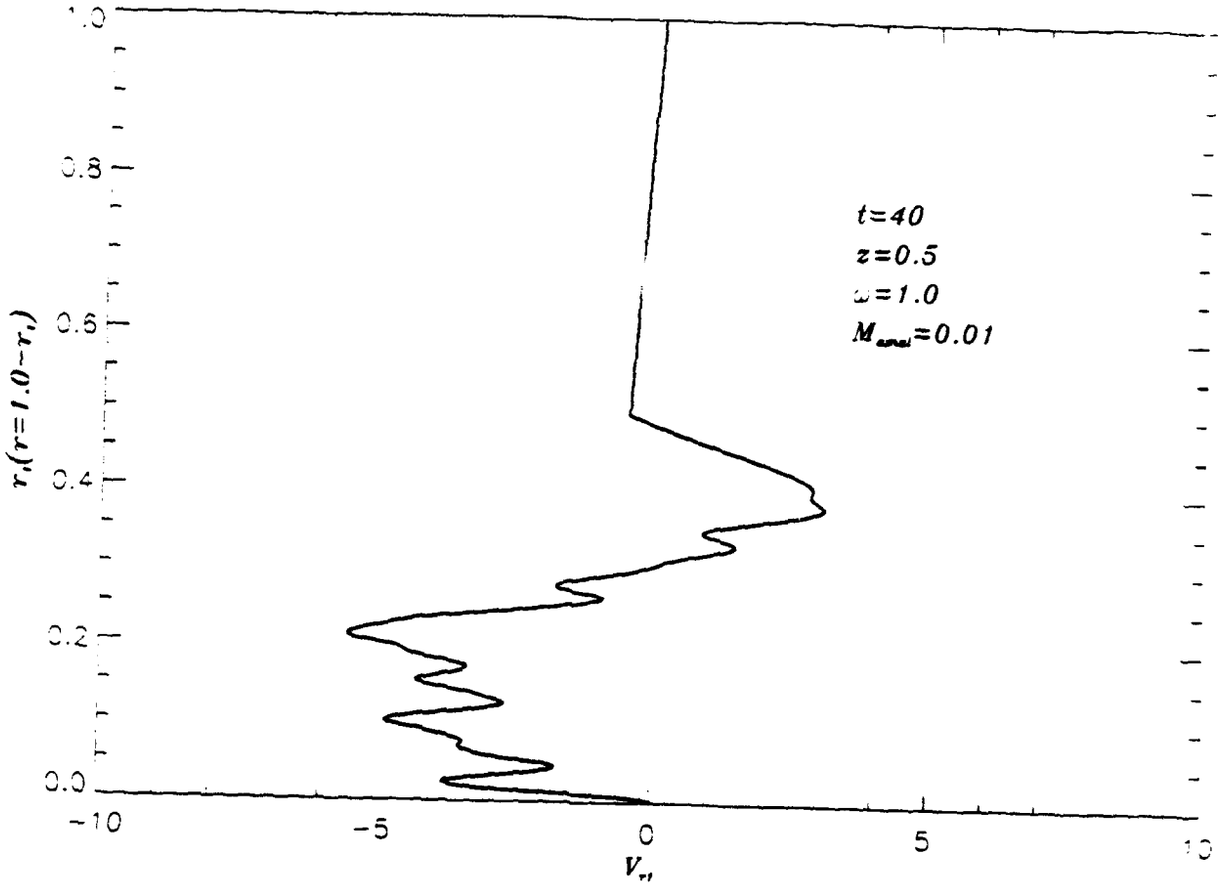

ZKC

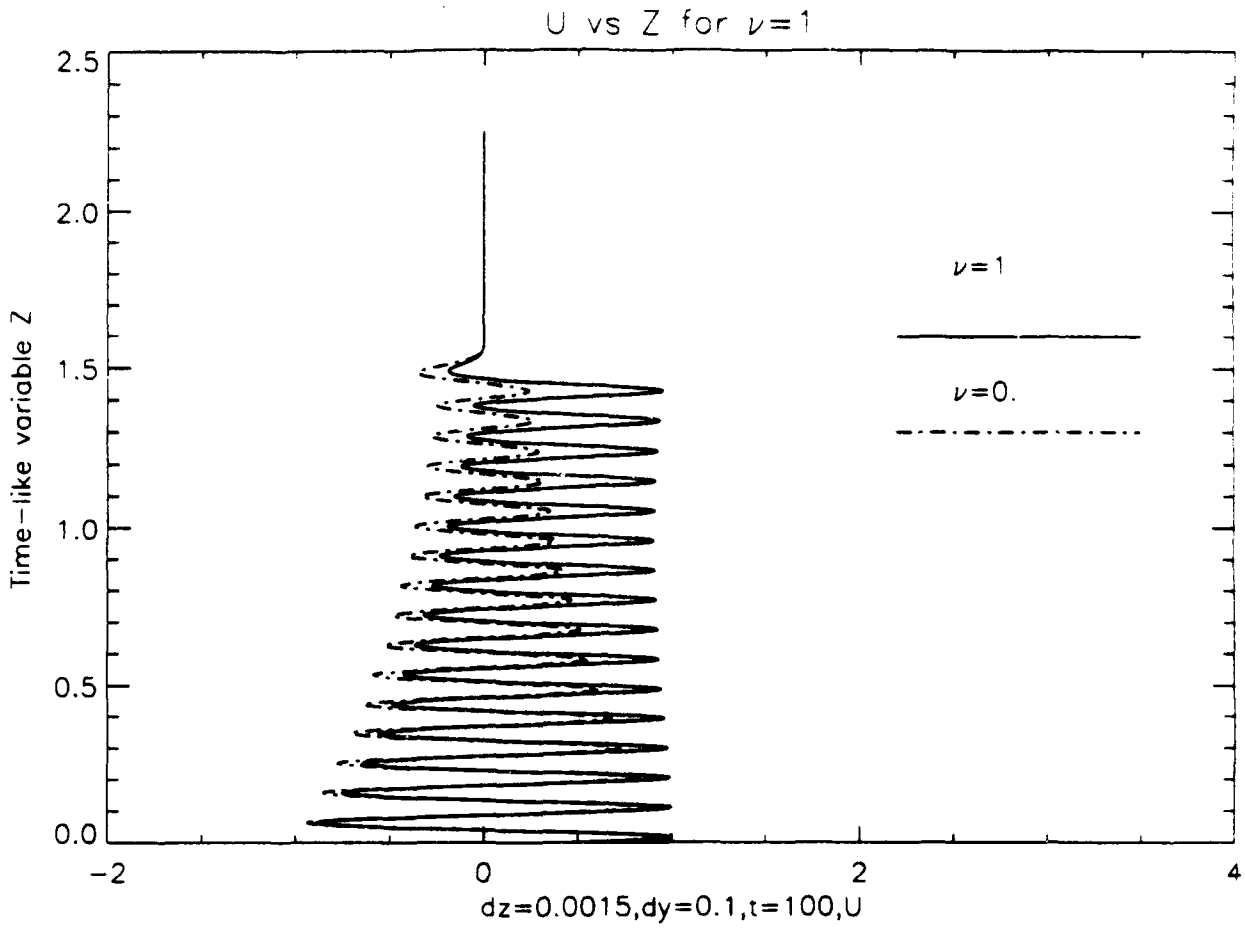
U vs Z for ν=1
2.5
2.0
1.5
1.0
0.5
0.0
Time-like variable Z
ν=1
ν=0.
−2
0
2
4
dz=0.0015,dy=0.1,t=100,U

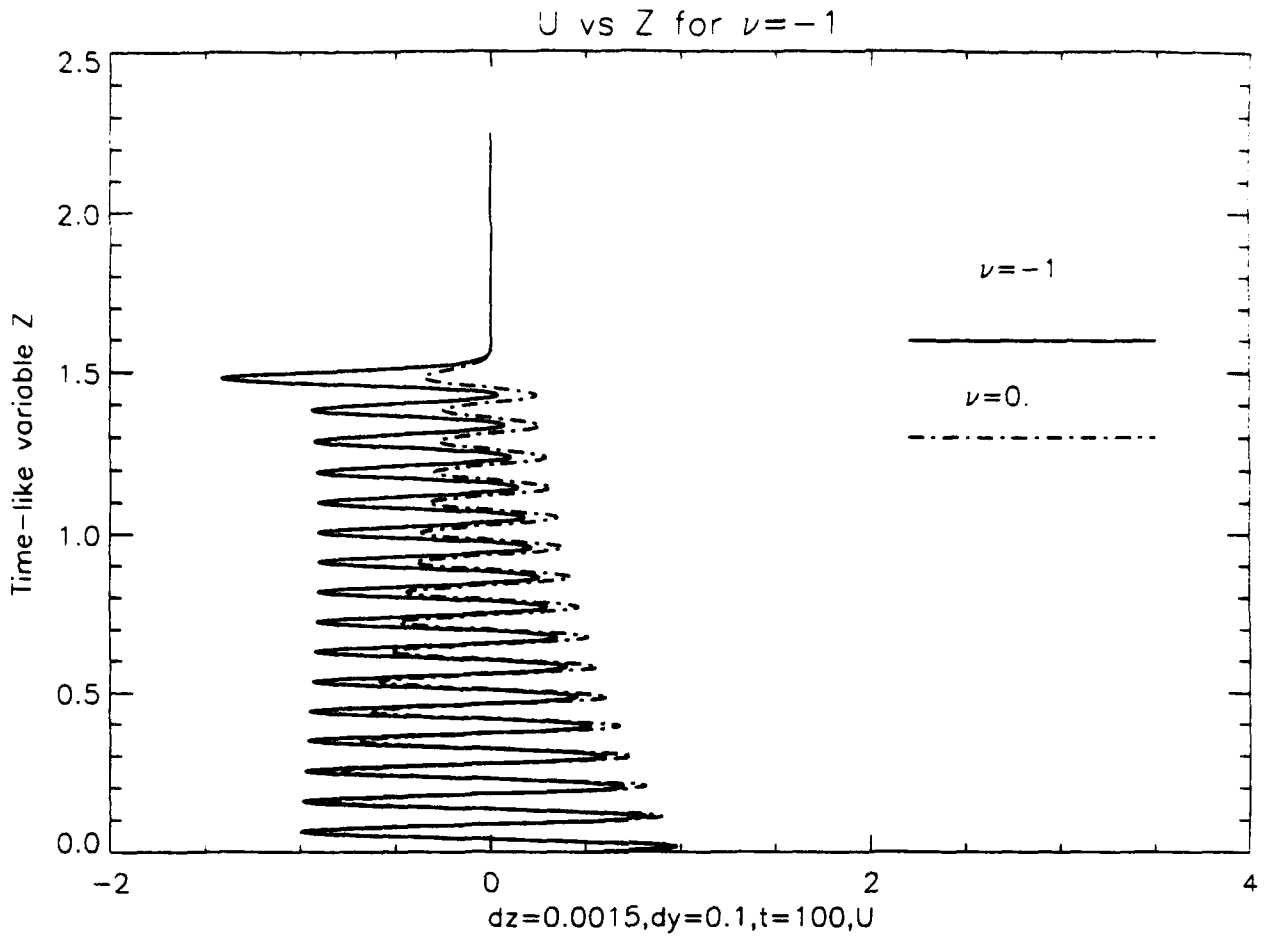
U vs Z for ν=−1
Time−like variable Z
2.5
2.0
1.5
1.0
0.5
0.0
−2
0
2
4
ν=−1
ν=0.
dz=0.0015,dy=0.1,t=100,U

Appendix c

Unsteady Vorticity Generation and Evolution in a Model of a Solid Rocket Engine Chamber

Unsteady Vorticity Generation and Evolution in a Model of a Solid Rocket Engine Chamber

Kadir Kırkköprü[1], David R. Kassoy[2] and Qing Zhao[3]

Department of Mechanical Engineering

University of Colorado

Boulder, CO 80309, U.S.A.

[1]Research Associate, Program in Applied Mathematics

[2]Professor, member AIAA

[3]Research Assistant

ABSTRACT

Two dimensional, axisymmetric Navier-Stokes equations are solved numerically to study the unsteady, nonlinear vortical field generation and evolution by an acoustic wave interaction with a sidewall injected flow in a cylindrical tube, that mimics the solid propellant surface burning in a rocket engine. The steady flow field, sustained by the sidewall injection, is perturbed by imposing a sinusoidal component on the exit plane static pressure. Amplitudes of the oscillatory pressure disturbances are chosen accordingly for different injection/ mean axial flow Mach numbers so that nonlinear processes affect the evolution of the vortical field. In the spirit of the study by Zhao et al.[28], the unsteady vortical part of the total velocity field is extracted from the numerical solutions to show explicitly the vorticity generation at the injecting side wall and evolution in time. Present results show that the unsteady vorticity eventually fills the entire chamber unlike that confined into traditional acoustic viscous layers adjacent to the sidewall.

I. INTRODUCTION

Transient flow dynamics in a solid rocket engine chamber are strongly coupled to propellant combustion processes and related directly to overall rocket motor stability. Traditionally, prediction models have been formulated in terms of acoustic stability theory. The earliest study was devised by Grad[1]. Subsequently, Culick and co-workers[2-11] developed linear and weakly nonlinear stability theories to describe the response of model systems to assumed acoustic disturbances. At about the same time, Hart and McClure[12] proposed a theory based on the acoustic balance approach for prediction of the flow stability in the rocket engine chamber. This theory, based on linearized inviscid equations, has been employed to evaluate laboratory and full-size rocket engine performance. Prediction of pressure responses compares well with those measured in experiments.

Recently, Brown et al.[13,14] conducted laboratory experiments in a cold flow rocket

engine chamber analogue. Velocity measurements taken along and across the cylindrical chamber show that there is a significant unsteady rotational flow component present everywhere. This type of vorticity is seen also in the study by Vuillot and Avalon[15] who used computational methods to solve the compressible Navier-Stokes equations in a channel with side wall mass injection. These experimental and numerical results suggest that stability predictions based on the traditional acoustic analysis should be reexamined.

Traditionally, stability predictions are based on mathematical models formulated in terms of linear or weakly nonlinear, inviscid, irrotational acoustic concepts. (Culick[2-11],Williams[16]). In these models, acoustic waves propagate through a quiescent chamber, and do not interact with side wall gas injection that mimics mass input to the chamber by solid propellant burning. These mathematical models cannot describe the vorticity distributions observed in laboratory and numerical experiments, which are discussed in a limited way by investigators concerned with classical acoustic boundary layers. (for example, Flandro[17], Wang and Kassoy[27]).

Flandro[17] demonstrated that rotational flow effects are of considerable importance in acoustic boundary layers where viscosity is significant. Vuillot and Kuentzman[18] employed Flandro's analysis to evaluate a laboratory scale rocket engine , and obtained good comparisons between theory and experiment. The main objective of these studies was to understand energy exchange between acoustic disturbances and the mean flow as the normally injected fluid is turned toward the axial direction. Baum and Levine[19] and Baum[20] numerically solved the complete Navier-Stokes equations in order to study energy exchange mechanisms in thin, viscous acoustic boundary layers. The numerical results of Vuillot and Avalon[15] demonstrate that unsteady vorticity is not always confined to thin viscous acoustic boundary layers adjacent to the injecting wall. Instead, the unsteady vorticity generated at the wall is convected away from the wall into the chamber, and persists over a significant part of the chamber for appropriate parameter values. The presence of vorticity in the chamber must be

accounted for in an accurate and reliable theory of engine stability.

Flandro and Roach[21] developed an approximate model and an analytical solution to describe vorticity generation at the injecting wall due to an interaction of axial acoustic waves and the injected flow. The model is based on purely inviscid equations. An effort was also made to simulate numerically the Brown et al.[13,14] laboratory experiments by solving the Navier-Stokes equations. This work implies that there are two important length scales for rotational effects; the tube radius and an $O(M)$ smaller length where significant local velocity variations are present.

Recently, Zhao and Kassoy[22] as well as Zhao et al.[28] used systematic asymptotic methods to formulate an initial boundary value problem that includes rotational flow effects. In particular, the theory describes the generation and evolution of unsteady vorticity produced at the cylinder wall by an interaction between the injected fluid and the propagating planar acoustic disturbances. It is demonstrated analytically, to a first order approximation for a large Re and low M flow, that the interaction between the acoustic disturbance and the injecting fluid is purely inviscid. Analysis is also used to show that the vorticity generated at the wall is convected out into the primarily inviscid core flow by the radial component of the injection-induced flow field. This asymptotic model formally incorporates two distinct length scales, similar to those described in the study by Flandro and Roach[21], in a multiple scale analysis which includes weak viscous and nonlinear effects.

The objective of the present study is to compute unsteady vorticity production and evolution in a finite cylinder with steady wall injection and an imposed disturbance on a downstream exit plane. Having invaluable information about the existence of two disparate length scales and their relationship to Mach number, enables grid size and spatial distribution to be chosen carefully in order to describe the flow dynamics accurately. Compressible Navier-Stokes equations are solved by utilizing the MacCormack explicit, predictor-corrector method[23]. A low Mach number, $M = O(10^{-2} - 10^{-1})$, high Reynolds number $Re = O(10^4 - 10^5)$, steady gas flow arising from constant side-

wall injection in a long, narrow cylindrical chamber is disturbed at the exit plane by a sinusoidally fluctuating planar pressure variation. Following the approach of Flandro and Roach[21], Zhao and Kassoy[22] and Zhao et al.[28], the rotational component of the velocity field is extracted from the numerical solutions for the total velocity. The computational results show that unsteady vorticity generated at the wall by an interaction between the injected fluid and planar propagating acoustic pressure waves is convected away from the wall towards the mainly inviscid core flow by the mean radial flow velocity field. Eventually, unsteady vorticity fills the entire chamber. The presence of rotational flow features imply that traditional acoustic balance theories, used widely to predict solid rocket engine chamber stability, must be reevaluated.

II. COMPUTATIONAL MODEL

A primary goal of the present numerical effort is to complement the analytical study by Zhao et al.[28] describing the unsteady nonlinear vorticity generation and evolution by acoustic wave interaction in a model of a solid propellant rocket engine chamber. For computational convenience a cylindrical geometry is chosen. The flow inside the chamber is sustained by constant velocity fluid injection through the sidewall of long, narrow cylindrical tube with one end closed.

The flow field is described by axisymmetric, two-dimensional, laminar, compressible Navier-Stokes equations that are written in nondimensional conservative form as follows:

$$\mathbf{q}_{,t} + \mathbf{e}_{,x} + \mathbf{f}_{,r} + \frac{\mathbf{h}}{\mathbf{r}} = \mathbf{0} \tag{1}$$

where

$$\mathbf{q} = \begin{pmatrix} \rho \\ E_t \\ \rho u \\ \rho v \end{pmatrix} \qquad \mathbf{e} = \begin{pmatrix} M\rho u \\ M[E_t + (\gamma - 1)p]u \\ M\rho u^2 + \frac{1}{\gamma M}p \\ M\rho uv \end{pmatrix}$$

$$\mathbf{f} = \begin{pmatrix} M\rho v \\ M[E_t + (\gamma-1)p]v - \frac{\gamma M\delta^2}{Re.Pr}T_{,r} \\ M\rho uv - \frac{M\delta^2}{Re}u_{,r} \\ M\rho v^2 + \frac{\delta^2}{\gamma M}p \end{pmatrix}$$

$$\mathbf{h} = \begin{pmatrix} M\rho v \\ M[E_t + (\gamma-1)p]v - \frac{\gamma M\delta^2}{Re.Pr}T_{,r} \\ M\rho uv - \frac{M\delta^2}{Re}u_{,r} \\ M\rho v^2 \end{pmatrix} \tag{2}$$

The equation of state for a perfect gas is

$$p = \rho T \tag{3}$$

Nondimensional variables, defined in terms of dimensional quantities denoted by a prime, are given by

$$\begin{aligned} x &= x'/L' \qquad r = r'/R' \qquad u = u'/U'_R \qquad v = v'/V'_R \\ \rho &= \rho'/\rho'_0 \qquad p = p'/p'_0 \qquad T = T'/T'_0 \qquad t = t'/t'_a \\ C_v &= C'_v/C'_{v0} \end{aligned} \tag{4}$$

Characteristic length scales for the axial and radial directions are chosen to be the length of the tube L' and the radius of the tube R', respectively. The characteristic sidewall injection speed of the fluid V'_R is related to the characteristic mean axial speed U'_R through the global mass conservation relationship $U'_R = \delta V'_R$ where $\delta = L'/R'$ is the aspect ratio of the tube. Pressure is nondimensionalized with respect to the static pressure at the open end (outlet) of the cylindrical chamber. Characteristic values for temperature and density, T'_0 and ρ'_0 respectively, represent the injected fluid properties. Time is nondimensionalized with respect to the tube axial acoustic time $t'_a = L'/a'_0$ where $a'_0 = (\gamma p'_0/\rho'_0)^{1/2}$ is the characteristic speed of sound. Here,

the ratio of specific heats $\gamma = 1.4$ is used in the present computations. The viscosity, specific heats and conductivity are treated as constants in this calculations because temperature variations are very small.

The following expressions

$$Re = \frac{\rho_0' U_R' L'}{\mu_0'} \quad Pr = \frac{\mu_0' C_{po}'}{k_o'} \quad M = \frac{U_R'}{a_o'} \tag{5}$$

define the Reynolds number, the Prandtl number and the mean axial flow Mach number, respectively. In a typical solid rocket engine chamber $Re >> 1$, $Pr = O(1)$ and $M = O(10^{-2} - 10^{-1})$.

Finally,

$$E_t = \rho C_v T + \gamma(\gamma - 1) M^2 \frac{\left[u^2 + (v/\delta)^2\right]}{2} \tag{6}$$

represents the nondimensional form of the total energy of the fluid.

The Navier-Stokes equations are simplified by ignoring the axial transport terms. Justification for the reduction is based on the asymptotic analysis in Zhao and Kassoy[22] and Zhao et al.[28] valid for large aspect ratio $\delta >> 1$ and the large Reynolds number $Re >> 1$ provided that $\delta^2/Re << 1$. The computation time for the simplified equations is reduced drastically without sacrificing the flow physics. Furthermore, the dissipative effects of the remaining transport terms are sufficient to avoid artificial damping terms needed in other similar computations[21,24].

The Navier-Stokes equations are solved by using the MacCormack explicit, predictor-corrector scheme :

$$\begin{aligned} \overline{q}_{i,j} &= q_{i,j}^n - \frac{\Delta t}{\Delta x}(e_{i+1,j}^n - e_{i,j}^n) - \frac{\Delta t}{\Delta r}(f_{i,j+1}^n - f_{i,j}^n) - \frac{\Delta t}{r} h_{i,j}^n \\ q_{i,j}^{n+1} &= \frac{1}{2}\left[q_{i,j}^n + \overline{q}_{i,j} - \frac{\Delta t}{\Delta x}(\overline{e}_{i,j} - \overline{e}_{i-1,j}) - \frac{\Delta t}{\Delta r}\left(\overline{f}_{i,j} - \overline{f}_{i,j-1}\right) - \frac{\Delta t}{r}\overline{h}_{i,j}\right] \end{aligned} \tag{7}$$

Here, the overbar denotes the predictor stage, while the superscripts n and $n+1$ represent the known and unknown time levels, respectively, separated by Δt. The subscripts i and j refer to axial and radial directions, respectively.

The upper half of the cylindrical chamber is taken as the computational domain because the flow is assumed axisymmetric.(see Fig. 1) A constant speed fluid is injected into the cylinder through the upper wall. The left side of the chamber is a closed rigid wall (head end) and the right side of the chamber is a flow exit where a specific transient pressure variation is assumed to exist.

The aspect ratio $\delta = 20$ for the present computations. Grid points are equally spaced in each direction. Radial grid size is dependent on the value of M for reasons that will be discussed in Section III.

II.a. Steady State Computations

A steady state flow solution is required as an initial condition for the transient flow computation. Boundary conditions include an impermeable wall at $x = 0$ ($u = 0$), a static pressure condition at the open end $x = 1$ ($p = 1$), a specified injection velocity ($v = -1$), temperature ($T = 1$) and no slip condition for the axial flow speed ($u = 0$) on the injecting upper sidewall at $r = 1$ and symmetry conditions on the lower (centerline) boundary, $r = 0$.

Two approaches have been used to compute the steady state flow configuration. In the first, the sidewall injection is initiated at $t = 0$, and the internal flow is started. Numerical integration is carried out until a specified convergence criterium assures a steady state. For example, the injected total mass flow rate must equal the total exiting mass flow rate and the sum of changes in axial and radial velocity components after each time step, $\Sigma|u(t + \Delta t) - u(t)|$ and $\Sigma|v(t + \Delta t) - v(t)|$, must be less than a specified small number. This approach, employed for a range of Mach numbers and Reynolds numbers with satisfactory results, requires large computation times.

The second approach is to use the analytically calculated velocity profiles for incompressible, inviscid flow in a long, narrow cylindrical tube (Culick[2]) as starting profiles for the steady, compressible, viscous flow computations. This approach reduces the computation time required to reach the final converged steady flow

configuration. Results given in Figs. 2a and 2b show the steady normalized axial, $u_S(x,r)/u_S(x,r=0)$, and radial velocity $v_S(x,r)$ profiles at different axial locations, $x = 0.025, 0.5$ and 1.0, when $M = 0.05$ and $Re = 3.10^5$, respectively. In these graphs, Culick[2] profiles are indistinguishable from the computed profiles.

The mean axial flow Mach number is small, $M = O(10^{-2} - 1O^{-1})$, which implies $O(M^2)$ differences between the Culick[2] solution for $\delta >> 1$ and the computational result. Nonetheless, it is useful to compute a steady state flow solution for each Mach number and Reynolds number. This prevents introducing unwanted noise into the unsteady computations.

Although the flow in the chamber , to a first order approximation, is basically inviscid in character as a result of large Reynolds number, it is useful to retain the radial transport terms in the Navier–Stokes equations. The steady flow solution is obtained faster and, at the same time, the largest important viscous effects in radial direction are responsible for physically meaningful damping, similar to the artificial damping terms that have been introduced in some earlier studies[21,24]. For the present computations Re number based on the characteristic mean axial flow speed is between 3.10^4–3.10^5.

II.b. Unsteady Flow Computations

Once a converged steady flow configuration for certain M and Re is obtained, the flow is disturbed by imposing a sinusoidally fluctuating component on the exit plane static pressure, a procedure similar to that of Vuillot and Avalon[15]. Therefore, the the static boundary condition at the exit plane is changed to

$$x = 1; \qquad p = 1 + A sin\omega t \tag{8}$$

where ω is the dimensionless angular frequency and A is the amplitude of the pressure oscillation. The other boundary conditions are the same as those for steady flow computations.

The weakly nonlinear theory of Zhao and Kassoy[22] and Zhao et al.[28] demonstrates

that when $A = O(M)$ changes in the axial velocity field are $O(1)$, e.g. $\Delta u = O(1)$. As a result, the amplitudes of the pressure oscillations in the present computations are chosen to be $A = M$. Therefore, nonlinear processes affect the evolution of the unsteady flow field.

With reference to the analytical study by Zhao et al.[28], it may be shown that the resonant frequencies of the planar part of the acoustical phenomenan described in this study are $\omega_n = (n - 1/2)\,\pi$ where $n = 1, 2, \ldots$. Unsteady computations are carried for several different angular frequencies including those for near-resonant cases.

III. RESULTS and DISCUSSION

Following a procedure described by Lagerstrom[25], and similar to that employed by Price and Flandro[26], Zhao and Kassoy[22] and Zhao et al.[28], the total unsteady axial flow speed may be divided into three parts

$$u(x, r, t) = u_S(x, r) + u_P(x, t) + u_V(x, r, t) \tag{9}$$

where u_S denotes the steady flow field which is known as an initial condition for unsteady computations, u_P represents the irrotational planar part of the flow field which can be computed as the difference between the unsteady axial speed and the steady axial speed on the centerline of the tube. The remaining part u_V is defined as the vortical (rotational, nonplanar) part of the unsteady axial flow speed. It is used to describe the generation and evolution of the nonlinear unsteady vorticity field in the cylinder. Following the asymptotic analysis described by Zhao et al.[28], one can show that the vortical part of the unsteady axial flow speed u_V vanishes at the centerline at all times.

It is noted that, for all cases to be discussed below, the pressure solution has been found to be purely planar (x-dependent), with no detectable transverse (radial) variation within computational accuracy. For example, Fig. 3 shows the axial pressure variation at three radial locations ($r = 0., 0.5$ and 1) for $t = 29.37$, $M = 0.1$, $Re = 3.10^4$, $\omega = 1$ and $A = 0.1$. In this figure, numerical pressure values , at $x = 1/2$, for

three radial locations, $r = 0, 0.5$ and 1 are 0.97071351, 0.97070410 and 0.97069881, respectively. This is a consequence of the large aspect ratio, $\delta = 20$.

Figures 4a-4c show the radial variation of the unsteady axial vortical flow speed at midchamber ($x = 1/2$) at three time values after the planar pressure disturbance is initiated at the exit plane. The flow parameters are $M = 0.1$ and $Re = 3.10^4$. The corresponding injection Mach number $M_i = M/\delta = 0.005$. The disturbance frequency is $\omega = 1.0$, a non-resonant frequency smaller than the first natural frequency of the tube, $\omega_1 = \pi/2$.

In the first of this sequence of graphs, Fig. 4a, one observes a strong radial velocity gradient extending out about 0.15 units from the wall at $t = 1.48$. This is the approximate radial distance travelled by the injected fluid during the time interval $t = 1.48$ to be discussed at the end of this section.

Figure 4b shows that the unsteady vortical axial velocity field extends out to 0.85 radial units from the injecting wall when $t = 11.81$. At time $t = 29.37$ the rotational flow field as seen in Fig. 4c is all over the entire chamber.

The spatial distribution of the vortical part of the unsteady axial flow velocity at each time may be explained in physical terms by considering an interaction between the steady injected flow field and the propagating planar acoustic disturbances originated and sustained at the exit plane of the tube. The motion of a fluid particle injected radially into the tube from the upper wall at a specified location is affected by the harmonic variation with time of the local axial planar pressure gradient. For instance, Fig. 5 shows the time variation of the axial pressure gradient, $\partial p/\partial x$, at a point where $x = 1/2$ and $r = 0.9$ for the case being discussed above, where the high frequency response in the first cycle, probably due to a start-up process, diseappears quickly. As a result, a given fluid particle emanating from the wall will be accelerated alternately in the positive and negative axial directions as it is convected toward the axis of the cylinder by the steady radial flow field. Part of the fluid particle response is associated with irrotational acoustic effects. The rest is rotational, resulting from

vorticity generation at the wall.

Figure 6a shows the time history of the planar part of the unsteady axial flow speed at midchamber when the flow parameters are $M = 0.1$, $Re = 3.10^4$, $\omega = 1$ and $A = 0.1$. The time history of the unsteady vortical axial flow speed at the injecting wall, $r = 1$, when $x = 1/2$ is shown in Fig. 6b. It is noted from this figure that, before $t = 0.5$, there is no spatial variation of the unsteady axial vortical speed with the radius r because the signal originated at the exit plane has not yet reached the midchamber. Once the signal arrives, unsteady vorticity is generated at the wall by the interaction of the acoustic disturbance and the injected gas, as seen by the behavior of u_V in Fig. 6b. Subsequently, the unsteady vorticity is convected towards the axis of the tube by the mean radial flow field, shown in Fig. 2b. There is also an associated pressure field which has the characteristics of a traditional planar acoustic wave system. This pressure field, as demonstrated in the asymptotic analysis of Zhao and Kassoy[22] and Zhao et al.[28], is not affected by the unsteady vorticity field generation and evolution, so that traditional acoustic theory yields transient pressure estimates that compare well with those found experimentally.

Figure 7 shows the radial variation of the difference between the unsteady radial flow speed v and the steady radial flow speed v_S in Fig. 2b, at $x = 0.5$ when $t = 29.37$ for the same parameter values above. The difference is used because the asymptotic formulation in Zhao and Kassoy[22] and Zhao et al.[28] demonstrates that the transient response to the boundary disturbance is $O(M)$ smaller than v_S itself. The maximum absolute value of the difference in Fig. 7, approximately 0.085, varifies this prediction.

Figures 8a-8c show the spatial oscillation of vortical axial velocity at midchamber with respect to the radius when $t = 1.488$,11.834 and 29.54 for a smaller axial Mach number $M = 0.05$ (corresponding to the weaker injection, $M_{inj} = 0.0025$) and for a higher $Re = 3.10^5$. The forcing frequency $\omega = 1.0$ is the same as for the previous case. The amplitude of the nonresonant exit plane pressure disturbance is 5 percent. The sharply defined region of large velocity gradient is seen in Fig. 8a at 0.07 units

from the wall at $t = 1.48$. One notes that at $t = 11.834$ the wavelength of the spatial oscillation of the vortical axial velocity field is smaller than that for the case when $M = 0.1$. This is an expected result because the mean radial velocity field for $M = 0.05$, which transports the fluid particles into the cylinder, is characterized by a relatively lower speed than that for the $M = 0.1$ case. Therefore, injected fluid particles are carried a shorter distance away from the sidewall towards the axis of the chamber in the same time interval, compared to that for the stronger injection speed case, $M = 0.1$. At $t = 29.54$ one notes spatial oscillations throughout the cylinder. It is also observed that the wavelength of the oscillatory structure decreases as the centerline is approached. This occurs basically because the mean radial flow speed vanishes as the centerline is approached.

Solution resolution requires 41 grid points in the axial direction and 101 grid points in the radial direction. Figure 8c shows that near the injecting wall one wavelength of the spatial oscillation of the vortical axial velocity is represented by approximately 35 radial grid points. In contrast, near the centerline, where the wavelength is smaller, approximately 10-15 grid points are available to resolve the velocity gradients.

The axial spatial variations in u_V do not have steep gradients, so that 41 equally spaced grid points have been found to give adequate resolution. For example, Fig. 9 shows the axial variation of the unsteady vortical axial velocity, u_V, at 3 radial locations, $r = 1., 0.9$ and 0.7 when $t = 29.37$ for $M = 0.1$, $Re = 3.10^4$, $\omega = 1.$ and $A = 0.1$. In fact, from Zhao and Kassoy[22] and Zhao et al.[28] one can show that the linear eigenfunctions for the finite cylinder with a pressure node exit plane can be written as $sin\,[(2n-1)/4]\,2\pi x$, $n = 1, 2, \ldots$. Thus even for n=9, where 4.25 harmonic waves are present in the cylinder, there are nearly 10 grid points per wave length.

The third case studied is for a smaller mean axial flow Mach number $M = 0.02$ ($M_{inj} = 0.001$), Reynolds number $Re = 3.10^5$ and the forcing frequency $\omega = 1.0$. The results for the previous cases, $M = 0.1$ and $M = 0.05$, imply that the number of radial grid points should be doubled for this weak injection case. There are 201

equally spaced grid points in the radial direction in order to represent the spatial variation of unsteady vortical axial velocity accurately. Figures 10a-10c show the unsteady vortical axial velocity variation with respect to the radius at $x = 0.5$ when $t = 3.00$, 15.00 and 30.00, somewhat different from the previuos cases. It can be seen from these figures that axial velocity gradients are larger than those for larger Mach number cases presented previously, as predicted by Zhao and Kassoy[22] and Zhao et al.[28] This implies that the absolute magnitude of the unsteady vorticity generated at the wall is much larger than that of the higher Mach number flows. This unsteady vorticity field is convected away from the wall towards the center of the chamber by a relatively slower steady radial velocity component. Therefore, at $t = 30.00$ only about 60 percent of the chamber is filled with the unsteady vorticity. Larger time computations for this case have not been carried out. However, one can conclude on the basis of the previous results and the work of Zhao and Kassoy[22] and Zhao et al.[28] that the vorticity field will spread out towards the axis as time increases. One should note that the convection process slows down near the axis because the radial velocity component becomes vanishingly small.

Figures 11a and 11b present the spatial variation of the unsteady vortical axial velocity with radius at two different axial locations $x = 1/4$ and $x = 3/4$ when $t = 30$ for $M = 0.02$. The corresponding result at $x = 1/2$ is given in Fig. 10c. It can be seen that the amplitudes of the oscillations at a given radial location decrease as the distance from the source of disturbance at $x = 1$ increases. The local peaks occur at the same radial location for each axial position.

Figures 12a-12c present the radial variation of unsteady vorticity at midchamber length for three cases, $M = 0.1, 0.05$ and 0.02, discussed above, respectively. Corresponding times are $t = 29.37, 29.54$ and 30., respectively. The unsteady vorticity is computed from the following expression

$$\Omega = -\left[\frac{\partial u_V}{\partial r} - \frac{1}{\delta^2}\frac{\partial (v - v_S)}{\partial x}\right] \tag{10}$$

The nondimensional vorticity is defined as $\Omega = \Omega'/(U'_R/R)$ where Ω' is the dimen-

sional vorticity. As analysis of the present numerical results and the asymptotic analysis of Zhao et al.[28] show, the main contribution to the unsteady vorticity is brought by the first term in (10). It is seen from Figs. 12a-12c that the magnitude of the unsteady vorticity increases with decreasing mean flow Mach number. One should notice that scales are different in each of Figs. 12a-c. An accompanying plot, Fig. 12d, shows the variation of the unsteady vorticity throughout the cylindrical chamber for the $M = 0.02$ case at $t = 30$, discussed above. The axial variation of the vorticity at each radial location is of the shape of the eigenfunction $sin[(2n-1)/4]2\pi x$ for $n = 1$, mentioned previously.

Figures 13a, 13b and 13c describe the effects of forcing frequency on the oscillatory spatial structure of the vortical axial speed at times close to $t = 17.5$ when $M = 0.1$,$Re = 3.10^4$ and $A = 0.1$. The chosen frequencies are $\omega = 1.0$, $\omega = 1.5$ (a near-resonant case) and $\omega = 2.5$. The scale in Fig. 13b for $\omega = 1.5$ is different from the others. It can be seen from these plots that the wavelength of the oscillatory spatial structure decreases when the forcing frequency increases. Were this done for smaller M the required number of radial grid points would have to be significantly larger to resolve the growing number of spatial oscillations at a given value of time. In addition, larger amounts of computer time are required because the incompressibility limit is approached when M is lowered.

It is noted from Figs. 13a-13c that the local spatial gradients of vortical velocity increase for larger forcing frequencies. This implies that the magnitude of the unsteady vorticity field increases for higher frequencies. One should notice the near-resonant forcing frequency effect on the increasing magnitude of the unsteady vortical axial speed.

The radial location of the front of the spatially oscillatory vortical part of the unsteady axial speed varies with time. Close to the sidewall the front location may be computed approximately from

$$r_F = 1 - Mt \tag{11}$$

where the mean radial convection speed is nearly one in nondimensional terms. Equation (11) yields reasonable results for $r_F \geq 0.5$, as shown in Table I. A more accurate expression that defines the location of the front may be obtained by employing the Culick[2] steady radial speed, $v_S(r) = -(1/r)sin\left[(\pi/2)\,r^2\right]$ in the integration of the differential form of time-distance relation, $dr' = v'_S(r')dt'$, where a prime denotes a dimensional quantity. This yields the radial location time variation,

$$r_F = \left[\frac{4}{\pi} tan^{-1}\left(e^{-\pi M t}\right)\right]^{1/2} \tag{12}$$

Table I shows the radial locations estimated from (11) and (12) and from numerical computations for the three mean axial flow Mach numbers discussed previously. There is an excellent agreement between estimated radial locations of the front from (12) and from numerical results. Although (11) gives good estimates near the wall, it yields unreasonable values for $r \geq 0.5$. This is a result of the vanishing steady radial velocity as $r \rightarrow 0$.

IV. SUMMARY and CONCLUSIONS

There is now a considerable body of evidence in support of the presence of an unsteady vorticity distribution within a physically reasonable model of a solid rocket engine chamber. The experiments of Brown et al.[13,14], the quasi-analytical modeling of Flandro and Roach[21], Zhao and Kassoy[22], Zhao et al.[28] as well as the computational solutions of Vuillot and Avalon[15], Flandro and Roach[21] and of the present work show unequivocally that unsteady vorticity is generated near the cylindrical surface and is convected into the chamber by the injected fluid. The core of the chamber is free of vorticity only during the very early phases of the transient process, prior to the arrival of a well defined unsteady vorticity front.(see, for example, Figs. 4a, 8a and 10a). The arrival times found from the present computational solution agree quite well with predictions found from generally valid concepts developed in the analytical problem formulation in Zhao and Kassoy[22], and Zhao et al.[28]. (Table I).

The computations in the present work are probably more accurate than those of

Vuillot and Avalon[15] because the analytically derived scaling is used to determine grid size and distribution. Unlike the former work, where grid points were concentrated near the sidewall to resolve an expected traditional acoustic boundary layer, the present choices assure that the short wavelength processes in the radial spatial distributions, predicted by the analysis, are adequately resolved. The time-averaged axial velocity variation with radius predicted by Vuillot and Avalon[15] (see their Fig. 7) is qualitatively similar to the instantaneous distributions for the vortical axial velocity described here.

One may reasonably conclude from the results of the aforementioned studies that the classical acoustic stability predictions used for scientific and engineering purposes should be reassessed to determine the prediction reliability. It is conceivable that the acoustic pressure predictions are reasonable because the presence of vorticity does not impact the primary acoustic pressure transient found in the Zhao and Kassoy[22] and Zhao et al.[28] theory. However, it is unlikely that velocity and shear stress predictions are accurate, given the irrotational basis of the acoustic stability analysis.

It is also conceivable that there are parameter ranges of Mach number (injection rate) and Reynolds number for which vorticity is really confined to thin, classical, but injected acoustic boundary layers like those discussed by Flandro[17], Baum and Levine[20] and more recently by Zhao et al.[28]. These structures can appear for relatively small injection rates and low Reynolds numbers, so that viscous damping of the vorticity amplitude is profound. Then, the cylinder core will contain the relatively weak vorticity of the steady Culick[2] solution and irrotational acoustic waves driven by the boundary forcing.

The amplitude of the transient vorticity distributions described by Zhao and Kassoy[22] and Zhao et al.[28], and in the present work (see Figs. 12a-c) are $O(M^{-1})$ larger than that of the Culick[2] steady solution. This implies that there will be a relatively large axial shear stress on the cylinder surface, particularly for smaller M values. One can speculate that these transient shear stresses will impact the burning

rate of an actual propellant which is the source of the "injected" fluid used in the present model. Perhaps there is a direct relationship between the effect of surface shear stress transients, predicted in the present work, and erosive burning concepts used in the solid rocket engineering literature[16].

ACKNOWLEDGEMENT

This work is financially supported by the Air Force Office of Scientific Research through a grant AFOSR 89-0023. The authors acknowledge useful discussions with Dr. Robert Roach.

REFERENCES

1. Grad,H., (1949) *Comm. Pure Appl. Math.*,**2**, 79-102.

2. Culick, F.E.C., (1966a), *AIAA J.*, **4**, 1462-1463

3. Culick, F.E.C., (1966b), *Astron. Acta*, **12**, 113-126

4. Culick, F.E.C., (1967), *Astron. Acta*, **13**, 221-238

5. Culick, F.E.C., (1968), *AIAA J.*, **6**, 2241-2255

6. Culick, F.E.C., (1970), *Comb. Sci. Tech* , **2**, 179-201

7. Culick, F.E.C., (1971), *Comb. Sci. Tech* , **3**, 1-16

8. Culick, F.E.C., (1973), *Comb. Sci. Tech* , **7**, 165-175

9. Culick, F.E.C., (1975), *Comb. Sci. Tech* , **10**, 109-124

10. Culick, F.E.C., (1976), *Comb. Sci. Tech* , **3**, 715-756

11. Culick, F.E.C., (1990), " Some Recent Results for Nonlinear Acoustics in Combustion Chambers," AIAA 90-3927, Aeroacoustics Conference, October.

12. Hart, R.W. and McClure, F.T., (1965), " Theory of Acoustic Instability in Solid Propellant Rocket Combustion," *10th International Symposium on Combustion*, Combustion Ins., Pittsburg, PA, 1047-1065.

13. Brown, R.S., Blackner, A.M., Willoughby, P.G. and Dunlap, R., (1986a), *J. Propulsion and Power* , **2**, 428-437.

14. Brown, R.S., Blackner, A.M., Willoughby, P.G. and Dunlap, R., (1986b), " Coupling Between Velocity Oscillations and Solid Propellant Combustion," AIAA 86-0531, AIAA Aerospace Sciences Meeting, January.

15. Vuillot, F. and Avalon, G., (1991), *J. Propulsion*, **7**, No 2, 231- 239.

16. Williams, F.A., (1985), *Combustion Theory*, Benjamin/ Cummings, Menlo Park.

Flandro, G.A., (1974), *J. Sound and Vibration*, **36**, 297-312.

8. Vuillot, F. and Kuentzman, P., (1986),*J. Propulsion and Power*, **2**, No 4, 345-353.

19. Baum, J.D. and Levine, J.N., (1987), *AIAA J.*, **25**, 1577-1586.

20. Baum, J.D., (1990), " Energy Exchange Mechanisms Between the Mean and Acoustic Fields in a Simulated Rocket Combustor," AFOSR Contractors Meeting, Atlanta, GA, June.

21. Flandro, G.A. and Roach, R.L., (1992), " Effects of Vorticity Production on Acoustic Waves ina Combustion Chamber." Final Technical Report, AFOSR-90-0159.

22. Zhao, Q. and Kassoy, D.R., (1994), " The Generation and Evolution of Unsteady Vorticity in a Solid Rocket Engine Chamber ," AIAA 94-0779, Aerospace Sciences Meeting, Reno, Nevada, January.

23. MacCormack, R.W. (1969). " The Effect of Viscosity in Hypervelocity Impact Cratering," AIAA 69-354, Cincinnati, Ohio.

24. Lupaglazoff, N. and Vuillot F. (1991). " Two-Dimensional Numerical Simulation of the Stability of a Solid Propellant Rocket Motor," AIAA 91-0205, Aerospace Sciences Meeting, Reno, Nevada, January.

25. Lagerstrom, P.A. (1964) in *Theory of Laminar Flows*, Section **B**. Moore, F.K., ed., Princeton University Press.

26. Price, E.W. and Flandro, G.A. (1993) *Combustion Instability in Solid Propellant Rockets.* Book manuscript in preparation.

27. Wang, M. and Kassoy, D.R. (1992), *J. Fluid Mech.*,238,509-536.

28. Zhao, Q., Kassoy, D.R. and Kirkkopru, K. (1994), " Nonlinear Unsteady Vorticity Generation in a Model of a Solid Rocket Engine Chamber," *submitted to J. Fluid Mech.*

TABLE CAPTION

Table I: The radial locations of the unsteady vortical axial velocity front at different time levels for $M = 0.02, 0.05$ and 0.1 . The second and third columns present the estimates from (11) and (12), respectively. Results in the last column have been found from Figs. 4, 8 and 10.

FIGURE CAPTIONS

Fig. 1: Computational domain and boundary conditions.

Fig. 2a: Normalized steady axial velocity profiles at $x = 0.025$, 0.5 and 1 for $M = 0.05$ and $Re = 3.10^5$.

Fig. 2b: Steady radial velocity profiles at axial locations $x = 0.025$ (solid line), 0.5 (dotted line) and 1 (dashed line) for $M = 0.05$ and $Re = 3.10^5$.

Fig. 3: The axial unsteady pressure variation at $r = 0$, 0.5 and 1 when $t = 29.37$ for $M = 0.1$, $Re = 3.10^4$, $\omega = 1$ and $A = M$.

Fig. 4a: The radial variation of the unsteady axial flow speed,u_V, at $x = 0.5$ when $t = 1.48$ for $M = 0.1$, $Re = 3.10^4$, $\omega = 1$ and $A = M$.

Fig. 4b: As Fig. 4a but when $t = 11.81$.

Fig. 4c: As Fig. 4a but when $t = 29.37$.

Fig. 5: The time history of axial pressure gradient, $\partial p/\partial x$, at $x = 0.5$, $r = 0.9$ for $M = 0.1$, $Re = 3.10^4$, $\omega = 1$ and $A = M$.

Fig. 6a: The time history of the planar part of the unsteady axial flow speed, u_P, at $x = 0.5$ for $M = 0.1$, $Re = 3.10^4$, $\omega = 1$ and $A = M$.

Fig. 6b: The time history of the unsteady vortical axial speed, u_V at $x = 0.5$, $r = 1$ for the same flow parameters as those in Fig. 6a.

Fig. 7: The radial variation of $(v - v_S)$ at $x = 0.5$ when $t = 29.37$ for the same flow parameters as those in Fig. 4c.

Fig. 8a: The radial variation of u_V at $x = 0.5$ when $t = 1.488$ for $M = 0.05$, $Re = 3.10^5$, $\omega = 1$ and $A = M$.

Fig. 8b: As Fig. 8a but for $t = 11.834$.

Fig. 8c: As Fig. 8a but for $t = 29.54$.

Fig. 9: The axial variation of u_V at $r = 1$ (solid line), $r = 0.9$ (dotted line) and $r = 0.7$ (dashed line) when $t = 29.37$ for $M = 0.1$, $Re = 3.10^4$, $\omega = 1$ and $A = M$.

Fig. 10a: The radial variation of u_V at $x = 0.5$ when $t = 3$ for $M = 0.02$, $Re = 3.10^5$, $\omega = 1$ and $A = M$.

Fig. 10b: As Fig. 10a but when $t = 15$.

Fig. 10c: As Fig. 10a but when $t = 30$.

Fig. 11a: As Fig. 10c but at $x = 0.25$.

Fig. 11b: As Fig. 11a but at $x = 0.75$.

Fig. 12a: The radial variation of unsteady vorticity, Ω, defined in (10) at $x = 0.5$ when $t = 29.37$ for $M = 0.1$.

Fig. 12b: As Fig. 12a but for $M = 0.05$, when $t = 29.54$.

Fig. 12c: As Fig. 12a but for $M = 0.02$, when $t = 30$.

Fig. 12d: Spatial unsteady vorticity variation Ω throughout the cylinder at $t = 30$ for $M = 0.02$.

Fig. 13a: The radial variation of u_V at $x = 0.5$ when $t = 17.71$ for $M = 0.1$, $Re = 3.10^4$; $A = M$ and $\omega = 1$.

Fig. 13b: As Fig. 13a but at $t = 17.38$ and for $\omega = 1.5$.

Fig. 13c: As Fig. 13a but at $t = 17.77$ and for $\omega = 2.5$.

Time	Front Locations		
t	1-Mt	r_F	Numerical
M=0.02			
3.	0.94	0.94	0.93
15.	0.70	0.69	0.67
30.	0.40	0.44	0.44
M=0.05			
1.48	0.93	0.92	0.92
11.83	0.41	0.44	0.45
29.54	-0.48	0.11	0
M=0.1			
1.48	0.85	0.85	0.85
11.81	-0.18	0.18	0.15
29.37	-1.94	0.01	0

Table I

KADIR K, D.R. KASSOY, Q.Z.

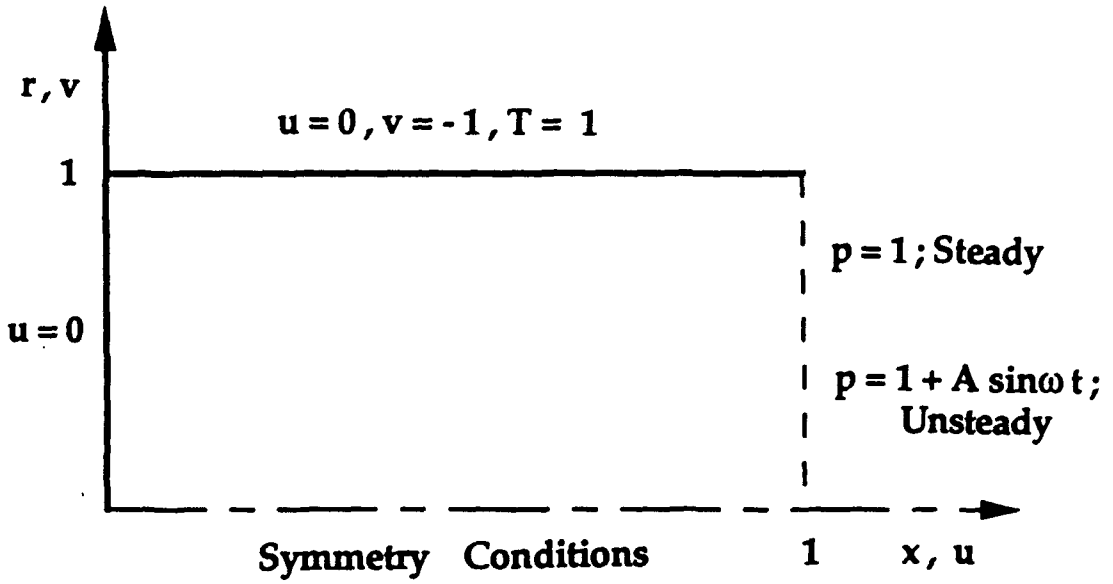

Fig. 1

KADIR K , D.R. KARSOY, Q 7

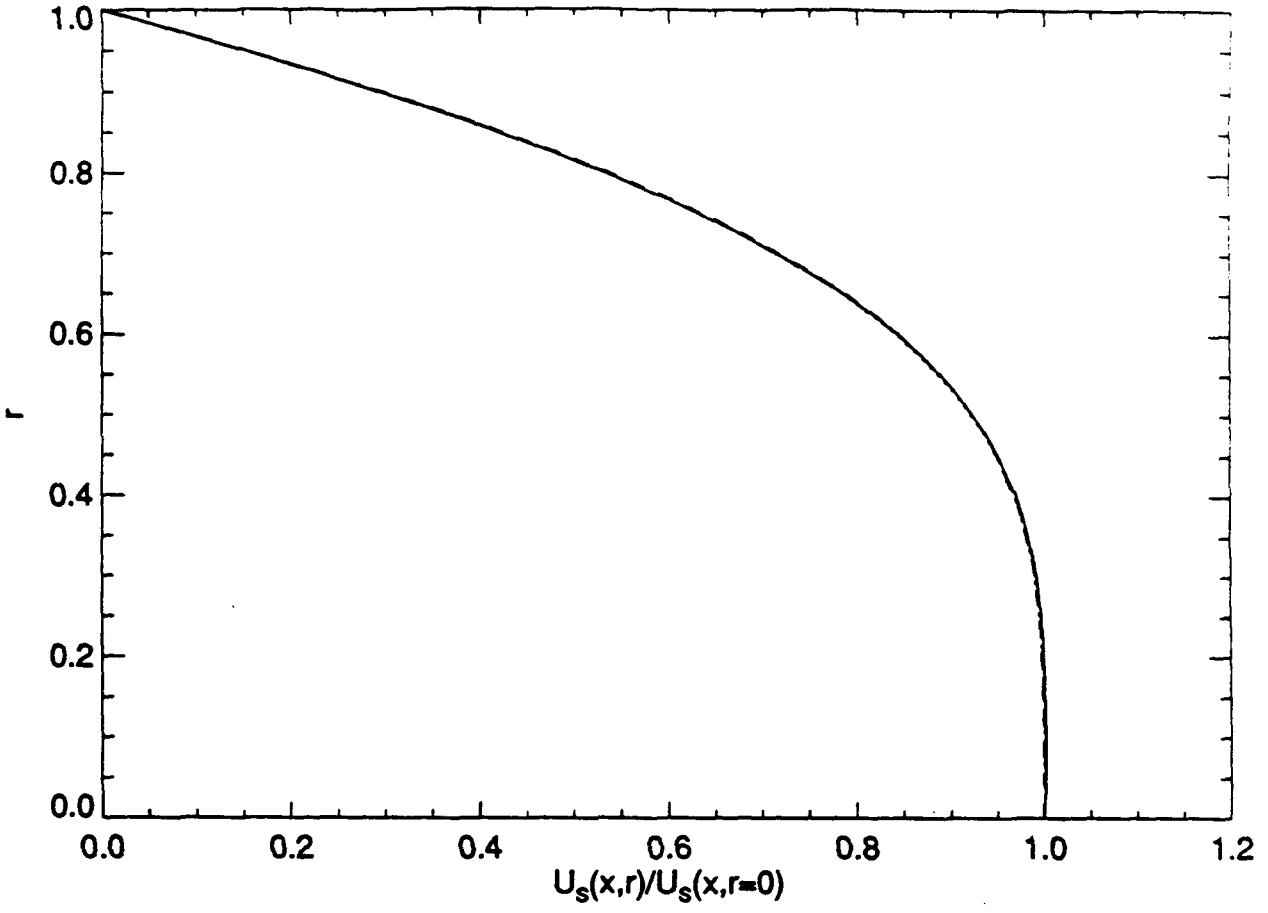

Fig. 2a

K.K, D.R. KASSOY, Q-Z.

Fig 2a

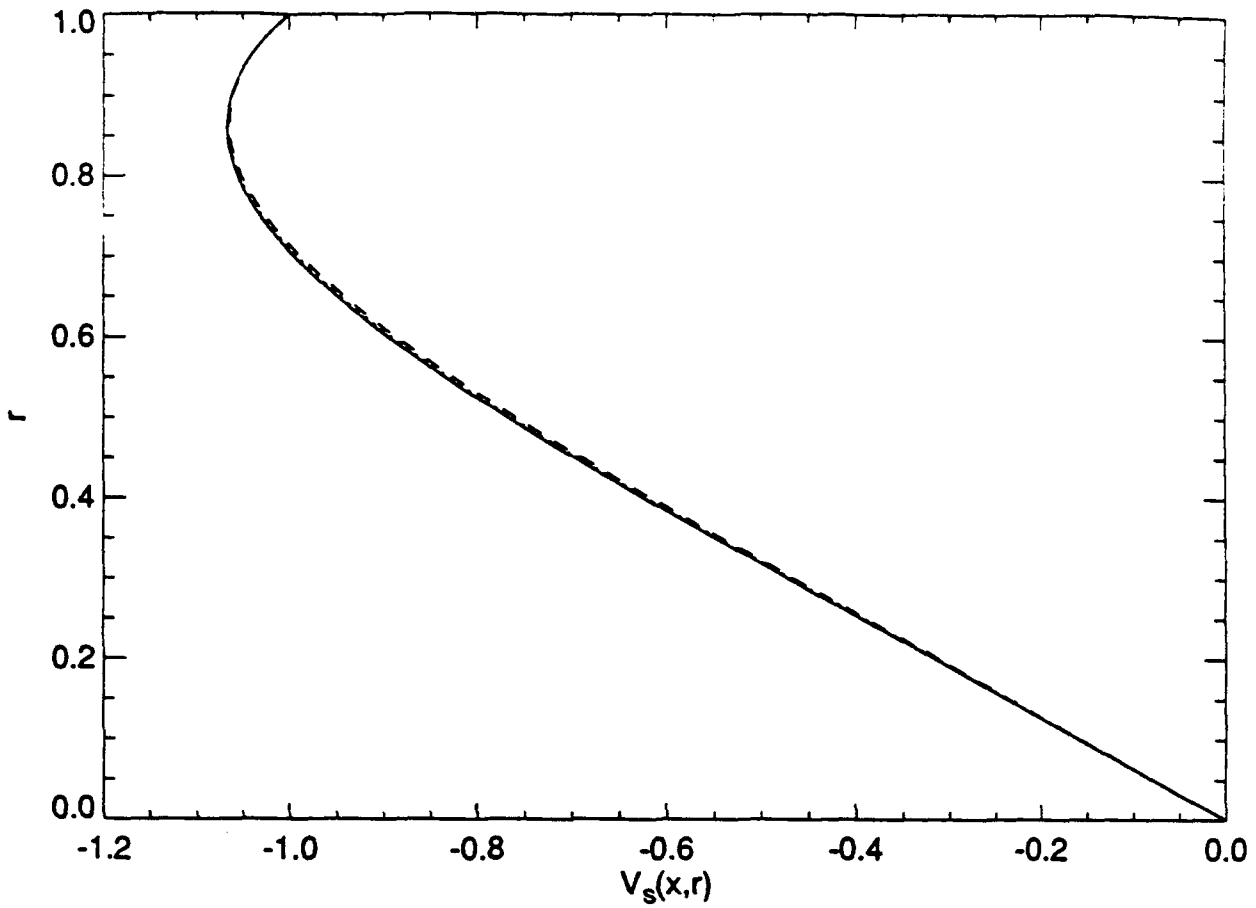

Fig. 2b

K·K, D·R. KASSOY, Q.Z.

Fig.2b

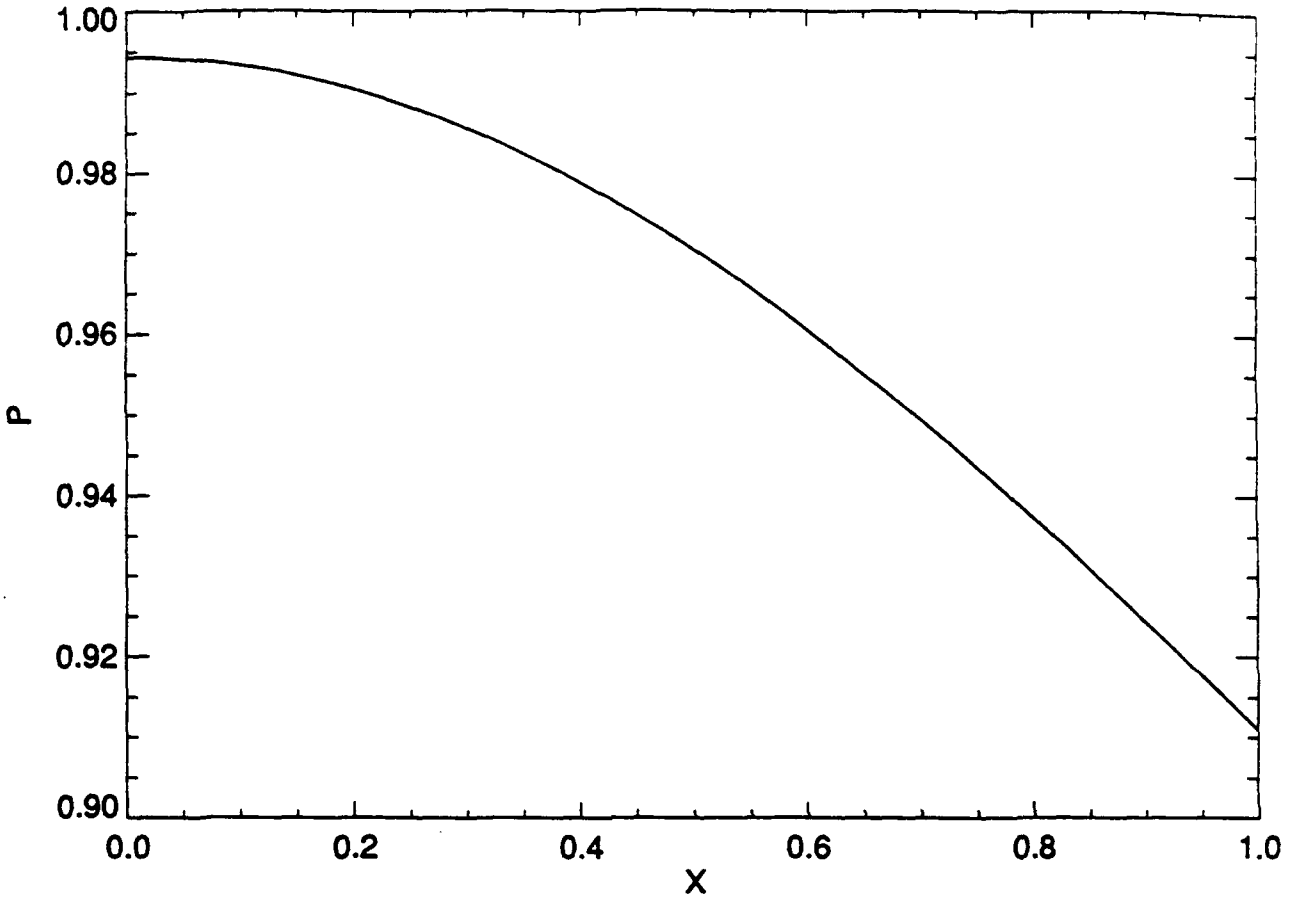

Fig. 3

K.K., D.R. KASSOY, Q.Z

Fig 3 t= 29 32

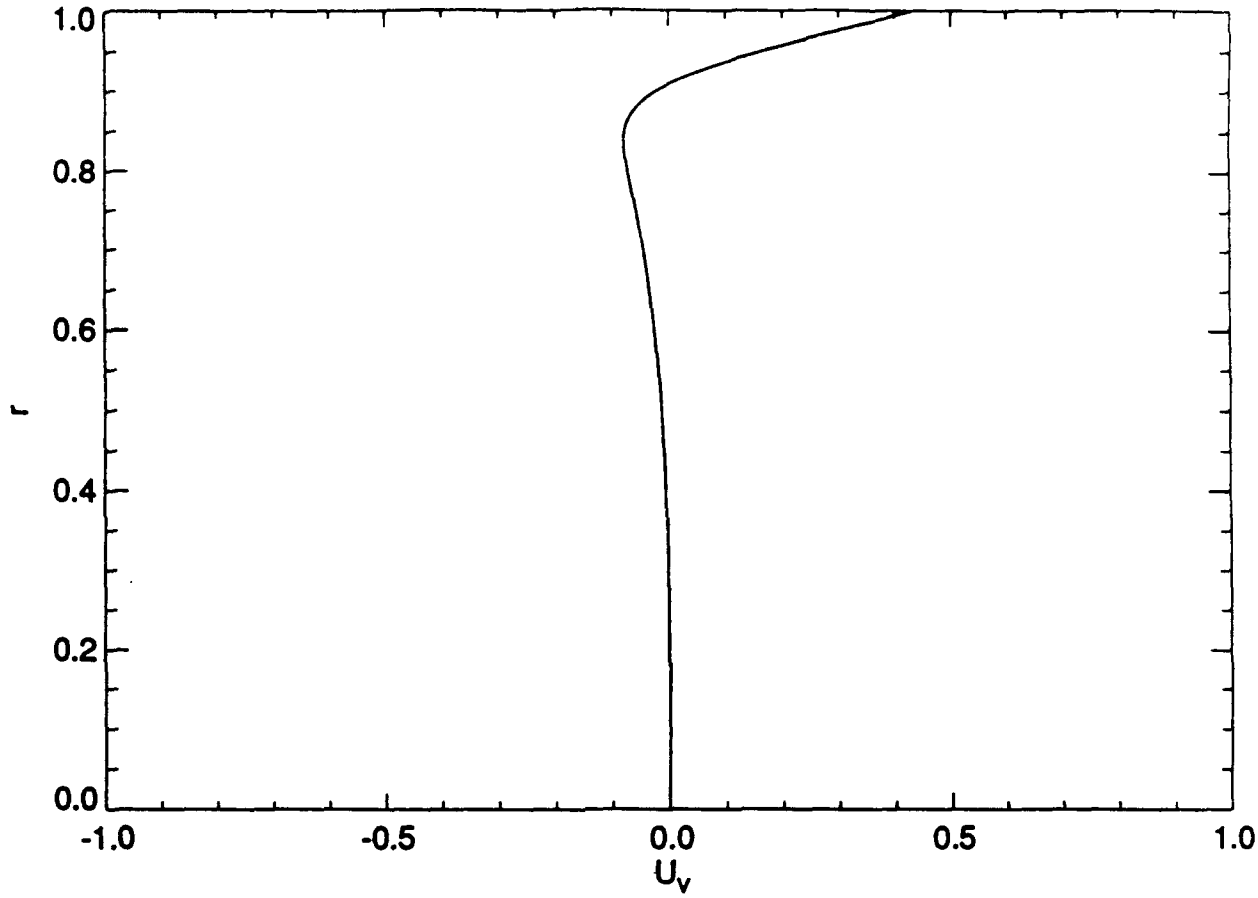

Fig. 4a

K.K., DR KASSOY, QZ

Fig 4a

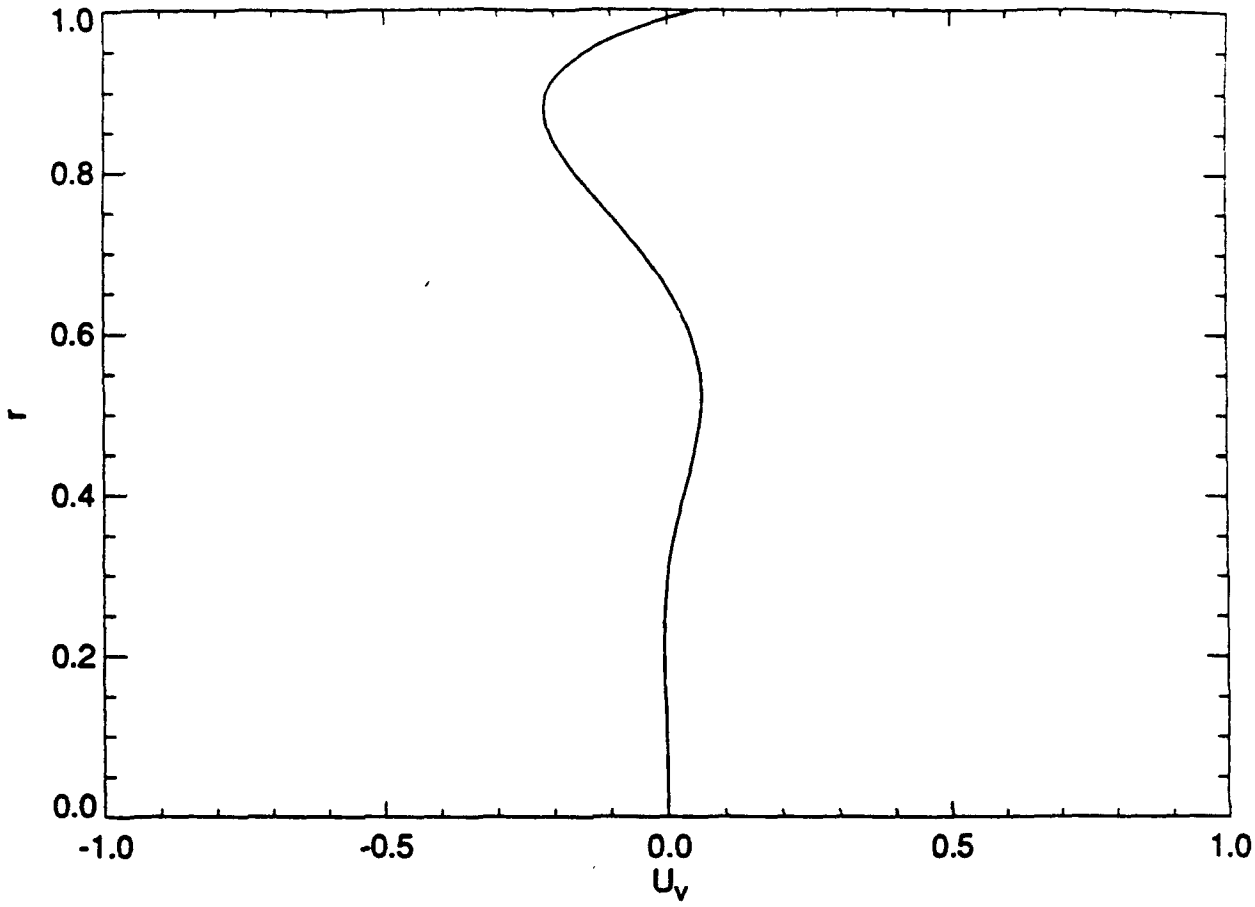

Fig. 4b

KK, DRKASSOY, Q.7.

Fig. 4b

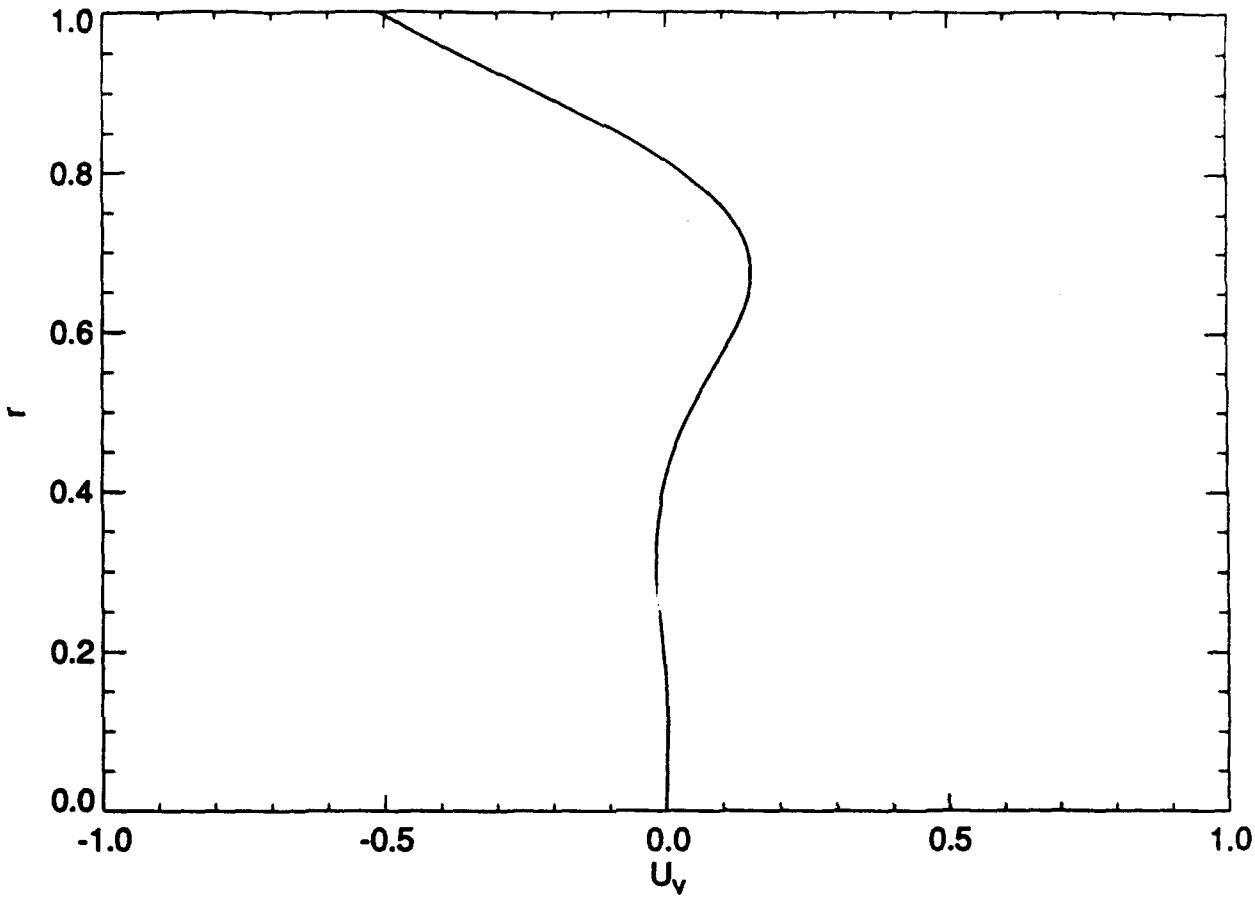

Fig. 4c

K.K, DR. KASSOY, Q.Z

Fig. 4C

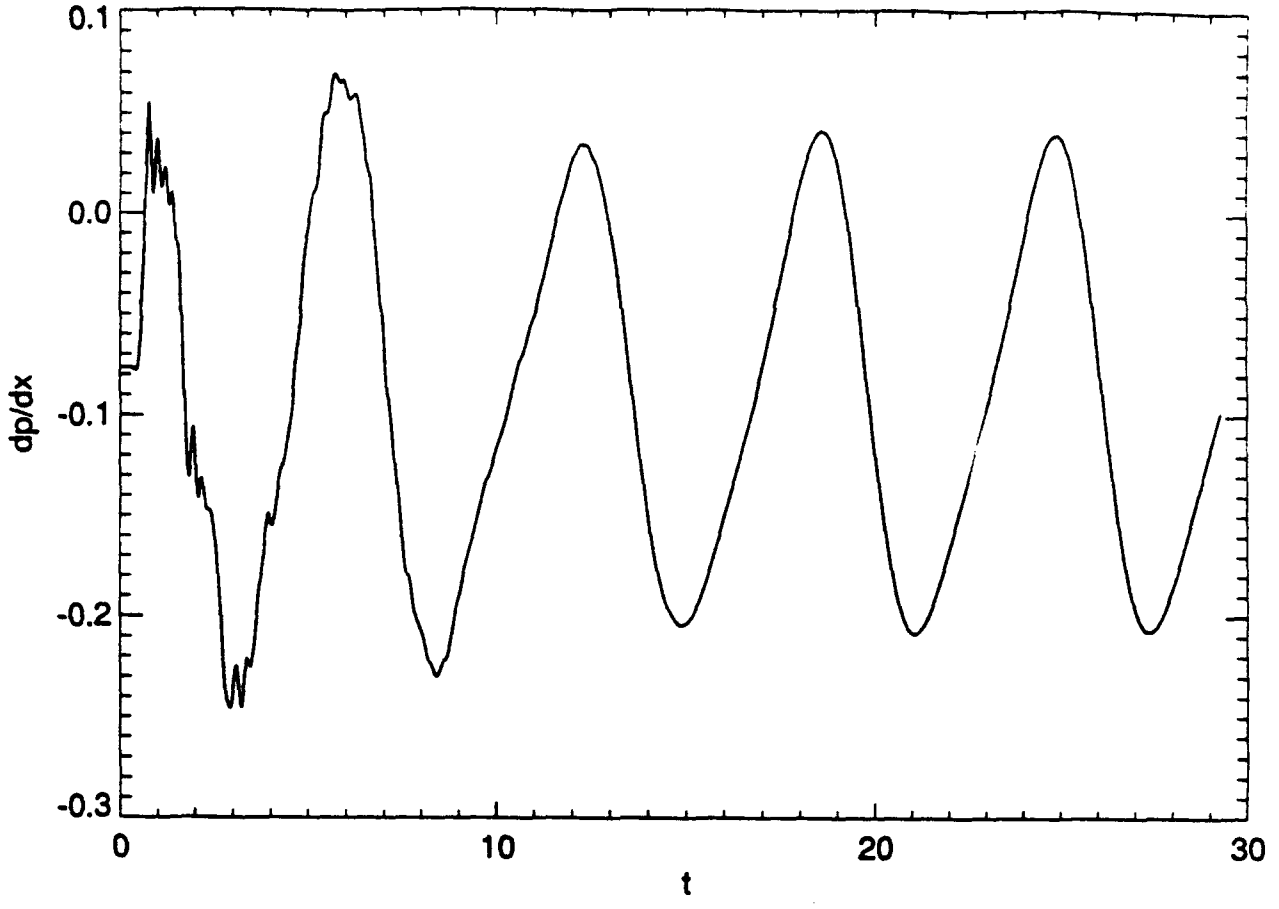

Fig. 5

K.K., D.R.KASSOY, Q.Z.

Fig. 5

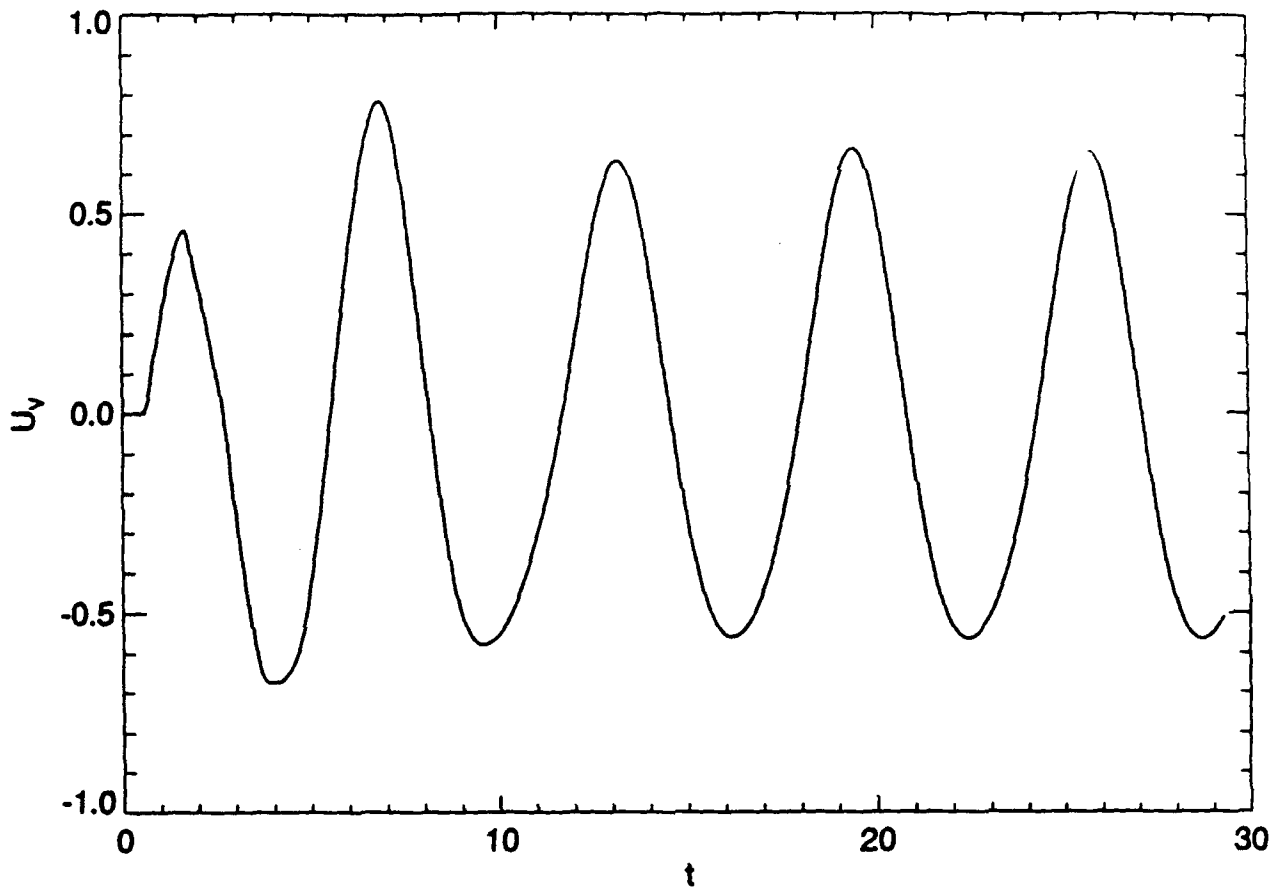

Fig. 6a

K.K., D.R. KASSOY, Q.Z.

Fig. 6a

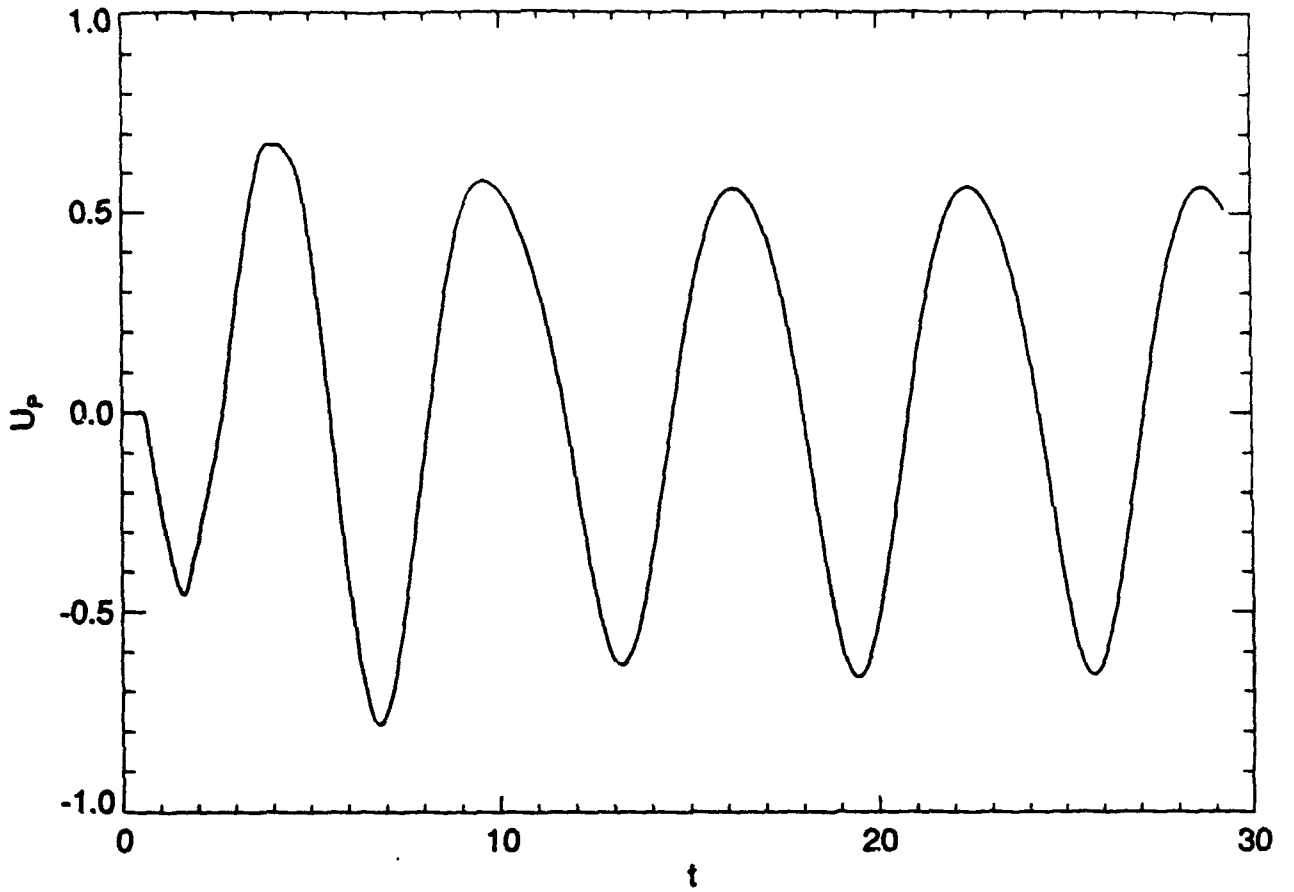

Fig. 6b

KADIR K., D.R KASSOY, Q.Z.

ig 6b

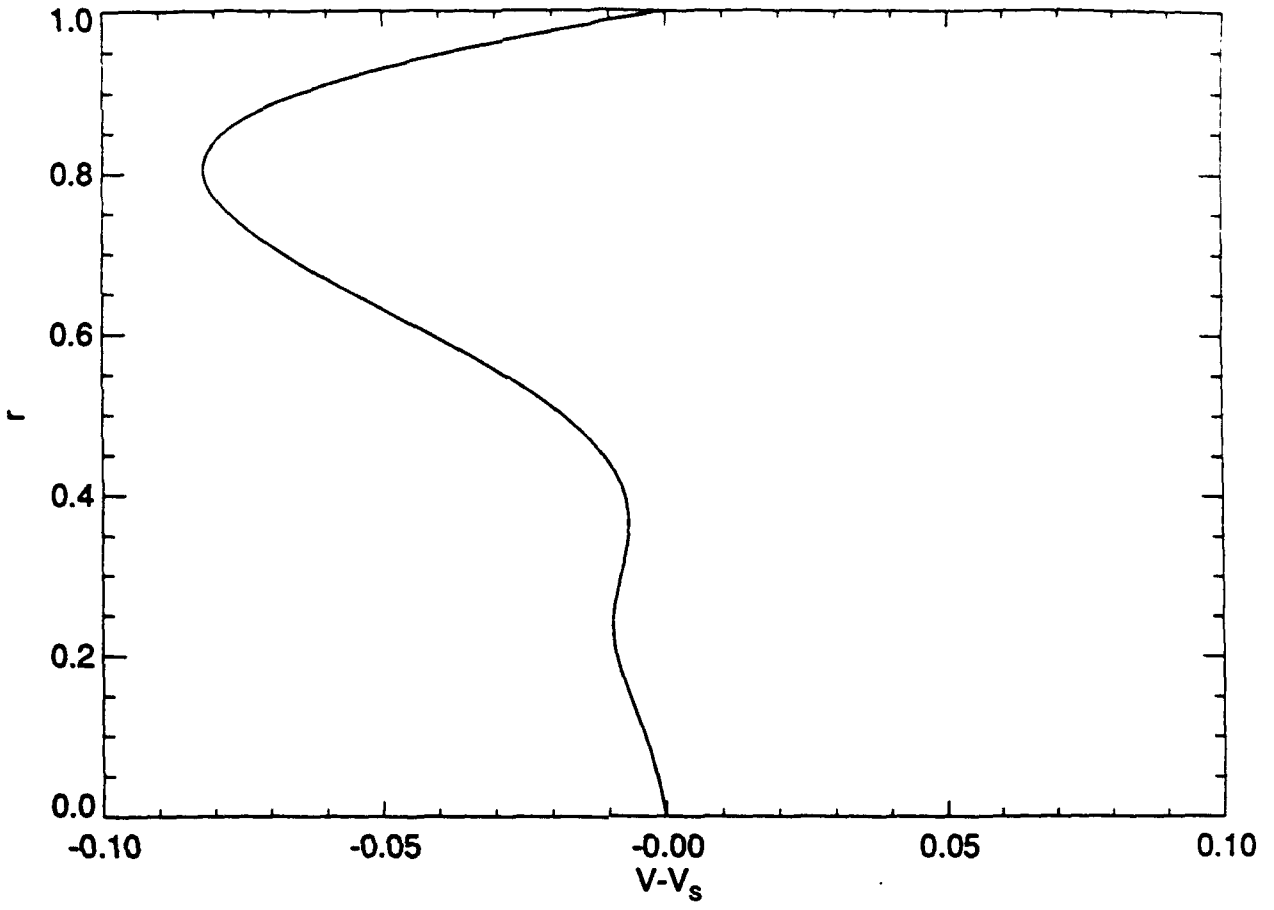

Fig. 7

KADIR K., D R. KASSOY, Q.Z.

Fig. 7

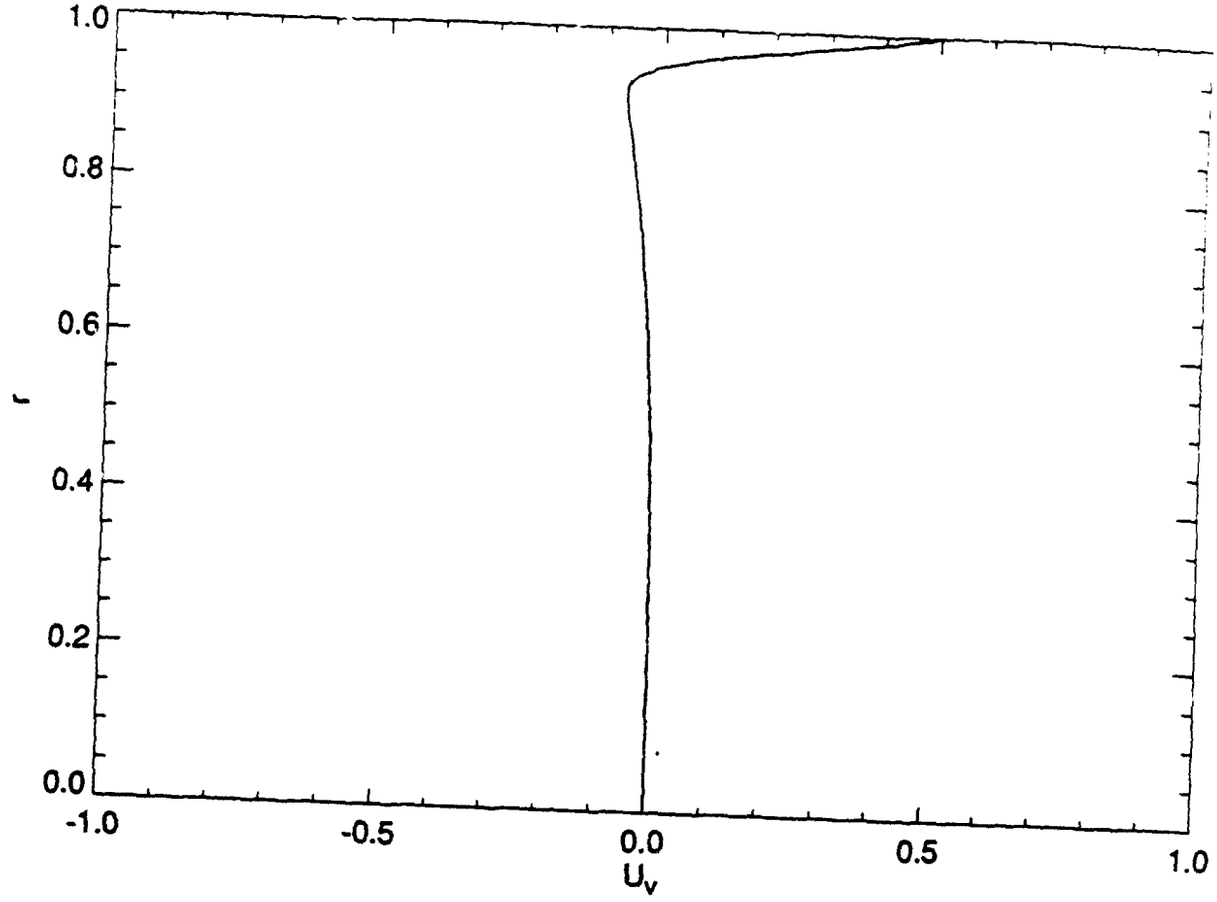

Fig. 8a

KADIR K, D.R. KASSOY, Q.Z.

g. 8a

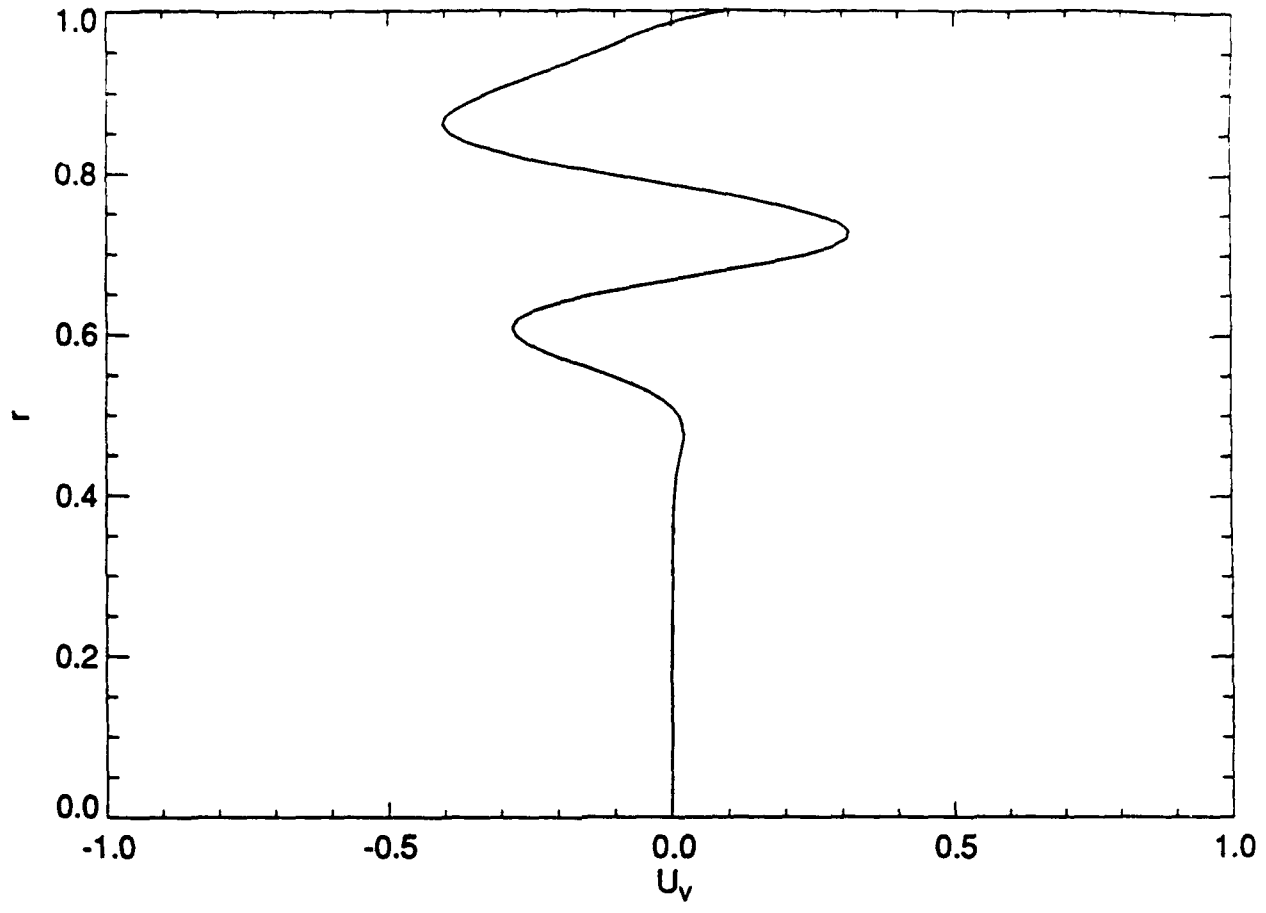

Fig. 8b

KADIR K., D.R. KASSOY, U.Z.

Fig. 8b

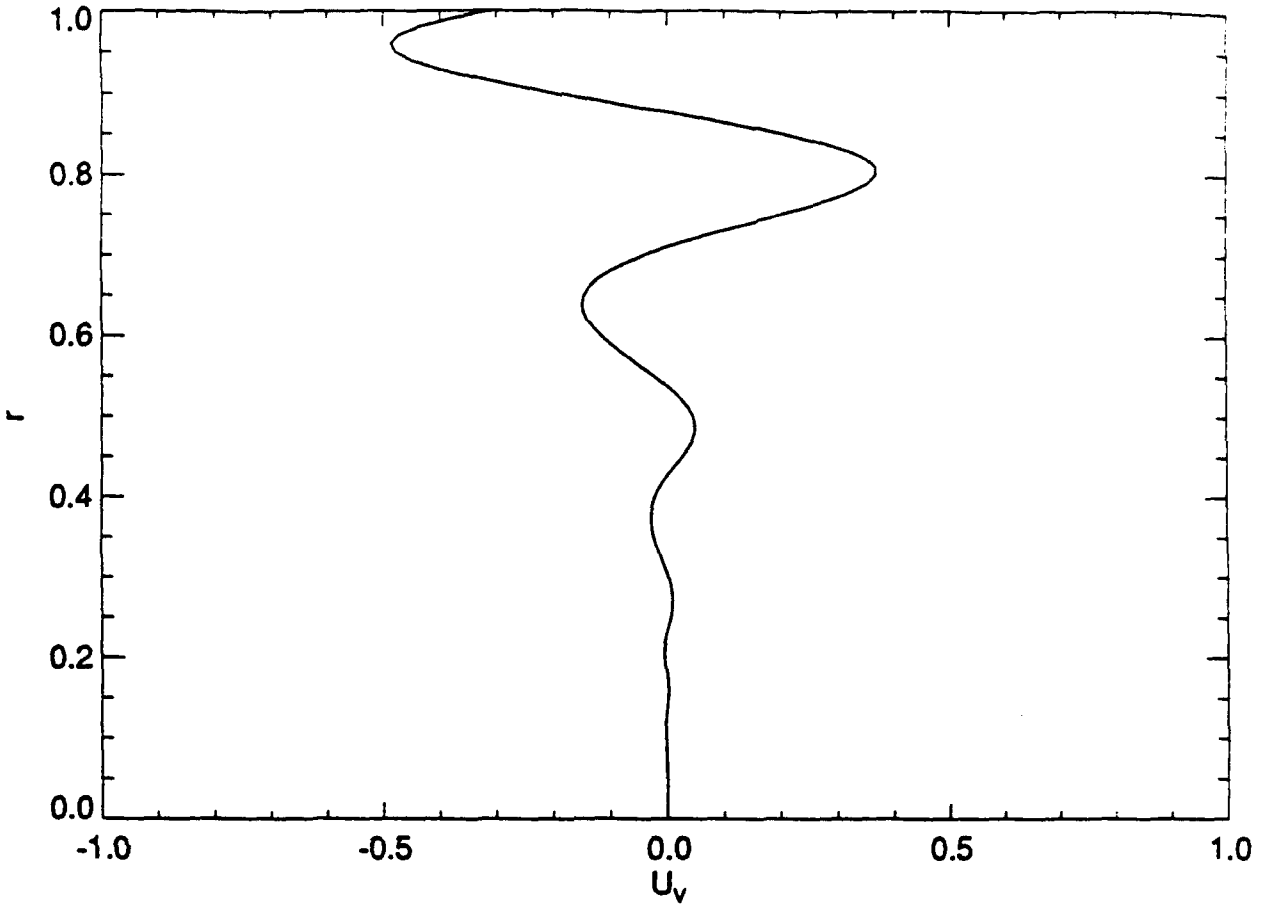

Fig. 8c

KADIR K., D R. KASSOY, Q.Z.

Fig 8c

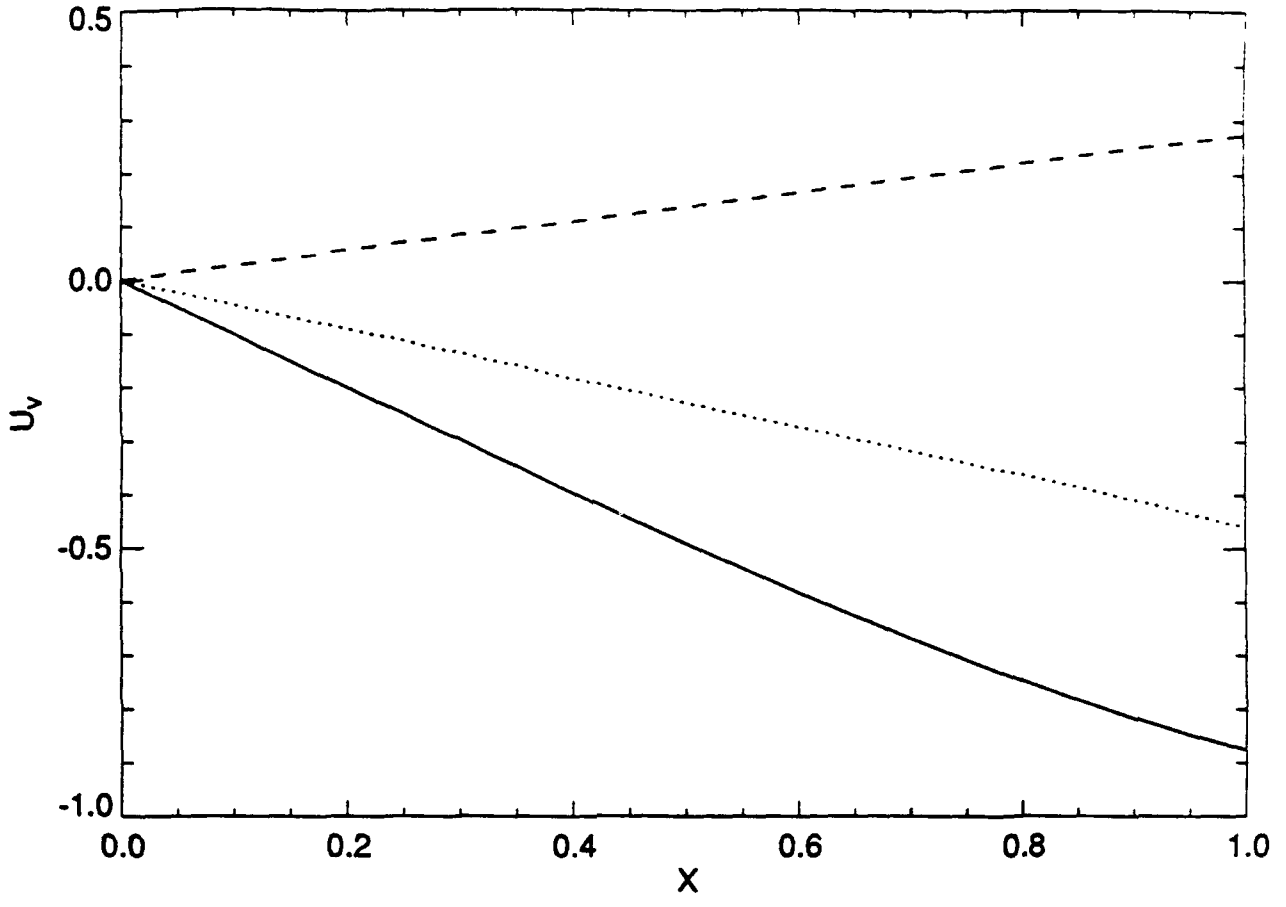

Fig. 9

KADIR K., D.R. KASSOY, QZ.

fig 9

—— r = 1
. . . r = 0.9
- - - - r = 0.7

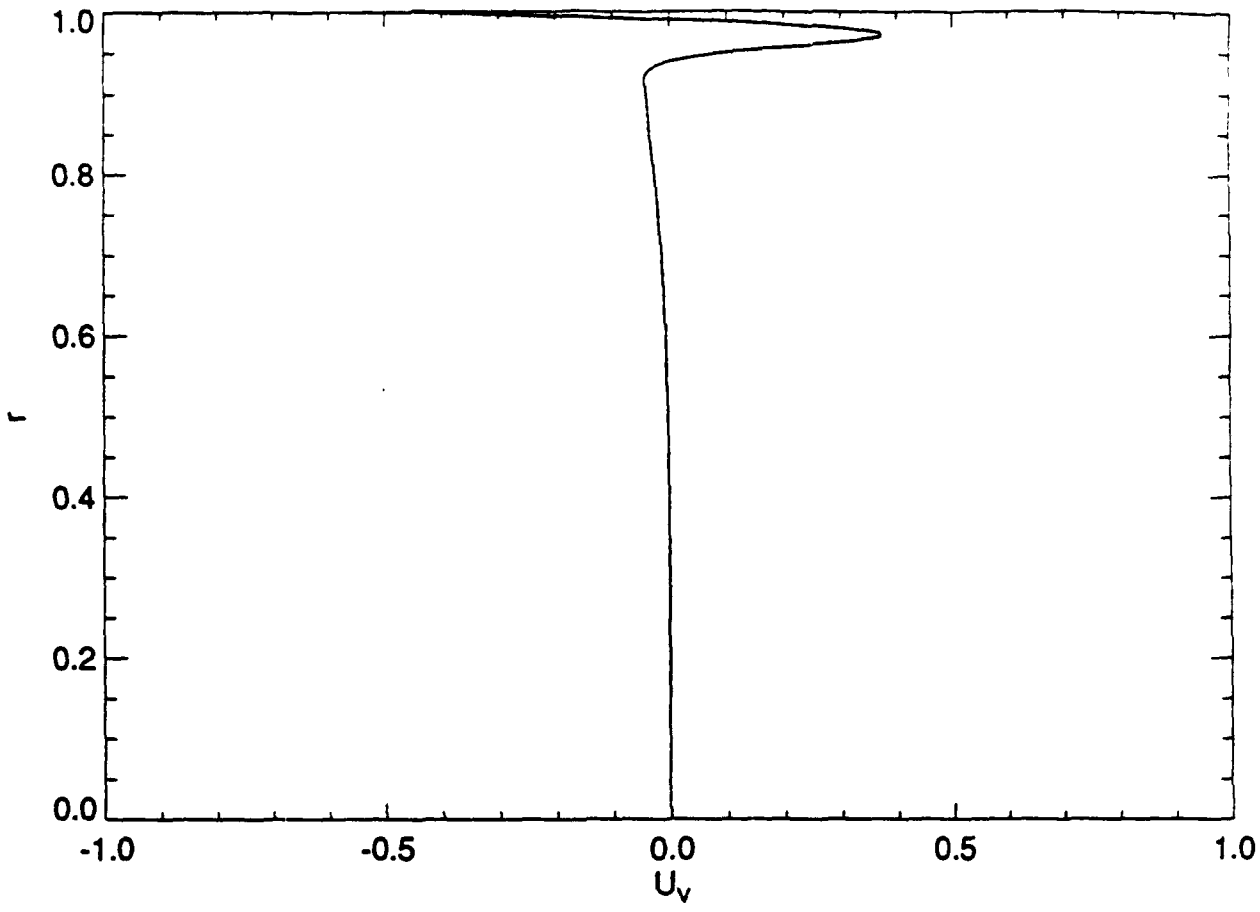

Fig. 10a

KADIR K., D R. KATSOY, Q Z

Fig. 10a

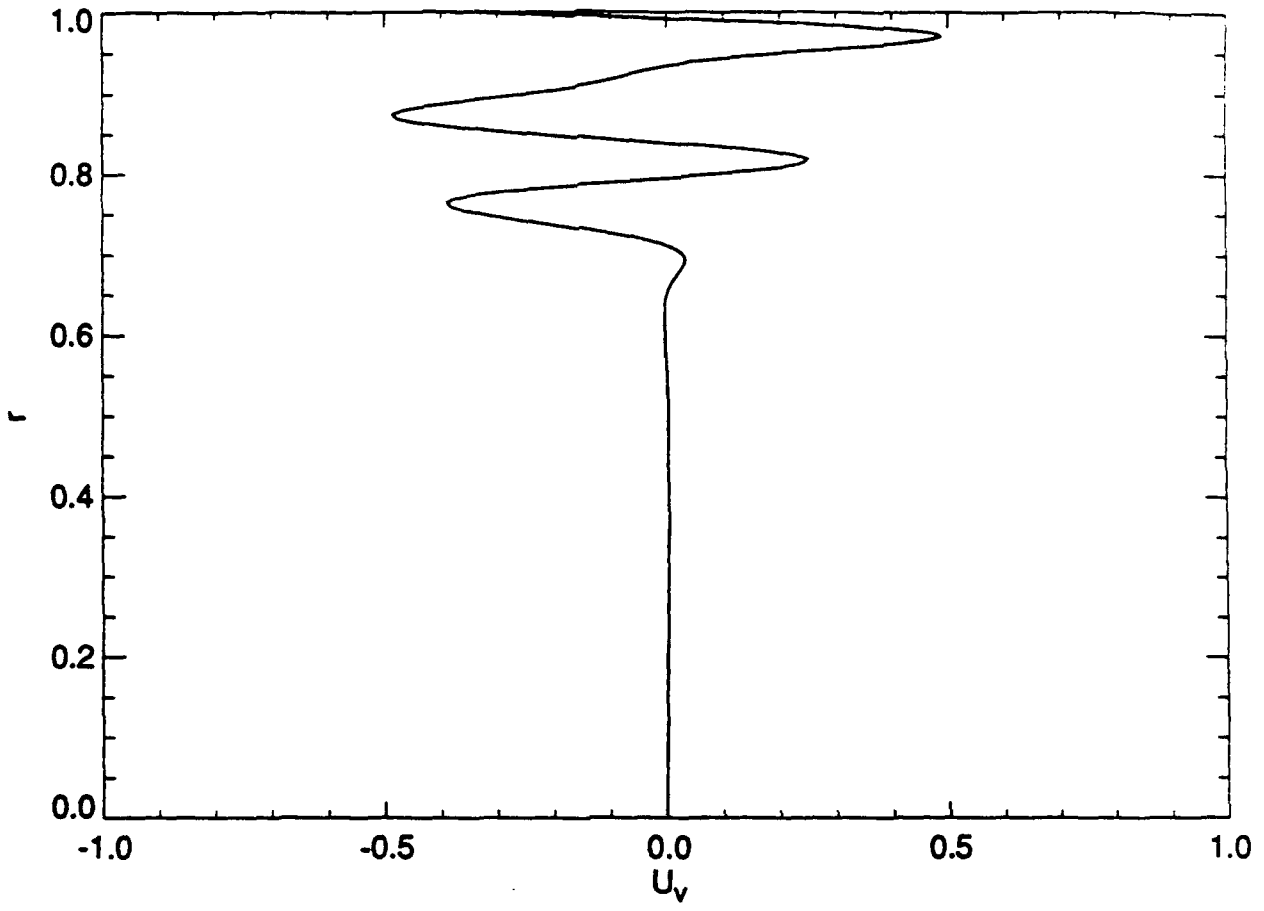

Fig. 10b

KADIR K., D.R. KASSOY, Q.Z.

Fig 10b

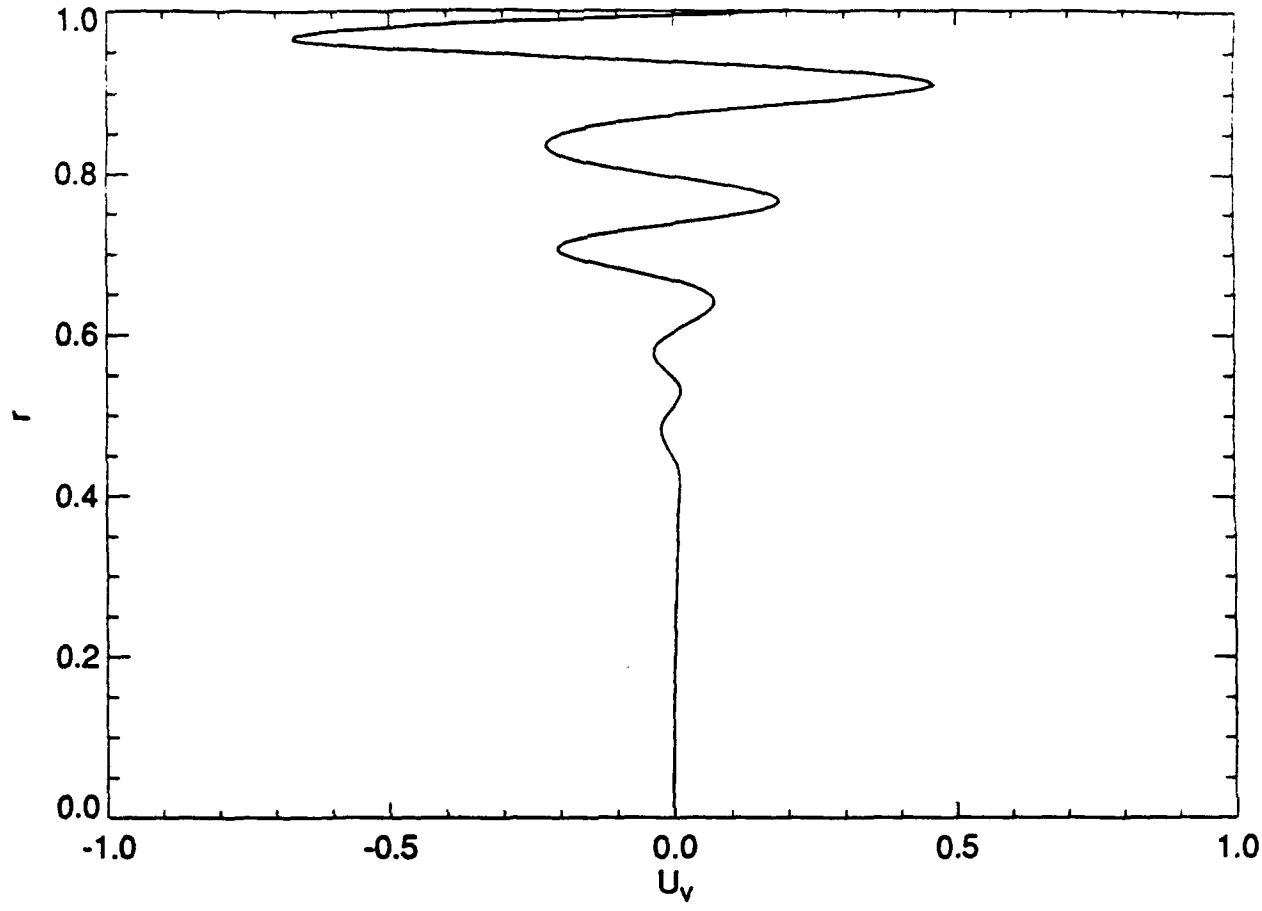

Fig. 10c

KADIR K, D.R KASSOY, Q.Z.

Fig 10c

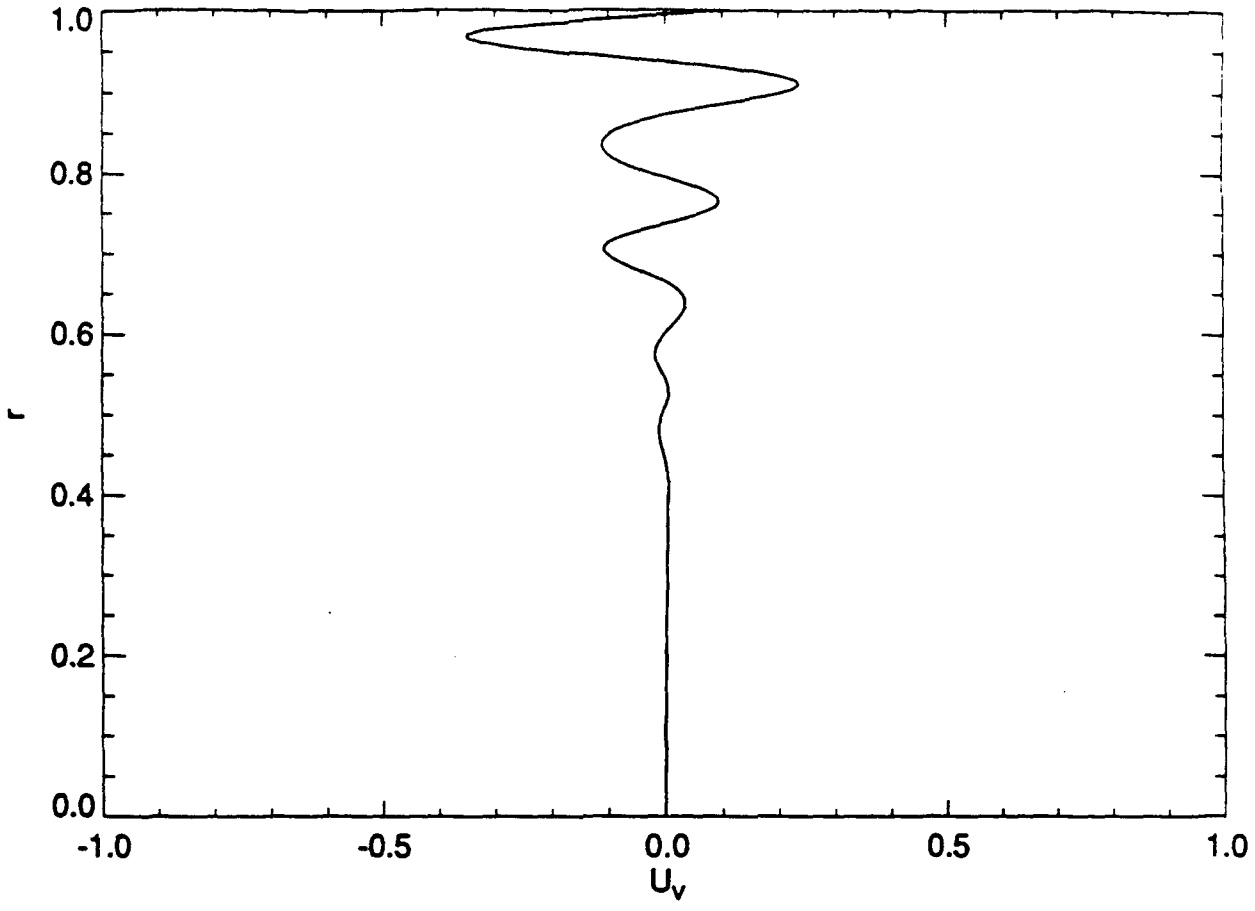

Fig. 11a

KADIR K., D. R. KASSOY, Q-Z.

Fig. 11a

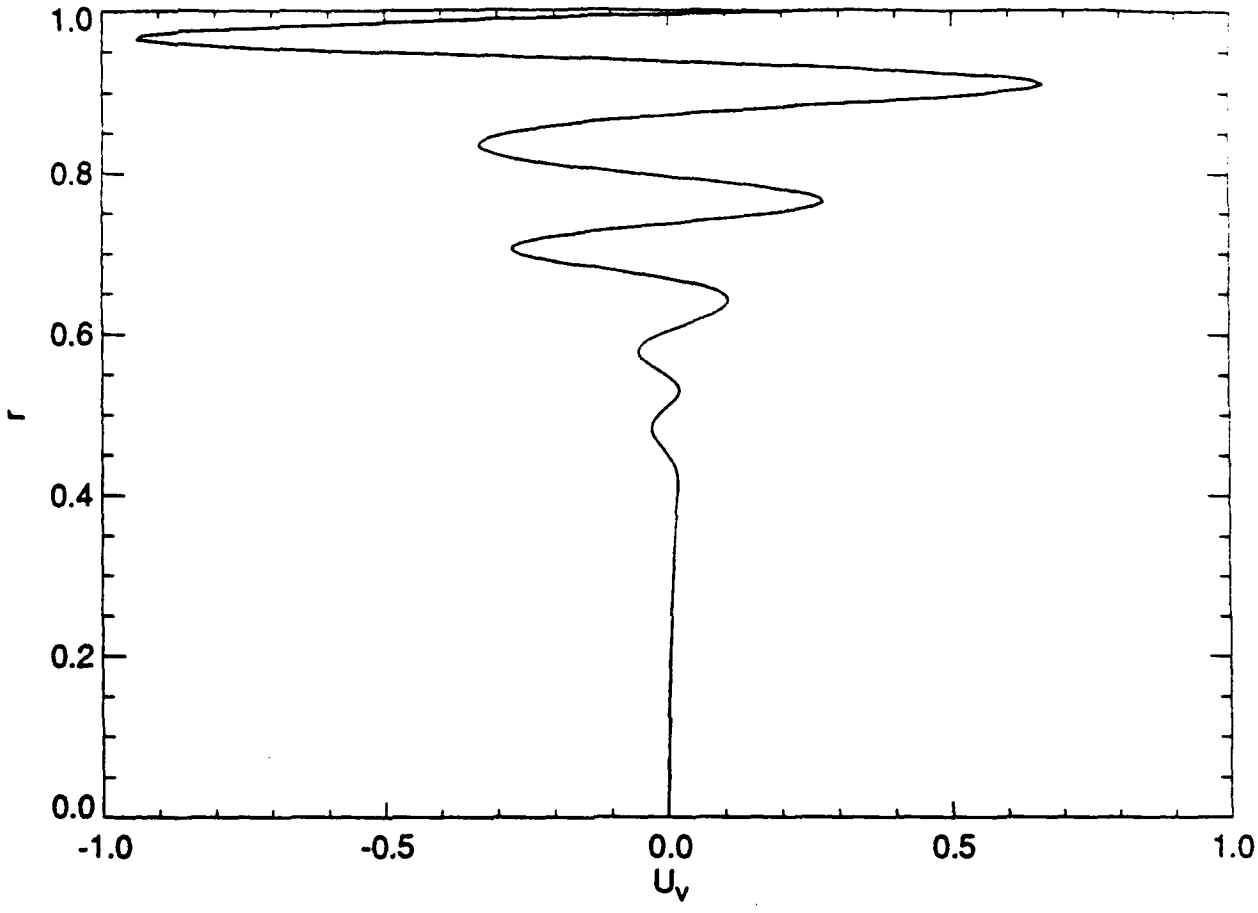

Fig. 11b

KADIR K., D.R. KASSOY, Q.Z.

Fig 11b

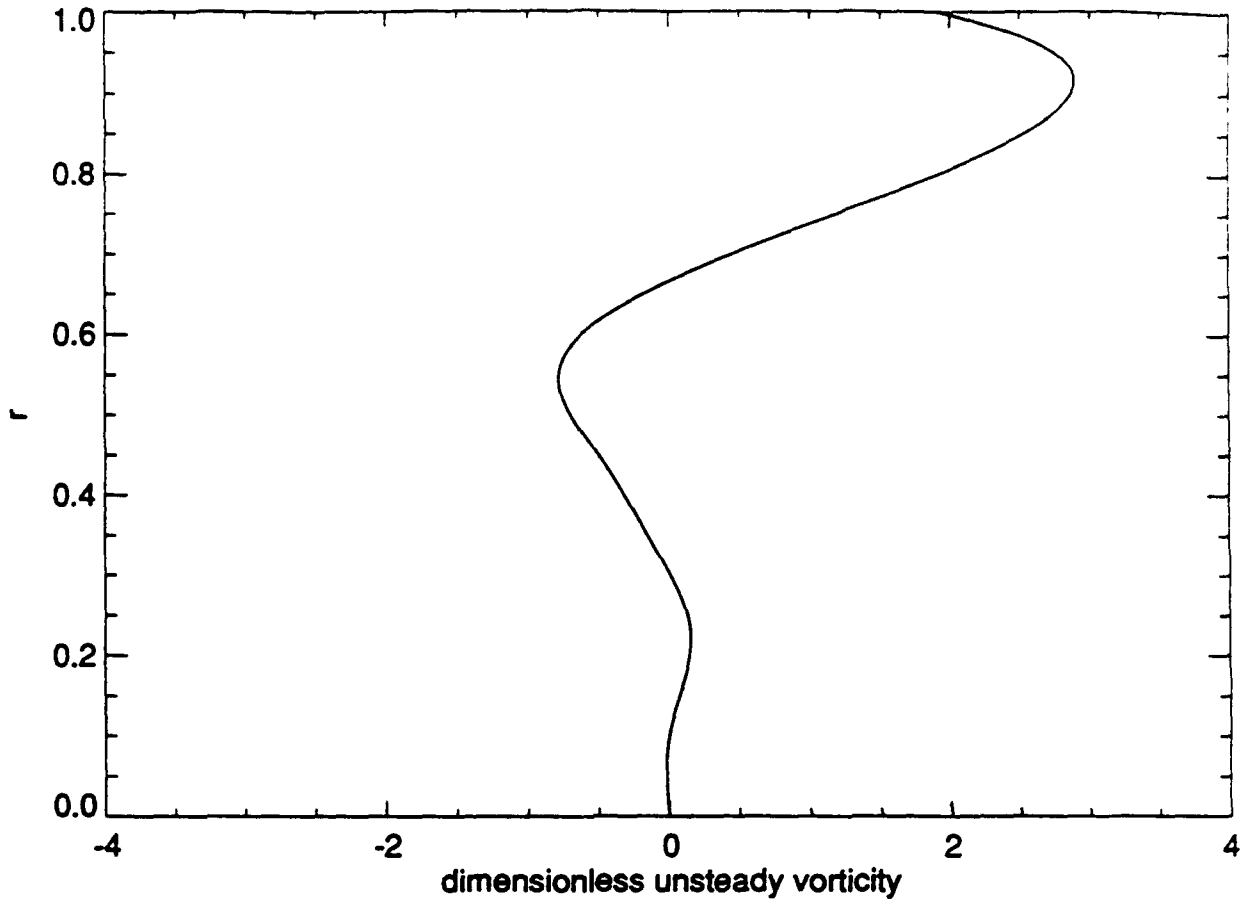

Fig. 12a

KADIR K., D. R. KASSOY, Q. Z.

Fig. 12a

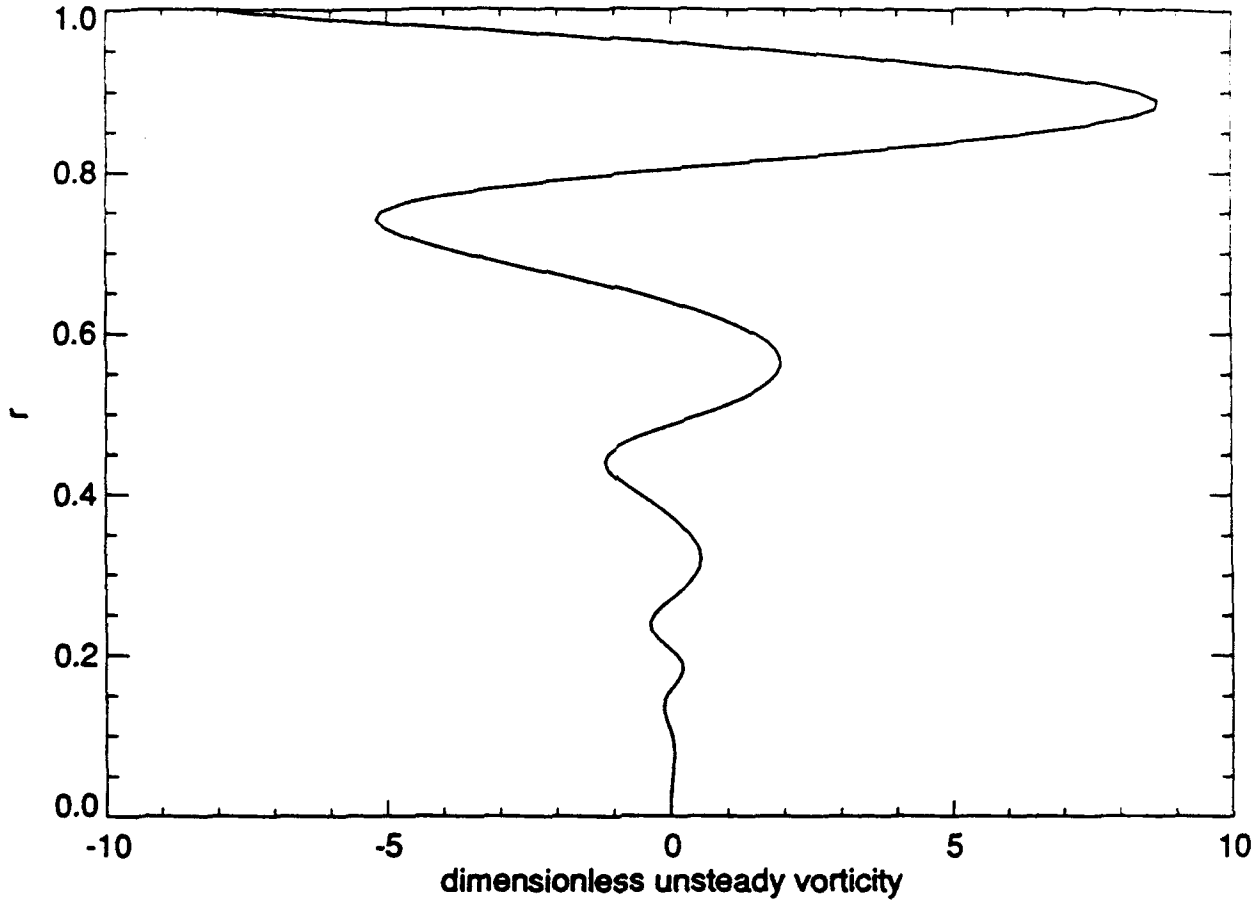

Fig. 12b

KADIR K., D.R. KASSOY, Q.Z.

Fig. 12b

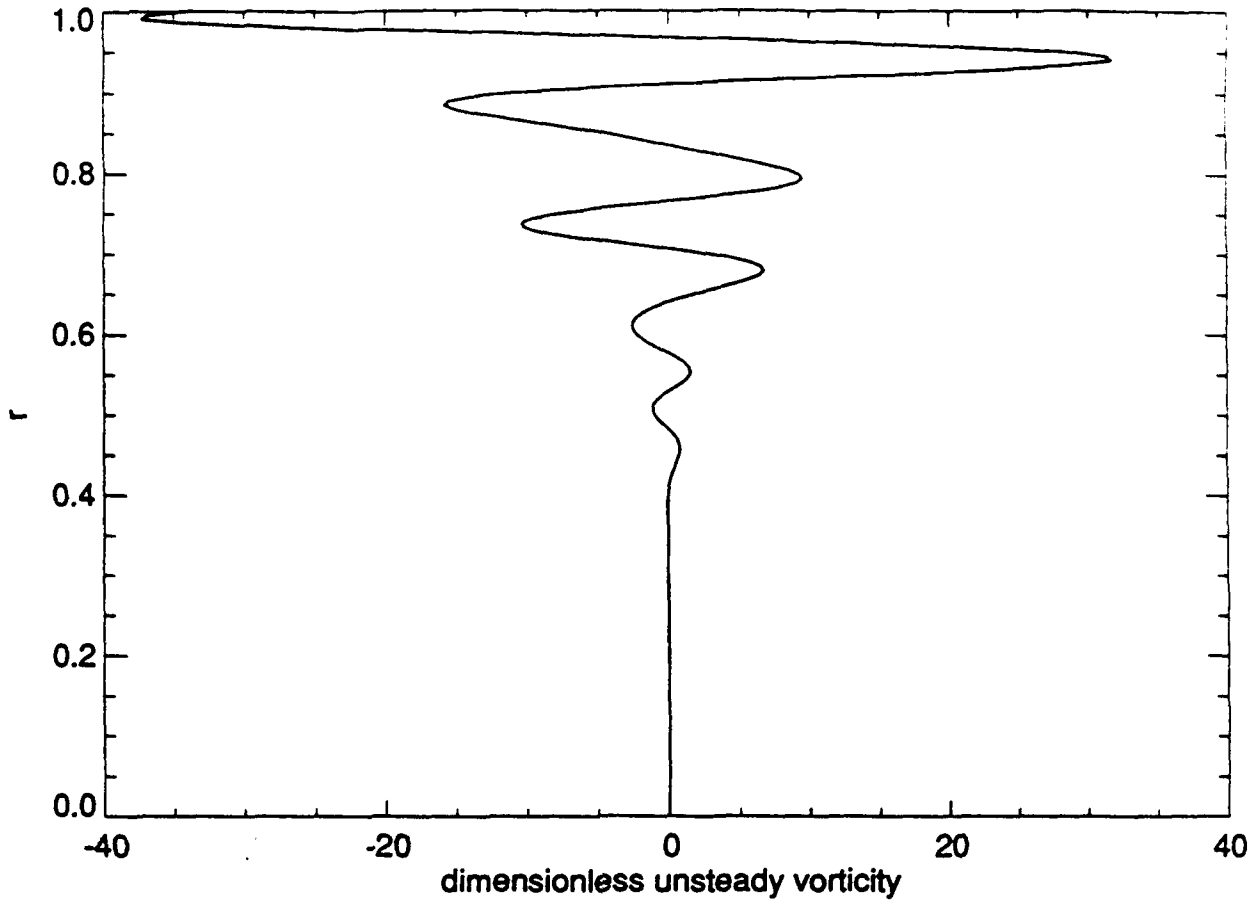

Fig. 12c

KADIR K, D.R. KASSOY, Q.Z.

Fig.12c

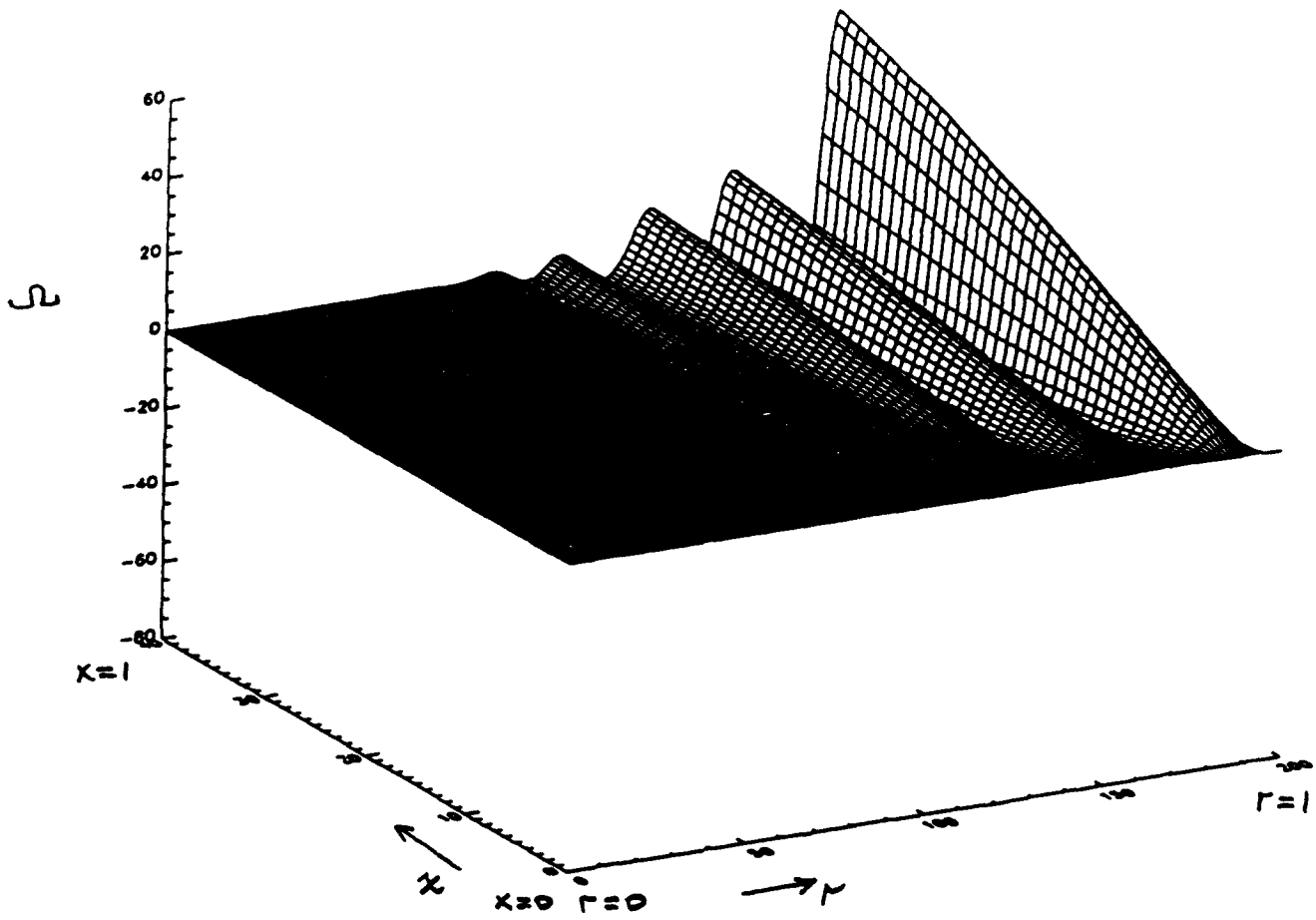

Fig. 12d

KADIR K., D.R. KASSOY, Q.Z.

Fig 12-d.

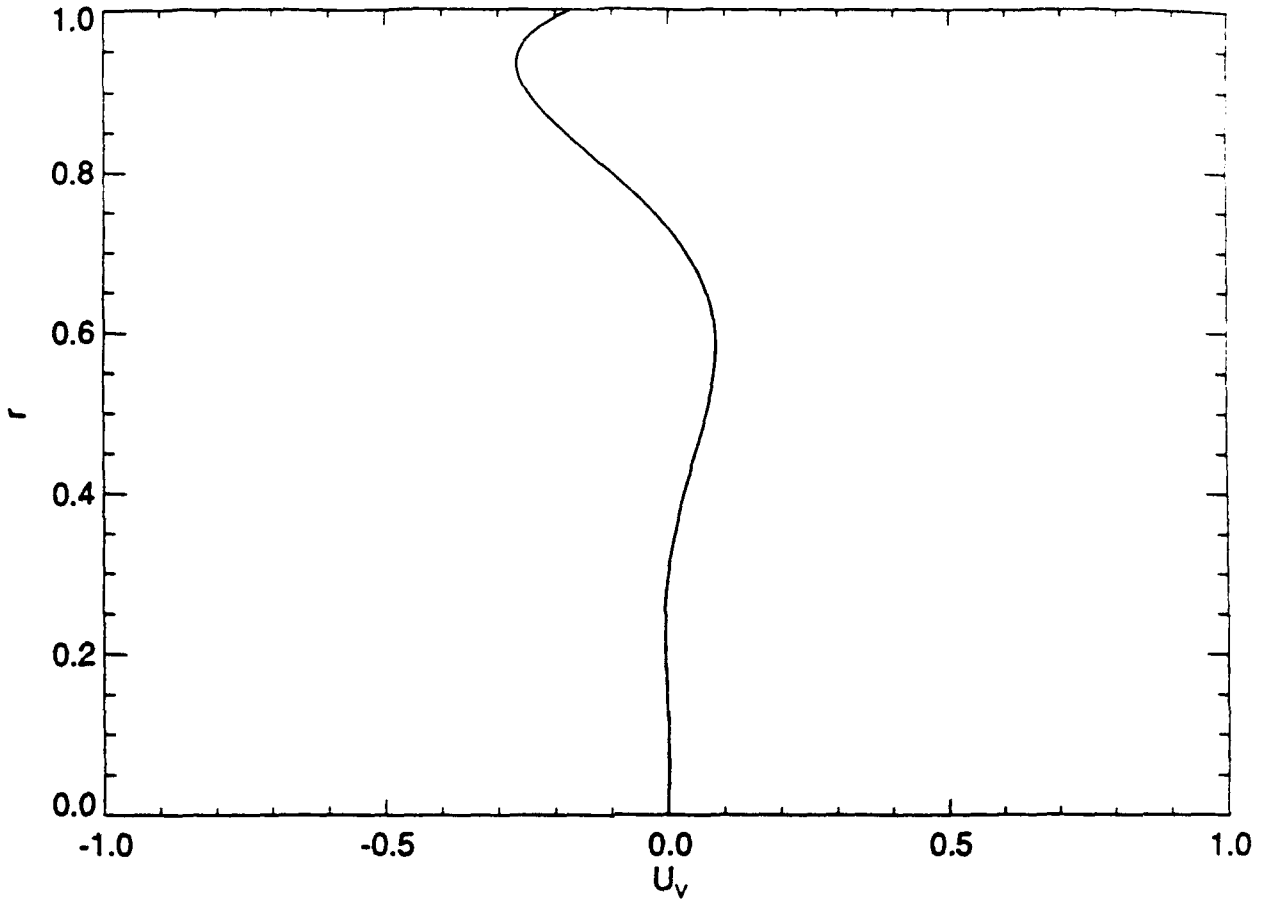

Fig. 13a

KADIR K., D. R. KASSOY, Q. Z.

Fig 13a

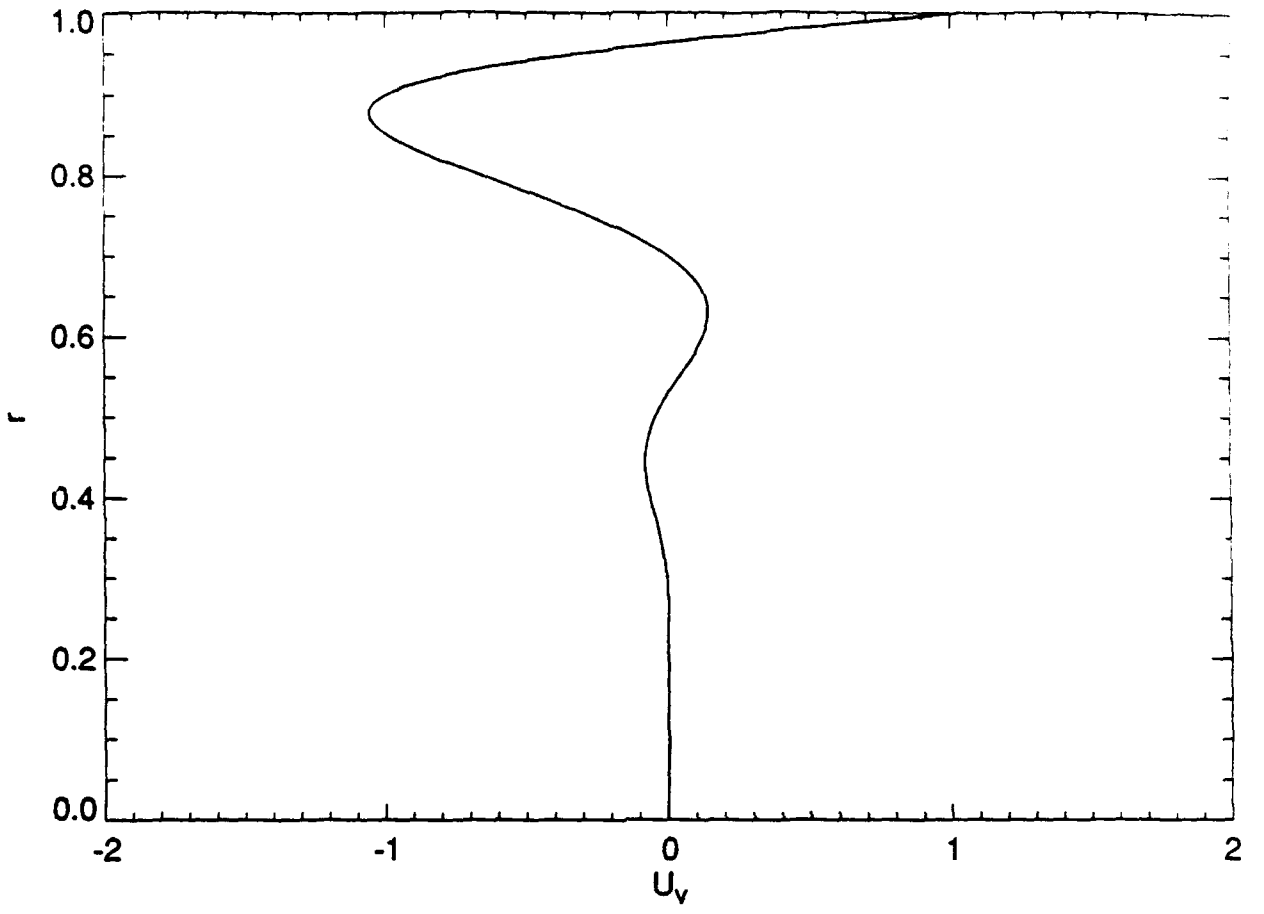

Fig. 13b

KADIR K., D. R. KASSOY, Q. Z.

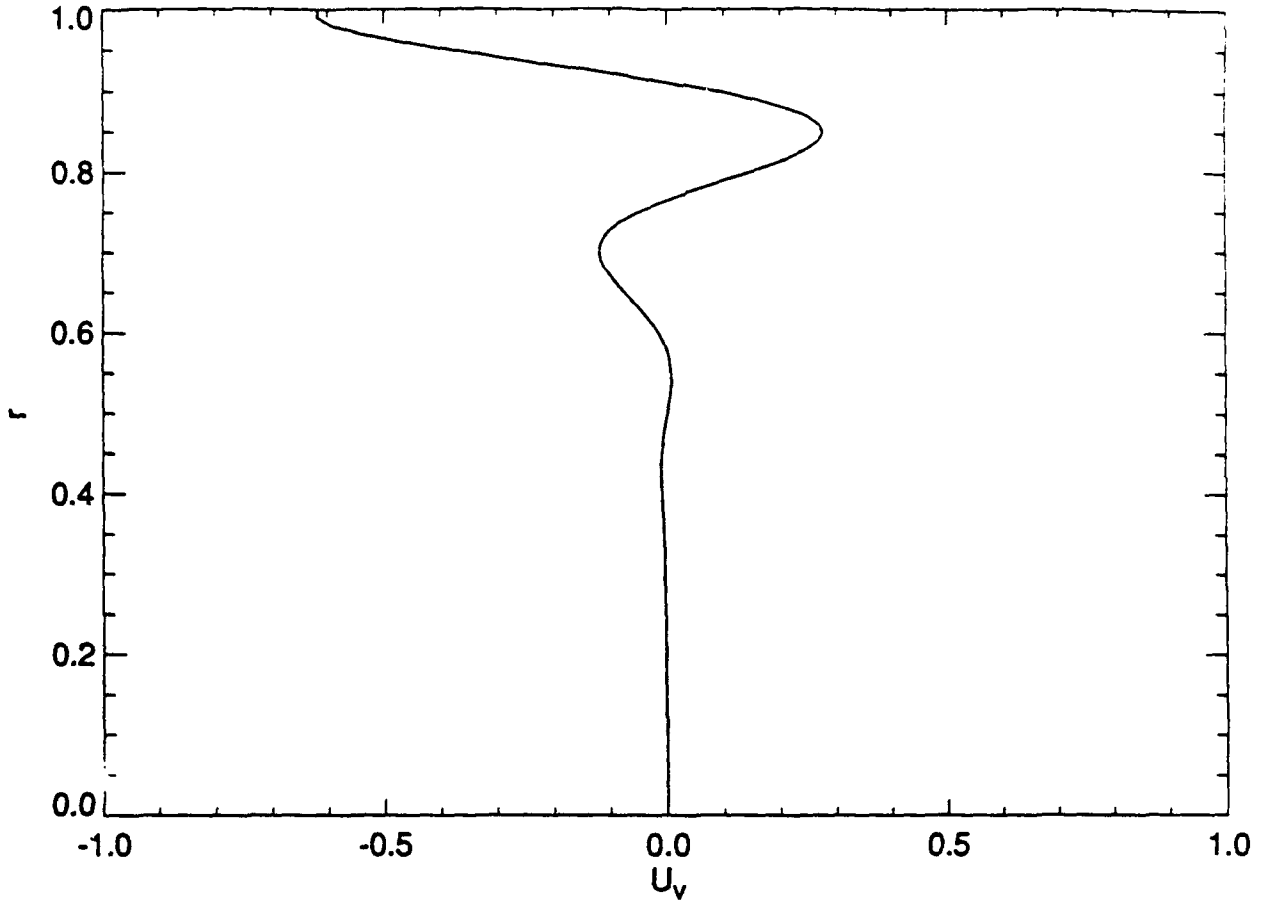

Fig. 13c

KADIR K., D.R. KASSOY, Q.Z.

Fig.13c